Modelling of Gas-Condensate Flow around Horizontal and Deviated wells and Cleanup Efficiency of Hydraulically Fractured Wells

By

Panteha Ghahri

Submitted for the degree of **Doctor of Philosophy** in

Petroleum Engineering

Heriot-Watt University

Institute of Petroleum Engineering

October 2010

ABSTRACT

Gas condensate reservoirs, when the pressure falls below dew point, are characterised by the appearance of condensate bank and exhibiting a complex phase and flow behaviour around the wellbore. The unique dependency of the gas and condensate relative permeability (k_r) on the velocity and interfacial tension (IFT) complicates the well productivity calculations both in field simulation models and in simple engineering calculations, especially for complex well geometries such as horizontal or deviated or hydraulically fractured wells.

The current research work has two parts. The first part is devoted to study the flow behaviour around horizontal wells (HWs) and deviated wells (DWs) in gas condensate reservoirs. Here, several in-house simulators have been developed for single-phase and two-phase gas condensate flows. The two phase in-house simulators accounts for the phase change and the dependency of relative permeability to interfacial tension and velocity, due to coupling (increase in k_r by an increase in velocity or decrease in IFT) and inertia (a decrease in k_r by an increase in velocity). The integrity of the in-house simulators has been verified by comparing some of its results with those obtained using the fine grid option of the ECLIPSE300 commercial reservoir simulator under the same flow conditions. Using the 3-D in-house simulator a large data bank has been generated covering a wide range of variations of pertinent geometrical and flow parameters. Then a general approach is proposed for estimation of an effective wellbore radius of an equivalent open-hole (EOH) radial 1-D system replicating flow around the 3-D HW system. The results of the proposed formulation, which benefits from suitable dimensionless numbers, has been tested against the simulator results not used in its development confirming the integrity of the approach. The proposed formulation, which is simple and easy to use, correctly converts to that suitable for single-phase non-Darcy (inertial) flow systems when total gas fractional flow (GTR) is unity. An extensive sensitivity study has also been conduct to highlight the limitations of current geometric skin formulations widely used in the petroleum industry for HW productivity calculations. The in-house improved geometric skin formulation is more efficient especially for anisotropy, partial penetration and location of HW in the vertical direction.

The same exercises have been performed to study the flow behaviour around deviated wells. That is, the corresponding proposed mechanical and flow skin factors

are converted into an effective wellbore radius, before being applied in the pseudo-pressure calculation of the equivalent open hole system. Here due to the similarity of flow around HWs and DWs a simple relationship is proposed between the corresponding skin factors of these two well geometries. Therefore, in the proposed general method for modelling of the two-phase flow of gas and condensate around a DW, effective wellbore radius estimated for the HW with the same well length is converted to skin and then included in the proposed formulation before being converted to the effective wellbore radius of the equivalent open hole model replicating flow around 3-D flow geometry.

Hydraulic fracturing is one of the most important stimulation techniques especially for tight gas reservoirs. The second part of this research work is devoted to conduct a parametric study to evaluate the impact of the pertinent parameters on the cleanup efficiency, as one of main reasons for poor performance of hydraulic fracturing operation, of gas and gas condensate reservoirs. This study has two parts. In the first part, a comprehensive sensitivity study conducted to evaluate the impact of pertinent parameters on the cleanup efficiency of a hydraulically (gas or gas-condensate) fractured well. Here the key parameters which have significant impact on the gas production loss (GPL) are identified. A new method is proposed to simulate a more realistic fracture fluid (FF) invasion into matrix and fracture, which proves to be one of the main reasons of the contradictory results found in the literature. However since none of such studies have embarked on a much needed extensive investigation of variation of all pertinent parameters, the second part of study is concentrated on a much more expanded study following statistical approaches. Here based on the results of the first part, key parameters have been identified. A 2-level full factorial statistical experimental design method has been used to sample a reasonably wide range of variation of pertinent parameters covering many practical cases for a total of 16 parameters. Since over 130000 simulation runs have been required, to cover the range of variation of all parameters the simulation process has been simplified and a computer code, which automatically links different stages of these simulations, has been developed. The analysis of the simulation runs using two response surface models (with and without interaction parameters) demonstrates the relative importance of the pertinent parameters after different periods.

Acknowledgements

I would like to express my deepest gratitude and respect to my principal supervisor, Dr Mahmoud Jamiolahmady. I have always benefited from his expertise supervision, brilliant ideas, valuable advice and extensive knowledge. His careful editing contributed enormously to the production of this thesis. I truly like my time working with him.

I am also most grateful to another supervisor, Dr Mehran Sohrabi, for his constructive guidance, generous support and inspired suggestions on my work during the years.

I always feel so lucky to have worked with the two excellent supervisors over these years.

I am also very grateful to my examiners, Dr Jim Somerville and Prof. Odd Steve Hustad for taking their time to read my thesis and sharing their valuable comments and suggestions, their role were very constructive. I did really enjoy my time during the viva.

My special thanks go to my husband, Mr Hossein Moradpour who left his job to accompany me for the years of this study. His infinite patients and invaluable support towards the end of this thesis was very encouraging.

I would like to thank my lovely and beautiful son Parsa for his understanding and patients during the time that I was not around him.

I also wish to express my warmest thanks to my colleague and friend, Mrs Farzaneh Sedighi who encouraged and supported me throughout the years.

The financial support of the National Iranian Oil Company, Research and Technology through the award of their full scholarship to conduct this work is sincerely acknowledged.

Table of Contents

List of Figures

List of Tables

List of Symbols

Nomenclature

a	extension of drainage volume of horizontal well in x direction
a_i	coefficients of the equation
B_o	oil formation factor
C	constant in Equation 3.15
C_L	leakoff coefficient
c_t	total compressibility factor
h	reservoir thickness
I_{ani}	$\sqrt{\frac{k_h}{k_v}}$
J	productivity index
k	absolute reservoir permeability
k_d	permeability after porosity blockage
k_v	vertical permeability
k_h	horizontal permeability
k_r	relative permeability
K_{max}	end point of the Corey relative permeability curve
L	length
$\dot{m}$	mass flow rate
$\mathbf{n_g}$	exponent of the gas Corey relative permeability curve
$\mathbf{n_w}$	exponent of the water Corey relative permeability curve
P	pressure
P_c	capillary pressure
P_d	threshold pressure
$\bar{p}$	volumetric average pressure
q	flow rate
r	radius
r_w'	effective wellbore radius
R	flow resistance
Re	Reynolds
R^2	the coefficient of multiple determination
S	skin factor

S_d	damage skin factor
S_f	flow skin factor
S_m	geometric skin factor
S_θ	pseudo skin factor
S_w	water saturation
S_z	horizontal well location skin
t	time
V	velocity
V_{rc}	relative volume
w_f	fracture width
x_i	variables of the equation
x_{ic}	scaled coded parameters
x_j	mass fraction of component j in liquid phase
x_f	Half length of the fracture
X_{res}	length of the reservoir
y_j	mass fraction of component j in vapour phase
Y_{res}	width of the reservoir
z	z direction
z_j	mass fraction of component j in the mixture of liquid and vapour

Greek Letters:

ϕ_d	porosity after damage
ϕ	undamaged porosity
μ	viscosity
M	mobility
ρ	density
β	inertia factor
Ψ	pseudo pressure
θ	deviation angle
λ	pore size distribution index
ϕ_d	porosity after damage
∇	Laplace operator

σ	interfacial tension
v	flow rate

Subscript

ave	average
bhp	bottom hole pressure
c	condensat
d	damage
dew	Dew point
Darcy	Darcy flow
DW	deviated well
e	external as in r_e.
eqphase	Equivalent phase
f	fracture
fp	fully penetrating
g	gas
h	horizontal
HW	horizontal well
i	an index
j	an index
m	matrix
o	oil
OH	open-hole
pp	partial penetrating
r	residual
x	x-direction
y	y-direction
w	refers to well-bore

Abbreviations

AD%	absolute deviation (percentage)
AAD%	average absolute deviation (percentage)
C1	methane
n-C4	normal butane
n-C10	normal decane

CCD	central composite design
CCE	constant composition expansion
CPU	computer science
CVD	constant volume depletion
1-D	one dimensional
2D	two dimensional
3-D	three dimensional
DW	deviated well
EOH	equivalent open-hole
EOS	equation of state
FVR	The ratio of injected fracture fluid to fracture volume
GTR	gas total ratio (in flow)
IFTR	interfacial tension ratio
HFW	hydraulically fractured well
HW	horizontal well
IFT	interfacial tension
IPE	institute of petroleum engineering
ILRM	linear with interaction response surface model
k_{rgtr}	relative permeability ratio
LRM	linear response surface model
OH	open-hole
PR	productivity ratio
PR3	3 parameter peng robinson equation of state
PSS	pseudo-steady state
SEE	standard error of estimate
SS	steady state
UFD	universal fracture design
dra	drainage
imb	imbibition
FF	fracture fluid
FFPT	total fracturing fluid production
FFR	fracture fluid residue
FFv	fracture fluid viscosity
FFV	fracture fluid volume
FFvP	fracture fluid viscosity during production time

FFVR	the ratio of the fracture fluid to fracture volume
GCR	Gas Condensate Research Group
HWU	Heriot Watt University
GPL	gas production loss
GPR	gas production rate
IFT	interfacial tension
k_{fd}	refers to the case with reduced fracture permeability
k_{md}	refers to the case with reduced matrix permeability of FF invaded zone
n-k_{rffg}	Corey exponent for fracturing fluid relative permeability curve
n-k_{rgff}	Corey exponent for gas relative permeability curve
$\overline{M}$	mass mobility ratio
P_{cmd}	refers to the case with increased capillary pressure of invaded zone
PDE	partial differential equation
RSM	response surface model
S_{ffm}	refers to the case with FF saturation in the matrix invaded zone
TGP	total gas production
MLDO	maximum liquid drop out
VW	vertical well

INTRODUCTION

It is well documented that flow behaviour of gas condensate reservoir differs from the conventional oil gas system (Jamiolahmady et al 2000). The reduction of the well productivity due to the accumulation of the condensate bank around the wellbore when the pressure falls below the dew point is the main issue for development of many gas condensate reservoirs. The dependency of relative permeability of such low IFT systems to interfacial tension (IFT) (Bardon and Longeron 1980, Asar and Handy 1988) and velocity (Danesh et. al, 1994, Henderson et. al 1995, Ali et. al 1997, Bloom et. al 1997) complicates the negative impact of condensate banking on well productivity.

In the last two decades, drilling horizontal (HWs) and deviated (DWs) wells has become a common practice around the world. An accurate estimation of productivity of such flow geometries for gas condensate systems using a numerical simulator is a challenging task. This is mainly because the 3-D simulation of flow requires fine grid to capture the abrupt variations of fluid and flow parameters around the wellbore. This can be cumbersome and impractical for field applications. The main body of this research work is devoted to review the available techniques for the estimation of the well productivity of horizontal (HWs) and deviated (DWs) wells both in field simulation models and in simple engineering calculations and propose a practical methodology for the flow calculations of such complex geometries in gas condensate reservoirs.

Hydraulic fracturing is one of the most important stimulation techniques especially for tight gas reservoirs. Over the last 60 years, there have been many reports on the poor performance of some of the hydraulically fractured wells albeit conflicting reports about the main causes. The second part of this research work is devoted to conduct a parametric study to evaluate the impact of the pertinent parameters on the cleanup efficiency, as one of main reasons for such poor performance, of gas and gas condensate reservoirs.

Chapter 2 of this thesis presents a brief description of the key features of gas condensate reservoirs. The condensate build up around the wellbore which is the main characteristic of such reservoirs will be discussed in the separate section. Next the gas condensate fluid composition, fluid properties and phase behaviour will be described. The phase diagram and fluid description of gas condensate fluids used in this study will

be also shown. Here the two most common PVT tests conducted on gas condensate fluids, at the reservoir temperature in the petroleum industry (i.e. the constant composition expansion (CCE) and the constant volume depletion (CVD)) will be briefly reviewed. In Sections 4 the dependency of the relative permeability (kr) of gas condensate system on IFT (Interfacial tension) and velocity will be discussed. The generalize correlation (Jamiolahmady et al. 2009) used in this study expressing the simultaneous impact of coupling (increase in kr by an increase in velocity or decrease in IFT) and inertia (a decrease in kr by an increase in velocity) will be also described. The compositional modelling of gas condensate fluid will be explained in Section 5 of this chapter. The last two sections of Chapter 2 are devoted to provide a short description of horizontal and deviated wells and cleanup efficiency of the hydraulically fractured wells. These sections also review previously published works in these two areas.

Chapter 3 focuses on the study of the single phase and two-phase flow (gas condensate) behaviour around horizontal wells. This chapter starts with the statement of the problem followed by a number of examples of the numerical simulation of such wells using the ECLIPSE300 commercial reservoir simulator. The results of a series of sensitivity analyses evaluating the impact of pertinent parameters, including reservoir thickness, layering, anisotropy, fluid richness, condensate liquid drop out, coupling and inertia on the efficiency of a single HW model will be also presented here. The single phase 3-D HW in-house simulator has been developed to simulate the flow of a single-phase around a HW will be described next. Finite element based Comsol mathematical package was used in this exercise. The details of governing equations and mathematical solution technique will be presented in section 3. In section 4, the effect of anisotropy on the HWs performance will be investigated comprehensively. The productivity of a HW calculated by the in-house simulator with that estimated by the model constructed using ECLIPSE and those predicted by widely used equations in the literature are compared in the next section. Based on the results of the in-house simulator a geometric skin has been driven using statistical tools response surface model in section 7. The impact of partial penetration and the horizontal wellbore location has been also studied in the separates sections and different skin formulations have been proposed using the data of the developed in-house simulators. Non-Darcy flow, where flow performance is adversely affected by the inertia at high velocities, around HWs is discussed next. Here it will be discussed the most appropriate approach for such well productivity calculations is to adopt the concept of effective wellbore radius, rather than skin, in the

1-D open hole radial model. This gives more reliable representation of the 3-D nature of the actual flow pattern. The proposed effective wellbore radius equation benefits from suitable dimensionless numbers which express the impact of pertinent parameters, i.e. velocity and geometric parameters. A methodology will be presented here for efficient implementation of the proposed formulation that depends on velocity.

To the best of the author‘s knowledge, the formulations available in the literature are for single phase Darcy flow. In gas condensate reservoirs, the flow behaviour around HWs is more complex due to the combined effects of coupling and inertia. Therefore, section 8 of this chapter is devoted to study two-phase flow of gas condensate around the HWs. 3-D and 1-D two-phase compositional HW and VW in-house simulators have been developed for this purpose. Here the proposed formulation for calculation of the effective wellbore radius for single phase non-Darcy flow is extended for two-phase flow of gas condensate. The validation of the proposed procedure and formulation will then be demonstrated over a wide range of the variation of the pertinent parameters. The last part of this chapter examines the application of the proposed general formulation (which extends to single-phase flow conditions when gas fractional flow is unity) and methodology developed for steady state conditions to pseudo steady state conditions for both single-phase and two-phase flow of gas and condensate.

In Chapter 4, which is devoted to the study of flow behaviour around the DWs, starts with a review of the published works including the problem statement. Similarly to the HWs study, first the structure of an in-house simulator developed to simulate the flow behaviour of single phase around a DW is presented. The results of the in-house simulator with those of a similar model constructed using ECLIPSE will be compared to demonstrate the integrity of the in-house model. The results of the in-house simulator are also compared with those of ECLIPSE and the predicted values using the available formulations in the literature with an emphasis on isotropic formations, as described in section 3. This exercise highlights the limitations of application of these formulations. Next, the proposed formulations for calculation of mechanical and single-phase non-Darcy flow skins for such well geometries which were developed based on the results of the developed in-house simulators, are presented. Similarly to the approach proposed for HWs in the previous chapter, the skin is converted into an effective wellbore radius, before being applied in the pseudo-pressure calculation of the equivalent open hole system. Since all available equations in the literature are only applicable for the single phase flow, the single-phase mathematical modelling approach has been extended to two-phase flow of gas and condensate by developing a 3-D two phase compositional in-

house simulator as described in section 6 of this chapter. Here the governing equations, structure and solution method will be discussed separately. The results of two phase DW in-house simulator with those of the same DW model constructed using ECLIPSE300 will be compared next. This study covers a range of the variation of the flow parameters for DWs with different deviation angles. A general method for modelling of the two-phase flow of gas and condensate around DWs has also been proposed using an equivalent open hole approach, which will be described in section 6 of chapter 4. The results of a comprehensive sensitivity study conducted to evaluate the impact of pertinent parameters including inertia and coupling on the performance of such wells will be presented before summarising the main conclusions of this study.

The last part of this research work focuses on the study of the cleanup efficiency of hydraulically fractured wells in gas and gas condensate reservoirs, which will be discussed in Chapter 5. The first section of this chapter is dedicated to stating the problem and exploring the research objectives. This study has two parts. In the first part, the results of a comprehensive sensitivity study conducted to evaluate the impact of pertinent parameters e.g. fracture permeability reduction due to fracture fluid residue and reservoir conditions (closure pressure and reservoir temperature) (k_{fd}), the fracturing fluid (FF) viscosity variation during cleanup, matrix capillary pressure (P_{cm}), FF invasion into matrix (i.e., the saturation of FF into the matrix, S_{ffm}), a reduction of permeability of the matrix invaded zone (k_{md}), an increase in capillary pressure of the matrix invaded zone (P_{cmd}), initial water saturation, hysteresis, FF relative permeability and pressure drawdown on the cleanup efficiency of a hydraulically (gas or gas-condensate) fractured well. Here the key parameters which have significant impact on the gas production loss (GPL) are identified. The conflicting reports in literature on this subject will be discussed. A new method will be presented to simulate a more realistic FF invasion into matrix and fracture, which proves to be one of the main reasons of the contradictory results found in the literature. None of these studies have embarked on a much needed extensive investigation of variation of all pertinent parameters. Section 4 of this chapter presents the finding of the second part of this study. Here based on the results of the first part, key parameters have been identified. A 2-level full factorial statistical experimental design method has been used to sample a reasonably wide range of variation of pertinent parameters covering many practical cases for a total of 16 parameters. The impact of fracture permeability (k_f), pressure drawdown, matrix permeability, pore size distribution index, threshold pressure, interfacial tension, porosity, residual gas saturation and the exponents and end points of Corey type relative

permeability curve for gas and FF in the matrix and fracture have been studied for two separate FF volumes. Since over 130000 simulation runs have been required, to cover the range of variation of all parameters the simulation process has been simplified and a computer code, which automatically links different stages of these simulations, has been developed. The structure and details of this code will be described separately in this section. The results of another exercise, which evaluates the validity of the simplified method for injection of FF introduced in this part, will also be discussed. The analysis of the simulation runs using two response surface models (with and without interaction parameters) will be discussed in the last part of this section. The relative importance of the pertinent parameters after different periods will be presented here.

The main conclusions of this thesis will be found in chapter 7. This chapter also includes some recommendations for further investigations of the research areas discussed in this work.

References

Ali J.K., McGauley P.J., and Wilson C.J., Oct. 1997: The Effects of High Velocity Flow and PVT Changes near the Wellbore on Condensate Well Performance, SPE 38923, Proc. of SPE Annual Technical Conference and Exhibition, Texas, pp. 823-838.

Asar H. and Handy L.L., Feb 1988: Influence of Interfacial Tension on Gas/Oil Relative in a Gas-Condensate System, SPE 11740, SPERE 3(1), 264-275.

Bardon C. and Longeron D.G., Oct 1980: Influence of Very Low Interfacial Tension on Relative Permeability, SPEJ 20(3), 391-401.

Blom S.M.P, Hagoort J. and Seotekouw D.P.N., Oct. 1997: Relative Permeability near the Wellbore Conditions, SPE 38935, Proc. of SPE Annual Technical Conference and Exhibition, Texas, pp. 957-967.

Danesh A., Khazem M., Henderson G.D., Tehrani D.H. and Peden J.M., June 1994: As Condensate Recovery Studies, Proc. of DTI Oil Recovery and Research Dissemination Seminar London.

Henderson G.D., Danesh A., Tehrani D.H., Al-Shaidi, S. and Peden J.M., Oct 22-25 1995: Measurement and Correlation of Gas Condensate Relative Permeability by the Steady State Method, SPE paper presented at the 1995 SPE annual Technical Conference and Exhibition, Dallas, Texas, USA.

Jamiolahmady M., Danesh A., Tehrani D.H. and Duncan D.B., 1999: A Mechanistic Model of Gas Condensate Flow in Pores, Trans Porous Media 41(1), 17-46.

Jamiolahmady M., Sohrabi M., Ireland S., and Ghahri P. , 2009: A Generalized Correlation for Predicting Gas-Condensate Relative Permeability at near the Wellbore Conditions, Journal of Petroleum Science and Engineering.

GAS CONDENSATE RESERVOIRS

2.1 INTRODUCTION

In recent years, Gas Condensate reservoirs are becoming more popular as development and operational technologies are being extended to greater depths and higher pressure formations.

Figure 2.1 shows a classic phase envelope diagram of a multi component mixture. The critical and cricondentherm points are also shown in this phase envelope diagram. The critical point is the point where the bubble and dew point lines meet, while the cricondentherm is the maximum temperature at which the two-phase gas and oil coexist. A reservoir with a temperature falling in between critical and cricondentherm points is characterized as a gas condensate reservoir.

In gas condensate reservoirs unlike gas reservoirs, two hydrocarbon phases (gas and condensate) can exit under reservoir conditions. This makes the phase and flow behaviour totally different from those for dry gas reservoirs. Also, it is well documented that fluid flow behaviour of near critical gas condensate systems is different from that of conventional oil gas systems, especially around the wellbore, a region, which significantly affects the well productivity. That is, gas condensate systems are characterized by very low interfacial tension. Thus, the relative permeability of gas condensate systems has a unique dependency on interfacial tension (Bardon and Longeron 1980, Asar and Handy 1988) and velocity (Danesh et. al, 1994, Henderson et. al 1995, Ali et. al 1997, Bloom et. al 1997), as will be explained later in this chapter.

The condensate phase can cause severe loss in gas production and recovery. For gas condensate reservoirs the composition of the well stream during the depletion process changes with time and also differs from the reservoir fluid. Therefore, an accurate and highly sophisticated prediction of the performance and recovery of such systems depends on a comprehensive understanding of their phase and flow behaviours.

Generally speaking, hydrocarbons in a gas condensate reservoir are single-phase during the time of discovery. Under the isothermal depletion process, once the pressure falls below the fluid dew-point pressure, retrograde condensation will commence in the reservoir and condensate saturation will increase as depletion continues. However, it will reach a maximum value, referred to as maximum liquid dropout (MLDO), after which condensate saturation will decrease and may it be vaporized, if depletion continues to a certain pressure in the fluid phase envelope. Apart from the gas produced,

retrograde condensate adds economic value for the total fluid recovery (if and only if we are able to ensure as much condensation process as possible at the surface instead of in the reservoir).

The main challenge in gas condensate reservoir development, therefore, is how to maximize fluid recovery with the minimum retrograde condensation at reservoir conditions. Reservoir condensation is undesirable due to the fact that the valuable retrograde liquid can be lost in the reservoir or most likely, will not be recovered, under the natural depletion process. Furthermore, reservoir condensation can cause a potential loss of well deliverability due to the liquid accumulation around the wellbore region (known as condensate banking or blockage), which reduces the gas relative permeability. The well performance in gas condensate systems also strongly depends on the dependency of their relative permeability on interfacial tension and velocity as well as phase behaviour. Accordingly, a reservoir simulator must take into account these effects in order to make a sufficiently accurate prediction of their performance.

In the forthcoming sections, a brief description of gas condensate reservoirs which is available in the literature as well as the work of the Gas Condensate Research Group at Heriot Watt University (GCR-HWU) will be discussed and related to the main body of the author‘s research.

2.2 CONDENSATE BUILD UP

The main characteristic of a gas condensate system is the appearance of retrograde condensate, which considerably affects the well productivity. First, the condensate liquid accumulates around the wellbore where bottom hole pressure is below dew point, Figure 2.1. The condensate bank will propagate away from the wellbore as the pressure drops below dew point across the reservoir, Figure 2.1. This process creates two regions across the reservoir. The first region is a two-phase region where both gas and condensate exist and flow to the wellbore. While away from the wellbore, a second region contains a single-phase gas only.

Several investigators (Saeidi and Handy 1974, Gravier et al. 1983, Asar and Handy 1988) have reported that condensate in the first region will be immobile until it reaches a critical condensate saturation, at which point it can flow. These studies reported very high critical condensate saturation. (Danesh et. al 1991) demonstrated experimentally by micro models that the critical condensate saturation is equal to or very close to zero. They also showed that condensate flows through the pores with the gas but that relative

permeability of the condensate is very small compared to that of the relative permeability of gas. Thus, the system around the wellbore reaches a steady state condition after a certain period of production. That is, condensate will accumulate around the wellbore due to the very small magnitude of its relative permeability until the flow towards the wellbore becomes equal to outflow from the well.

Since 1986, many studies on two phase flow of gas and condensate have been conducted experimentally and theoretically in GCR-HWU. These results cover a wide range of velocity and IFT. These experiments were conducted under steady state conditions to mimic the flow conditions in the near-wellbore region. The results indicated that the time required to reach steady state condition is different depending on the rock pore structure and characteristics. This time increases for tight rocks, where the pressure drop across the core is high. As will be discussed later in this chapter, this data bank of relative permeability curves measurements has been used to develop a generalized correlation (Jamiolahmady et al. 2009) for relative permeability prediction in the near wellbore region.

2.3 GAS CONDENSATE RESERVOIR FLUID

Hydrocarbon reservoir fluids are divided into five groups (black oil, volatile oil, gas condensate, wet gas and dry gas), according to their phase behaviour. These groups are described as specified regions in the phase envelope diagram, Figure 2.1. It should be noticed that wet gas is gaseous in the reservoir condition that contains heavy components which are condensable when it brought up to the surface, while gas condensate is both gaseous and liquid in the reservoir conditions. From production data analysis, a reservoir which produces gas and oil with ratio between 8000 and 70000 Scf/bbl is considered as a gas condensate reservoir.

A typical gas condensate reservoir fluid is a multi-component mixture. Table 2.1 shows the composition of such a typical reservoir fluid. Generally, composition data are used to predict the fluid phase behaviour and physical properties. These data can be obtained by flashing the reservoir fluid at atmospheric pressure and measuring the composition of the gas and liquid phases (Danesh et al. 1998). The phase behaviour of the gas condensate system is very sensitive to the amount of heavy components. The PVT tests are conducted to simulate the flow behaviour in the reservoirs and also provide reliable composition and volumetric data. The two most common PVT tests conducted at the reservoir temperature in the petroleum industry are the constant

composition expansion (CCE) and the constant volume depletion (CVD). In the constant composition test, a required amount of gas condensate at a pressure above the initial reservoir pressure is injected into the visual cell, and then the cell pressure is reduced in a stepwise manner and the volume of gas and condensate at each pressure step are recorded. In the constant volume depletion test the cell is originally loaded with reservoir fluid and expanded in several steps. The equilibrium gas phase at each step is released in such a way that the volume of the cell is kept constant.

One of the most important properties being measured during both these tests is the relative volume of condensate, known also as the maximum liquid dropout (MLDO), defined using the following equations:

$$V_{rc} = \frac{V_c}{V_d}$$

or

$$V_{rc} = \frac{V_c}{V_t}$$

The difference between these two definitions is the relative volume in the denominators of these two equations. Equation one is the relative volume to the volume at the dew point pressure, while equation two is the relative volume to the total volume of gas and condensate volume. This relative volume or (MLDO) is often used to represent the richness-degree of the fluid. Note that this fluid richness increases as the amount of heavy components increase in the mixture. The potential for hydrocarbon condensation also increases as the reservoir fluid richness increases.

As explained by Danesh et al. (1998), the phase behaviour of multi compound fluids is usually close to that of binary mixture systems. In this study, a binary mixture of two compounds of C1 (methane) and n-C10 (normal decane) and C1 and n-C4 (normal butane) were used to describe the gas condensate reservoir fluid. For the first set of the binary mixture (C1 and n-C10), three gas condensate models with 95, 91.8 and 88 % of C1 (methane) were used. Figure 2.3 shows the phase diagrams for C1-nC4 and rich C1-nC10 (88 % of C1). However, it should be noted that the phase diagram of the reservoir fluid changes according to the fluid composition. The corresponding maximum liquid drop and dew point pressures of these models are 6, 15 and 30 % and 4325, 5089, and 5404 psi at the reservoir temperatures 250^0F. The molar composition of C1 in the binary mixture C1-nC4 was 73.6%. The corresponding values for the dew point and maximum liquid drop of this fluid system are 1917 psi and 27%. It should be noted that for C1-nC4 these values are the reported experimental data from the gas condensate laboratory.

However, for the set of the binary mixture (C1-n-C10) they were obtained by simulating these fluid systems using PVTi option of ECLIPSE simulator.

2.4 GAS CONDENSATE RELATIVE PERMEABILITY

For multiphase systems, relative permeability plays an important role in defining the well productivity. The flow behaviour of gas condensate systems is further complicated by the unique dependency of near wellbore relative permeability on velocity and interfacial tension. The reduction of effective permeability at high velocities due to negative inertia (non- Darcy flow) was first introduced by Forchhiemer (1914). The dependency of relative permeability of low IFT systems on interfacial tension was first reported by Bardon (1980). The improvement of relative permeability of gas and condensate fluids due to an increase in velocity was first reported experimentally by GCR-HWU (Danesh et al. 1994, Henderson et al. 1996). The positive coupling effect, which refers to the improvement of relative permeability as velocity increases and/or IFT decreases, has been proven theoretically and experimentally to be due to the simultaneous coupled flow of the gas and condensate phases with intermittent opening and closure of gas passage by the condensate at the pore level (Jamiolahmady et al. 2000, 2003). His micro models showed that both gas and condensate were following through the pores, as condensate had filled some of pores. At some places, the condensate phase was evolving to form a bridge at a pore throat blocking the way for the gas flow. At this stage, the pressure of the gas behind the condensate bridge seems to build up gradually pushing the condensate out until it overcame the resistance to flow, and opened its way through the liquid bridge (Jamiolahmady et al. 2000).

Experimental work conducted by Henderson et al. (2000) shows that inertia is dominant for a saturated core with 100% gas. However as the condensate forms, the impact of inertia reduces. They showed that increasing velocity in high condensate saturation improves the gas relative permeability due to coupling but for low condensate saturation, the same velocity alteration will decrease the gas relative permeability due to inertia, Figure 2.4.

In fact, the importance of positive coupling and negative inertial effect on the gas condensate relative permeability is a complex function of many parameters such as rock properties, fluid properties (density, viscosity, fluid richness, interfacial tension) and pore velocity. In reality, these two opposite effects are always in competition.

Many empirical correlations have been developed to predict the dependency of relative permeability on velocity and IFT (positive coupling and negative inertia).

Comprehensive literature reviews on this subject as well as details of these empirical correlations are available elsewhere (Jamiolahmady et al. 2009). It should be stated that the saturation-based correlations available in the literature account for inertia and coupling effects separately. Hence, both gas and condensate relative permeability are interpolated between a base curve and a miscible curve to account for positive coupling effects only. Negative inertial effect is then estimated, using a separate formula, in order to correct the interpolated gas and condensate relative permeability curves. Furthermore, in order to use these correlations we need to measure core specific constants which are a function of rock pore structure. Thus, using these correlations to study the impact of coupling and inertia for a wide range of IFT, velocity, and rock types would be a cumbersome process if not technically infeasible.

In this work, the author used a generalized correlation developed by Jamiolahmady et al. 2009. The main advantages of this correlation compared to the aforementioned ones are that it uses either universal parameters or those parameters that can be estimated from readily available petrophysical data and it also accounts for the combined effect of inertia and coupling.

In this correlation, gas relative permeability is interpolated between a base curve and a miscible curve, both corrected for the effect of inertia, using a generalised interpolation function. The correlation is based on the relative permeability ratio ($k_{rgtr} = k_{rg} / k_{rg}+k_{rc}$) as the main variable, which is closely related to fractional flow. The condensate relative permeability is calculated using the definition of relative permeability ratio. It should be noted that in gas/condensate systems, fractional flow is directly related to fluid composition and pressure at the steady-state conditions generally prevailing near the wellbore, hence, making it much more attractive practically compared to saturation, which depends on core characteristics.

2.5 COMPOSITIONAL MODELING OF GAS CONDENSATE RESERVOIRS

A good understanding of fluid flow through a porous medium requires a good prediction of physical properties and the fluid phase behaviour. A typical representative gas condensate fluid consists of many components which are distributed between the vapour and liquid phase under equilibrium phase changes. The phase behaviour and fluid properties of such systems depend on the pressure and also on fluid composition at the reservoir temperature. For that reason, the study of flow behaviour in these systems requires a compositional model to adequately describe the fluid phase behaviour and

properties. A compositional model uses equations of state (EOS) to estimate the phase behaviour and physical properties of the fluid. An equation of state presents a theoretical relationship between pressure, volume and temperature. The Peng-Robinson and Soave-Redlich-Knowng equations of state are commonly used in the petroleum industry. The phase composition is determined by flashing the fluid over a wide range of pressures. The equations which need to be solved by compositional simulation are the mass balance equation for each component, the sum of all phases saturations to 1.0, and the phase behaviour which has to be consistent with temperature, pressure and composition in each cell. The number of these equations that the simulation should solve increases as the number of components increases. Nowadays, with the rapid advancements in computing techniques, a fully compositional simulation is becoming more feasible; however for multi-millions of cells it is still impractical.

2.6 HORIZONTAL AND DEVIATED WELLS

A horizontal well generally is a well drilled parallel to the horizontal reservoir plane. The main advantages of horizontal wells over vertical wells are:

1) Large drain volume
2) A higher production rate specially from thin layer reservoirs
3) Minimizing water and gas coning problems
4) Significantly reducing the velocity near the wellbore of the gas reservoir to minimize the negative impact of inertia
5) Increasing the chance of the intersection of a large number of fractures for wells in naturally fractured reservoirs
6) Providing better well injectivity for injection wells in the EOR purposes

The main disadvantages of horizontal wells are the added cost and overcoming the problems that occur during drilling. The horizontal well drilling techniques depend on the turning radius, which is the radius required to bend from a vertical well to a horizontal well. Horizontal wells can also be classified into three groups according to their turning radius; short-radius, medium-radius, and long-radius. The horizontal well length that can be drilled depending on the variation of the turning radius between 100 to 4000 ft (Joshi 1991).

The flow behaviour around horizontal wells is more complicated than that for the vertical wells due to 3-D flow geometry. The flow regime is a combination of linear and radial flow. Many authors have proposed a formulation for horizontal well productivity

for steady state and pseudo steady conditions (Borosive 1984, Joshi 1985, Giger 1985, Ronal and Dupuy 1991, Permadi 1995, Shedid 1996, Economides 1996, Helmy and Wattenbarger 1998, Lu 2001, Furui 2003, Tiab 2007, Helmy, and Wattenbarger 1998, Babu-Odeh 1989 and Goode 1991). However, these equations are only applicable for single phase, Darcy flow conditions. Furthermore there are limitations on the range of applicability of these formulations especially for anisotropic reservoirs as highlighted in Chapter 3.

For gas condensate reservoirs the flow behaviour is very complex, due to phase change, inertia and coupling. An accurate estimation of productivity of such systems using a numerical simulator is a challenging task, because this 3-D compositional simulation requires a fine grid exercise to capture the abrupt variation of fluid and flow parameters around the wellbore. This is cumbersome and impractical for field applications. The first part of this study is devoted to studying flow behaviour around a horizontal well by developing a 3-D horizontal well single-phase and two-phase compositional (gas condensate) mathematical simulator under steady state conditions, and proposing a practical approach and formulation to calculate horizontal well productivity. In this approach, using the results of developed 3-D in-house simulators, an effective wellbore radius is defined for an equivalent 1-D open hole radial system replicating two phase of gas and condensate around horizontal well. The application of the proposed approach and formulation has also been validated for pseudo steady state conditions as described in Chapter 3.

In most practical cases, the wells are not horizontal and they are deviated from the vertical plane. Furthermore the productivity of HWs is significantly affected by the reservoir anisotropy. For many cases, drilling deviated and highly deviated wells is more attractive than HWs. The formulations, which are available in the literature for estimating deviated well productivity, are only applicable for single-phase, Darcy flow. They are also limited in application for deviated wells where the deviation angle less than 75^0. Chapter 4 of this study is dedicated to studying the flow behaviour around deviated wells. A procedure similar to that described for horizontal wells is followed. That is, based on the results of 3-D and 1-D in-house simulators a general formulation for calculation of effective wellbore radius of an open hole system is proposed, which is applicable to both single-phase and two-phase flow systems. Here the impact of deviation angle is included in the formulation proposed for horizontal wells to ensure an efficient and practically attractive formulation.

2.7 CLEAN UP EFFICIENCY

Hydraulic fracturing is one of the most important stimulation techniques, especially for tight gas reservoirs. Over the last 60 years, there have been many reports on the poor performance of some of the hydraulically fractured wells. Poor cleanup efficiency of the injected fracture fluid (FF) has been considered as one of the factors contributing to the low productivity of such wells. Fracturing fluid (FF) impairs the gas production, through various mechanisms, by invasion into the matrix and fracture. A number of parametric studies have been conducted, evaluating the impact of a number of pertinent parameters affecting the FF cleanup efficiency (Cooke (1973, 1975), Holditch 1979, Voneiff 1996, Gdanski et al. 2005, Friedel 2006, Barati 2008 and Wang 2009). There are conflicting reports in some of these studies mainly due to the assumptions made when simulating this process (e.g., Bennion et al., 2000, Gdanski et al., 2005). A comprehensive literature review on this subject is available in the chapter 5. In the present research work, study has been conducted to evaluate the impact of pertinent parameters on the clean up efficiency in gas and gas condensate reservoir using the ECLIPSE commercial reservoir simulator. The material this chapter consists of two sections, in the first part, by conducting a series of sensitivities the impact of the pertinent parameters are highlighted including the source of conflicting reports found in the literature simulating this process. It seems that the presence of fracture fluid (FF) in the damage zone influences the gas recovery by reducing the gas relative permeability. It can increase gas production loss (GPL) significantly, if FF invasion was simulated more realistically, as was performed here by allowing the FF to invade all fracture blocks. In the second part, the author embarks on a much more extensive simulation exercise by conducting over 130000 simulations covering the range of variation of pertinent parameters over their range of practical applications. A computer code has also been developed, which links different stages of this process reducing the required CPU time as described in Chapter 5. The analysis of data using the statistical tools, linear response surface model (with and without interaction terms) indicated that the impact of fracture permeability on GPL is most. The other important parameters which influence GPL are FF exponent and end point of Corey type relative permeability curve in the fracture, gas exponent of Corey type relative permeability curve in fracture and matrix, differential pressure across the reservoir, interfacial tension, pore size distribution index, matrix permeability, the end points of Corey type relative permeability curve in the matrix, residual gas saturation in the matrix and porosity.

These results also showed that the relative importance of the parameters decreases as the FF injection volume increases.

References

Ali J.K., McGauley P.J. and Wilson C.J., Oct. 1997: The Effects of High Velocity Flow and PVT Changes near the Wellbore on Condensate Well Performance, SPE 38923, Proc. of SPE Annual Technical Conference and Exhibition, Texas, pp. 823-838.

Asar H. and Handy L.L. , Feb 1988: Influence of Interfacial Tension on Gas/Oil Relative in a Gas-Condensate System, SPE 11740, SPERE 3(1), 264-275.

Bardon C. and Longeron D.G. ,Oct 1980: Influence of Very Low Interfacial Tension on Relative Permeability, SPEJ 20(3), 391-401.

Babu D.K. and Odeh A.S. , Nov. 1989: Productivity of a Horizontal well, SPE Reservoir Engineering, 4(4), 417-421.

Barati R., Hutchins R.D., Friedel T., Ayoub J.A., Dessinges M. and England K.W. , 13–15 February 2008: Impact of Yield Stress and Fracture-Face Damage on Production Using a Three-Phase, 2D Model, SPE 111457.

Bennion D. B., Thomas F. B. and Ma T., 12-15 March 2001: Recent Advances in Laboratory Test Protocols to Evaluate Optimum Drilling, Completion and Stimulation Practices for Low Permeability Gas Reservoirs, SPE 60324.

Blom S.M.P, Hagoort J. and Seotekouw D.P.N., Oct. 1997: Relative Permeability near the Wellbore Conditions, SPE 38935, Proc. of SPE Annual Technical Conference and Exhibition, Texas, pp. 957-967.

Borisov Ju. P., 1984: Oil Production Using Horizontal and Multiple Deviation Wells, Nedra, Moscowfl 964, Translated by J.Strauss, S. D. Joshi (ed.) Phillips Petroleum Co., the R&D library translation, Bartlesville.

Cooke C.E., Sep 1973: Conductivity of Fracture Proppants in Multiple Layers, SPE 4117, JPT.

Cooke C.E., October 1975: Effect of fracturing fluids on fracture conductivity, JPT, pp. 1273-83, Trans., AIME, 259.

Danesh, A., Henderson, G.D. and Peden J.M. , Aug. 1991: Experimental investigation of critical condensate saturation and its dependence on connate saturation in water wet rocks, SPE 19695, SPE Journal of Reservoir Engineering, pp.336-342.

Danesh, A., Khazam, M., Henderson G.D., Tehrani, D.H. and Peden J.M., June 1994: Gas condensate recovery studies, presented at Proceedings of the UK DTI Improved Oil Recovery and Research Dissemination Seminar, London.

Danesh A., 1998: PVT and phase behaviour of petroleum reservoir fluids, Elsevier Science B.V., Amsterdam, Netherland.

Economides, M.J., Brand, C.W. and Frick, T.P., Dec. 1996: Well Configurations in Anisotropic Reservoirs, SPEFE, 257-262. (Also Paper SPE 27980, 1994.).

Forchheimer, P., 1914: Hydraulik, Chapter15, pp. 116-8, Leipzik and Berlin.

K. Furui, D. Zhu and A.D. Hill, 5-8 Oct 2003: A Comprehensive Model of Horizontal Well Completion Performance, SPE 84401-MS.

Friedel T., Mtchedlishvili G., Behr A., Voigt H-D. and Hafner F. , 30 May-1 June 2007: Comparative Analysis of Damage Mechanism in Fractured Gas Wells, SPE 107662.

Gdanski, R., Weaver, J., Slabaugh, B., Walters H. and Parker M., May 2005: Fracture Face Damage-It Matters, SPE 94649.

Gravier, J.F., Lemouzy, P., Barroux, C. and Abed A.F., 1983: Determination of Gas Condensate Relative Permeability on Whole Cores under Reservoir Conditions, SPE 11493-PA.

Giger F., May 1983: Reduction du nombre de puits pm I'tilisation de forages horizontals, Reveue de L'institute Gancais du Petrole, 38.

Giger, FM., Reiss, L.H. and Jourdan, A.P., Sep 1984: The Reservoir Engineering Aspects of Horizontal Drilling, SPE 13024, presented at the 1984 meeting SPE Annual Technical Conference and Exhibition, Houston.

Goode, P.A., and Kuchuk F.J., Aug 1991: Inflow Performance of Horizontal Wells, SPE Reservoir Engineering, p 319-323.

Helmy, M. W. and Wattenbarger, R.A., Sep. 1998: Simplified Productivity Equations for Horizontal Wells Producing at Constant Rate and Constant Pressure, SPE 49090, Presented at the 1998 Annual Technical Conference and Exhibition, New Orleans, Louisiana.

Henderson G.D., Danesh A., Tehrani D.H., Al-Shaidi, S. and Peden J.M., 1995: The Effect of Velocity and Interfacial Tension on the Relative Permeability of Gas Condensate Fluid in the Wellbore Region, 8th IOR Symposium, Vienna.

Henderson G.D., Danesh A., Tehrani D.H. and Al-Shaidi S., June 1996: Measurement and Correlation of Gas Condensate Relative Permeability by the Steady State Method, SPE Journal, 191-201.

Henderson, G.D., Danesh, A., Tehrani, D.H. and Badr Al-kharusi, 3-6 Oct. 2000: The Relative Significance Of Positive Coupling And Inertial Effects On Gas Condensate Relative Permeabilities At High Velocity, SPE 62933, Proceedings of the SPE Annual Technical Conference and Exhibition, Dallas, 193-202.

Holditch, S. A., Dec 1979: Factors Affecting Water Blocking and Gas Flow from Hydraulically Fractured Gas Wells, JPT 1515-1524.

Lu J. and Tiab D. , 31 March-3 April 2007: A Simple Productivity Equation for a Horizontal Well in Pseudo Steady State in a Closed Anisotropic Box-Shaped Reservoir, SPE 106970, Presented at the 2007 SPE Production and Operations Symposium held in Oklahoma, U.S.A.

Lu J., Oct 2001: New Productivity Formulae of Horizontal Wells, Journal of .Canadian Petroleum Technology, 40(10):55-67.

Jamiolahmady M., Danesh A., Tehrani D.H., Duncan D.B., 2000: A Mechanistic Model of Gas Condensate Flow in Pores, Trans Porous Media 41(1), 17-46.

Jamiolahmady M., Danesh A, Henderson G.D. and Tehrani D.H., September 2003: Variations of Gas Condensate Relative Permeability with Production Rate at Near Wellbore Conditions: A general Correlation, SPE 83960, presented at SPE offshore Europe Conference, Aberdeen, UK.

Jamiolahmady M., Sohrabi M., Ireland S. and Ghahri P., 2009: A Generalized Correlation for Predicting Gas-Condensate Relative Permeability at near the Wellbore Conditions, Journal of Petroleum Science and Engineering.

Permadi p., 20-22 March 1995: practical Methods to Forecast Production Performance of Horizontal Wells, SPE paper presented at the Asia Pacific Oil and Gas Conference, held in Kuala Lumpur, Malaysia.

Renard G. and Dupuy J.M., 1991: Formation Damage Effects on Horizontal-Well Flow Efficiency (includes associated papers 23526 and 23833 and 23839), SPE 19414-PA.

Saeidi A. and Handy L.L. , 4-5 April 1974: Flow and Phase Behaviour of Gas Condensate and Volatile Oils in Porous Media, paper SPE 4891 presented at the 1974 SPE California Regional Meeting, San Francisco.

Shedid, S. A., Osisanyia, S. and Tiab D. ,1996: A Simple Productivity Equation for Horizontal Wells Based Upon Drainage Area Concept, SPE 35713 paper presented at the Western Regional Meeting held in Anchorage, Alaska.

Voneiff G.W., Robinson B.M. and Holditch S.A., Nov 1996: The Effects of Unbroken Fracture Fluid on Gas well Performance, SPE-26664.

Wang J.Y., Holditch S.A. and MacVay D. , Jan 2009: Modelling Fracture Fluid Cleanup in Tight Gas Wells, SPE-119624.

Gas Condensate Recovery Project (1999-2002) Final Report, 2002, IPE, Heriot Watt University, UK.

Gas Condensate Recovery Project (2002-2005) Final Report, 2005, IPE, Heriot Watt University, UK.

Gas Condensate Recovery Project (2005-2008) Final Report, 2008, IPE, Heriot Watt University, UK.

Table 2.1: Detailed composition data for a gas condensate fluid (Danesh 1998).

Components	Mol%
Nitrogen	0.298
Carbon dioxide	1.72
Methane	79.139
Ethane	7.483
Propane	3.293
i-Butane	0.515
n-Butane	1.255
i-Pentanes	0.359
n-Pentane	0.551
i-Hexanes	0.282
n-Hexane	0.334
i-Hepanes	0.111
Benzene	0.271
Cyclanes C7	0.389
n-Heptane	0.235
i-Octanes	0.145
Toluene	0.150
Cyclanes C8	0.253
n-Octane	0.168
i-Nonanes	0.158
Aromatics C8	0.143
Cyclanes C9	0.061
n-Nonane	0.113
i-Decanes	0.176
Aromatics C9	0.054
n-Decane	0.084
Undecanes	0.318
Dodecanes	0.273
Tridecanes	0.253
Tetradecanes	0.225
Pentadecanes	0.178
Hexadecanes	0.144
Heptadecanes	0.126
Octadecanes	0.127
Nonadecanes	0.063
Eicosanes-plus	0.553

Molecular Weight= 27.3

"Eicosanes-plus" characteristics: Molecular Weight=353, Density at 288 K=852.1 kg/m^3

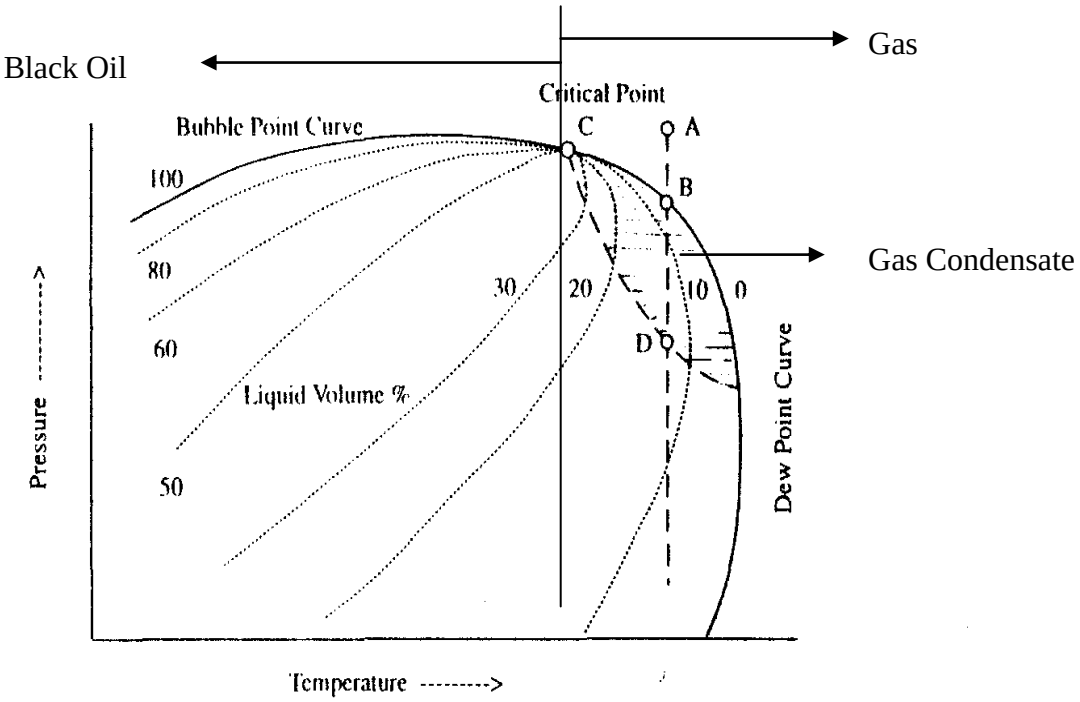

Figure 2.1: A phase diagram of a multi component mixture (Danesh et al. 1998).

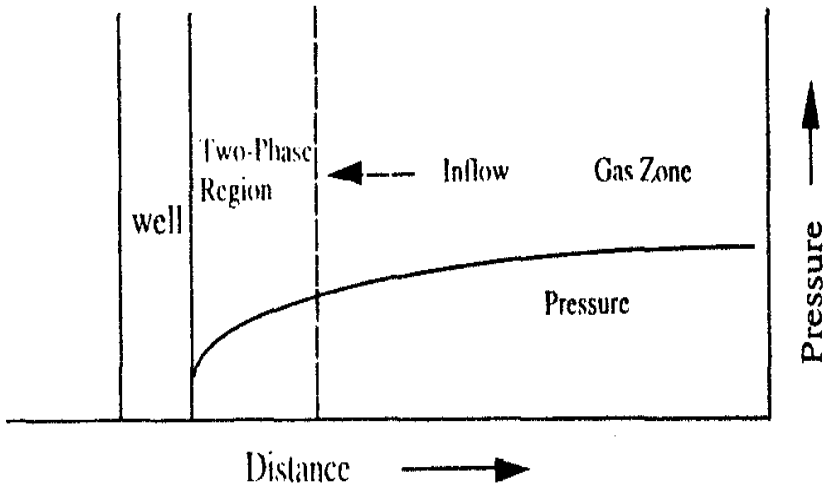

Figure 2.2: The pressure profile around the wellbore in a gas condensate reservoir (Danesh et al. 1998).

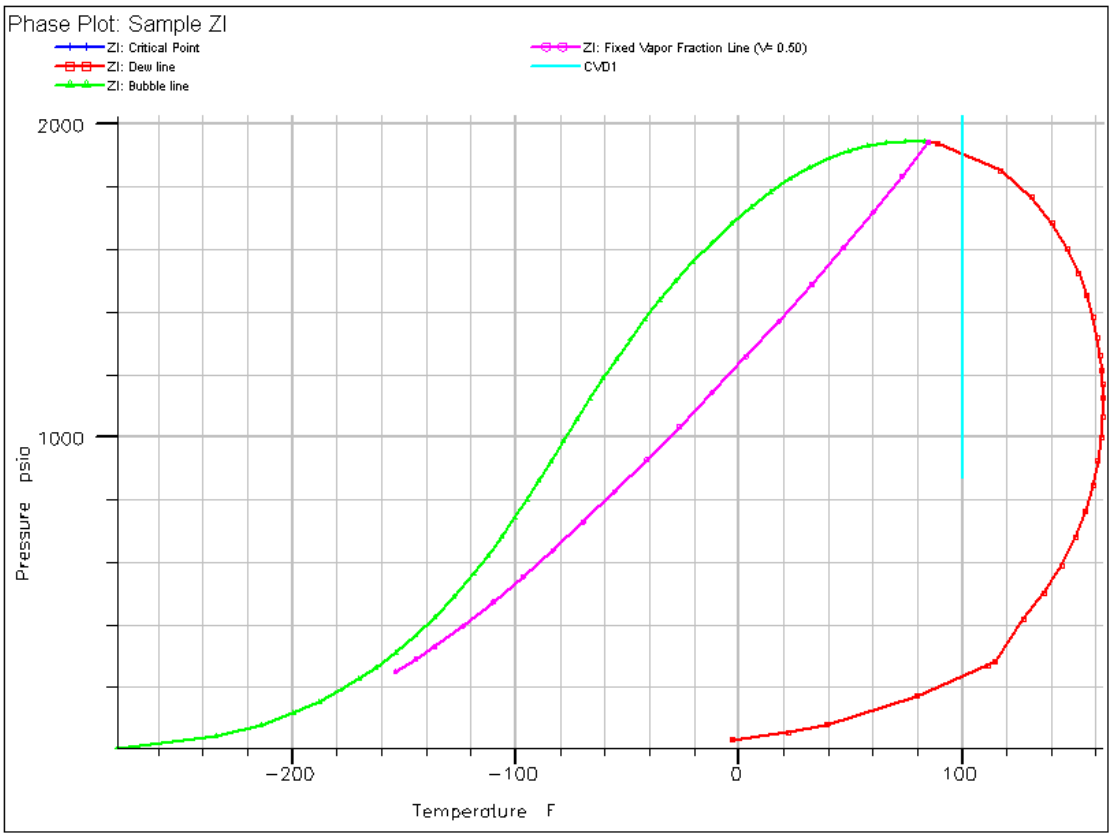

(a)

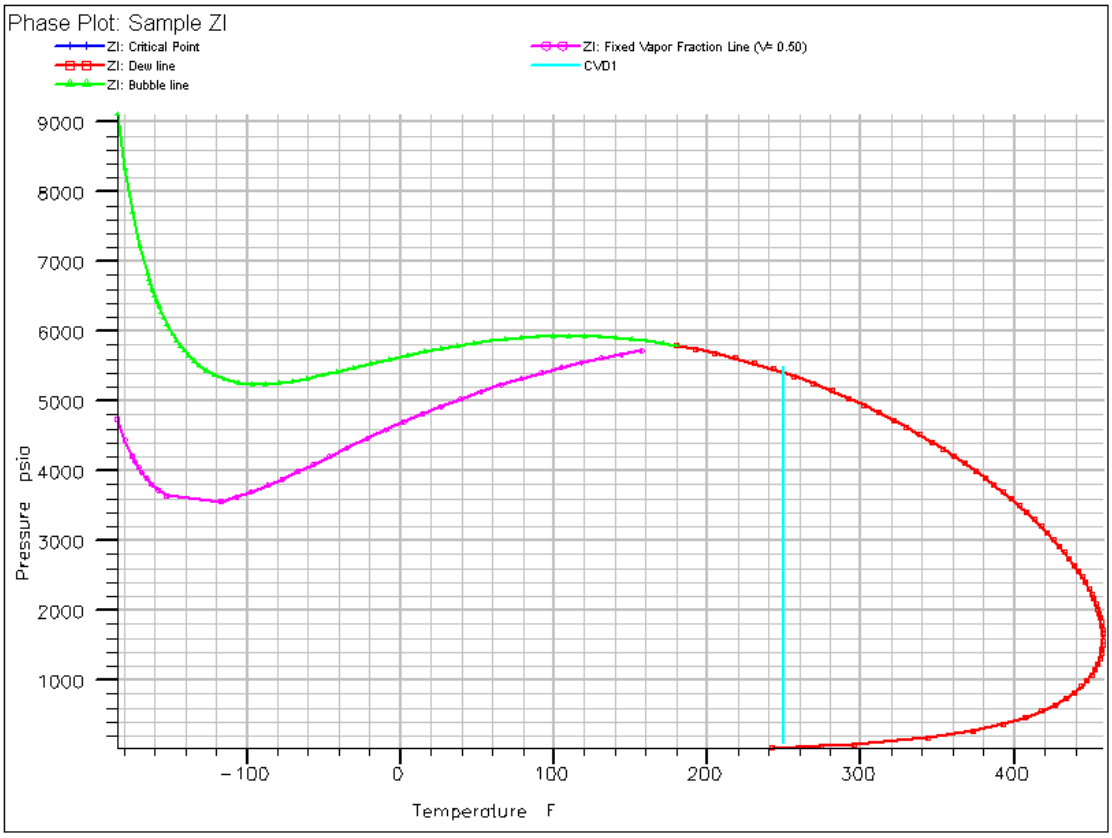

(b)_

Figure 2.3: The phase diagram of two binary mixture reservoir fluids used in the present study, a) C1-nC4 (C1 73.6%), t_{res}=100 ^{0}f b) C1-nC10 (C1 88%), t_{res}=250 ^{0}f

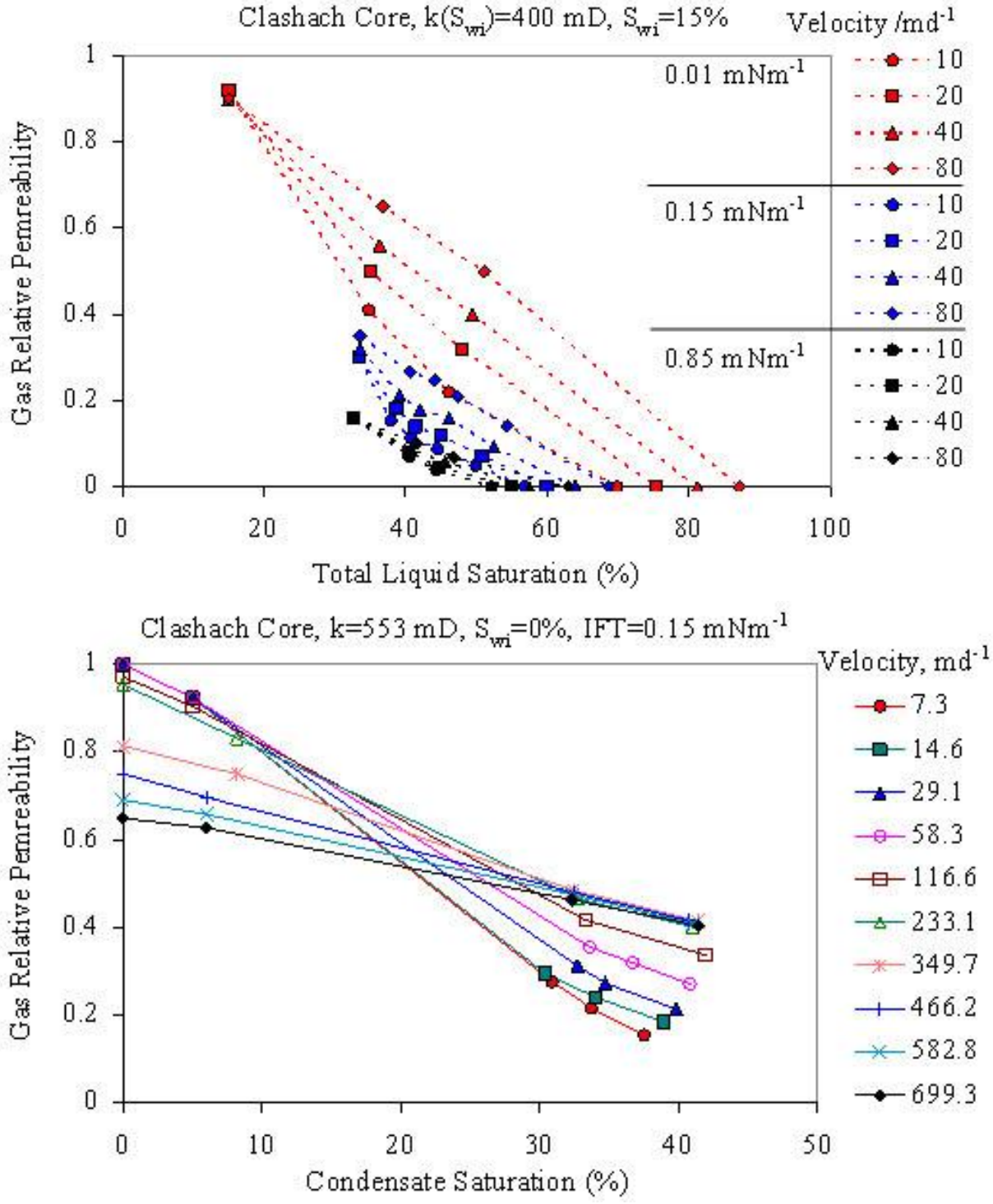

Figure 2.4: The velocity effect on the gas relative permeability (Final Report of Gas Condensate Research Group 1999-2002).

FLOW AROUND HORIZONTAL WELLS

3.1 INTRODUCTION

Over the last few years, many horizontal wells (HWs) have been drilled around the world. The major purpose of a HW is to enhance reservoir contact and thereby enhance well productivity. Often, the productivity index of a HW is 3 to 4 times that of a vertical well (VW) in the same reservoir; as a result several VWs can be replaced by one HW. However, the main disadvantage of a HW is the cost of drilling and operational risk which is much more than that for a VW.

The flow behavior around the horizontal wells is more complicated than that for the vertical wells due to 3-D flow geometry. The flow regime is a combination of linear and radial flow. Simulating such a complex 3-D flow using numerical commercial simulators requires the fine grid approach, which is very impractical and cumbersome. This is especially important for gas condensate reservoirs where the phase change and velocity dependencies of their relative permeability further complicates the flow calculation. In gas condensate reservoirs, as the pressure falls below dew point, a bank of condensate forms around the wellbore, which is affecting the well productivity and flow behaviour around the wellbore. The flow behaviour is further complicated by the variation of relative permeability due to the coupling (increase in kr by an increase in velocity or decrease in IFT) and inertial (a decrease in kr by an increase in velocity) effects.

This study aims to propose new methodologies to include the impact of geometrical and flow parameters affecting the performance of a HW in gas condensate reservoirs. The approach is based on proposing an appropriate expression of skin (or effective wellbore radius) for an equivalent open hole system of a VW.

3.2 LITERATURE REVIEW

Due to the popularity of drilling HWs, many studies have been conducted to propose an accurate formulation for productivity of such wells at steady state (SS) or pseudo steady state (PSS) conditions. However, these are only applicable for single phase conditions. (Borosiv 1984; Joshi 1985; Giger, 1985, Ronal and Dupuy, 1991, Permadi 1995, Shedid 1996, Economides 1996, Helmy,.and Wattenbarger 1998, Jin Lu 2001, Furui 2003, Lu and Taib 2007, Helmy, and Wattenbarger 1998, Babu-Odeh 1989 and

Goode 1991). Theses equations were obtained using semi-mathematical methods and some simplifying assumptions. Here in this section, the author reviews comprehensively the previously published works and also the limitation on the application of theses equations is given.

First equation for HWs productivity calculation at steady state conditions was presented by Borosiv in 1984. He used potential flow theory to obtain his equation based on assuming an elliptical shape for a HW drainage area as follows:

$$q_{HW} = \frac{2\pi kh \Delta p / (\mu_o B_o)}{\ln\left(\frac{4r_e}{L}\right) + \frac{h}{L}\ln\left(\frac{h}{2\pi r_w}\right)} \tag{3.1}$$

where k_h, q and ΔP are the reservoir permeability, flow rate and pressure drawdown in the reservoir, r_w, r_{eh}, L, and h are the wellbore radius, reservoir external radius, horizontal well length, and reservoir thickness, respectively. μ_o is oil viscosity and B_o is the oil formation volume factor.

It should be noted that the above equation is only applicable for isotropic formations.

Joshi (1985) developed another equation to calculate the productivity of HWs at steady state conditions, which is very popular in the petroleum industry. He assumed that the HW was located in the centre of an elliptical drainage area, Figure 3.1a. He divided a three-dimensional (3-D) problem into two two-dimensional (2-D) problems, Figure 3.1b. The 2-D flow of horizontal and vertical planes was calculated using potential flow theory and an electrical analogy concept. The derived equation is based on the uniform flux distribution along the wellbore. Joshi's equation is expressed as follows:

$$q_{HW} = \frac{2\pi kh \Delta p / (\mu_o B_o)}{\ln\left(\frac{a + \sqrt{a^2 - \left(\frac{L}{2}\right)^2}}{L/2}\right) + \frac{h}{L}\ln\left(\frac{h}{2r_w}\right)}, \tag{3.2}$$

where

$$a = \frac{L}{2} \cdot \sqrt{\frac{1}{2} + \sqrt{\frac{1}{4} + \frac{1}{\left(0.5 \cdot \frac{L}{r_e}\right)^4}}}\,. \tag{3.3}$$

The above equation is also only applicable for calculation of HW productivity in an isotropic formation. For an anisotropic formation, he adapted Muskat's vertical axis transformation ($z^{'} = h\sqrt{k_h / k_v}$) and proposed a different equation as follows:

$$z^{'} = h\sqrt{k_h / k_v}\,, \tag{3.4}$$

$$q_{HW} = \frac{2\pi k h \Delta p / (\mu_o B_o)}{\ln\left(\dfrac{a + \sqrt{a^2 - \left(\frac{L}{2}\right)^2}}{L/2}\right) + \dfrac{I_{ani} h}{L} \ln\left(\dfrac{I_{ani} h}{2 r_w}\right)}. \tag{3.5}$$

where

$$I_{ani} = \sqrt{k_h / k_v}\,. \tag{3.6}$$

where k_v and k_h are vertical and horizontal well permeability.

It should be noted that Joshi ignored the effect of the vertical z-direction transformation on the wellbore radius.

He also developed the following equation to account for the effect of the wellbore location in the perpendicular axis (Z) using Muskat's off-centred wells formulation:

$$q_{HW} = \frac{2\pi k h \Delta p / (\mu_o B_o)}{\ln\left(\dfrac{a + \sqrt{a^2 - \left(\frac{L}{2}\right)^2}}{L/2}\right) + \dfrac{h}{L} \ln\left(\dfrac{\left(h/2\right)^2 - l_\delta^2}{2 r_w}\right)}. \tag{3.7}$$

l_δ is the distance of the HW wellbore from middle of the reservoir thickness.

The HW productivity can also be expressed using the VW productivity with a geometric skin factor.

$$q_{HW} = \frac{2\pi k h \Delta P}{\mu\left(\ln\left(\dfrac{r_e}{r_w}\right) + S_m\right)} \tag{3.8}$$

S_m is the geometric skin and r_e is the exterior radius of the reservoir model, which for a square drainage area can be calculated as follows:

$$r_e = \frac{X_{res}}{\sqrt{\pi}}\,. \tag{3.9}$$

A HW can also be replaced by a VW with an effective wellbore radius as below:

$$q_{HW} = \frac{2\pi k h \Delta P}{\mu\left(\ln\left(\frac{r_e}{r_w^{'}}\right)\right)} \tag{3.10}$$

$$r_w^{'} = r_w \times e^{-Sm} \tag{3.11}$$

The geometric skin can be obtained by comparing the productivity index of the VW with that of the HW. The geometric skin represents the impact of well and reservoir geometry on the well productivity.

Giger (1985) expressed another analytical solution by reducing the HW 3-D to two 2-D flow geometries. The HW drainage area shape here is rectangular with one semi-circles at each ends, Figure 3.2. Shedid (2001) showed that Giger‘s equation provides the similar results to Joshi’s equation for the productivity of HWs with length less than 2500 ft.

Renarld and Dupuy (1991) pointed out that the current solution introduced by Giger and Joshi is not appropriate for HWs that have a length much longer than the distance between the tip of the HW and the reservoir boundaries in the HW drilled direction. It should be noted that their approach to calculate the HW productivity was similar to that of Joshi and Giger by dividing the 3-D flow geometry into two 2-D problems. They also used a similar HW drainage area shape to Giger (Figure 3.2). In their method the flow pattern around the HW is divided into i) a linear flow to the HW length with a rectangular drainage shape area and ii) each radial flows at each end with two semi-circular drainage area shapes. The formula proposed for the HW productivity calculation by Renarld and Dupuy (1991) is:

$$q_h = \frac{2\pi k_h h \Delta p \big/ \left(\mu_o B_o\right)}{\cosh^{-1}(X) + \frac{I_{ani} h}{L}\ln\left(\frac{h}{2\pi r_w^{'}}\right)}, \tag{3.12}$$

where

$$X = \frac{Cosh(\pi a/(2b))}{Sin(\pi L/(2b))}, \tag{3.13}$$

$$r_w^{'} = \left[\frac{1+I_{ani}}{2I_{ani}}\right] r_w . \tag{3.14}$$

a and b are the reservoir drainage dimensions in the y and x directions, respectively.

Shedid (1996) introduced a method based on varying the drainage area of the two semi-circles, at both sides of the HW proposed by Renarld and Dupuy (1991). He

divided the HW's drainage area into three parts, i) a rectangular area with length L ii) a small rectangle of length rL/C at the heel side, constant C is calculated by matching the results of the flow rates calculated for the heel-end of HW and the corresponding values of Borosiv and Joshi's equation and iii) a semi-circle of radius r at the toe-end. The analogy between Darcy and Ohm's equation was used to obtain the flow resistance for each part. His formula is expressed as follows:

$$q_h = \frac{2\pi k_h h \Delta p / (\mu_o B_o)}{\frac{\ln(h/2r_w)}{(L/h)} + \left(0.25 + \frac{C}{L}\right)\left(\frac{1}{r_w} - \frac{2}{h}\right)}. \tag{3.15}$$

His formulation is only valid for calculating the HW productivity in isotropic formations.

It was well documented that the HWs productivity decreases significantly by decreasing anisotropy. As mentioned earlier, above equations were obtained based on assumption of the isotropic formation and then as explained before they adopted for anisotropic formation. That is, the application of these equations in the anisotropic formations is always questionable. It will be discussed later this was a topic of many researchers which their work was to give a better formulation for the HWs productivity in the anisotropic formations.

Later a simulator based on finite volume was developed by Economides et al. (1996) to study the well productivity of HWs in anisotropic reservoirs. They used local grid refinement to capture the complexity of flow around HWs. They also compared their simulation results with the corresponding values obtained using Joshi's equation. They reported a significant difference between these two results. They also concluded that Joshi's equation may not predict HW productivity accurately specially for anisotropic reservoirs. They applied the effect of anisotropy on the wellbore radius and on the reservoir thickness using the Peaceman's equation and Muskat's transformation on Joshi's equation (3.2) as follows:

$$q_h = \frac{2\pi k h \Delta p / (\mu_o B_o)}{\ln\left(\frac{a + \sqrt{a^2 - \left(\frac{L}{2}\right)^2}}{L/(2)}\right) + \frac{I_{ani} h}{L} \ln\left(\frac{I_{ani} h}{r_w (I_{ani} + 1)}\right)}. \tag{3.16}$$

As was discussed by Sheng (2007), the solution for an anisotropic problem can not be obtained directly by transforming it into an isotropic system. The flow geometry

around the wellbore is highly complex and there are a lot of factors which may need to be taken into account.

Lu (2001) developed an equation based on a solution to this 3-D problem obtained using fluid potential theory. This approach was similar to that followed by Joshi and Giger but assumed that the HW is in a very large drainage area, so the pressure distribution has not met the reservoir boundary during production time. He demonstrated that there are significant differences between the results obtained using this equation and Joshi and Borosiv's equations for some cases.

In 2003, Furi et al. developed a semi-analytical model to evaluate the formation damage around the HW including reservoir anisotropy and damage heterogeneity. He also derived an inflow equation for HW based on dividing the flow into two regions. The first flow region has a cylindrical shape around the HW, i.e. it is a radial flow pattern with a radius of $h\frac{\sqrt{2}}{2}$. The linear flow region, the second region, starts from the end of the first region and continues to the reservoir boundary. The formula for pressure drop is expressed as summation of the pressure drop in these two regions.

Wange et al. (2007) presented another equation to predict the productivity of the HW. In his model, the flow geometry around the HW is described by dividing the reservoir thickness into three parts. These parts consist of three rectangular box- shaped sections with a thickness of $h/2 - r_w$, $2r_w$ and $h/2 - r_w$. It was assumed that the flow to the second part is purely horizontal while the first and third parts have horizontal and vertical elements. Their proposed formula for HW productivity includes the wellbore eccentric (location) effects. They concluded that Joshi's equation does not apply to HWs which are not located at the mid point.

Shedid (2001) conducted a series of sensitivity studies to estimate the flow rate for HWs using steady state equations proposed by other investigators mentioned above (Joshi, Giger, Borosiv, Renarld and Dupuy, Permadi and Shedid (1996)). He concluded that these equations provided similar values for HW productivity for a HW length less than 1000 ft. For the HWs with the length of over 1000 ft, Joshi and Borosiv's equations still provided similar results. However the productivity of HWs calculated using the rest of equations of the other researchers were significantly different. His results also confirmed that the relative advantages of HWs to VWs are decreased as the reservoir thickness increases. Thus the use of HWs is predominantly recommended for reservoirs with thin formations. Humberto (2008) also conducted a series of similar sensitive studies and came to the same conclusion. He also proposed another equation,

which is a combination of the Joshi and Renarld‘s equations using some weight coefficients, which were determined using a trial and error procedure by comparing them with his numerical simulation results.

The aforementioned equations can be applied for a single-phase flow, incompressible fluid at steady state conditions.

Many investigators (Economides 1996, Helmy and Wattenbarger 1998, Lu, and Tiab 2007) studied the HW single phase productivity index (PI) under pseudo steady state (PSS) conditions. In the case of PSS flow, where the pressure gradient within the reservoir, with constant pressure at the outer boundary, drops at the same rate, it is necessary to solve the diffusivity equation. Solving the diffusivity equation for the 3-D HW geometry analytically is a complex task; therefore there are a number of oversimplifying assumptions for the HW flow geometry in these approaches. Among them, the HW PI equations introduced by Babu-Odeh (1989) and Goode (1991) are more popular than others. These equations were derived by developing a semi analytical solution to the PSS pressure drop of a HW in the centre of a box shaped drainage area. The PSS model presented by Babu -Odeh (1989) used the uniform flux distribution assumption along the wellbore (constant rate), whilst Goode (1991) made the assumption of uniform (constant pressure) wellbore pressure along the wellbore. These equations are quite complicated and require intensive calculations, which can be facilitated partly by developing an appropriate computer code. The former, Babu-Odeh ‘s equation, is easier to use than the latter, which involves more complex infinite series in the HW PI expression, but it is less accurate. Economides (1996) pointed out that there are differences between the predicted HW productivity indexes using these equations. However, these differences decrease as the partial penetration increases.

Kamkom and Zhu (2006) presented the IPR (Inflow Performance Relationship) equation for horizontal gas wells. Their equation was obtained simply by converting the IPR equation for oil wells to gas wells by using Boyles Law. However this is limited to a single phase and is not applicable to gas condensate reservoirs.

There are only a few sensitivity studies, which have discussed the application and productivity of the HWs in gas condensate reservoirs. Hashemi et al. (2005) conducted a series of sensitivity studies to compare the well productivity of horizontal, hydraulically fractured and VWs in a lean gas condensate reservoir. Their results showed that the HW improve productivity significantly when the bottom hole pressure is below dew point. Numerical simulations (Dehane 2000, Boualem 2006 and Jamiolahmady et al. 2007) conducted on the HWs have mainly been focused on the

sensitivity of pertinent parameters on the performance of such wells. Therefore an equation and a methodology for estimation of well productivity of HWs in gas condensate reservoirs are required, as proposed in this study.

This study is divided into three parts. The first part is devoted to conducting a series of sensitivity analyses evaluating the impact of pertinent parameters, including reservoir thickness, layering, anisotropy, fluid richness, condensate liquid drop out, coupling and inertia on the efficiency of a single HW model using ECLIPSE300. Difficulties faced with using the commercial reservoir simulators will be also discussed during this exercise. This is one of the reasons that the author developed in-house simulators to study the flow behaviour around HWs in gas condensate reservoirs.

In the second part, in a systematic mathematical modelling approach, the flow of a single-phase around a HW has been simulated. The integrity of the simulator has been confirmed by comparing some of its results with those of the ECLIPSE. It is demonstrated that the anisotropy has a significant effect on HW productivity, when k_v/k_h is less than 0.6. To capture the anisotropy effect accurately, a very fine grid is required using commercial reservoir simulators. The limitations of Joshi, Joshi-Economides semi-analytical skin expressions for anisotropic formation are also examined.

Next, based on the results of the in-house simulator, a geometric skin correlation developed for an undamaged formation penetrated by a HW is presented. In this exercise the efficient statistical response surface method has been used. This approach will be briefly described in a separate section (section 6).

The accuracy of the geometric skin formulation has also been confirmed by comparing its prediction for the data points not used in its development and also the predictions of some of the semi-analytical formulations described above.

The effect of partial penetration on the productivity ratio (PR) and geometric skin have also been studied extensively.

For the non-Darcy flow system, where the flow performance at high velocity is negatively affected by the inertia, an effective wellbore radius formulation has been developed, based on the results of the developed simulator. The proposed equation benefits from suitable dimensionless numbers which express the impact of pertinent parameters, i.e. velocity and geometric parameters.

As discussed earlier, the formulations available in the literature are for single phase Darcy flow. In gas condensate reservoirs, the flow behaviour around HWs is more complex due to the combined effect of coupling and inertia. Gas condensate fluid also

involves complex thermodynamic behaviour, due to fluid compositions. A fully compositional modelling is required to predict accurately the well performance of HWs in gas condensate reservoirs. Therefore, in line with the objectives of this study, this part is devoted to mathematical modelling of gas condensate flow around the HWs. A two phase compositional simulator has been developed, which incorporates new generalised k_{rgtr} correlation (Jamiolahmady et al. 2009). This correlation accounts for the combined effect of inertia and coupling with universal parameters. The integrity of the simulator has been confirmed by comparing its results with the results of the ECLIPSE commercial reservoir simulator under the same flowing conditions. Next, a comprehensive sensitive study has also been conducted to evaluate the impact of pertinent parameters on the performance of HWs in gas condensate reservoirs.

The second part of this study is devoted to developing a methodology for prediction of the well productivity of HWs in gas condensate reservoirs. Here the effective wellbore radius approach mentioned above is extended from single phase non-Darcy flow to a two-phase flow of gas and condensate. The integrity of the proposed method has been confirmed by comparing the results of the developed 1-D open hole compositional in-house simulator with the effective wellbore radius with the corresponding values obtained using the 3-D HW compositional simulator.

Finally, an in-house simulator is introduced that has been developed to study the flow behaviour of single phase gas around HWs at pseudo steady state conditions. The results of the in-house simulator are shown to be in good agreement with the corresponding values obtained for a fine grid model created using ECLIPSE. The applicability of the methodology, initially proposed for steady state conditions, to pseudo steady state conditions has been investigated comprehensively. This study demonstrates that the proposed methodology is general and can be used as a standard technique for steady state, pseudo steady state and transient state conditions. An equivalent phase approach has also been proposed to model two phase flow of gas condensate for pseudo steady condition. A two phase 3-D HW and 1-D EOH in-house simulator has been developed to verify the accuracy of the proposed formulation and approach for pseudo steady conditions.

3.3 GAS-CONDENSATE HW MODEL, ECLIPSE 300

In this part of the study, the single well model constructed in ECLIPSE300 is used to evaluate the impact of pertinent parameters including the HW length and the

reservoir thickness on the gas condensate HW productivity. The model will then be used to examine the effects of inertia and coupling.

3.3.1 *Effect of* HW Length and Reservoir Thickness

The aim of this exercise is to quantify the impact of the HW length and reservoir thickness on the total gas production of a gas condensate HW.

Reservoir Modelling

Here, a single well model was constructed using ECLIPSE300 with a 3-D Cartesian fine grid system. The reservoir model is a homogenous reservoir model. The core properties are those of Texas Cream core used in the laboratory of a research gas condensate project. The basic properties of the core samples used in this study are found in Table 3.1. The core specific constants of the velocity dependent relative permeability correlations in ECLIPSE 300 were those experimentally measured on these cores in this laboratory. The pseudo-pressure option of ECLIPSE 300 has been used to account for positive coupling and negative inertial effects around the wellbore. The reservoir dimensions for a set of sensitivity studies are those listed in Table 3.2 for a model referred to as model A. The initial reservoir pressure was above dew point of the reservoir fluid. However the bottom hole pressure was kept below the reservoir fluid dew point, which created a two phase gas and condensate region around the wellbore. The initial gas production plateau rate is maintained at 50 Mscf for all runs till the bottom hole pressure approaches 4400 psi, which is below the dew point. For all models used here the effect of pressure drop inside the HWs due to the friction on the HW productivity was ignored.

Fluid Properties

Three C1-nC10 gas condensate binary model fluids with 7, 16 and 30% v/v, maximum liquid dropout (MLDO) in the constant composition expansion (CCE) test at the reservoir temperature of 250^{o}F were used in this study. The corresponding dew point pressure values were 4132, 5180 and 5405 psia, respectively. In ECLIPSE 300 the Lorentz Bray Clark viscosity correlation and Peng Robinson equation of the state were used to estimate the corresponding fluid properties. In the majority of the simulations conducted here, a fluid system with intermediate richness was used unless otherwise stated.

Results & Discussion:

Many simulation runs were performed for different HW lengths varying from 700 to 3100 ft in a reservoir with the thickness of 50, 100, and 200 ft. As the model is symmetrical in a Cartesian system, in order to reduce computing time for these simulations, only half of the model has been selected.

As expected, increasing the length of the HW improved well productivity, although as the length increased, the extra benefit diminished. For example, a 35% increase in the length (from 1150 to 1550 ft) would increase the total production by only 0.48 %, while increasing the HW length from 350 to 472 ft (35% increase in the length) increases the total production by 1.5%, Figure 3.3. It is also noted that the gas recovery is always achieved faster using the HW compared to that of the VW in the reservoir.

Figure 3.4 shows the relative increase in cumulative gas production for the HW compared to that of the VW versus time for three reservoir models with a thickness of 50, 100 and 200 ft. In the case of a HW length of 350 ft, the relative increase in cumulative gas production amounts to maxima of 33%, 18%, and 11% for the reservoir with 50, 100, and 200 ft thickness while the corresponding values for the HW length of 1550 ft are 95%, 52%, and 27%, respectively. It is concluded that increasing the thickness of the reservoir decreases the relative gain in the total gas production compared to that of a VW. Increasing the length of the horizontal section from 350 to 1550 ft in the reservoir 50 ft thick increased the relative gain in the total gas production compared to that of a VW from 33% to 95%, while the corresponding value in the reservoir 200 ft thick increased only from 11% to 27%. It is concluded that the effect of the length of the horizontal section on the total gas productivity is more pronounced in the case of the reservoirs with smaller thicknesses.

3.3.2 Effect of Inertia and Coupling

This part of the study attempts to quantify the effect of inertia and coupling, fluid richness and rock properties on gas condensate HW performance.

Reservoir Modelling

The reservoir dimensions are those listed in Table 3.2 for a case referred to as Model B. All runs were made for a period of one years' production with the bottom hole pressure at 4000 psi and the initial reservoir pressure at 7500 psi. The single layer reservoir model properties were described by Texas Cream properties, Table 3.1.

Fluid Properties

The reservoir fluid is a binary mixture of C1-C10 with maximum liquid dropout 16% (moderate condensate).

Results & Discussion

Figure 3.5 compares the total gas production for a HW with a length of 100 ft for the case with and without the inertial and coupling effects and also with only the inertial effect being active. It should be noted that when velocity effects (i.e. both coupling and inertia) are ignored for the HW with 100 ft, there is minimal difference in total gas production, compared to the case where velocity effects are considered, Figure 3.5. However the total gas production decreased considerably if only the inertial effect is applied on the model. This demonstrates that the positive coupling effect compensates the negative impact of inertia on the gas production. The effect of coupling becomes even more pronounced as the length of HW increased, Figures 3.6 to 3.8. It is important to point out that the negative inertial effect reduced due to decreasing velocity. It is also worth mentioning that decreasing or increasing the bottom hole pressure resulted in a lot of numerical convergence problems for many cases, which could not be removed despite the considerable efforts of the author.

From Figures 3.9 and 3.10, the same conclusion can be drawn for the reservoir model described by the Berea core properties, Table 3.1. It should be noted that all the reservoir model characteristics here e.g. reservoir fluid, grid cells sizes, HW length, wellbore radius and the pressure drop across the reservoir model were the same as those used for the former one. However, many convergence problems were experienced for the HW longer than 500 ft, which is why the reported results here are only for the HWs with a length less than 500 ft.

For the last series of simulations, the reservoir model properties were described by RC1b properties, Table 3.1. As the inertial effect reduces due to the decreased velocity of this tight rock, the coupling effect becomes more dominant, improving the gas production significantly, Figures 3.11 to 3.14. It is obvious that the velocity and IFT determine the impact of coupling or inertia.

It should be pointed out that drilling of a HW in a gas condensate reservoir, similarly to that in a dry gas reservoir, decreases the negative impact of the inertia, due to decreasing the velocity. However, the pronounced effect of the coupling in the former also improves the total gas production.

It is important to note that due to numerical instability problems, none of the above runs converged when the reservoir fluid is a rich gas.

In summary, as mentioned previously, the main difficulty in modelling gas condensate flow around HWs is the complexity of the flow behaviour around the wellbore for these low IFT systems. Significant effort was directed to simulate gas condensate flow around HWs using ECLIPSE 300 under different flow conditions. The results of this exercise concluded that:

1) The flow around HWs is very complex and requires a full 3-D compositional approach to describe it accurately. However, it does not provide accurate results around the wellbore unless an extremely fine grid is used, which is costly and cumbersome.
2) Furthermore, performing this exercise using commercial compositional simulators results in convergence problems due to numerical instability. An increase in the length of HW increases numerical convergence problems. The problem of convergences is more severe in the cases of using moderate and rich gas condensate fluid systems. It should be noticed that the reservoir fluid here was a binary mixture (C1-C10), but in reality the number of components of the typical gas condensate reservoir is much greater than two. This makes the calculation procedure more complicated for most practical cases. Furthermore the implicit computing and iteration nature of the calculations require much longer CPU times.
3) The velocity dependent k_r formulations (Henderson et al. 2000) are available in ECLIPSE not the new more efficient generalised k_r correlation (Jamiolahmady et al. 2009). The former has separate formulae to take account of the effects of inertia and coupling requiring core specific constants. This correlation would not be able to acknowledge the impact of coupling and inertia for a wide range of velocity and IFT.

To this end, a reliable approach, which tackles all uncertainty associated with the well performance of gas condensate HWs is desirable. The author therefore embarked on a modelling approach, different from that using the commercial simulators, and developed different mathematical simulators using Comsol multi-physics mathematical package, which is based on finite-element methods. In a systematic approach, first the flow of a single-phase around a HW was simulated. Then it was extended to two phase flow of the gas and condensate fluids as described below.

3.4 SINGLE PHASE HW MODEL, ISOTROPIC FORMATION

At this stage of the study, the flow of a single-phase compressible fluid around the wellbore of a HW has been simulated. As mentioned earlier, the main objective of this study is to expand the mathematical modelling approach to two phase flow of gas condensate fluids.

It should be noticed that the current developed single phase flow in-house simulator has an option to account for the change in fluid properties with pressure and the effects of inertia. Initially, these effects have been ignored to develop a geometric skin for HWs, which is independent of flow rate and fluid properties. Next flow skin, which accounts for the effects of a change in fluid properties with pressure and non-Darcy flow, is studied.

This part of the study consists of two sections. The first section describes the in-house simulator. Next the integrity of the 3-D HW in-house simulator is confirmed by comparing some of its results with those of the same HW constructed by the ECLIPSE simulator.

3.4.1 In-House Mathematical Single Phase HW Model

The main aim of the present study is to develop a 3-D simulator that can be used for creating a large bank of data for HWs with different lengths and wellbore radii in a reservoir with different dimensions and thicknesses.

The 3-D system considered in this study consists of a HW with radius of r_w and length of L, in a single layer cubic reservoir, as shown in Figure 3.15. This homogenous porous medium has an absolute permeability k and formation thickness of h. The length of the reservoir in the x and y directions is assumed to be 2.5 times the length of the HW. Later in this chapter, it will be shown that the impact of partial penetration on the productivity of HWs and geometric skin for Xres/L>1.5 is negligible.

Due to the existing symmetry only a quarter of the model has been considered in this study. This saves the computation time and reduces the complexity of having a high quality mesh. This later point is discussed further in the next section.

Governing Equations

The equations employed in this study are similar to those described for gas condensate flow in a perforated region (Jamiolahmady et al. 2006). These equations are:

1) Continuity equation for a compressible fluid

$$\nabla.(\rho v) = 0. \qquad (3.17)$$

2) The 3-D form of the Forchheimer equation is:

$$\nabla P = \frac{\mu}{k} V + \beta \rho |V| V \,. \tag{3.18}$$

Combining continuity and the 3-D form of the Forchheimer equation, after some mathematical manipulation, gives:

$$\nabla . \left[2 \left[\frac{k}{\mu} \right] . \frac{\rho \nabla P}{1 + \sqrt{1 + 4\beta\rho \left(\frac{k}{\mu} \right)^2 |\nabla P|}} \right] = 0 \,. \tag{3.19}$$

Mathematical Solution Technique

The governing non-linear partial differential equation (PDE), Equation 3.19, is solved using Comsol multi-physic software (version 3.4, 2007), which uses the finite element method. The main dependent variable in this equation is P (pressure).

The boundary conditions applied to this system are:

1) Infinite conductivity for the wellbore (the pressure gradient in the wellbore has been ignored),

2) The pressure at outer boundary (external radius) is known,

3) The pressure at the inner boundary (wellbore radius) is known.

Initially an attempt was made to construct a full 3-D single HW in a rectangular reservoir model using options available in the composite toolbar of Comsol user interface. It should be mentioned that there is a significant difference in the dimensions of different parts of the reservoir models, e.g. the wellbore radius, the HW length and the reservoir dimensions. This caused considerable difficulties when creating the mesh geometry, in some cases, it was even impossible. Significant efforts were dedicated to improving the procedure. It was concluded that the construction of such a 3-D object is not feasible for most cases considered. It is well known that creating 2-D or 1-D geometry is simpler than 3-D geometry. Therefore, the author has benefited from the symmetry of the system and initially created a 2-D geometry which was then extruded to a complete 3-D system. This method proved very efficient in removing all the problems associated with directly constructing the 3-D HW model. The important point here is that adding and subtracting regions to create the complicated geometry under study has been performed in the 2-D plane of the geometry.

It should be noticed that the mesh design plays an important role in the finite element analysis. The most important parameter of mesh design, which affects both the accuracy and convergence of a numerical solution, is the mesh quality. The mesh quality option of the mesh toolbar of Comsol allows the user to identify the poor quality elements. As a rule of thumb; it can be said that mesh quality higher than 0.3 yields accurate results. Generally, the poor quality mesh is defined for elements with one of the following characteristics (see Figure 3.16):

1) High aspect ratio (Ratio of maximum side length to minimum side length) more than 10.
2) Minimum interior angle smaller than 20 degrees.
3) Maximum interior angle larger than 120 degrees.

Considerable attempts were made to generate consistent mesh files for different 3-D HW geometries. In this exercise, in order to capture the complexity of flow behaviour around the HW accurately, the 3-D system was divided into two regions, 1) the inner shell, which starts from wellbore and expands to a certain distance into the reservoir which is 10 times the wellbore radius. It should be noted that this number was determined by conducting a comprehensive sensitive study with the aim of minimising the difficulties of constructing the required 3-D geometries, 2) the second region starts from the outer boundary of the first region and ends at the outer dimension of the reservoir model.

Here all HW models were meshed manually according to the author's base knowledge of the flow behaviour for different prevailing conditions. Figure 3.17 shows the mesh map constructed for one of the geometries defined in this study. As explained earlier, the aim of this exercise was to generate a very high quality mesh and subsequently reliable results. Figure 3.18 displays the quality of mesh for the selected model. As can be seen, the majority of the elements have a quality value of more than 0.8. The minimum mesh quality is higher than 0.6, which ensures the accuracy of the results under different conditions. Figure 3.19 shows the pressure profile for this geometry. It should be noted that the maximum and minimum mesh quality criteria were honoured for all the constructed geometries.

3.4.2 ECLIPSE Single Phase HW Model

In order to confirm the integrity of the in-house single phase mathematical simulator, a single HW was constructed using the fine grid option of ECLIPSE 100.

The core properties of Texas Cream (Table 3.1) with porosity 0.21 and permeability 11.1 mD were used to describe the reservoir in this model. The PVT tables were set up based on information from the study of flow around perforated region by Jamiolahmady et al. (2007). That is, single phase gas with specific gravity of 0.7, viscosity of 0.0352 cp and the formation volume factor of 0.0103 Rm^3/Sm^3. The reservoir was 250 m in the x and 125 m in y directions and 16 m in the Z direction. The length of HW was 100 m. The reservoir pressure was 82.737 bar and the HW was producing with a controlled bottom hole pressure of 68.9476 bar. Fine grids were used to capture the complexity flow near the wellbore.

Forty injection wells were located in the boundary of the reservoir to make the reservoir pressure at the drainage boundary constant.

The results of the in-house mathematical simulator were compared with those of similar simulations conducted using the ECLIPSE simulator. Figure 3.20 shows the good agreement between the two results. The arithmetic average absolute percentage deviations (AAD%) of the predicted mass flow rates values by the ECLIPSE simulator compared to those estimated by the HW simulator was 1.43 % for the simulation with a constant pressure drop (ΔP) of 1300 psi maintained over the drainage area. The corresponding values for a constant pressure drop (ΔP) of 200 and 100 psi were 1.39% and 0.23%, respectively.

3.5 SINGLE PHASE HW MODEL: ANISTROPIC FORMATION

This study is aimed at investigating the effect of anisotropy on the well performance of HWs. First the author's attempts to refine the ECLIPSE model to improve the accuracy of the results are discussed. Next, these results are compared with the in-house simulator outcomes, followed by a comparison between the results of the in-house simulator and those of Joshi's semi-analytical equation. The author has also extended the study for a high anisotropic case, in which vertical permeability is equal to zero. This last section includes the simulation of HWs in a thin layer flow model with a thickness equal to that of the wellbore diameter.

3.5.1 In-house Simulator Versus ECLIPSE

The ECLIPSE model used in this study was the same as the one described in Section 3.3.2 (in terms of the well dimension and reservoir properties). The permeability anisotropy can be considered in ECLIPSE using the multiplier factor in transmissibility of grid blocks. When the permeability anisotropy index decreases; a sharp pressure drop

occurs around the wellbore region in the vertical flow direction. Consequently, a very fine grid in the perpendicular direction is required to properly model the pressure distribution around the wellbore.

Figure 3.21 shows the productivity ratio (ratio of flow rates of HW to VW) versus anisotropy values for the ECLIPSE model using different grid sizes. The results using three grid sizes show a reduction in estimated flow rate, which is an indication in the improvement of the accuracy, as the grid is refined. As discussed by Jamiolahmady et al. (2007), studying flow around a perforated region, an inadequate number of grids and refinement resulting in an overestimation of flow rate is something also observed here for coarser grids. An important point noted was that refining more the ECLIPSE model was not achievable here, due to the high CPU required. It is clear that noticeable differences between ECLIPSE productivity values from normal and fine grids models and those calculated by in-house simulator are observed particularly for low anisotropy values. The extremely fine-grid ECLIPSE model and in-house simulator (with linear Lagrange element) match very well over a wide range of anisotropy values, although a clear deviation exists for anisotropy values below than 0.1. The in-house simulator is more accurate as will be discussed later. It is well known that the strength of the finite element method technology is its robustness, modularity and reliability (Hughes 1987). The finite element method is very flexible to cope with complex geometries with various inner and outer boundary conditions. The finite element method is used to find an approximation function for the response by dividing domain into finite smaller subdomains called elements. The shape of the function inside the elements is determined using an interpolation scheme. The function inside the elements is used to find an approximation solution for the main domain. This function could be a linear, quadratic or cubic polynomial. It should be mentioned that there are two techniques which can be used to enhance the accuracy of the solution. The first, which has been used in this study, is to keep the polynomial order of element shape function low or constant, while the mesh is refined by increasing the number of elements. The second method is to keep the mesh fixed and increase the order of polynomial element function resulting in the refinement of the solution to obtain the desired convergence and accuracy (Babus ka et al. 1981, Hughes 1987, Babus ka, and Suri 1990 and Szabo and Babus ka 1991). Considerable effort was directed to improve the accuracy of the in-house simulator using a combination of these two major techniques. Mesh refining was performed, which increased the computational time significantly. It should be noted that decreasing the anisotropy ratio significantly changes the flow behaviour around the

HW. It affects the pressure profile counters, making the counter closer near to the wellbore, i.e. the pressure changes very sharply near the wellbore. Note that the polynomial shape function element was initially linear. Using higher polynomial order element shape function (quadratic Lagrange element) and mesh refinement proved to be effective and efficient to capture these effects for anisotropy values between 0.01 and 1. However, it was noted that for anisotropies less than 0.01, capturing the sharp changes in the pressure very close to the wellbore in the z direction proved very difficult. This was mainly because the large number of mesh elements required for the z-direction could not be generated. Therefore a new feature (z-scale) was utilised, which allows the user to generate anisotropic meshes, i.e. more elements lie in the z direction than the other two directions (x and y). It should be noted that scaling in the z direction for isotropic formations reduced the accuracy, i.e. the calculated mass flow rates were overestimated by 9%. Therefore, this was only applied for anisotropic formations. As a rule of thumb, the z-scale less than 5 can satisfy the required accuracy of the results.

3.5.2 In-house Simulator Versus Joshi (1985), Joshi-Economides (1991) and Borosiv (1984) Equations

Isotropic Formation

As mentioned previously, many equations have been developed to estimate steady state flow rate in HWs. Among them, two equations, Equation 3.2 (Joshi 1985) and Equation 3.1 (Borosiv 1984) are widely used in the petroleum industry.

If these two equations are compared with Equation 3.8 the following geometric skin expressions are obtained:

$$S_m = \ln\left(\frac{4r_{eh}}{L}\right) + \frac{h}{L}\ln\left(\frac{h}{2\pi r_w}\right) - \ln\frac{r_{eh}}{r_w} \tag{3.20}$$

$$S_m = \ln\left(\frac{a + \sqrt{a^2 - \left(\frac{L}{2}\right)^2}}{L/(2)}\right) + \frac{h}{L}\ln\left(\frac{h}{2r_w}\right) - \ln\frac{r_e}{r_w} \tag{3.21}$$

Principally, these analytical equations were obtained by simplifying the 3-D system to two 2-D problems. This assumption is only appropriate if the thickness of the reservoir model is small compared to the length of HW, that is, the flow is mainly provided by the HW length compared to the reservoir thickness. Figure 3.22 (a) presents absolute deviation in percentage (AD%) between the calculated skin values using Joshi's equation (Equation 3.21) and those of the in-house simulator, which were

calculated using Equation 3.8, and the estimated flow rates by the in-house simulator. It is noted that when the length of the HW is equal to the thickness of the reservoir, the gas productivity prediction is poor, using Equation 3.20. However, with increasing length of the HW, AD% decreases drastically. It seems that Joshi's equation provides an accurate result if L/h is more than 8 for an isotropic formation. In addition, a comparison of the results of Borosiv's Equation (Equation 3.20) with the in-house skin values shows that Borosiv's equation gives better results for lower values of L/h compared to Joshi's equation. However, the calculated skin is still significantly underestimated when L/h is less than 3 (Figure 3.22 (b)).

Anisotropic Formation

The effect of anisotropy on the skin values calculated by the in-house simulator and those by Joshi (1985) and Joshi-Economides (1996) semi-analytical expressions has also been examined as described here.

As mentioned earlier, Joshi modified his equation by transforming h to $h\sqrt{\frac{k_h}{k_v}}$ to take into account the reservoir anisotropy (Equation 3.5).

If this equation is compared with radial flow for a VW it gives a geometric skin formulation expressed by Equation 3.22.

$$S_m = \ln\left(\frac{a+\sqrt{a^2-\left(\frac{L}{2}\right)^2}}{L/(2)}\right) + \frac{I_{ani}h}{L}\ln\left(\frac{I_{ani}h}{2r_w}\right) - \ln\frac{r_e}{r_w}. \qquad (3.22)$$

As mentioned earlier, Economides et al. (1996) modified Joshi's equation. If their proposed formulation (Equation 3.15) is compared with that of radial flow for a VW it gives a geometric skin formulation expressed by Equation 3.23.

$$S_m = \ln\left(\frac{a+\sqrt{a^2-\left(\frac{L}{2}\right)^2}}{L/(2)}\right) + \frac{I_{ani}h}{L}\ln\left(\frac{I_{ani}h}{r_w(I_{ani}+1)}\right) - \ln\frac{r_e}{r_w} \qquad (3.23)$$

Figure 3.23 and 3.24 compare the calculated skin, for anisotropic formations, using Joshi's (Equation 3.22) and Joshi-Economides's (Equation 3.23) equations with the corresponding values obtained by applying the calculated in-house simulator mass flow

rates into Equation 3.8. The latter values were calculated using Equation 3.8 and flow rates estimated by the in-house simulator.

There is a noticeable deviation between the calculated skin values using Joshi and Joshi-Economides equations with those obtained using Equation 3.8 and flow rates estimated by the in-house simulator, especially for lower kv/kh and L/h values. When kv/kh is 0.6, the result of the in-house simulator converges with Joshi (1985) and Joshi-Economides (1996)'s equations for L/h above 12 (see Figure 3.23 (a)). As discussed earlier, these semi-analytical equations were developed by dividing the 3-D solution into two 2-D solutions, which is only valid for the long HWs. It is noted that a decrease of the anisotropy ratio from 0.6 to 0.4 increases the error between the calculated skin values using their semi-analytical equations (Joshi and Joshi-Economides) and those of the in-house simulator (see Figure 3.23 (b)). Figure 3.24 shows that the overestimated flow rates from these two equations are more pronounced at a lower kvkh of 0.1 and 0.01. However, the skin values from these two Equations and the in-house simulator results converge for L/h above 25. In summary, the deviations are more pronounced at lower L/h and lower kv/kh values. In general, it is concluded that the use of these equations is appropriate for L/h greater than 25. In the next section, the performance of the in-house simulator when $k_v = 0$ is compared with a thin layer flow HW model to further verify the integrity of the in-house simulator.

Thin Layer Flow HW Model

A new model was developed to study flow around HWs when $k_v = 0$. In this model the thickness of the layer is the same as diameter of the wellbore. Figure 3.25a shows a schematic diagram of the thin layer HW flow model simulated using Comsol. The rock properties and PVT tables were those used for the HW in-house simulator in Section 3.3.2. The pressure drop across the reservoir drainage area was 100 psi. The thin layer model can represent one of the HW models described in Section 3.3.2 if kv =0. The calculated mass flow rate for the thin layer model and that of 3-D model were 0.0068, and 0.0076 kg/s, respectively. The standard and absolute deviation errors between these two values are 0.0008 and 10, which confirms the accuracy of HWs in-house simulator. It should be noted that even with scaling for the HWs in-house simulator, the number of elements of the thin layer model (557051) is still significantly higher than that of the HWs in-house simulator with 27386. Figure 3.25b shows the pressure profile across the HWs in-house simulator. As can be seen, the 3-D HWs in-house simulator with kv=0, has predicted a pressure profile similar to that of the thin layer model, i.e. fluid flows

horizontally in a plate with thickness equal to the HW diameter. It was mentioned previously that z-scale and quadratic Lagrange significantly improved the results of the in-house simulator especially for anisotropy values above 0.001, Figures 3.21 (b) to 3.25, considering that it is unlikely to drill a HW in the formation with kv=0. The use of results of the in-house simulator for development of a new and more efficient geometric skin has been limited to formations with anisotropy values varying between 0.001-1.0. It should also be mentioned that the equations widely used in the petroleum industry incorrectly predict zero flow rates for the kv=0 condition according to their .

3.6 RESPONSE SURFACE METHODOLOGY

To develop a more general skin formulation, the author used the response surface method. It was introduced by Myers and Montgomery (1995) as a statistical tool to simulate a physical phenomenon in the range of its pertinent parameters. In this method, the response (quality characteristic or performance measure) is usually a nonlinear function of several input variables. Typically, the approximation function that relates structural responses and design variables (important factors which affect the response), is a polynomial. The most used polynomial approximation surface fit is a quadratic multidimensional polynomial. The response surface for such cases is described as follows:

$$y = a_0 + \sum a_i x_i + \sum\sum a_{ij} x_i x_j + \sum a_{ii} x_{ii} \qquad (3.24)$$

The least square method is used to estimate the constant and coefficients of this function at certain sample points. In this statistical method, each variable is scaled such that it varies between 0 and 1. The distribution of a scaled variable is carefully defined within its maximum and minimum values by a number of nodes and based on a design criterion. Various techniques, referred to as experimental designs, have been developed to select sample points. The common experimental design is 2-level factorial, which includes the upper and lower limits for the variables involved. For this experimental design, 2^k runs are needed, where k is the number of variables or factors. The sampling points are selected in the $\alpha \pm r$ range, where $\alpha \& r$ are the vectors of mean and standard variation of the variables, respectively.

3.7 SINGLE PHASE DARCY FLOW

3.7.1 Geometric skin Correlation

In this part of the study a correlation for a geometric skin is proposed. The geometric skin, which accounts for the impact of HW geometry on the flow, is employed in an open-hole VW productivity equation ,giving the same flow rate as that of the HW as expressed by Equation 3.8. The in-house simulator was used to create a large bank of experimental data. Using these data, the coefficients of the skin formulation are determined through a multi-regression exercise.

The main geometrical parameters that influence S_m of HWs are thickness of the reservoir, radius of the well, length of the HW. To obtain the relevant dimensionless numbers to be included in the formulations, the author looked at a special case for which a mathematical expression can be derived as described below.

As can be seen in Figure 3.26, the flow behaviour around a fully penetrating HW is similar to that around a VW with a circular drainage area and radius h/2. Consequently, the flow rate of a fully penetrating HW with length of L can be written as follows:

$$Q_h = \frac{2\pi k L \Delta p}{Ln(h/2r_w)} \tag{3.25}$$

Comparing Equations 3.25 and 3.8 gives the S_m formulation for this system as expressed by Equation 3.26.

$$S_m = \frac{h}{L} Ln(\frac{h}{2r_w}) - Ln(\frac{r_e}{r_w}). \tag{3.26}$$

Therefore, it is suggested that geometric skin in an isotropic reservoir could be a linear function of $\frac{h}{L} Ln(\frac{h}{2r_w})$, $Ln(\frac{h}{2r_w})$ and $Ln(\frac{r_e}{r_w})$ parameters.

$$S_m = f(\frac{h}{L} Ln(\frac{h}{2r_w}), Ln(\frac{r_e}{r_w}), Ln(\frac{h}{2r_w})). \tag{3.27}$$

As discussed earlier, the well productivity of HWs is greatly affected by anisotropy. Thus, for an anisotropic reservoir, one can write:

$$S_m = f(\frac{h}{L} Ln(\frac{h}{2r_w}), Ln(\frac{r_e}{r_w}), Ln(\frac{h}{2r_w}), I'_{ani}).$$

$$I'_{ani} = \frac{k_v}{k_h}, \tag{3.28}$$

where k_v and k_h are vertical and horizontal permeability, respectively.

Furthermore, to account for the anisotropy effect, according to Muskat‘s transformation, the vertical axis can be modified by:

$$h = \frac{h}{\sqrt{I'_{ani}}}, \tag{3.29}$$

Thus the first parameter in Equation 3.28 is replaced by:

$$x_1 = \frac{h}{L\sqrt{I'_{ani}}} \ln\left(\frac{h}{2r_w\sqrt{I'_{ani}}}\right). \tag{3.30}$$

Further sensitivity analysis showed that transformation of the vertical axis for the third parameter decreased the accuracy of the fitting model and using natural log of I_{ani} rather than I_{ani} proved to give a better fit. Therefore, S_m has been suggested to be a function of $\frac{h}{L\sqrt{I'_{ani}}} \ln\left(\frac{h}{2r_w\sqrt{I'_{ani}}}\right), \ln\left(\frac{r_e}{r_w}\right), \ln\left(\frac{h}{2r_w}\right)$ and $\ln(I'_{ani})$.

$$S_m = f\left(\frac{h}{L\sqrt{I'_{ani}}} \ln\left(\frac{h}{2r_w\sqrt{I'_{ani}}}\right), \ln\left(\frac{r_e}{r_w}\right), \ln\left(\frac{h}{2r_w}\right), \ln(I'_{ani})\right). \tag{3.31}$$

Selection of these dimensionless numbers proved suitable in obtaining an efficient skin formulation. It is also worth noting that $X_{res} = 2.5 \times L$ and the effect of partial penetration is discussed separately in the following sections.

The quadratic Response Surface model was chosen as described by Equation 3.32.

$$S_m = a_0 + \sum_{i=1}^{4} a_i x_i + \sum_{i=1}^{4} a_{ii} x_i^2 + \sum_{i=1}^{4} \sum_{j=i+1}^{4} a_{ij} x_i x_j . \tag{3.32}$$

More than 600 simulations runs were performed to ensure adequate resolution of pertinent parameters, based on the 2^k factorial experimental design criterion. The proposed dimensionless numbers were scaled according to the following equation:

$$x_{ic} = \frac{(2 \times x_i - x_{i\max} - x_{i\min})}{(x_{i\max} - x_{i\min})}, \tag{3.33}$$

where x_{ic} is the scaled coded parameter (expressing the impact of reservoir and well parameters) and $x_{i\max}$ and $x_{i\min}$ are the maximum and minimum of each parameters, respectively. The maximum and minimum values of the parameters were selected based on the parameter distribution within their practical range of applications. The corresponding variables and their range of variations in this study, representing these three parameters, are shown in Tables 3.3 and 3.4.

Table 3.5 gives the coefficients, upper and lower limits and standard error of the coefficients of Equation 3.32. The standard error coefficient is used to determine how a selected parameter is statistically significant. As a rule of thumb, if the value of the coefficient and its standard error are in the same order of magnitude, the estimated parameter is not statistically considerable. Here, the results in Table 3.5 indicate that the chosen parameters are appropriate. Generally the coefficient of multiple determination (R^2) is used to evaluate the accuracy of the fitted model. If the coefficient of multiple

determination is 1, it provides an excellent response to the input parameters and if the residual error increases, the multiple determination coefficient reduces in the range of 1 to 0. For the fitted model, the coefficient of multiple determination was 0.9996, which is satisfactory.

3.7.2 Verification of Geometric skin Formulation

Comparison with Results of In-house Simulator

Figure 3.27 presents a comparison between the S_m values obtained by applying the in-house simulator mass flow rates into Equation 3.8 and those values predicted using the developed correlation. The average absolute deviation (AAD %) error for these data points which have been used for the development of the geometric skin is 2.7%. This low AAD% value indicates that the accuracy of the correlation is good. The results of S_m predicted by the correlation have also been compared with new data points not used in its development. In this exercise about 57 data points that have been obtained from the in-house simulator and cover a broad range of variation of input parameters were compared with the corresponding values predicted by the correlation as shown in Figure 3.28. The AAD% for this data set is 0.6%. As can be seen, an excellent agreement between predicted geometric skin using the S_m correlation and outcome of the in-house simulator has been established.

Comparison with the Joshi (1985) and Borosiv (1984) Equations

Here the results obtained using the proposed correlations are compared with those using Joshi's and Borosiv's equations. As discussed earlier in section 3.4, these equations should be applied within their range of applications, considering the simplifying assumption made for their development, otherwise the results could be highly erroneous, something which was honoured in this exercise.

Figure 3.29 shows the predicted geometric skin using the correlation and the corresponding values using Joshi's (1985) and Borosiv's (1984) equations. In this study, the length of HWs, reservoir thickness, and wellbore radius varied between 180-400 (m), 15-30 (m), and 0.07-0.12 (m), respectively. The comparison, depicted in Figure 3.29, is for three different HWs in isotropic reservoirs producing at steady state conditions. It can be seen that the results are in a very good agreement.

The above results indicate that the correlation is very reliable for a wide range of variation of pertinent parameters, i.e., reservoir thickness, anisotropy, wellbore radius, and length of HW.

3.7.3 Application of Geometric Skin Formulation

It was demonstrated earlier, in Section 3.4, that all equations available in the literature may not predict the well productivity of HWs properly in an anisotropic reservoir. Moreover a sensitivity study performed by Shedid (2001) showed that the productivity values of HWs predicted using different steady state equations are not reliable when L is more than 300 m, especially in thinner reservoirs. This was later confirmed by Humberto (2008). The new equation provides a reliable prediction for the productivity of HWs over a wide range of L, h and I_{ani}.

A sensitivity analysis was conducted using the new skin formulation to evaluate the impact of important parameters on the productivity ratio (PR), as described below. PR is defined as the ratio of flow rate of a HW to that of a VW, both operating under the same pressure drop. PR in terms of skin can be obtained by noting that the Darcy Law for the flow around a VW can be written as:

$$q_v = \frac{2\pi kh\Delta p}{Ln(r_e / r_w)}. \tag{3.34}$$

The corresponding flow equation for a HW under the same ΔP is:

$$q_h = \frac{2\pi kh\Delta p}{Ln(r_e / r_w) + S_m}. \tag{3.35}$$

Comparing Equations 3.34 and 3.35 gives:

$$PR = \left(\frac{q_h}{q_v}\right) = \frac{1}{1 + S_m / Ln(r_e / r_w)} == \left(\frac{J_h}{J_v}\right). \tag{3.36}$$

It should be noticed that the geometric skin accounts for geometrical parameters and anisotropy, and is calculated using Equation 3.32, with its parameters given in Table 3.5.

Effect of Reservoir Thickness and HW Length

Figure 3.30 compares PR for different reservoir thicknesses in an isotropic reservoir versus the HW length (L). As can be seen, PR increases considerably with increasing L. Furthermore, the extent of this increase is more pronounced for shorter L. Moreover, PR is always higher for reservoirs with a thinner pay zone: that is, the contact area for flow compared to drainage volume in a thin reservoir with a HW is much greater than that in a thick one. However, as L increases the difference between PRs decreases

substantially. For example, when L=1120 m, the difference between PRs of 45 and 15 m thick formation is nearly 0.5 whereas the corresponding value is 1.3 at L=120 m.

Effect of Wellbore Radius

From Figure 3.31, it is clear that the effect of wellbore radius on the productivity ratio is not significant. Decreasing the wellbore radius from 0.14 to 0.07 m improved PR slightly. This minimal impact is mainly due to the presence of the wellbore radius in the log term of the denominator of Equation 3.36.

Effect of Anisotropy

Figure 3.32 presents a comparison of PR versus the HW length (L) for different anisotropy levels. As discussed above, an increase in L increases the total gas production in an isotropic formation. As can be seen, decreasing vertical permeability decreases PR considerably. This decrease is more pronounced at lower anisotropy values, i.e. most pronounced at k_v/k_h=0.001. It should be noticed that the incremental improvement in PR by increasing L is more gradual at lower k_v/k_h. In other words for the reservoir with lower anisotropy values the advantage of the relative increase in HW length is decreased.

Partial Penetration

For all the results presented above, the extent of the square drainage area in x (Xres) and y (Yres) directions has been considered 2.5 times HW length (L), i.e. L/X_{res}=0.4. A comprehensive sensitivity study was conducted to evaluate the effect of partial penetration (PP) for other ratios of X_{res} (or Y_{res}) to L on the well performance of the HW (HW) and geometric skin (S_m).

Figure 3.33 and 3.34 illustrate the flow pattern of a fully and partially penetrating HW, respectively. As can be seen in Figure 3.34, in the case of PP HW, when the flow approaches the end of wellbore, an extra pressure drop is required around the wellbore as flow converges in that area. This is not observed in Figure 3.33. This extra pressure drop decreases the productivity of the HW. Hence, the effect of PP on the HW productivity and then on S_m are investigated.

Using Equations 3.35 and 3.36, the ratio of productivity of a partially to a fully penetrating HW for the same pressure drawdown can be defined by:

$$PR_{pp-fp} = \frac{q_{pp}}{q_{fp}} = \frac{Ln(r_e/r_w) + S_{m\,fp}}{Ln(r_e/r_w) + S_{m\,pp}}. \qquad (3.37)$$

where $S_{m\,pp}$ and $S_{m\,fp}$ are geometric skin for a partially and a fully penetrating HW, respectively.

It should be noted that the external reservoir radius r_e is calculated using Equation 3.9.

Figure 3.35 presents the productivity ratio of a partially to a fully penetrating HW versus partial penetration ratio (L/X_{res}) for three different L values. The data on the y-axis of this Figure has been obtained by dividing the flow rates calculated using the in-house simulator for partially and fully penetrating HWs. For the set of sensitivity studies presented here the well radius and reservoir thickness are 0.14 and 30 m, respectively. It is clear that decreasing PP (by increasing X_{res} of L/X_{res} in this figure) decreases the well performance of partially penetrating HWs compared to that of fully penetrating ones. This is mainly due to increasing $Ln(r_e/r_w)$, Equation 3.37, resulting in an increase in the flow resistance. Looking at the results in Figure 3.35, it also indicates that an incremental gain in productivity ratio increases as L decreases.

Figure 3.36 shows the effect of PP on S_{mpp}. It is interesting to note that if $L/X_{res}<=0.7$, geometric skin is almost independent of the extent of PP. However at larger L/X_{res} values (all the way up to $L/X_{res}=1$) the geometric skin decreases, i.e., there is slightly better flow performance. It is also noticed that this relative decrease between calculated geometric skins for a partially and fully penetrating HW diminishes at larger L. This is due to a decrease in the contribution of the flow convergence around partially penetrating HWs on the overall total pressure drop at higher L values. It should be noted that the effect of PP on S_{mpp} for short HWs is significant, Figure 3.37. This can be observed more closely by looking at the data of Figure 3.37 b.

The effect of partial penetration can be looked at from a different angle: that is, the effect of PP on S_{mpp} can be expressed in terms of a partial penetration skin, S_{pp}. As mentioned before, in this study geometric skin has been formulated for partially penetrating HWs with L/Xres=0.4. Consequently, S_{mpp} can be expressed as follows:

$$S_{mpp} = S_{mfp} + S_{pp}. \tag{3.38}$$

By rearranging Equation 3.38 S_{pp} can be obtained as follows:

$$S_{pp} = S_{mpp} - S_{mfp}. \tag{3.39}$$

Figure 3.38 shows the $(S_{pp}/S_{m\,pp})$ ratio versus L/h at two different reservoir thickness values (h). To obtain the data on the y-axis of this Figure, first S_{mpp} and S_{mfp} have been calculated by Equation 3.35, using the flow rates obtained from the in-house

simulator for the partially (with L/X_{res}=0.4) and fully penetrating (L/X_{res}=1) HW models, respectively. Then S_{pp} is calculated by Equation 3.39 before being divided by S_{mpp}. It is noted that at low L/h, an increase in L decreases S_{pp}/S_{mpp} ratio significantly. The corresponding value of S_{pp}/S_{mpp} at L/h greater than 12 is almost constant, decreases slightly with increasing h and is negligible, i.e. S_{pp} is less than 0.05.

Based on these results it can be concluded that the partial penetration ratio (L/X_{res}) does not have a significant impact on the geometric skin unless one works at L/X_{res} >0.7 and low L values or at L/h<12 and low h values.

As discussed above, as the HW length increases the impact of PP on the geometric skin decreases significantly. However if it is ignored for short HWs, the predicted values for the HW productivity could be erroneous. Therefore, for such conditions and based on the results of the in-house simulator, a partial penetrating skin formulation has been developed. For such geometries, geometric skin can be written as follows:

$$S_{mpp} = S_m + S_{pp}, \tag{3.40}$$

A sensitivity analysis indicated that the key parameters, which have considerable impact on the geometric skin, were the HW length, reservoir thickness and partial penetrating ratio. A further analysis of data shows that the partial penetrating skin can be approximately expressed as below:

$$S_{pp} = \frac{a}{\left(L/h\right)}\left(\frac{L}{X_{res}}\right)^{b}. \tag{3.41}$$

Many simulation runs were performed with different penetration ratios. The parameters were varied as follows:

1) L (m): 15,30,60,90,120,180,360,540,720,900,1260,1380,1440,1500
2) $\frac{L}{X_{res}}$: 1 , 1.25, 1.5, 2.0, 2.5
3) h (m):15,30,45.
4) r_w (m):0.07,0.14,0.21.

The constant values a and b are -0.67 and 8, respectively, and were obtained by minimising the errors between the values predicted by Equation 3.41 and the skin obtained by applying the calculated in-house simulator mass flow rates into Equation 3.35, using a multi-regression exercise analysis.

Figure 3.39 confirmed the integrity of the correlation by comparing the geometric skin calculated using Equations 3.40 and 3.41 versus the corresponding values obtained by applying the calculated in-house simulator mass flow rates into Equation 3.35, the

in-house simulator for partial penetrating ratio 1 and 0.8. The average absolute deviation error for 200 data points is only 2%. Note that S_{pp} approaches zero for long HWs and also for HWs with a partial penetrating ratio less than 0.7.

3.7.4 Impact of Well Location in z Direction on Geometric Skin

For all the results presented here, HW has been assumed to be located in the centre of the box shaped reservoir drainage area. This assumption makes the application of the proposed geometric skin formulation for scenarios where the flow is not symmetrical questionable. That is, if the well is not centred in the z-direction, there will be an additional resistance, due to the close proximity to one of the two no-flow boundary conditions at the top and bottom of the producing formation. Therefore, the geometric skin and consequently HW productivity will be different in these scenarios. This section is aimed at determining the impact of HW location in the z-direction on the geometric skin and productivity. For each case, different scenarios have been studied by changing the HW location in the z coordinate.

In such systems, the distance from the centre of formation in the z direction, HW length and the reservoir thickness are the important parameters affecting the well productivity. Thus, the well location effect can be expressed as a positive skin by the following equation:

$$S_t = S_m + S_z, \tag{3.42}$$

where S_m and S_z are the geometric skin and the HW location skin.

Figure 3.40 shows the variation of geometric skin versus the HW length for different well locations. It should be noted that the HW geometric parameters e.g., wellbore radius, HW length, the reservoir drainage volume, are the same for these results. Reservoir thickness (h) and the well bore radius are 30 m, and 0.14 m. The results show that if HW is located up to $\frac{h}{6}$ from the centre of the formation (h/2) to the top or bottom, the impact of well location in the z direction on the HW productivity and geometric skin is negligible. It should be noted that since the impact of gravity in this study has been neglected, the distance from the formation centre in both directions has similar effects.

However, when HW is located closer to the no-flow boundaries (top or bottom), the geometric skin increases gradually. This effect is more pronounced for short HWs where the contribution of asymmetrical flow around the wellbore is greater compared to that of long HWs.

As discussed earlier, S_z, HW location skin is a function of $\frac{h}{L}$ and z_{HW}, where z_{HW} is the distance of HW from the centre in the z direction. It was shown that the effect of HW location in the z direction on the geometric skin for a HW located $\frac{h}{6}$ away from the centre is negligible. Thus, a dimensionless number has been introduced to account for the effect of distance of HW from the centre as follows:

$$zd_{HW} = \frac{h/6}{z_{HW}}, \tag{3.43}$$

$$S_z = f(zd_{HW}, \frac{h}{L}), \tag{3.44}$$

The contribution of this dimensionless number increases as HW becomes closer to the (top or bottom) boundaries. Many simulation runs were performed with different well locations. The parameters were varied as follows:

1) L (m):15,30,45,60,90,180,270,360,450,630,690,720,750
2) $z_{HW}: \frac{h}{6}, \frac{3h}{10}, \frac{3h}{4}$
3) h=30 m.

The results of the simulations were correlated to the two pertinent dimensionless parameters ($zd_{HW}, \frac{h}{L}$) to obtain the corresponding expression for S_z as described by Equation 3.45.

$$S_z = \frac{zd_{HW}}{12} \times \frac{h}{L}. \tag{3.45}$$

Figure 3.41 shows that the total skin calculated by the Equation 3.45 versus the skin obtained by applying the calculated in-house simulator mass flow rates into Equation 3.35, confirms the integrity of the proposed approach and the correlations developed. It should be noted that the above correlation is consistent with the earlier results demonstrating that S_z decreases for longer HWs. However, ignoring S_z for short HWs could cause overestimation in the well productivity, sometimes as much as 100%.

It has to be noted that for anisotropic reservoirs the impact of the well location in the z direction on the geometric skin decreases as the vertical flow contribution decreases, by increasing anisotropy.

3.8 SINGLE PHASE NON-DARCY FLOW

According to the Darcy law, Equation 3.46, the pressure drop inside a porous media is a linear function of velocity.

$$V = -\frac{k}{\mu}\nabla P . \tag{3.46}$$

However, this linear function is not valid for high volumetric flow rates. Forchheimer (1914) added a quadratic term to the Darcy flow equation to express nonlinear flow nature at higher velocities, given by:

$$-\nabla P = \frac{\mu}{k}V + \rho\beta|v|v , \tag{3.47}$$

Comparing Equations 3.49 and 3.50, the inertial effect could be defined by a relative permeability term, in the Darcy equation, which depends on the Reynolds number as follows:

$$k_r = \frac{1}{1+R_e} \Rightarrow -\nabla P = \frac{\mu}{kk_r}V , \tag{3.48}$$

$$R_e = \frac{\rho|V|k\beta}{\mu} . \tag{3.49}$$

As noted earlier the flow of a HW can be defined by the flow equation of a VW with a geometric skin, Equation 3.8. In the case of non-Darcy flow, Equation 3.8 can be replaced by Equation 3.50 (Jamiolahmady et al. 2005):

$$m = \frac{2\pi kh\Delta\psi}{Ln\left(\frac{r_e}{r_w}\right) + S_t} , \tag{3.50}$$

where ψ is the pseudo pressure and S_t is the total skin effect, which can be mathematically expressed as follows:

$$\psi = \int \frac{k_r}{\mu} dp \tag{3.51}$$

$$S_t = S_m + S_f . \tag{3.52}$$

In this equation, S_m and S_f are the mechanical and flow skin, respectively. For Darcy flow, the effect of inertia is ignored, therefore the flow skin is zero. Unlike S_m, in the case of Darcy flow, S_f depends on the fluid properties and flow rates, in addition to geometrical parameters. As ψ and S_f are both functions of the volumetric flow rate and fluid properties, obtaining S_f is not a straightforward task.

3.8.1 Flow Skin, Effective Wellbore Radius, Non-Darcy Flow

The objective is to have a 1-D model, which generates the same flow performance as that of the 3-D HW model. Therefore a 1-D open hole simulator similar to the 3-D model has been developed, which simulates the steady state single phase flow around a single VW in an isotropic reservoir model with constant pressure boundary conditions at the same external and wellbore radii as those of the 3-D model of a HW. Here, the author proposal is to convert S_t to the effective wellbore radius, which can be given by:

$$r_w^{'} = r_w \times e^{-S_t}, \tag{3.53}$$

The rearrangement of Equation 3.50 using the effective wellbore radius can be written as follows:

$$m = \frac{2\pi kh\Delta\psi}{Ln\left(\frac{r_e}{r_w^{'}}\right)}. \tag{3.54}$$

Because ψ and $r_w^{'}$ (S_f) are both functions of the volumetric flow rate and fluid properties, $r_w^{'}$ is unknown and its estimation requires an iterative procedure as described below:

1. The mass flow rate of the HW model (m_{hw}) is known from the 3-D in-house simulator for the case under study.

2. S_m is calculated using Equation 3.32.

3. An initial guess for $r_w^{'}$, is obtained based on $S_{m,}$ as follows:

$$\left(r_w^{'}\right)_m = r_w \times e^{-S_m}. \tag{3.55}$$

4. With this $r_w^{'}$, the pressure profile and mass flow rate of the equivalent open hole system (m_{EOH}) is estimated by the 1-D in-house simulator. It should be noted that this calculation is conducted based on a pseudo pressure calculation (Equation 3.50), which is a function of velocity; therefore, another round of iteration is required to estimate the pressure profile and mass flow rate.

5. Absolute deviation (%) between m_{hw} and m_{EOH} is calculated by:

$$AD = \frac{m_{hw} - m_{EOH}}{m_{EOH}} \times 100. \tag{3.56}$$

6. If the AD% is less than the error tolerance threshold, defined value 0.001, then the effective well bore radius is used to estimate the flow skin, $S_{f,}$ using Equation 3.57. Otherwise, the programme adjusts the effective wellbore radius using the following equations:

$$\mathrm{S_f} = \frac{\mathrm{m_{hw}} - \mathrm{m_{EOH}}}{\mathrm{m_{EOH}}} \times \mathrm{Ln}\left(\mathrm{r_e}/\mathrm{r_w^{'}}\right), \tag{3.57}$$

$$r_w' = r_w \times e^{-(S_m+S_f)} = r_w \times e^{-S_m} \times e^{-S_f} = \left(r_w'\right)_m e^{-S_f} . \quad (3.58)$$

Using the new value of the effective wellbore radius, the programme goes back to step 4 to re-calculate the pressure profile around the wellbore and m_{EOH}.

A wide range of variation of pertinent parameters, model geometries and velocities, were considered in this exercise, as shown in Table 3.6, to generate the large data bank required to develop a general flow skin correlation. The physical properties of Texas Cream and Berea cores, with permeability of 11 and 110 mD, respectively, were used to describe the reservoir rock model in this study.

Figures 3.42 and 3.43 confirm the integrity of this approach by comparing the mass flow rates calculated using the EOH 1-D in-house simulator with r_w' and those of the HW 3-D in-house simulator. For 1500 data points, AAD% is only 0.2. These r_w' values were used to develop a general formulation for the effective wellbore radius of the 1-D equivalent open hole system, as described in the next section.

3.8.2 Impact of the inertia on the HW productivity

Figures 3.44a and 3.44b show iso-pressure contour maps for a HW model with 15 m length and wellbore radius of 0.14 m with (non-Darcy flow) and without (Darcy flow) considering inertia. Here, the reservoir thickness was 15 m and the pressure drop across the reservoir was 2700 psi. The reservoir fluid properties are listed in Table 3.7. As expected, due to the effect of inertia on the gas production the iso- pressure curves for this case are closer and more elliptical than those for the case without considering inertia. Figure 3.45 presents k_r (Equation 3.48) distribution around the HW-1. As can be seen, k_r decreased considerably around the wellbore. However, away from the wellbore, inside the reservoir, where the velocity is significantly reduced and Darcy flow prevails, k_r is 1.

As noted in the previous section a large data bank was generated using the 3-D HW and 1-D EOH in-house simulators. This data bank was used to map all important parameters on the effective well bore radius and consequently the flow skin.

Figures 3.46 and 3.47 show the flow skin versus horizontal well length at different reservoir thickness and wellbore radius values, respectively. For the set of simulation runs shown in these two figures, the pressure drop across the reservoir models was 5200 psi. The reservoir properties are similar to those for HW-2 shown in Table 3.6. Figure 3.46 compares the calculated flow skin versus L at three different values of h. It is clear that, for the same pressure drop, the flow skin increases as h increases due to an increase

in the inertial effect at higher flow rates. Figure 3.47 displays the effect of r_w variation on the flow skin versus L. As expected, decreasing r_w, which increases the flow velocity due to reduced flow area, increases S_f. Another important point which can be concluded is that as the HW length increases, flow skins approach zero for all cases considered here.

As discussed in the pervious section, in the proposed approach, the HW productivity is calculated using the VW productivity formulation representing the effect of geometric and flow parameters as a skin or based on r_w'. To obtain a suitable expression for calculation of $S_{f,}$ a number of dimensionless numbers are considered. The first parameter that significantly affects the flow performance is the dimensionless number L/h, the HW length to the reservoir thickness ratio. The effect of non-Darcy flow on the HW productivity deceases as the length increases because velocity around the HW decreases at higher HW lengths. However, it increases as the reservoir thickness increases, because of increased flow rate for the same pressure drop.

Figures 3.48 and 3.49 show the variation of S_f versus velocity for different L/h at the same constant pressure drop of 5200 psi. The velocity has been calculated by dividing the flow rate by the surface area of the HW. Note that the flow skin increases gradually as the velocity increases. For constant velocity, it also decreases sharply as HW length increases. In Figure 3.48, S_f is negligible for L/h>= 12, whilst the corresponding limit in Figure 3.49 is L/h>=16. It should be noted that the study conducted here covers a wide range of velocity. Therefore, it is suggested that when L/h>=20, the effective wellbore radius to be calculated using Equation 3.55, which is based on geometric skin, as the flow skin is negligible. That is, the performance of 1-D EOH, based on the geometric skin is the same as that of the 3-D HW.

Figure 3.50 shows productivity ratio (PR) (Equation 3.59) versus velocity for HW lengths of 90, 120, 180, and 360 m.

$$PR = \left(\frac{J_h}{J_v}\right) = \left(\frac{m_h}{m_v}\right). \tag{3.59}$$

In these simulations, the same pressure drop of 5200 psi was applied in the 1-D openhole radial VW and 3-D HW models. The wellbore radius was 0.14 m and formation thickness was 15 m. Two cores, Berea and Texas Cream, with properties listed in Table 3.1, were used to describe the reservoir model properties. The fluid properties for both models are those listed in Table 3.7. Velocities have been calculated by dividing the volumetric flow rate by the area of the HW. The data in this figure demonstrates that PR increases gradually as the velocity increases, which is more

pronounced at higher HW length. At lower L values, the non-Darcy flow decreases the performance of a HW and VW almost to the same extent. However, at higher L values, the negative impact of inertia on a VW is more pronounced than that on a HW.

Figure 3.51 compares the non-Darcy flow productivity ratio of a HW to a VW with the corresponding values calculated based on the Darcy flow equation in both the VW and HW. Here, the pressure drop, reservoir thickness and wellbore radius were the same as those in Figure 3.50. It should be noted that the productivity ratios corresponding to non-Darcy flow cases are always higher than those obtained for Darcy flow cases. This is because of the more pronounced adverse effect of inertia on the VW performance compared to that on the HW performance. It should be noted that the difference between these two plots is small at lower L values but increases at higher L values and reaches a plateau at very large L values. Moreover, the difference between these two curves (PR based on non-Darcy and Darcy flow regimes) is less, Figure 3.51b, when using lower permeability Texas Cream, which reduces the velocities, rather than higher permeability [Berea] core properties, for the reservoir model description.

The effect of the wellbore radius on PR is shown in Figures 3.52 a and b, which show, similarly to the previous figures, PR improves as the velocity increases. However, the level of improvement for the case with the wellbore radius of 0.07 m is higher compared to those with the wellbore radii of 0.14 and 0.21 m at velocity values of less than 1000 m/day. At velocity values of more than 1000 m/day, the trend is changed and as wellbore radius increases, PR increases. In the case of the lower velocity than 1000 m/day, increasing the wellbore radius decreases the negative impact of inertia in the VW simulation to a greater extent compared to HW, i.e. PR decreases. However, in the cases which range of velocity variation is higher than 1000 m/day, it increases the flow area of the HW more, hence, improving the HW flow performance to a greater extent, i.e. PR increases.

Figure 3.53 highlight that the rock properties could influence the PR significantly. The HW length, wellbore radius and the reservoir thickness are 90, 0.14 and 15 m, respectively. Texas Cream and Berea core samples have different permeability and single-phase inertia factor β. The corresponding values of the $k\beta$ product for Texas Cream and Berea, which affect the Reynolds number calculation (Equation 3.49), are 3.57E+10 and 2.04E+10, respectively. The higher values of $k\beta$ for Texas Cream are resulting in higher inertial effect for the corresponding VWs and PR is higher compared to the case with Berea core properties. This is consistent with what was demonstrated above, i.e. drilling a HW is more beneficial when the impact of inertia is more

pronounced, or in other words for the same production rate the benefits of having a HW is greater for a Texas Cream core.

Figure 3.54 presents the PR of a HW (with or without inertia) versus velocity. For all these cases, the pressure drop across the system was the same. It should be noted that there is a strong dependency between the inertial effect and the HW length, i.e., the impact of inertia is more pronounced at lower L values and higher velocities, decreasing the PR.

The above discussion indicates that the HW performance under a non-Darcy flow regime strongly depends on the velocity, as well as the HW geometrical parameters.

3.8.3 Flow Skin Correlation

As was discussed earlier, HW productivity can be calculated by using an equivalent open hole (EOH) system with an effective wellbore radius, which is derived based on total (mechanical plus flow) skin factor. It was shown that for many cases, the HW productivity can be predicted accurately by the EOH approach with an effective wellbore radius calculated based on the geometric skin, i.e. the flow area around HWs, which is affected by inertia, is also very small. Therefore, an EOH with a wellbore radius defined based on geometric skin (Equation 3.55) used to represent the HW system is a good approximation. In such a case, the velocity effect on the well productivity of both systems, the HW and EOH, would likely be approximately the same, i.e. the flow behaviour around the HW is the same as that of the EOH. This would not be the case if the geometric skin and the actual wellbore radius are included in the well calculation. This was checked by conducting many simulation runs and two-phase pseudo pressure calculations. In other words, the computation of the two-phase pseudo pressure function depends strongly on the wellbore radius and the calculation which is based on effective wellbore radius acknowledges properly the relative permeabilities and physical properties locally across the reservoir drainage area. A similar observation was made for flow around perforated completions (Jamiolahmady et al. 2009).

However, for short to medium HW length, where the flow is less symmetrical and the velocity is higher, the EOH approach with an effective wellbore radius calculated based on the geometric skin would not be a good approximation, because the effect of inertia is significant. The above discussion indicates the need for a more general and effective approach for prediction of the HW productivity.

As discussed earlier, the inertial effect is defined as a single-phase relative permeability (Equation 3.48). For very long HWs, as the velocity decreases, the single-

phase relative permeability approaches 1. However, for predicting the well productivity of short to medium HWs, where the inertia reduces the gas production significantly, kr is less than one and the effective well bore radius should be corrected to account for the high velocity inertial effect.

The magnitude of inertial effect can be expressed by single-phase relative permeability as:

$$k_r = \frac{1}{1+R_e}, \tag{3.60}$$

$$R_e = \frac{\rho|V|k\beta}{\mu}. \tag{3.61}$$

It is proposed that a combination of geometric skin, the two dimensionless numbers, defined in Equations 3.62 and 3.63, and the single-phase inertial factor express the impact of all pertinent parameters.

$$L_D = \frac{L}{h} \tag{3.62}$$

$$h_D = \frac{h}{r_w} \tag{3.63}$$

Further analysis showed that Equation 3.64 can represent this relationship.

$$r_w^{'} = \frac{r_w \times e^{-Sm}}{1 + a \times \left(\frac{\mathrm{Re} \times h_D}{L_D} \right)^b} \tag{3.64}$$

The above equation is very simple and easy to use, i.e. there are only two coefficients (a and b) that need to be estimated. Here, two sets of the data bank which was generated based on the basic physical properties of two different rocks were used to confirm the integrity of the proposed formulation. The effective wellbore radius varies substantially when the reservoir permeability is varied from 11 to 110 mD for the same pressure drop, as the velocity is significantly higher for the latter. The coefficients a and b were estimated as 0.04 and 0.6, respectively, using one of these sets of data; the set data referred to HW-2 in Table 3.6. The other data set, referred to as HW-1 in Table 3.6, was used to verify the reliability of the correlation as described in Section 3.8.5.

3.8.4 Iterative Procedure for Effective Wellbore Radius Estimation

As noted in the previous section, the above effective wellbore radius formulation depends on the velocity. Thus, the calculation of the effective wellbore radius needs an iterative procedure, as described below:

1) An initial guess for r_w', is obtained based on $S_{m,}$ as follows:

$$r_w')_1 = r_w \times e^{-S_m}. \quad (3.65)$$

2) With this r_w', the pressure profile and mass flow rate of the equivalent open hole system (m_{EOH}) are estimated by the 1-D in-house simulator. It should be noticed that this calculation is conducted based on the pseudo pressure calculation (Equation 3.50), which is a function of velocity; therefore, another round of iteration is required to estimate the pressure profile and mass flow rate.
3) The new effective wellbore radius is estimated using Equation 3.64.
4) Absolute deviation (%) between the new effective well bore radius and the previous one is calculated by:

$$AD\% = \frac{r_w')_2 - r_w')_1}{r_w')_1} \times 100. \quad (3.66)$$

5) If the AD% is greater than the error tolerance threshold, defined as 0.01, then, with the new value of the effective wellbore radius, the programme goes back to step 2 to re-calculate the pressure profile around the wellbore Otherwise the iterations stop and the effective wellbore radius and mass flow rate is reported.

It is important to point out that the iterative procedure is converged rapidly. Furthermore, increasing L/h decreases the number of iterations. In the majority of cases the solution converges after 2-3 iterations highlighting the integrity of the approach.

3.8.5 Verification

Figure 3.55 confirms the accuracy of the developed flow skin equation by comparing the calculated mass flow rate obtained using the EOH 1-D simulator, in which the developed r_w' formulation, Equation 3.64, and the iterative procedure described previously have been incorporated, with those of the HW 3-D in-house simulator. The reservoir models and the range of velocities are those listed in Table 3.6, the HW-2 data set. The AAD% (average absolute deviation error) for 270 data points in this study is only 2%.

The accuracy of this developed formulation for flow skin was further verified by applying the proposed method to another reservoir model, with different permeability and velocity. Here, Texas Cream core properties with permeability 11 mD describe the reservoir model. A wide range of variation of HW length, wellbore radius, and thickness of the reservoir were covered for the 220 data points in this data set, as shown in Table 3.6, the HW-1 data set. Figure 3.56 compares the calculated mass flow rate

using the EOH 1-D simulator, incorporating the flow skin formulation and the corresponding proposed iterative procedure, with that of the HW 3-D in-house simulator. This figure shows the accuracy of the developed formulation and proposed method is acceptable, with average absolute deviation of 2%.

3.9 GAS CONDENSATE FLOW

As noted earlier, the flow behaviour around HWs is complex, considering the 3-D flow geometry around the wellbore. That is, it is very difficult to obtain a 3-D analytical solution to forecast accurately the HW productivity. All available semi analytical equations in the literature are applicable only to single phase Darcy flow, and incompressible fluids. In gas condensate reservoirs, as the pressure falls below dew point, a bank of condensate forms around the wellbore, which affects the well productivity and flow behaviour around the wellbore. Fine grid compositional numerical simulation, similar to that of the in-house simulator, is usually required to predict gas-condensate well productivity to account for high velocity phenomena, which result in variation of relative permeability due to the coupling and inertial effects. A simple and reliable method for the HW productivity calculation in gas and condensate reservoirs is very desirable, as the above procedure is computationally very expensive and cumbersome.

To this end, the main aim of the study is to extend the mathematical modelling approach discussed previously to study two-phase flow around HWs in gas condensate reservoirs. To achieve this objective, an in-house simulator has been developed, simulating steady state flow of gas and condensate around a single HW. In the simulator, the generalised relative permeability correlation developed by Jamiolahmady et al. (2009) with universal parameters was employed, which accounts for the combined effects of positive coupling and negative inertia on k_r. To confirm the integrity of the structure of the simulator, limited numbers of simulations were also conducted using ECLIPSE 300 commercial software. Next an extensive bank of data was generated using the in-house simulator. The data bank was employed to find a general practical method for simulating the two-phase flow of gas and condensate around HWs.

3.9.1 In-house 3-D Two-Phase HW Model

The 3-D geometry which is used to model the gas condensate flow around a HW is the same as that for the single-phase flow case, Figure 3.15. However, the governing equations solved for this flow domain are different, as described below.

Governing Equations

The equations describing the two-phase flow of gas and condensate around a HW are those used by Jamiolahmady et al. (2005) in the study of flow behaviour around perforations:

1) The continuity equation for gas and condensate flow at steady state conditions

$$\nabla.\left((\rho v)_g + (\rho v)_c\right) = 0\,, \tag{3.67}$$

where g and c represent the gas and condensate phase respectively.

2) The flow equation for each phase:

$$v_i = \frac{k k_{ri}}{\mu_i} \nabla P \text{ . i=g,c} \tag{3.68}$$

Combining continuity and flow equations, after some mathematical manipulation, gives:

$$\nabla.\left(\left\{ \left[\frac{\rho k_r}{\mu} \right]_g + \left[\frac{\rho k_r}{\mu} \right]_c \right\} k \nabla P \right) = 0\,. \tag{3.69}$$

The total fluid composition (z_j) is constant as the fluid flows through the porous media. However, for each component, there is mass transfer between two phases as expressed by the following equation:

$$z_j = \frac{\rho_g y_j GTR + \rho_c x_j (1 - GTR)}{\rho_g GTR + \rho_c (1 - GTR)} = cons.\,, \tag{3.70}$$

where GTR is the total gas fraction ratio defined by Equation 3.71.

$$GTR = \frac{Q_g}{Q_g + Q_c} = \frac{1}{1 + \frac{k_{rg}}{k_{rc}} \times \frac{\mu_c}{\mu_g}}\,. \tag{3.71}$$

where Q is the volumetric flow rate and g and c refer to gas and condensate.

In Equation 3.69, relative permeability which varies with interfacial tension (i.e. pressure for a given fluid composition) and velocity is estimated using the correlation by Jamiolahmady et al. (2009). In this correlation, gas relative permeability is interpolated between a base curve and a miscible curve, both corrected for the effect of inertia, using a generalised interpolation function. The correlation has either universal parameters or those parameters that can be estimated from readily available

petrophysical data. The correlation is based on the relative permeability ratio ($k_{rgtr}=k_{rg}/k_{rg}+k_{rc}$) as the main variable, which is closely related to fractional flow. The condensate relative permeability is calculated using the definition of relative permeability ratio. It should be noted that in gas/condensate systems, fractional flow is directly related to fluid composition and pressure at steady-state, which is generally prevailing near the wellbore, hence making it much more attractive practically, compared to saturation, which depends on core characteristics.

The composition and fluid properties of equilibrated phases of a fixed overall composition depend only on the pressure for a given temperature. A binary mixture of C1 (methane) and n-C4 (normal butane) was used as a model gas-condensate fluid. The values of composition, density (ρ□□), viscosity (μ□) and interfacial tension (IFT) of C1-nC4 mixtures are those measured in the gas condensate group laboratory as well as literature data (Sage et al., 1940; SUPERTRAPP User's Guide, 1992; Weinaug and Katz, 1943) at 311 K over a wide pressure range, which were implemented in the model in a tabular form, Table 3.8.

Mathematical Solution Technique

Similarly to the single phase modelling approach, the governing non-linear partial differential equation (PDE), Equation 3.69, is solved using Comsol multi-physic software (Version 3.5, 2008), which uses the finite element method. The main variable in this equation is P (pressure). However, the equations are solved for both P and GTR.

The boundary conditions applied to this system are:

1) The pressure at outer boundary (external radius) is known.
2) The pressure at the inner boundary (wellbore radius) is known.
3) The pressure gradient in the wellbore has been ignored, i.e. infinite conductivity for the HW bore.
4) As noted earlier, the total composition is constant, so either the GTR or the total fluid composition is known.

3.9.2 ECLIPSE 3-D Two Phase HW Model

The accuracy of the two-phase mathematical in-house simulator was confirmed by comparing some of its results with those of ECLIPSE300 at the same prevailing conditions.

The reservoir model in this exercise had the core properties of Texas Cream with porosity 0.21 and permeability 9.1 mD. The reservoir fluid was a binary mixture of C1

(methane) and n-C4 (normal butane) described in the previous section. The reservoir was 38 m in x and y directions and 4 m in z direction. The HW length was 15 m. Many different cases were simulated using the ECLIPSE300 and in-house simulators, over a wide range of velocity. The fractional flow at average reservoir pressure was the same in both simulators. The very fine grid was used to capture the abrupt changes in flow parameters near the wellbore. As the k_r correlations used in these two models (i.e. Comsol & ECLIPSE300 models) are different, the base curve relative permeability was used to describe flow around the HW. This is the relative permeability curve measured at a high IFT (above which kr is independent of coupling) and low velocity (below which kr is independent of coupling and inertial effects).

In ECLIPSE 300, seventy injection wells were placed at the boundary of the reservoir to keep the reservoir pressure at the drainage boundary constant.

Figure 3.57 shows the good agreement between the two results. The arithmetic average absolute percentage deviation (AAD%) of the predicted flow rate values by the ECLIPSE simulator compared to those estimated by the HW simulator was 2.9 %.

3.9.3 In-house 1-D Two-Phase Open-Hole Well Model

Since the proposed approach is similar to that used for single phase flow, a 1-D two-phase open hole in-house simulator was also developed, simulating the steady state two-phase flow of gas and condensate around a single VW. The structure of this simulator is similar to that of the single-phase flow simulator (described in Section 3.7.1) but the flow equations governing the two-phase flow of gas and condensate, as described above, are solved.

3.9.4 Results of Two-Phase HW Models

As it was mentioned previously, the objective of this exercise is to generate a large data bank required for proposing a technique for modelling two-phase flow around HW in gas condensate reservoirs. Here, two rock properties, i.e. those of Texas Cream and Berea, were chosen to describe the reservoir rock characteristics. The reservoir and wellbore pressures were changed to between 1800 to 700 psi and 1750 to 400 psi, respectively. The reservoir models are those used for the single-phase flow system, as shown in Table 3.3. The length of the HW was varied from 15 m to 1500 m, the reservoir thicknesses were 15, 30 and 45 m. The total composition of C1 of the binary mixture was varied from 0.55 to 0.2. In addition, the gas fractional flow was changed from 0.80 to 0.999.

Figure 3.58 presents productivity ratio (PR, horizontal to vertical well) versus HW length at r_w of (a) 0.14 m and (b) 0.21 m. The reservoir pressure was 1800 psi; the pressure drop across the drainage area was maintained at 500 psi. The reservoir rock properties were those of Berea sample core properties, Table 3.1. The total gas fractional flows (GTR) were 0.941, 0.907, and 0.809. The corresponding velocity values of the HW changed from 4 to 970 m/day. These values were estimated by dividing the total flow rate (gas and condensate) by the HW area. For all cases considered here, as expected, an increase in the HW length (L) increases PR. Furthermore, as the total gas fractional flow decreases the PR increases. It should be noted that at these low flow velocities and low GTR values, the positive coupling effect is more dominant in HW compared to that in VW, resulting in an increase in PR as GTR is reduced. At higher GTR, the impact of positive coupling is less pronounced in the HW, whilst inertia is still dominant in the VW system. Furthermore, for HWs with lower L, the absolute variation of PR as GTR is varied is less pronounced. This is mainly due to the fact that there is little difference between the velocity in VWs and HWs at such flow conditions.

Figure 3.59 shows PR versus the HW length at three different wellbore radii and GTR_w=0.809. The PR of the smallest wellbore radius (0.07 m) is slightly higher than the corresponding values for the wellbore radii of 0.14 m and 0.21 m. This is mainly due to the more pronounced negative impact of inertia (high velocity non-Darcy flow) on the flow of the corresponding VW for the low r_w values.

The effect of velocity on PR is shown in Figure 3.60. For this part of the study, three different pressure drops of 200 psi, 300 psi, and 400 psi and two GTR_w of 0.941 and 0.809 were studied. Furthermore, the wellbore pressure was 1300 psi. The actual velocity in these simulations at ΔP of 400, 300, 200 psi and GTR_w of 0.81 and 0.94, as HW length was varied, from 3, 2, 1, 8.4, 5.6, and 3.5 to 197, 125, 72, 496, 296, and 166 m/day, respectively. These values were obtained by dividing the flow rate by the flow area of the HW wellbore. At each GTR_w, as can be seen, decreasing the pressure drop, slightly improves PR because of the more pronounced effect of coupling in the HW system. Furthermore, the negative effect of inertia is more pronounced at a higher GTR_w of 0.941 for the VW: hence, the PR values are lower at this GTR_w. In other words, at the lower GTR_w value of 0.809, the positive coupling effect is more dominant for HWs. This results in an improved PR at lower GTR_w compared to that at higher GTR_w. At each GTR_w and lower HW lengths, the impact of velocity on the flow performance of HWs and VWs does not vary with the variation of ΔP, i.e. PR is independent of the applied ΔP. The similarity between the variation of velocity in HWs

and VWs for these low L values also explains the small difference observed between the PR values corresponding to these two GTR_w values.

The same exercises were repeated by changing the reservoir properties. Here, Texas Cream(TC) core properties were used in the reservoir model. It should be noted that the core properties of these two rocks are different, i.e. permeability, porosity, pore size distribution and base curve relative permeability. The velocity varied from 1 to 98 m/day in these simulations. The velocity values for TC are substantially lower than the corresponding values for the reservoir model with Berea core properties. This results in decreasing the velocity effect on both HWs and VWs. Figure 3.61 compares PR versus HW length at three GTR of 0.941, 0.907, and 0.809. It is noted that decreasing the GTR does not alter the PR. That is, a low value of velocity in both HW and VW decreases the effect of negative inertia and positive coupling on the relative permeability.

3.9.5 Equivalent Effective Wellbore Radius

As noted earlier S_t total skin, in Equation 3.53 is the summation of geometric skin and flow skin, neglecting damaged skin. S_m depends on the geometrical parameters and anisotropy. S_f is the flow skin and is defined as the difference between the effect of fluid properties and velocities around HW and EOH systems. Here the objective is to introduce an EOH system, which produces the same flow performance, gas and condensate production rate, as that of a HW system as follows:

$$m^0 = \frac{2\pi kh \int_{Pw}^{Pe} \left(\frac{\rho_l k_{rl}}{\mu_l} + \frac{\rho_g k_{rg}}{\mu_g} \right) dp}{Ln\left(\frac{r_e}{r_w^{'}} \right)}, \qquad (3.72)$$

where $r_w^{'}$ is the effective wellbore radius calculated by Equation 3.53.

An approach similar to that followed for the single-phase flow system described in Sections 3.8.1 to 3.8.3 has been followed. That is, the mass flow rates of the 1-D two phase open hole simulator and that of 3-D two phase HW in-house simulators were matched iteratively by varying $r_w^{'}$. $r_w^{'}$ is then converted to S_f using Equation 3.58.

A large bank of data, over 1375 data points, was generated to evaluate two-phase flow skin for different conditions. For this part of study, the Texas Cream described the reservoir rock properties. The reservoir and wellbore pressures were varied to 1800 psi and 1750 psi and to 700 psi and 400 psi, respectively. GTR was changed from 0.846 to

0.999. The characters of the reservoir model are those listed in Table 3.9. These conditions cover a wide range of actual velocity varying from 0.06 to 841 m/day.

In Section 3.8.3, a flow skin factor correlation for high velocity non-Darcy flow of a single-phase fluid is presented. However, the results also demonstrated that for many cases, the single phase single phase flow skin was negligible if an equivalent well bore radius was calculated based on geometric skin. For a gas condensate system the flow regime is controlled by coupling, operating at moderate to high velocities, and inertia, operating at high velocities. These two act in opposite directions, i.e. the former improves the flow performance whilst the latter reduces the flow efficiency. With these in mind, it is expected that the two phase skin values would be smaller than those of the single-phase flow, i.e. the two-phase flow skin would be negligible, as was reported for gas condensate flow in perforated regions (Final Report, 2005-2008). Below, the author verifies this for a wide range of variations of flow parameters.

Figure 3.63 shows pressure and condensate saturation distribution maps in a drainage area of a HW. As discussed earlier, the new generalized k_r correlation (Jamiolahmady et al. 2009) was employed in the two-phase HW in-house simulator. In this correlation, which generates k_r at different velocity and IFT, the main independent variable is the relative permeability ratio ($k_{rgtr}=k_{rg}/(k_{rg}+k_{rc})$) rather than local saturation. However ,the values of saturation as a function of k_{rgtr} are known for the base k_r curve. Considering that saturation values do not enter into the pseudo-pressure calculation, these saturation values are assigned to the corresponding k_{rgtr} at any time and location: that is, the saturation map across the reservoir could be calculated by knowing k_{rgtr} across the reservoir. The HW length is 15 m in a reservoir with 4 m thickness. The wellbore radius is 0.14 m. It is clear that the shapes of condensate and pressure profile distributions are similar.

Figures 3.64 (a and b) compare GTR and pressure contour profiles for a short and long HW, referred to as HW-1 and HW-2 respectively in Table 3.9. It should be noted that the iso pressure counter map for the long HW are closer compared to those for the short HW. For the short HW the lines are almost circular, whilst those for the long HW length are elliptical. The shape of the pressure profile determines the extension of the condensate bank around the wellbore deep into the reservoir drainage area. The above discussion indicates that the flow behaviour around the long and short HWs are totally different and the method used for long HWs can not be applied for shorter ones. Thus, as will be described later in the next section, a general formulation has been developed for the calculation of the effective wellbore radius of an equivalent open hole system

(EOH) for gas condensate HWs, which accounts for the inertia and coupling effects applicable to both short and long HWs.

In a sensitivity study it was noted that is similar to single-phase non-Darcy flow, for a long HW, the effective wellbore radius can be calculated based on the geometric skin, Equation 3.55.

The other important parameters, which could affect well productivity, are the density over viscosity ratio of each flowing (gas and condensate) phase. Here a single factor, mass mobility, expressed by Equation 3.73, is used to express the effect of three important parameters on the effective wellbore radius.

$$\overline{M}_r = \frac{\rho_g k_{rg}}{\mu_g} + \frac{\rho_c k_{rc}}{\mu_c}, \tag{3.73}$$

where $\frac{\rho_g k_{rg}}{\mu_g}$ and $\frac{\rho_c k_{rc}}{\mu_c}$ are absolute mass mobility for gas and condensate, respectively.

As noted earlier, the effective wellbore radius is a function of the two-phase mass mobility. Thus, an effective multiplication factor has been proposed to use in Equation 3.64, that accounts for the mass mobility effects on the HW productivity. This term is defined as the ratio of (two-phase gas and condensate) mass mobility of the actual flow to that of the base case, without coupling and inertia. For this latter special case, the base relative permeability is used in Equation 3.64. Hence, Equation 3.64 can be rewritten by the following equation:

$$r_w^{'} = \frac{r_w \times e^{-Sm}}{1 + a \times \frac{\mathrm{Re} \times h_D}{L_D}} \times \left(\frac{\overline{M}_{rEOH}}{\overline{M}_{rHW})_{Darcy}} \right)_{ave} = \frac{r_w \times e^{-Sm}}{1 + a \times \frac{\mathrm{Re} \times h_D}{L_D}} \times \left(\frac{\overline{M}_{rEOH}}{\overline{M}_{rEOH})_{Darcy}} \right)_{ave}, \tag{3.74}$$

where $\overline{M}_{rEOH}$ and $\overline{M}_{rEOH})_{Darcy}$ are the average mass mobility for EOH with and without considering the velocity effects, respectively. Or in another form, Equation 3.74 can be rewritten as:

$$r_w^{'} = \frac{r_w \times e^{-Sm}}{1 + a \times \left(\frac{\mathrm{Re} \times h_D}{L_D} \right)^b} \times \left(\frac{\left(\frac{\rho_g k_{rg}}{\mu_g} + \frac{\rho_c k_{rc}}{\mu_c} \right)_{EOH}}{\left(\frac{\rho_g k_{rg}}{\mu_g} + \frac{\rho_c k_{rc}}{\mu_c} \right)_{EOH-Darcy}} \right)_{ave} = \frac{r_w \times e^{-Sm}}{1 + a \times \left(\frac{\mathrm{Re} \times h_D}{L_D} \right)^b} \times \left(\frac{\left(\frac{\rho_g k_{rg}}{\mu_g} + \frac{\rho_c k_{rc}}{\mu_c} \right)_{EOH}}{\left(\frac{\rho_g k_{rgb}}{\mu_g} + \frac{\rho_c k_{rcb}}{\mu_c} \right)_{EOH}} \right)_{ave} \quad (3.75)$$

This formula can be used to predict the effective EOH wellbore radius for two-phase flow of gas and condensate. The average mobility ratio term depends on the fluid properties and relative permeability across the reservoir drainage area. It is important to point out that the above formulation includes the gas and condensate relative permeability and hence, the impact of velocity and IFT in the form of coupling and inertial effects has been included. This formula expresses the HW performance accurately, but it is possible to make it simpler for practical purposes.

Based on a pseudo-pressure calculation approach, the condensate relative permeability can be estimated by the definition of fractional flow using the following equation (Jamiolahmady et. al. 2006):

$$k_{rc} = k_{rg} \times \frac{1 - GTR}{GTR} \times \frac{\mu_c}{\mu_g}, \quad (3.76)$$

where GTR , μ_c and μ_g are the total gas fraction, condensate and gas viscosity, respectively. Substituting above equation into equation 3.75 results in:

$$r_w^{'} = \frac{r_w \times e^{-Sm}}{1 + a \times \left(\frac{\mathrm{Re} \times h_D}{L_D} \right)^b} \times \left(\frac{\left(\frac{k_{rg}}{\mu_g} \left(\rho_g + \rho_c \times \frac{1 - GTR}{GTR} \right)_{EOH} \right)_{ave}}{\left(\frac{k_{rgb}}{\mu_g} \left(\rho_g + \rho_c \times \frac{1 - GTR}{GTR} \right)_{EOH} \right)_{ave}} \right), \quad (3.77)$$

Rearranging Equation 3.77 gives:

$$r_w^{'} = \frac{r_w \times e^{-Sm}}{1 + a \times \left(\frac{\mathrm{Re} \times h_D}{L_D} \right)^b} \times \left(\frac{\left(\frac{k_{rg}}{\mu_g \times GTR} \left(\rho_g \times GTR + \rho_c \times (1 - GTR) \right)_{EOH} \right)_{ave}}{\left(\frac{k_{rgb}}{\mu_g \times GTR} \left(\rho_g \times GTR + \rho_c \times (1 - GTR) \right)_{EOH} \right)_{ave}} \right), \quad (3.78)$$

or

$$r_w^{'} = \frac{r_w \times e^{-Sm}}{1 + a \times \left(\frac{\mathrm{Re} \times h_D}{L_D} \right)^b} \times \left(\frac{\left(\frac{k_{rg}}{\mu_g \times GTR} (\overline{\rho}_{ave})_{EOH} \right)_{ave}}{\left(\frac{k_{rgb}}{\mu_g \times GTR} (\overline{\rho}_{ave})_{EOH} \right)_{ave}} \right), \tag{3.79}$$

where $\overline{\rho}_{ave}$ is the volumetric average density of two-phase gas and condensate which is defined by:

$$\overline{\rho}_{ave} = \rho_g \times GTR + \rho_c \times (1 - GTR), \tag{3.80}$$

The fluid properties and GTR variation in the reservoir depend on the pressure profile. It should be noted that, due to the velocity effects, the pressure and GTR profile distribution in the reservoir for the base EOH (without the coupling and inertial effect) is different from that considering the velocity and IFT effect. However, the pressures and GTR values are the same at the wellbore and exterior boundaries. This implies that the effect of fluid properties would be minimal. This simplifying assumption implies that the mobility ratio can be approximately estimated by the following equation:

$$\left(\frac{\left(\frac{\mathrm{k_{rg}}}{\mu_g \times \mathrm{GTR}} (\overline{\rho}_{\mathrm{ave}})_{\mathrm{EOH}} \right)_{\mathrm{ave}}}{\left(\frac{\mathrm{k_{rgb}}}{\mu_g \times \mathrm{GTR}} (\overline{\rho}_{\mathrm{ave}})_{\mathrm{EOH}} \right)_{\mathrm{ave}}} \right) \cong \frac{(\mathrm{k_{rg}})_{\mathrm{EOH\,ave}}}{(\mathrm{k_{rgb}})_{\mathrm{EOH\,ave}}}, \tag{3.81}$$

Figure 3.65 shows the base and affected (by coupling and inertia) gas relative permeability for EOH of HW-3 and HW-4. As can be seen, the gas relative permeability (k_{rg}) values have changed mostly around the wellbore, where the velocity is high and the two important parameters, coupling and inertia, control the HW productivity. Far away from the wellbore, the difference between these two curves, k_{rgb} and k_{rg}, is almost constant. Thus $\frac{(k_{rg})_{EOH\,ave}}{(k_{rgb})_{EOH\,ave}}$ could be approximately predicted by an average value corresponding to that around the wellbore. Therefore the following equation can be used to estimate approximately the effective EOH wellbore radius:

$$r_w^{'} = \frac{r_w \times e^{-Sm}}{1 + a \times \left(\frac{\mathrm{Re} \times h_D}{L_D} \right)^b} \times \frac{k_{rg}}{k_{rgb}}. \tag{3.82}$$

It should be noted that Equation 3.82 and 3.74 can be applied for both single- and two-phase, gas and condensate, flow cases. That is, for the single-phase flow case, k_r=1.0 and Equation 3.82 converts to Equation 3.64.

3.9.6 Iterative Procedure for Effective EOH Wellbore Radius

As noted earlier, the effective EOH wellbore radius is a function of the fluid properties, coupling and inertial effects. These parameters are determined by the pressure profile distribution into the reservoir during the well production. Therefore, a similar iterative method, which was introduced for the single phase non-Darcy flow case, can be applied here to evaluate the effective EOH wellbore radius of gas condensate systems:

1) First the effective wellbore radius is estimated based on the geometric skin:

$$r_w^{'} = r_w \times e^{-Sm}. \tag{3.83}$$

2) Based on the effective well bore radius, the pressure profile and flow rate are calculated using Equation 3.72. It should be noticed that the pseudo pressure calculation is a function of relative permeability or in other words of velocity; therefore an iterative procedure is required to estimate the pressure profile and the mass flow rate.
3) Using Equation 3.74, the effective wellbore radius is calculated.
4) If the difference between the new effective EOH wellbore radius calculated and the previous one is not negligible, the calculation is repeated from step 2, otherwise the calculated effective well bore radius and mass flow rate are reported.

3.9.7 Verification

Figures 3.66, 3.67 and 3.68 confirm the accuracy of the proposed approach by comparing the calculated mass flow rates obtained using the EOH 1-D simulator, in which the developed effective wellbore radius, Equation 3.74, and the iterative procedure described in the previous section, have been used, with those of the HW 3-D in-house simulator. The reservoir models and the range of the variables are those listed in Table 3.9. The average absolute deviation error, AAD%, for 700 data points in this study is only 4%.

3.10 PSEUDO STEADY STATE FLOW

As noted earlier, when a well commences to produce at a constant rate or pressure, the first flow regime which develops in the reservoir is transient flow. For a system with no flow across the exterior boundaries, a transient flow is changed to PSS flow. At pseudo steady state conditions, the derivate of pressure with time through the reservoir

drainage area remains constant. In other words, the difference between the well bore pressure and average pressure in the reservoir drainage area stays constant.

In Section 3.7, a geometric skin has been developed to account for the effect of geometric parameters and anisotropy on the HW productivity for single phase steady state conditions. This part of study is devoted to investigate the application of this geometric skin formulation for pseudo steady state conditions. A HW pseudo steady in-house simulator has been developed for this part of the study, which will be described first. To confirm the integrity of the in-house simulator, its results have been compared with those of the ECLIPSE commercial simulator for the same prevailing flow conditions. Then the results of the pseudo steady state and steady state in-house simulators are compared. Similarly to the steady state study, the main objective of this study is to extend the proposed approach for the single-phase to two- phase flow (gas and condensate) systems under pseudo steady state conditions, which will be discussed afterwards.

3.10.1 Mathematical Single Phase Pseudo Steady State HW Model

Here the 3-D HW geometry, which was developed using the Comsol mathematical package for studying the flow behaviour at steady state conditions, was used in this study, Figure 3.15. However, the governing equations are those for pseudo-steady state conditions, as described in the next section.

Governing Equations

The equations employed in this study are:

1) The continuity equation for a compressible fluid:

$$\nabla.(\rho v) = \frac{\partial(\rho\varphi)}{\partial t}. \tag{3.84}$$

in which ρ and φ are fluid density and rock porosity.

2) The flow equation is the Forchheimer equation:

$$\nabla P = \frac{\mu}{k} v + \beta\rho|v|v. \tag{3.85}$$

Combining the continuity and 3-D form of the Forchheimer equation, after some mathematical manipulation, gives:

$$\nabla.\left[2\left[\frac{k}{\mu}\right].\frac{\rho\nabla P}{1+\sqrt{1+4\beta\left(\frac{k}{\mu}\right)^2|\nabla P|}}\right]=\frac{\partial(\rho\varphi)}{\partial t}, \tag{3.86}$$

Manipulating the right hand Equation 3.86, using the chain rule of differentiation gives:

$$\frac{\partial(\rho\phi)}{\partial t}=\frac{\partial(\rho\phi)}{\partial p}\times\frac{\partial p}{\partial t}, \tag{3.87}$$

Substituting Equation 3.87 back into Equation 3.86 gives:

$$\nabla.\left[2\left[\frac{k}{\mu}\right].\frac{\rho\nabla P}{1+\sqrt{1+4\beta\left(\frac{k}{\mu}\right)^2|\nabla P|}}\right]=\frac{\partial(\rho\phi)}{\partial p}\times\frac{\partial p}{\partial t}, \tag{3.88}$$

where the term $\frac{\partial(\rho\phi)}{\partial p}$ can be can be expanded to:

$$\frac{\partial(\rho\phi)}{\partial p}=\rho\times\frac{\partial\phi}{\partial p}+\phi\times\frac{\partial\rho}{\partial p}=\rho\phi\left(\frac{1}{\phi}\frac{\partial\phi}{\partial p}+\frac{1}{\rho}\frac{\partial\rho}{\partial p}\right), \tag{3.89}$$

The term $\left(\frac{1}{\phi}\frac{\partial\phi}{\partial p}+\frac{1}{\rho}\frac{\partial\rho}{\partial p}\right)$ on the left hand side of Equation 3.89 can be considered as a total compressibility, c_t Equation 3.89 becomes as follows:

$$\frac{\partial(\rho\phi)}{\partial p}=\rho\times\phi\times c_t, \tag{3.90}$$

Thus, the following equation by substituting the above equation back into Equation 3.88 can be obtained.

$$\nabla.\left[2\left[\frac{k}{\mu}\right].\frac{\rho\nabla P}{1+\sqrt{1+4\beta\left(\frac{k}{\mu}\right)^2|\nabla P|}}\right]=\rho\times\phi\times c_t\times\frac{\partial p}{\partial t} \tag{3.91}$$

As pointed out earlier, for PSS conditions, the pressure derivative with time across the reservoir becomes constant. This can be expressed mathematically as follows:

$$\frac{\partial P}{\partial t}=\frac{\partial\overline{P}}{\partial t}=cons. \tag{3.92}$$

$\overline{p}$ is the volumetric average pressure defined by:

$$\bar{p} = \frac{\int pdV}{V} \tag{3.93}$$

where V and p are the volume and pressure , respectively.

The compressibility, c_t , is defined by Equation 3.94 .

$$c_t = \frac{-1}{V}\frac{\partial V}{\partial p} \tag{3.94}$$

In PSS conditions, producing a total constant flow rate, one can write:

$$c_t \times V \times \partial p = \partial V \tag{3.95}$$

Differentiating the above Equation to time results in the following equation:

$$c_t \times V \times \frac{\partial p}{\partial t} = \frac{\partial V}{\partial t} \tag{3.96}$$

For PSS conditions one can write:

$$\frac{\partial V}{\partial t} = q_w . \tag{3.97}$$

Combining Equations 3.95 and 3.94 and after some manipulations, the pressure derivative to time can be related to q_w as follows:

$$\frac{\partial p}{\partial t} = \frac{q_w}{c_t V} \tag{3.98}$$

Note that V is the pore volume defined by Equation 3.99.

$$V = \phi \times V_t \tag{3.99}$$

Combining Equation 3.99 and 3.98 and substituting this in Equation 3.91 results in the following equation:

$$\nabla . \left[2\left[\frac{k}{\mu}\right] . \frac{\rho \nabla P}{1 + \sqrt{1 + 4\beta\left(\frac{k}{\mu}\right)^2 |\nabla P|}} \right] = \frac{\rho_w q_w}{V_t} . \tag{3.100}$$

Mathematical Solution Technique

The governing non-linear partial differential equation (PDE), Equation 3.89, is solved using Comsol multi-physic software (Version 3.5, 2008). The main dependent variable in this equation is P (pressure).

The boundary conditions applied to this system are:

1) Infinite conductivity for flow within the wellbore (the pressure gradient in the wellbore has been ignored),

2) At the outer boundary (external radius) there are no flow boundaries:

$$\frac{\partial P}{\partial x} = 0 , \qquad (3.101)$$

$$\frac{\partial P}{\partial y} = 0 ,$$

$$\frac{\partial P}{\partial z} = 0 .$$

3) The flow rate at the inner boundary (wellbore radius) is known, q_w.

3.10.2 ECLIPSE Single-Phase Pseudo Steady State HW Model

The accuracy of the pseudo steady state HW in-house simulator was confirmed by comparing its results with those of a similar model constructed using ECLIPSE. The core properties of Texas Cream, with porosity 0.21 and permeability 9.1 mD, were used to describe the reservoir in this model. The PVT tables were similar to those of the steady state model described in Section 3.3.2. The reservoir is 250 m in the x and 125 m in y directions and 16 m in the z direction. The length of HW is 100 m. The initial reservoir pressure is 82.737 bar. In ECLIPSE, to simulate pseudo steady state condition, the inflow at the outer boundary of the steady state model described in Sections was set to zero. The flow rate at the wellbore was kept constant during production time. In ECLIPSE simulations, the volumetric average pressure derivative with time was monitored and when it stabilised, Equation 3.92, it was concluded that the pseudo steady state conditions had been achieved. For each time step, the wellbore pressure, and then the volumetric average reservoir pressure, Equation 3.93, were calculated and compared. Moreover, the fine grid has been used to capture the abrupt changes in the flow parameters near the wellbore.

The average pressures calculated by the in-house mathematical simulator were compared with those of similar simulations conducted using the ECLIPSE simulator. Figure 3.69 shows the good agreement between the two results. The arithmetic average absolute percentage deviation (AAD %) of the predicted PR values by the ECLIPSE simulator compared to those estimated by the HW simulator was 1 %.

3.10.3 Pseudo Steady State: Geometric skin

As discussed previously, the HW productivity can be expressed by the VW productivity equation considering the geometric parameters as a geometric skin. The

PSS VW productivity index is (Heriot Watt Lecture Notes of Reservoir Engineering 2002) expressed by:

$$J_D = \frac{\mu}{2\pi kh} \times \frac{q}{\bar{P} - P_w} = \frac{1}{\ln \frac{r_e}{r_w'} - \frac{3}{4} + \frac{r_{wD}^2}{2} + \frac{r_{wD}^4}{4}}, \quad (3.102)$$

where r_w' and r_{wD} are the effective well-bore radius and the dimensionless effective well-bore radius, respectively.

$$r_{wD} = \frac{r_w'}{r_e} \quad (3.103)$$

It should be noted that in most practical applications, the third and fourth terms in the denominator of Equation 3.102 are ignored. This will be addressed later in this section.

A study was conducted to evaluate the applicability of the effective wellbore radius approach, based on the geometric skin formulation proposed for SS conditions for PSS conditions. Using HWs in-house simulators, many simulation runs were performed for SS and PSS conditions and the calculated geometric skin values were compared. The SS geometric skin was calculated as described previously in Section 3.4.2, using Equation 3.8, and the estimated flow rates by the SS 3-D HW in-house simulator. The corresponding PSS geometric skin was calculated using Equations 3.102 and 3.103 and the average volumetric pressure calculated using the PSS 3-D HW in-house simulator. Figure 3.70 shows the variation of SS and PSS geometric skins calculated using PSS and SS HW in-house simulators versus HW length. The reservoir thicknesses are 15 and 30 m and the HW length is varied from 15 to 1500 m. The data show that the differences between the geometric skins of these two flow regimes are minimal. Here the average deviation error for 51 data points is only 4%, which validates the applicability to PSS conditions of the proposed geometric skin originally developed for SS conditions.

The impact of ignoring the third and fourth terms in the dominator of the productivity index formulation (Equation 3.102) has also been studied. Many simulation runs using the PSS HWs in-simulator were performed. The ranges of variation of the parameters were:

1) L (m): 15,30,60,90,120,180,360,540,720,900,1260,1380,1440,1500
2) $\frac{X_{res}}{L}$: 1 , 1.25, 1.5, 2.5
3) h (m):15,

4) r_w (m):0.07,0.14,0.21.

The results indicate that ignoring these two terms on the PI can produce highly erroneous results for the productivity of HWs with partial penetration ratios below 1.5. Figure 3.71 shows the variation of overestimation of the well productivity index by neglecting the third and fourth terms of Equation 3.93 versus the HW length for the HWs with partial penetration ratios of 1.5. It seems that neglecting these two terms in the well productivity index has little effect on the well productivity of a short HW; however, as the HW length increases, the effect increases gradually and reaches a plateau for very long HWs.

3.10.4 Mathematical Two-Phase Pseudo Steady State HW Model

At PSS conditions the fluid composition and properties could vary with time and location. This suggests that for the two-phase flow conditions, the saturation equation needs to be solved. This further complicates an already complex set of calculations for these low IFT fluid systems. Therefore the author proposes a new approach, which is based on the definition of an equivalent phase to facilitate the gas condensate flow modelling around such complex flow geometries under PSS conditions. In this approach there is a fixed total composition over the whole reservoir at any time during run. It should be noted that the total fluid composition varies with respect to time. The equivalent single-phase fluid properties are weighted based on the fractional flow of the two flowing phases. The fractional flow of gas and condensate is changing with respect to the time and also through the reservoir drainage area.

A mathematical simulator was constructed to verify the integrity of this approach. The 3-D geometry, which is used in this section, is the same as that for the single- phase flow case, Figure 3.15. The HW is producing at a constant total flow rate (gas and condensate).

Governing Equations

The equations describing the two-phase flow of gas and condensate around horizontal well are:

1) The continuity equation for the equivalent phase is:

$$\nabla.\left((\rho v)_{eqphase}\right) = \frac{d(\rho_{eqphase}\varphi)}{dt}, \tag{3.104}$$

where the equivalent phase density is defined as follows:

$$\rho_{eqphase} = \rho_g GTR + \rho_c (1 - GTR) = \frac{(\rho v)_g}{v_g + v_c} + \frac{(\rho v)_c}{v_g + v_c}, \quad (3.105)$$

$$(\rho v)_{eqphase} = \left(\rho_{eqphase}(v_g + v_c)\right) = (\rho v)_g + (\rho v)_c, \quad (3.106)$$

Substituting from Equation 3.106 into Equation 3.104 gives:

$$\nabla.\left((\rho v)_g + (\rho v)_c\right) = \frac{d(\rho_{eqphase}\varphi)}{dt}, \quad (3.107)$$

where g and c represent the gas and condensate phase respectively.

2) The flow equation for each phase is:

$$v_i = \frac{k k_{ri}}{\mu_i} \nabla P \text{ . i=g,c,} \quad (3.108)$$

Combining continuity and flow equations, after some mathematical manipulation, gives:

$$\nabla.\left(\left\{\left[\frac{\rho k_r}{\mu}\right]_g + \left[\frac{\rho k_r}{\mu}\right]_c\right\} k \nabla P\right) = \frac{d(\rho_{eqphase}\varphi)}{dt}. \quad (3.109)$$

Similarly to what was mentioned for the single-phase flow conditions, at PSS conditions, the pressure derivative to the time across the reservoir is constant (Equation 3.87). Following the procedure described in Section 3.9.1, Equation 3.109 can be written as follows:

$$\nabla.\left(\left\{\left[\frac{\rho k_r}{\mu}\right]_g + \left[\frac{\rho k_r}{\mu}\right]_c\right\} k \nabla P\right) = \frac{\rho_{eqphase_w} q_w}{V}. \quad (3.110)$$

where $q_w = \left(q_g + q_c\right)_w$.

Furthermore, as mentioned above, at any time the total fluid composition (z_j) (Fevang &Whitson (1996)) is constant as fluid flows through the porous media. However, there is mass transfer between the two phases for each component as expressed by the following equation.

$$z_j = \frac{\rho_g y_j GTR + \rho_c x_j (1 - GTR)}{\rho_g GTR + \rho_c (1 - GTR)} = cons., \quad (3.111)$$

where GTR is the total gas fraction. The same binary fluid system as that used for the SS simulator was used here.

Mathematical Solution Technique

Similarly to the single phase modelling approach, the governing non-linear partial differential equation (PDE), Equation 3.101, is solved using Comsol multi-physic

software (Version 3.5, 2008), which uses the finite element method. The main dependent variable in this equation is P (pressure).

The boundary conditions applied to this system are:

1) Infinite conductivity for the horizontal wellbore (the pressure gradient in the wellbore has been ignored),
2) The outer boundary (external radius) has no flow boundary :

$$\frac{\partial P}{\partial x} = 0 , \qquad (3.114)$$

$$\frac{\partial P}{\partial y} = 0 ,$$

$$\frac{\partial P}{\partial z} = 0 .$$

3) The flow rate at the inner boundary (wellbore radius) is known, $q_w = q_g + q_c$.
4) Total fluid composition (or fractional flow at volumetric average reservoir pressure (or a given point in the flow domain), (Equation 3.111) is known.

3.10.5 ECLIPSE Two-Phase Pseudo Steady State Horizontal Well Model

The accuracy of the two-phase mathematical in-house simulator was confirmed by comparing its results with those of ECLIPSE300 at the same prevailing conditions.

The reservoir model in this exercise has the core properties of Texas Cream with porosity of 0.21 and permeability of 9.1 mD. The reservoir fluid is a binary mixture of C1 (methane) and n-C4 (normal butane) described in the previous section. The reservoir is 38 m in x and y directions and 4 m in z direction. The length of the horizontal well is 15 m. Two different cases were simulated, using the ECLIPSE300 and in house simulators. The fractional flow at average reservoir pressure was the same for both simulators. The initial reservoir conditions and the total flow rates for these cases are listed in Table 3.10. In addition, the fine grid has been used to capture the complexity of flow near the wellbore. As the k_r correlations used in these two models (i.e. Comsol & ECLIPSE300 models) are different, the base curve relative permeability has been used to describe the flow around the HW. To achieve PSS conditions for the two-phase flow of gas and condensate in ECLIPSE300, first the pressure at the boundaries was kept constant by injecting gas condensate through injection wells in this area, after SS conditions were achieved, these wells shut down and the HW produces gas and condensate with a total constant flow rate. It should be noted that achieving PSS

conditions by natural production in the model constructed by ECLIPSE300 was very difficult. This was mainly due to the considerable time it took for the current model to complete the transient period.

The volumetric average reservoir pressures (P_{ave}) calculated by ECLIPSE300 and the in-house simulator have been compared at different time steps. Figure 3.72 and Figure 3.73 show the good agreement between the two results. The arithmetic average absolute percentage deviation (AAD %) of the predicted P_{ave} (psi) values by the ECLIPSE simulator compared to those estimated by the HW simulator was 0.3 %.

3.10.6 In-House Radial Two-Phase Open-Hole Well Model: Pseudo Steady State Conditions

A two-phase open hole in-house simulator was also developed to investigate the PSS two-phase flow of gas and condensate around a single vertical well. The modelling approach is similar to that used for single-phase flow but solved flow equations governing the two phase flow of gas and condensate by finite element method, as described above.

3.10.7 The Effective EOH Wellbore Radius for Pseudo Steady State Conditions

In Section 3.9.5, a formula was developed for the estimation of effective wellbore radius of an EOH operating under SS conditions. It was also shown that the for single- phase Darcy flow, geometric skin calculated by the HW in-house SS simulator were in good agreement with those obtained from the HW in-house PSS simulator. For the gas condensate system, a procedure similar to that was used for single-phase Darcy flow was used to confirm the integrity of the proposed effective wellbore radius formulation when applied in an EOH operating under PSS conditions. In this exercise the SS and PSS HW and EOH in-house simulators were used. . Here the author intends to verify the applicability of the proposed formulation and approach for gas condensate flow systems under SS condition for gas condensate flow systems under PSS. To achieve this, different 3-D HW and 1-D EOH in-house simulators that are operating under SS or PSS conditions are employed.

First a 3-D HW model is constructed using the SS HW in-house simulator. Then following the proposed procedure, its corresponding 1-D EOH model is created using EOH in-house simulator. In these two models the total mass flow rate, fractional flow rates at the wellbore and pressure drop across the systems are equal. The average pressure of these two systems is almost the same too.

In the next step, it is intended to construct a PSS EOH model that has the same average pressure as that of SS EOH but would produce at a different total mass flow rate. Therefore an iterative backward procedure is required. That is, as noted earlier, for PSS conditions, as the reservoir is depleted by *the constant rate*, the pressure across the reservoir is decreasing with time, no flow boundary conditions. For each time step the average pressure can be calculated by knowing the pressure profile across the reservoir. This pressure profile varies with time and is calculated by solving the PSS diffusivity equation across the reservoir model, Equation 3.110, which is based on an equivalent phase approach.

To complete this step, the geometry, fluid properties, wellbore pressure and GTR of the PSS EOH are set to be similar to those of the SS EOH system. Then the constant flow rate required to solve Equation 3.110 is iteratively adjusted to obtain an average pressure equal to that of the PSS EOH model. The different stages of this iterative procedure are as follows:

1. The initial guess for the mass flow rate is the corresponding one calculated for SS EOH at the same conditions.
2. Then the average pressure for PSS EOH is calculated by solving the diffusivity equation.
3. Absolute deviation (%) between the average pressure of PSS and SS EOH is calculated.
4. If AD% is greater than the error tolerance threshold, defined value 0.0001 (0.01%), then with the new guess for the mass flow rate we go back to step 2. The iteration stops, and the mass flow rate is reported.

Then the estimated mass flow rate for PSS- EOH is used an input data for the solution of diffusivity equation (Equation 3.110) for the PSS HW model. The solution of diffusivity equation produces a pressure profile and an average pressure for the 3-D HW model. If the calculated average pressure of PSS- EOH and HW are the same, the EOH approach and formula which was developed for two phase flow of gas condensate under SS conditions can be applied to PSS conditions.

Two different cases here were chosen, the dimension of the reservoir models and fluid properties can be found in Table 3.11. Figure 3.74 compares the flow skin calculated by the EOH and HW SS simulators with the corresponding values estimated by the EOH and HW PSS simulators. A good agreement is noted between these two results. It seems that the average pressure of the HW under SS and PSS condition are identical although their boundary conditions and flow rates are different.

3.11 SUMMARY AND CONCLUSIONS

A number of in-house simulators were developed to simulate the well performance of horizontal wells in gas and gas condensate reservoirs for steady state and pseudo steady state conditions. A limited number of simulations was also performed using ECLIPSE100 or ECLIPSE300 commercial reservoir simulators with fine grid. The main conclusions of this chapter are as follows:

1. There were good agreements between the results of the in-house simulators with those obtained using ECLIPSE commercial reservoir simulators with fine grid and for the same prevailing flow conditions.

2. Extremely fine grid is required using the commercial simulator (ECLIPSE) to capture the effect of anisotropy with good accuracy.

3. A combination of increased number of mesh elements and using second order Lagrange function were required in the finite element based in-house simulator to obtain accurate results for anisotropic formations.

4. Horizontal well performance is affected strongly by anisotropy values for (horizontal well length (L)) / (reservoir thickness (h)) less than 25.

5. A deviation between the results of the in-house simulator with those obtained using two well-known equations (Joshi (1985) and Economides (1996)) indicated that these equations may not predict horizontal well performance properly in anisotropic formations for L/h less than 25.

6. A geometric skin was developed as a function of pertinent parameters, i.e., length of horizontal well, radius of the well, reservoir thickness and anisotropy, using the efficient statistical Response Surface method. The integrity of the geometric skin formulation was validated by comparing its results for data points not used in its development. This exercise also included comparing some of its predictions with those of Joshi's (1985) & Borosiv's (1984) semi-analytical equations, with reasonable accuracy. These later data points were carefully selected to be within the range of applicability of these equations.

7. The effect of partial penetration (PP) on the well performance of horizontal well (HW) and geometric skin was studied comprehensively. The results indicated that the partial penetration ratio (L/X_{res}(the reservoir dimension in x direction)) does not have a significant impact on the geometric skin unless one works at L/X_{res} >0.6 and low L values or at L/h<12 and low h values.

8. The impact of asymmetry of the HW location in the z direction was studied. It was found that its impact on the HW flow performance is negligible for long HWs.

9. A SS single-phase flow skin formulation, based on the effective wellbore radius of an equivalent open hole system replicating 3-D flow around a HW, was developed. The integrity of the effective wellbore radius formulation was validated by comparing its prediction with the corresponding estimated values using the in-house simulator. Because of the dependency of the effective wellbore radius on velocity, its implementation in the pseudo-pressure calculation requires an iterative procedure. A second round of iteration for calculation is also required for the velocity which is involved in the pseudo-pressure calculation

10. It was shown that the flow skin increases as the velocity increases. However, as HW length increases, flow skin decreases sharply.

11. Flow skin increases as the thickness of the reservoir increases, due to increased inertial effect at higher flow rates.

12. The flow skin approaches zero for L/h>=20.

13. Productivity ratio (PR) (ratio of HW to vertical well (VW) flow rates) is almost constant for short HW lengths at different velocity values. However, it increases as L increases, due to decreasing inertial effect on the well productivity.

14. There is a strong dependency between the inertial effect and the HW length. At higher L (HW length) values, the negative impact of inertia on VW performance is more than that on HW performance. This results in higher PR (productivity of HW to VW) values.

15. The impact of inertia on the HW performance is more pronounced at lower L values and higher velocities, both decreasing PR.

16. The effect of the wellbore radius on PR is negligible.

17. In the case of two-phase flow of gas and condensate, the effect of inertia on PR (HW/VW) is more pronounced at higher the total gas fractional flow (GTR) values. At higher GTR, the impact of positive coupling is less pronounced in the HW, whilst inertia is still dominant in the VW system.

18. As the total gas fractional flow decreases the PR(HW/VW) increases that is, the positive coupling effect is more dominant in HW compared to that in VW, resulting in an increase in PR as GTR is reduced.

19. The study of flow around HWs in gas and condensate systems indicated that for long HWs, the assumption of the effective radius of the EOH based on the geometric skin is a good approximation. However for short to medium length HWs, this

assumption is not valid and the results could be highly erroneous. Therefore a generalized effective radius of an equivalent open hole system was developed, which captures the impact of important flow parameters and correctly extended to single-phase flow conditions. Similarly to the single-phase inertial flow case, the implementation of this wellbore radius also requires an iterative procedure. The accuracy of this formulation was confirmed by comparing its results with the corresponding values obtained using the HW in-house simulator.

20. The results showed that the proposed SS (steady state) effective wellbore radius formulations are also applicable to PSS (pseudo steady state) conditions.

References

Babu D.K. and Odeh A.S., Nov. 1989: Productivity of a Horizontal well, SPE Reservoir Engineering, 4(4), 417-421.

Babusˇka I., Szabo B.A. and Katz I.N., 1981: The p-version of the finite element method, SIAM Journal on Numerical Analysis 18 (1981) 515–545.

Babusˇka I. and Suri M., 1990: The p- and h–p versions of the finite element method an overview, Computer methods in Applied Mechanics and Engineering, 80 (1990) 5–26.

Borisov Ju. P., 1984: Oil Production Using Horizontal and Multiple Deviation Wells, Nedra, Moscowfl 964. Translated by J.Strauss, S. D. Joshi (ed.) Phillips Petroleum Co., the R&D library translation, Bartlesville.

Boualem Marir, Sonatrach Inc. and Tiab Djebbar, Oct 2006: Performance of Horizontal Wells in Gas Condensate Reservoirs Hassi R'Mel Field, Algeria, SPE 100753.

Dehane A., Sonatrach PED, Tiab D., and S.O. Osisanya, Nov 2000: Performance of Horizontal Wells in Gas condensate Reservoirs ,Djebel Bissa Field, SPE CIM 65504.

Ding Y., Ha-Duong T., Giroire J. and Moumas V., 2004: Modelling of Single-Phase Flow for Horizontal Wells in a Stratified Medium, Elsevier Publishers, Computer & Fluid, 33.

Economides Michael J., Deimbacher Franz X., Brand Clement W. and Heinmann E. Zoltan, Dec 1991: Comprehensive Simulation of Horizontal Well Performance, SPE 20717.

Economides M.J., Brand C.W. and Frick T.P., Dec. 1996: Well Configurations in Anisotropic Reservoirs, SPEFE, 257-262. (Also Paper SPE 27980, 1994.).

Escobar, F.H. and M. Montealegre, 2008: A More Accurate Correlation For The Productivity Index Of Horizontal Wells., J. Eng. Applied Sciences, 3: 70-7811.

K. Furui, D. Zhu and A.D. Hill, 5-8 Oct 2003: A Comprehensive Model of Horizontal Well Completion Performance, SPE 84401-MS.

Fevang Ø. And Whitson C.H., 1996: Modeling Gas-Condensate Well Deliverability, SPE reservoir engineering.

Giger, F., May 1985: Reduction du nombre de puits pm I'tilisation de forages horizontals, Reveue de L'institute Gancais du Petrole, 38.

Gas Condensate Recovery Project (2005-2008) Final Report, 2008, IPE, Heriot Watt University, UK.

Giger, FM., Reiss, L.H. and Jourdan A.P., Sep 1984: The Reservoir Engineering Aspects of Horizontal Drilling, SPE 13024, presented at the 1984 meeting SPE Annual Technical Conference and Exhibition, Houston.

Goode P.A. and Kuchuk F.J., Aug 1991: Inflow Performance of Horizontal Wells, SPE Reservoir Engineering, p 319-323.

Hashemi A. and Gringarten A.C, June 2005: Comparison of Well Productivity between Vertical, Horizontal and Hydraulically Fractured Wells in Gas Condensate Reservoirs, SPE 94178.

Helmy, M. W. and Wattenbarger, R.A., Sep. 1998: Simplified Productivity Equations for Horizontal Wells Producing at Constant Rate and Constant Pressure, SPE 49090, Presented at the 1998 Annual Technical Conference and Exhibition, New Orleans, Louisiana.

Henderson G.D., Danesh A., Tehrani D.H. and Badr Al-kharusi, 3-6 Oct. 2000 : The Relative Significance Of Positive Coupling And Inertial Effects On Gas Condensate Relative Permeabilities At High Velocity, SPE 62933, Proceedings of the SPE Annual Technical Conference and Exhibition, Dallas, 193-202.

Hughes T.J.R., 1987: The Finite Element Method, Linear Static and Dynamic F.E., Analysis, Prentice-Hall, Englewood Cliffs, NJ.

Joshi S.D., 1991: Horizontal Well Technology, PennWell, Tulsa, Oklahoma.

Jamiolahmady M. and Sohrabi M. , 2005: Single-phase flow in and around perforation tunnel, IASME Transactions, Issue 7, Volume 2, pp 1288-1297.

Jamiolahmady M., Danesh A. and Sohrabi M., June 2005: Gas Condensate Flow in Perforated Region, SPE 94072, Proceedings of the SPE Europec Conference, SPE 94072.

Jamiolahmady M., Danesh A., Sohrabi M. and Duncan D. B, February 2006: Flow around a rock perforation surrounded by damaged zone: Experiments vs. Theory, Journal of Petroleum Engineering and Science, 50 (2), pp. 102-114..

Jamiolahmady M., Ghahri P., Victor O.E and Danesh A. , June 2007: Comparison of Vertical and Horizontal Wells Productivity in Layered Gas-condensate Reservoirs, Proceedings of the SPE Europec Conference, SPE 107168, London.

Jamiolahmady M., Danesh A., Sohrabi M. and Ataei R., March 2007: Gas condensate flow in perforated region, SPE Journal, 12 (1), pp. 89-99.

Jamiolahmady M., Sohrabi M., Ireland S., and Ghahri P., 2009: A Generalized Correlation for Predicting Gas-Condensate Relative Permeability at near the Wellbore Conditions, Journal of Petroleum Science and Engineering.

Kamkom R. and Zhu, April 2006: Generalized Horizontal Well Inflow Relationships for Liquid, Gas, or Two-Phase Flow, SPE 99712.

Lee S.H., May 1986: Analysis of Productivity of Inclined Wells and Its Implication for Finite-Difference Reservoir Simulation, SPE 16002.

Lu J. and Tiab D. , 31 March-3 April 2007: A Simple Productivity Equation for a Horizontal Well in Pseudo Steady State in a Closed Anisotropic Box-Shaped Reservoir, SPE 106970, Presented at the 2007 SPE Production and Operations Symposium held in Oklahoma, U.S.A.

Lu J., Oct. 2001: New Productivity Formulae of Horizontal Wells, Journal of .Canadian Petroleum Technology, 40(10):55-67.

Muskat M., 1937: The Flow of Homogeneous Fluid through a Porous Media, Intl. Human Resources Development Crop. , Boston.

Myers, R.H. and Montgomery D.C., 1995: Response Surface Methodology: Process and Product Optimization Using Experiment, New York, Wiley.

Peaceman D.W., 1993: Representation of a Horizontal Well in Numerical Reservoir Simulation, SPE21217.

Permadi p., 20-22 March 1995: practical Methods to Forecast Production Performance of Horizontal Wells, SPE paper presented at the Asia Pacific Oil and Gas Conference, held in Kuala Lumpur, Malaysia.

Renard Gerard and Dupuy J.M., 1991: Formation Damage Effects on Horizontal-Well Flow Efficiency, (includes associated papers 23526 and 23833 and 23839), SPE 19414-PA.

Sage B.H, Hick B.L. and Lacey W.N. , 1940: Phase Equilibria in hydrocarbon system-the methane-n-butane systems in the two-phase region, Ind. Eng. Chem. 32, 1058-1092.

SUPERTRAPP (NIST Thermophysical Properties of Hydrocarbon Mixture Database) User‘s Guide by National Institute of Standards and Technology (NIST), NIST Standard Reference Database 4, July 1992, Version 1.0.

Shedid S. A., Osisanyia S., and Tiab D., 1996: A Simple Productivity Equation for Horizontal Wells Based Upon Drainage Area Concept, SPE 35713 paper presented at the Western Regional Meeting held in Anchorage, Alaska.

Shedid A., Abdulrazag and Zekri Y., Oct 2001: Sensitivity Analysis of Horizontal Well Productivity under Steady-State Conditions, SPE 72121.

Sheng J.: Discussion of Permeability Anisotropy Effect, 2007, SPE 114504.

Szabo B. and Babusˇka I., 1991: Finite Element Analysis, John Wiley & Sons, Inc., New York.

Wang Sh. and Eaton J. , 2007: Predicting Productivity Index of Horizontal Wells, Journal of Energy Resources Technology , Vol. 129, pp89-95.

Weinage C.F. and Katz D.L., 1943: Surface Tension of Methane-Propane Mixtures, Industrial Engineering Chem. 35(2), 239-246.

Table 3.1: Basic Core Properties.

Core type	**Porosity**	**Permeability (mD)**	**Single-phase inertia factor (1/m)**
RC1b	0.08	0.18	
Texas Cream	0.21	11.1	3.93E+9
Berea	0.185	100	1.08E+8

Table 3.2: Properties of the ECLIPSE 300 reservoir models constructed for sensitivity studies.

Model	**Dimension -X (ft)**	**Dimension -Y (ft)**
(Model A)	10500	10500
(Model B)	6320	6320

Table 3.3: Parameters of the author's proposed geometric skin correlation, Equation 3.32, and the corresponding range of variation of the scaled variables.

Variables	**Scaled Factors (Parameters)**	**Practical Range**
x_1	Ln (re/ rw)	rw:0.07-0.21 (m) re= $\alpha \times L$
x_2	Ln (h/(2rw))	rw:0.07-0.21 (m) h:15-45 (m)
x_3	h/(L $\sqrt{I_{ani}}$)×Ln (h/((2rw $\sqrt{I_{ani}}$))	L:15-1500(m) L=Length of horizontal well
x_4	$Ln(I_{ani})$	$I_{ani} = k_v / k_h$:1.0-0.001

Table 3.4: Maximum and minimum values (scaling variables) of parameters of the author's proposed geometric skin correlation, Equation 3.32.

	x_1	x_2	x_3	x_4
Max	10.23296	5.772737	291.7704	0
Min	4.625838	3.575527	0.035755	-6.90771

Table 3.5: Coefficients of the geometric skin correlation, Equation 3.32.

Coefficients	Value	Upper-limit	Low-limit	S.E.
a0	103.5686	109.1115	98.02564	2.828037
a1	51.8554	56.95519	46.75561	2.601933
a2	-9.93358	-7.66612	-12.201	1.156866
a3	112.2508	118.9199	105.5817	3.402609
a4	45.49969	48.7889	42.21048	1.678167
a11	-0.11611	0.083984	-0.31621	0.10209
a22	-0.15714	-0.09776	-0.21652	0.030296
a33	2.091544	3.016957	1.166132	0.472149
a44	-0.45557	-0.33003	-0.58111	0.064051
a12	0.159738	0.327122	-0.00765	0.0854
a13	53.70282	58.41658	48.98906	2.404982
a14	-0.65525	-0.3441	-0.96639	0.158748
a23	-9.35982	-7.26048	-11.4592	1.071091
a24	0.401992	0.53183	0.272155	0.066244
a34	44.33314	47.31587	41.35042	1.521798

Table 3.6: Parameters of the horizontal well model used to develop the flow skin, S_f.

	HW-1	HW-2
Rock properties	Texas Cream k=9.1mD β=3.927E+9	Berea k=110mD β=1.854E+8
Length of horizontal well (HW)	15-1500 m	15-1500 m
Reservoir thickness	15-45 m	15-45 m
Wellbore radius	0.07-0.21 m	0.07-0.21 m
Velocity	3-2400 m/day	30-13000 m/day

Table 3.7: Fluid Properties of a natural gas

P/psi	ρ / kgm^{-3}	μ / cp
1000	77.34	0.145

Table 3.8: Properties of the mixture C1-C4, %C1: 73.6%, P_{Dew}=1865 psi.

P(psi)	**x1**	**y1**	ρ_c **(kg/m^3)**	ρ_g **(kg/m^3)**	μ_c **cp**	μ_g **cp**	**IFT mN.m**
1865	0.4195	0.4195	223.3	223.3	0.0261	0.0261	0
1850	0.3521	0.5049	307.5	220.5	0.0398	0.0255	0.008
1840	0.343	0.5146	317.4	211.4	0.0405	0.0249	0.036
1800	0.3069	0.5535	341.1	188.7	0.0431	0.0211	0.112
1790	0.3018	0.5583	345.1	184.8	0.0474	0.0206	0.149
1750	0.2814	0.5776	359.5	171.3	0.0462	0.0195	0.2809
1700	0.2609	0.5944	374.7	157.4	0.0491	0.0184	0.4318
1650	0.2444	0.6088	387	146.5	0.052	0.0176	0.5785
1600	0.2279	0.6232	397.8	137.8	0.0549	0.017	0.7329
1565	0.2192	0.6297	404	132.6	0.0601	0.0172	0.852
1500	0.203	0.6418	421.76	118.39	0.0608	0.016	1.1106
1400	0.1821	0.655	438.62	106.44	0.0669	0.0152	1.5938
1250	0.154	0.6664	459.64	91.27	0.0762	0.0144	2.3971
1200	0.1452	0.669	466.06	86.68	0.0793	0.0141	2.6907
1000	0.1136	0.6712	487.63	69.89	0.0908	0.0133	3.9239
800	0.0859	0.664	505.63	54.71	0.1015	0.0126	5.2907
600	0.0604	0.6335	522.29	41.17	0.1121	0.012	6.8104
500	0.0484	0.605	530.06	34.86	0.1173	0.0117	7.6186
400	0.0368	0.5636	537.53	28.78	0.1234	0.0114	8.4582
300	0.0257	0.4985	544.48	22.93	0.1283	0.0111	9.3119
200	0.0152	0.3948	551.22	17.16	0.133	0.0106	10.2085
150	0.01	0.3128	554.66	14.33	0.1356	0.0101	10.6795
100	0.0049	0.1901	557.94	11.55	0.1383	0.0094	11.15
80	0.0029	0.123	559.11	10.45	0.1393	0.009	11.3299
60	0.0008	0.0408	560.48	9.35	0.1405	0.0083	11.5268
51.61	0	0	560.87	8.9	0.1411	0.008	11.595

Table 3.9: Parameters of different HWs studied in this work.

	HW-1	**HW-2**	**HW-3**	**HW-4**
Reservoir **Core Properties**	Texas Cream k=9.1mD β=3.927E+9	Texas Cream k=9.1mD β=3.927E+9	Texas Cream k=9.1mD β=3.927E+9	Texas Cream k=9.1mD β=3.927E+9
Fluid	C_1-C_4 T=311K, P_D=1865 psia	C_1-C_4 T=311K, P_D=1865 psia	C_1-C_4 T=311K, P_D=1865 psia	C_1-C_4 T=311K, P_D=1865 psia
Number of Data Points	1	1	1	1
Formation thickness/m	4	4	15	15
HW Length (m)	60	180	15	15
P_{wf}/psia (range)	1700	1700	1780	1700
GTR_w	0.8	0.8	0.86	0.85
P_e/psia	1850	1850	1850	1800
r_w(m)	0.14	0.14	0.07	0.07
Comment	Two-Phase	Two-Phase	Two-Phase	Two-Phase

Table 3.9: Parameters of different HWs studied in this work.

	HWs-5	**HWs-6**	**HWs-7**	**HWs-8**	**HWs-9**
Reservoir Core Properties	Texas Cream k=9.1mD β=3.927E+9	Texas Cream k=9.1mD β=3.927E+9	Texas Cream k=9.1mD β=3.927E+9	Texas Cream k=9.1mD β=3.927E+9	Texas Cream k=9.1mD β=3.927E+9
Fluid	C1-C4 T=311K, PD=1865 psia	C1-C4 T=311K, PD=1865 psia	C1-C4 T=311K, PD=1865 psia	C1-C4 T=311K, PD=1865 psia	C1-C4 T=311K, PD=1865 psia
Number of Data Points	16	16	16	16	16
Formation thickness/m	15	15	15	15	15
HW Length (m)	(15-180)	(15-180)	(15-180)	(15-180)	(15-180)
P_{wf}/psia (range)	1700	1780	1720	1600	1750
GTR_w	0.86	0.86	0.85	0.87	0.95
P_e/psia	1850	1850	1850	1850	1850
r_w(m)	(0.07-0.21)	(0.07-0.21)	(0.07-0.21)	(0.07-0.21)	(0.07-0.21)
Comment	Two-Phase	Two-Phase	Two-Phase	Two-Phase	Two-Phase

Table 3.9: Parameters of different HWs studied in this work.

	HWs-10	**HWs-11**	**HWs-12**	**HWs-13**
Reservoir Core Properties	Texas Cream k=9.1mD β=3.927E+9	Texas Cream k=9.1mD β=3.927E+9	Texas Cream k=9.1mD β=3.927E+9	Texas Cream k=9.1mD β=3.927E+9
Fluid	C_1-C_4 T=311K, P_D=1697 psia	C_1-C_4 T=311K, P_D=1865 psia	C_1-C_4 T=311K, P_D=1865 psia	C_1-C_4 T=311K, P_D=1697 psia
Number of Data Points	16	16	16	16
Formation thickness/m	15	15	15	15
HW Length (m)	(15-180)	(15-180)	(15-180)	(15-180)
P_{wf}/psia (range)	1720	1565	1300	1365
GTR_w	0.94	0.92	0.94	0.93
P_e/psia	1800	1765	1800	1565
r_w(m)	(0.07-0.21)	(0.07-0.21)	(0.07-0.21)	(0.07-0.21)
Comment	Two-Phase	Two-Phase	Two-Phase	Two-Phase

Table 3.9: Parameters of different HWs studied in this work.

	HWs-14	**HWs-15**	**HWs-16**	**HWs-17**
Reservoir Core Properties	Texas Cream k=9.1mD β=3.927E+9	Texas Cream k=9.1mD β=3.927E+9	Texas Cream k=9.1mD β=3.927E+9	Texas Cream k=9.1mD β=3.927E+9
Fluid	C_1-C_4 T=311K, P_D=1865 psia	C_1-C_4 T=311K, P_D=1865 psia	C_1-C_4 T=311K, P_D=1865 psia	C_1-C_4 T=311K, P_D=1865 psia
Number of Data Points	16	16	16	16
Formation thickness/m	15	15	15	30
HW Length (m)	(15-180)	(15-180)	(15-180)	(15-180)
P_{wf}/psia (range)	800	1780	1750	1700
GTR_w	0.97	0.72	0.69	0.86
P_e/psia	1800	1850	1855	1850
r_w(m)	(0.07-0.21)	(0.07-0.21)	(0.07-0.21)	(0.07-0.21)
Comment	Two-Phase	Two-Phase	Two-Phase	Two-Phase

Table 3.9: Parameters of different HWs studied in this work.

	HWs-14	**HWs-15**	**HWs-16**	**HWs-17**
Reservoir Core Properties	Texas Cream k=9.1mD β=3.927E+9	Texas Cream k=9.1mD β=3.927E+9	Texas Cream k=9.1mD β=3.927E+9	Texas Cream k=9.1mD β=3.927E+9
Fluid	C_1-C_4 T=311K, P_D=1865 psia	C_1-C_4 T=311K, P_D=1697 psia	C_1-C_4 T=311K, P_D=1865 psia	C_1-C_4 T=311K, P_D=1865 psia
Number of Data Points	16	16	16	16
Formation thickness/m	30	30	30	30
HW Length (m)	(15-180)	(15-180)	(15-180)	(15-180)
P_{wf}/psia (range)	1780	1720	1600	1750
GTR_w	0.86	0.85	0.87	0.95
P_e/psia	1850	1850	1850	1850
r_w(m)	(0.07-0.21)	(0.07-0.21)	(0.07-0.21)	(0.07-0.21)
Comment	Two-Phase	Two-Phase	Two-Phase	Two-Phase

Table 3.9: Parameters of different HWs studied in this work.

	HWs-18	**HWs-19**	**HWs-20**	**HWs-21**
Reservoir Core Properties	Texas Cream k=9.1mD β=3.927E+9	Texas Cream k=9.1mD β=3.927E+9	Texas Cream k=9.1mD β=3.927E+9	Texas Cream k=9.1mD β=3.927E+9
Fluid	C_1-C_4 T=311K, P_D=1697 psia	C_1-C_4 T=311K, P_D=1865 psia	C_1-C_4 T=311K, P_D=1865 psia	C_1-C_4 T=311K, P_D=1697 psia
Number of Data Points	16	16	16	16
Formation thickness/m	30	30	30	30
HW Length (m)	(15-180)	(15-180)	(15-180)	(15-180)
P_{wf}/psia (range)	1720	1565	1300	1365
GTR_w	0.94	0.92	0.94	0.93
P_e/psia	1800	1765	1800	1565
r_w(m)	(0.07-0.21)	(0.07-0.21)	(0.07-0.21)	(0.07-0.21)
Comment	Two-Phase	Two-Phase	Two-Phase	Two-Phase

Table 3.9: Parameters of different HWs studied in this work.

	HWs-22	**HWs-23**	**HWs-24**	**HWs-25**	**HWs-26**
Reservoir Core Properties	Texas Cream k=9.1mD β=3.927E+9	Texas Cream k=9.1mD β=3.927E+9	Texas Cream k=9.1mD β=3.927E+9	Texas Cream k=9.1mD β=3.927E+9	Texas Cream k=9.1mD β=3.927E+9
Fluid	C_1-C_4 T=311K, P_D=1865 psia	C_1-C_4 T=311K, P_D=1865 psia	C_1-C_4 T=311K, P_D=1697 psia	C_1-C_4 T=311K, P_D=1865 psia	C_1-C_4 T=311K, P_D=1865 psia
Number of Data Points	16	16	16	16	16
Formation thickness/m	30	45	45	45	45
HW Length (m)	(15-180)	(15-180)	(15-180)	(15-180)	(15-180)
P_{wf}/psia (range)	800	800	1365	1700	1780
GTR_w	0.97	0.97	0.93	0.86	0.86
P_e/psia	1800	1800	1565	1850	1850
r_w(m)	(0.07-0.21)	(0.07-0.21)	(0.07-0.21)	(0.07-0.21)	(0.07-0.21)
Comment	Two-Phase	Two-Phase	Two-Phase	Two-Phase	Two-Phase

Table 3.9: Parameters of different HWs studied in this work.

	HWs-27	**HWs-28**	**HWs-29**	**HWs-30**
Reservoir Core Properties	Texas Cream k=9.1mD β=3.927E+9	Texas Cream k=9.1mD β=3.927E+9	Texas Cream k=9.1mD β=3.927E+9	Texas Cream k=9.1mD β=3.927E+9
Fluid	C_1-C_4 T=311K, P_D=1697 psia	C_1-C_4 T=311K, P_D=1865 psia	C_1-C_4 T=311K, P_D=1865 psia	C_1-C_4 T=311K, P_D=1697 psia
Number of Data Points	16	16	16	16
Formation thickness/m	45	45	45	45
HW Length (m)	(15-180)	(15-180)	(15-180)	(15-180)
P_{wf}/psia (range)	1720	1600	1750	1720
GTR_w	0.85	0.87	0.95	0.94
P_e/psia	1850	1850	1850	1800
r_w(m)	(0.07-0.21)	(0.07-0.21)	(0.07-0.21)	(0.07-0.21)
Comment	Two-Phase	Two-Phase	Two-Phase	Two-Phase

Table 3.9: Parameters of different HWs studied in this work.

	HWs-31	**HWs-32**	**HWs-33**	**HWs-34**
Reservoir Core Properties	Texas Cream k=9.1mD β=3.927E+9	Texas Cream k=9.1mD β=3.927E+9	Texas Cream k=9.1mD β=3.927E+9	Texas Cream k=9.1mD β=3.927E+9
Fluid	C_1-C_4 T=311K, P_D=1865 psia	C_1-C_4 T=311K, P_D=1865 psia	C_1-C_4 T=311K, P_D=1697 psia	C_1-C_4 T=311K, P_D=1865 psia
Number of Data Points	16	16	16	16
Formation thickness/m	45	45	45	45
HW Length (m)	(15-180)	(15-180)	(15-180)	(15-180)
P_{wf}/psia (range)	1565	1300	1365	800
GTR_w	0.92	0.94	0.93	0.97
P_e/psia	1765	1800	1565	1800
r_w(m)	(0.07-0.21)	(0.07-0.21)	(0.07-0.21)	(0.07-0.21)
Comment	Two-Phase	Two-Phase	Two-Phase	Two-Phase

Table 3.9: Parameters of different HWs studied in this work.

	HWs-35	**HWs-36**
Reservoir Core Properties	Texas Cream k=9.1mD β=3.927E+9	Texas Cream k=9.1mD β=3.927E+9
Fluid	C_1-C_4 T=311K, P_D=1865 psia	C_1-C_4 T=311K, P_D=1865 psia
Number of Data Points	1	1
Formation thickness/m	15	15
HW Length (m)	15	15
P_{wf}/psia (range)	1565	1365
GTR_w	0.87	0.9
P_e/psia	---	---
r_w(m)	0.07	0.07
Comment	Two-Phase	Two-Phase

Table 3.10: The initial reservoir conditions and mass flow rates for Two-Phase PSS HWs models studied here.

HWs Model	Pres (psi)	$Q_t(m^3/day)$	GTR_{well}
A	1557	31.36	0.79
B	1493	35	0.89

Table 3.11: The well geometries and initial reservoir conditions for two-phase PSS HWs models studied here.

	HWs-PSS1	**HWs-PSS2**
Reservoir Core Properties	Texas Cream k=9.1mD β=3.927E+9	Texas Cream k=9.1mD β=3.927E+9
Fluid	C_1-C_4 T=311K, P_D=1865 psia	C_1-C_4 T=311K, P_D=1865 psia
Number of Data Points	1	1
Formation thickness/m	15	15
HW Length (m)	15	15
P_{wf}/psia (range)	1565	1365
GTR_w	0.87	0.9
P_e/psia	---	---
r_w(m)	0.07	0.07
Comment	Two-Phase	Two-Phase

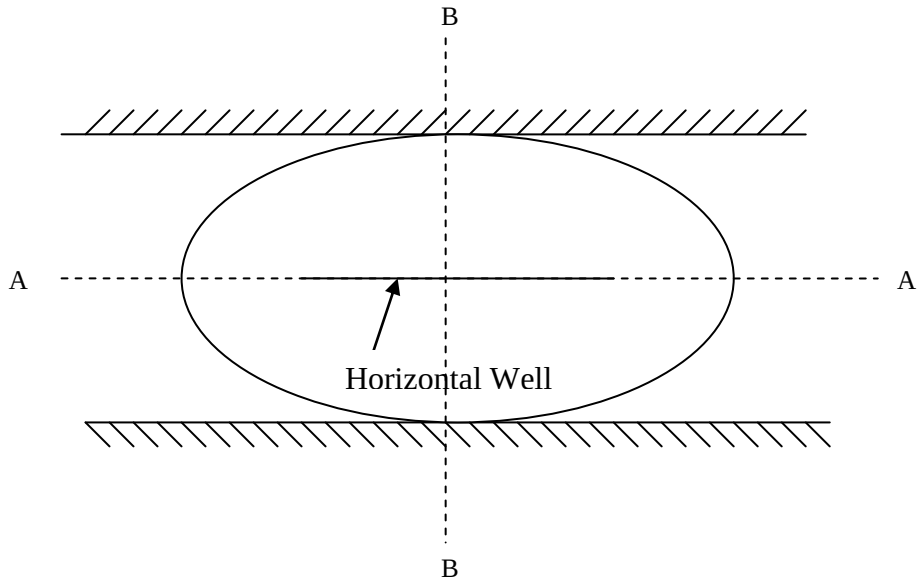

(a)

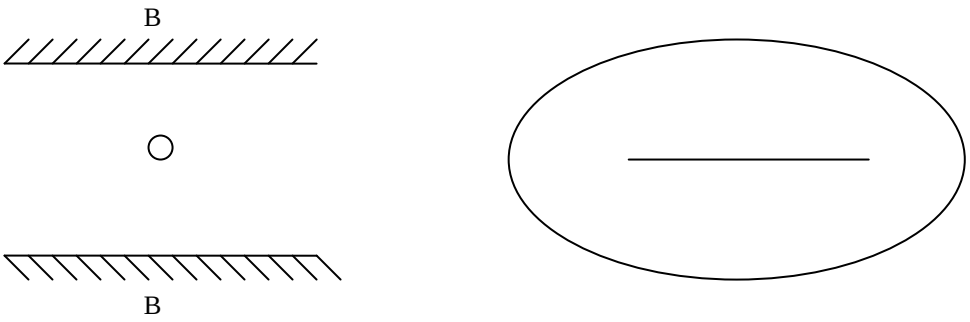

(b)

Figure 3.1: a) An ellipsoid drainage volume; b) Dividing 3-D problems into two 2D problems (vertical and horizontal planes), Joshi (1988).

Figure 3.2: The HW drainage area, a rectangular with two semi circles at the ends, used for semi analytical solutions by Giger (1985) and Renarld and Dupuy (1991).

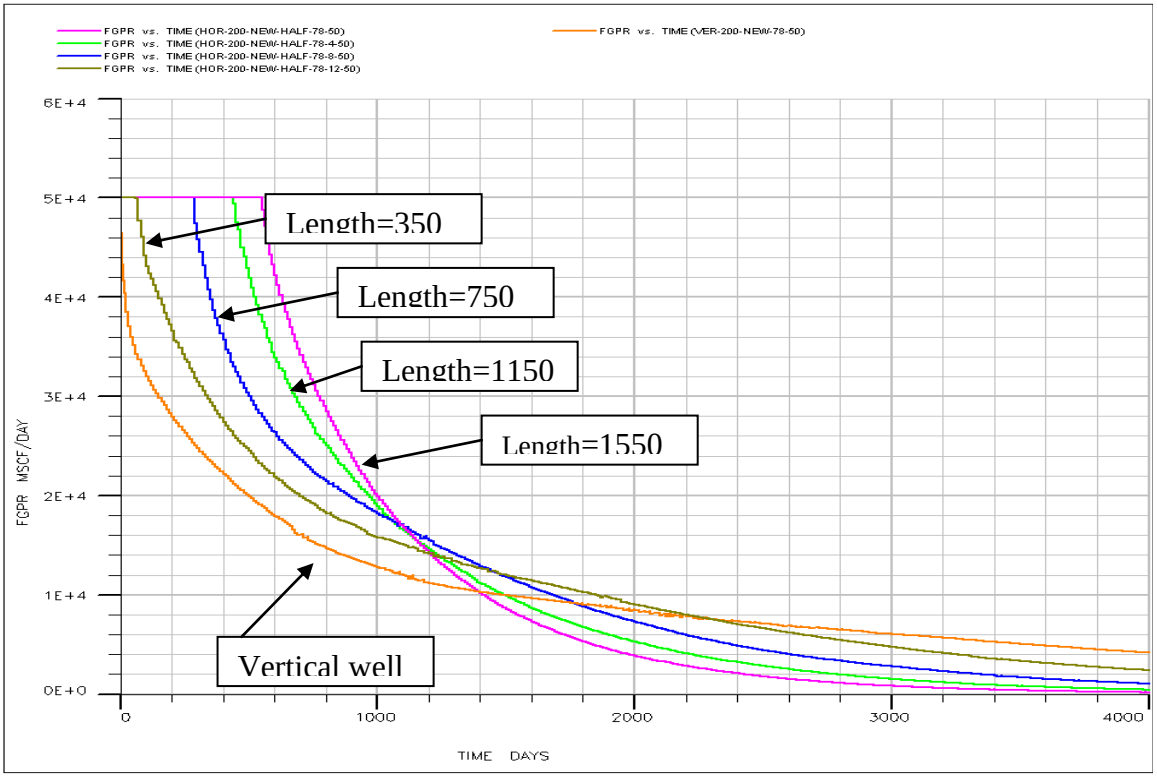

(a)

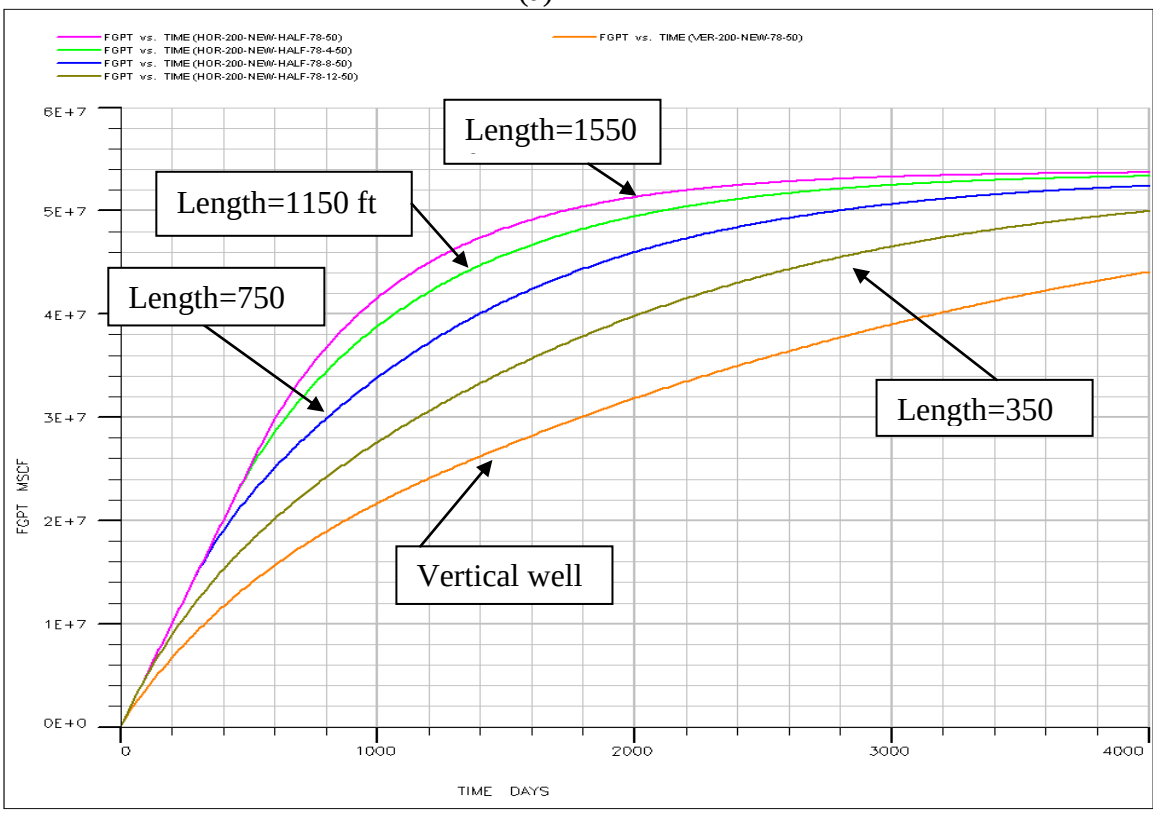

(b)

Figure 3.3: (a) Gas production rate and (b) Total gas production versus time for the horizontal wells with length of 1550, 1150, 750, and 350 ft, and a vertical well, all in the reservoir with 50 ft thickness, Model A of Table 3.1.

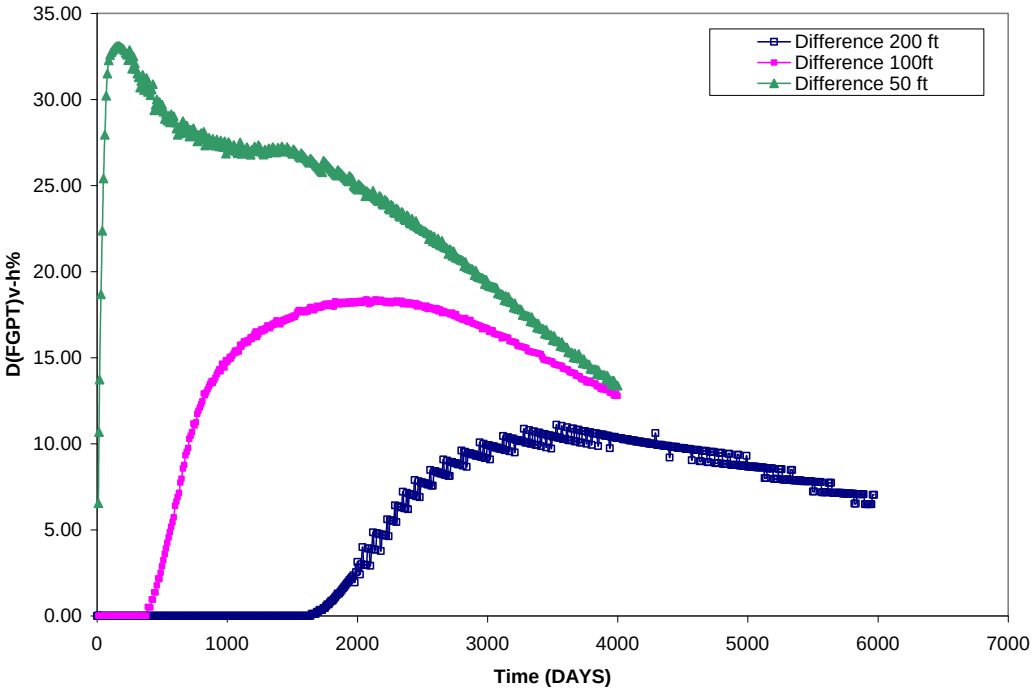

(a)

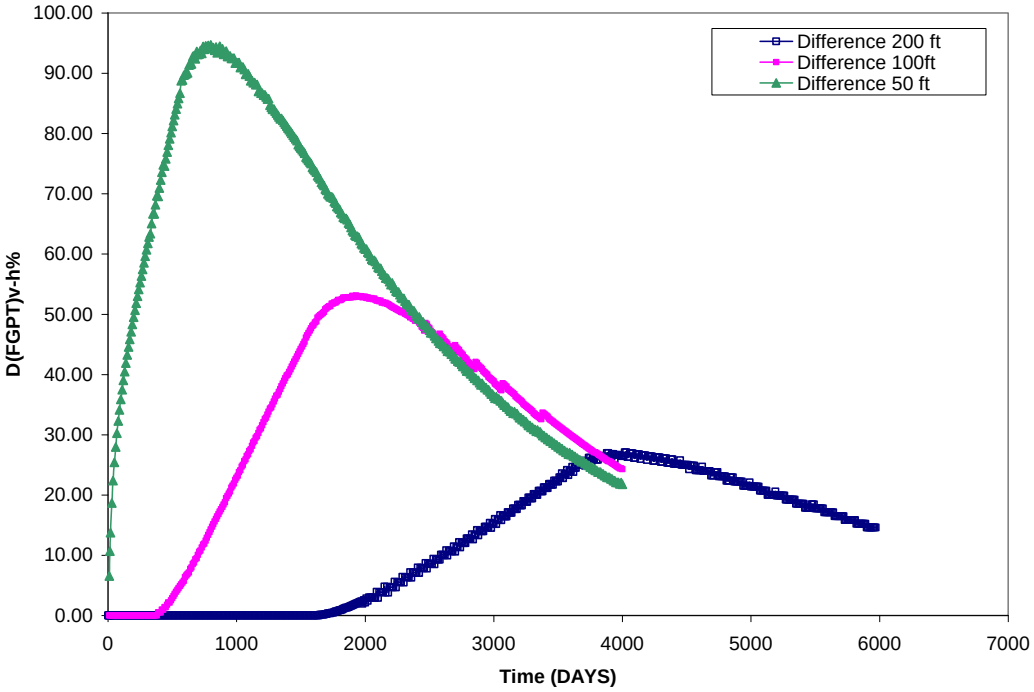

(b)

Figure 3.4: Relative increase in cumulative gas production in horizontal wells compared to that of the vertical well $P_w<P_{dew}$: a) horizontal well length= 350; ft b) horizontal well length= 1550 ft, Model A of Table 3.2.

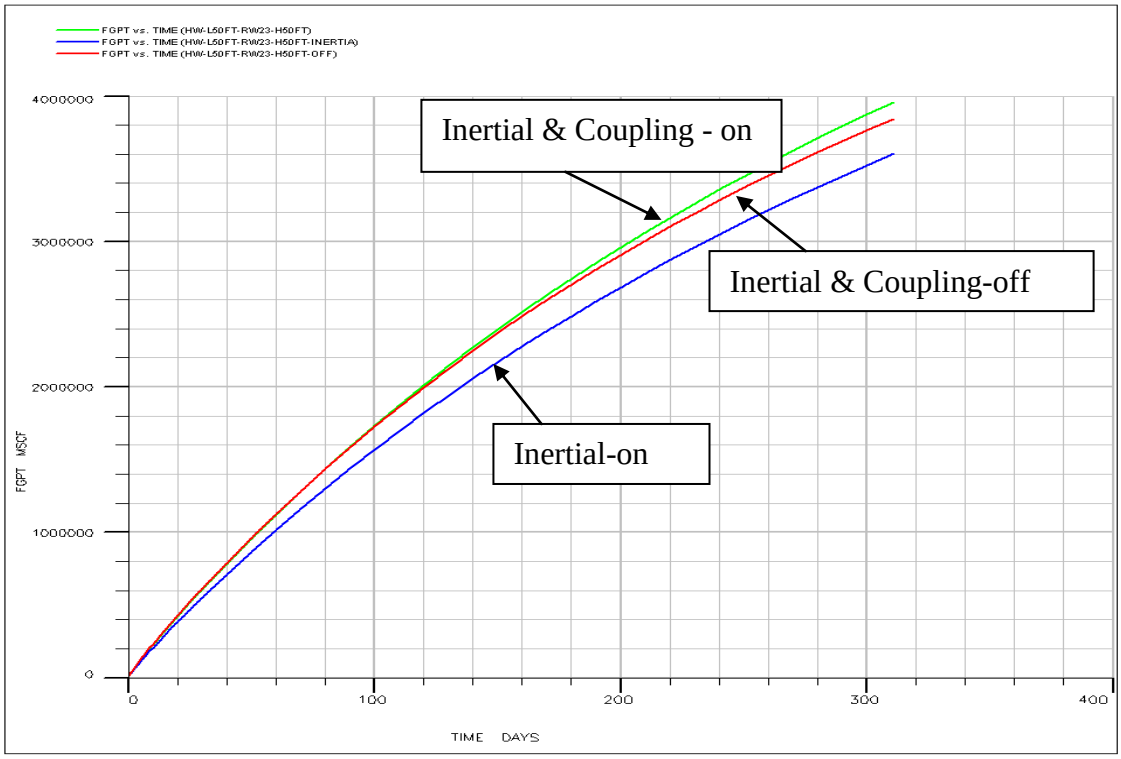

Figure 3.5: Total gas production vs. time, with and without considering coupling and inertial effects, Model B (Table 3. 2), Texas Cream core properties, Lhw=100 ft.

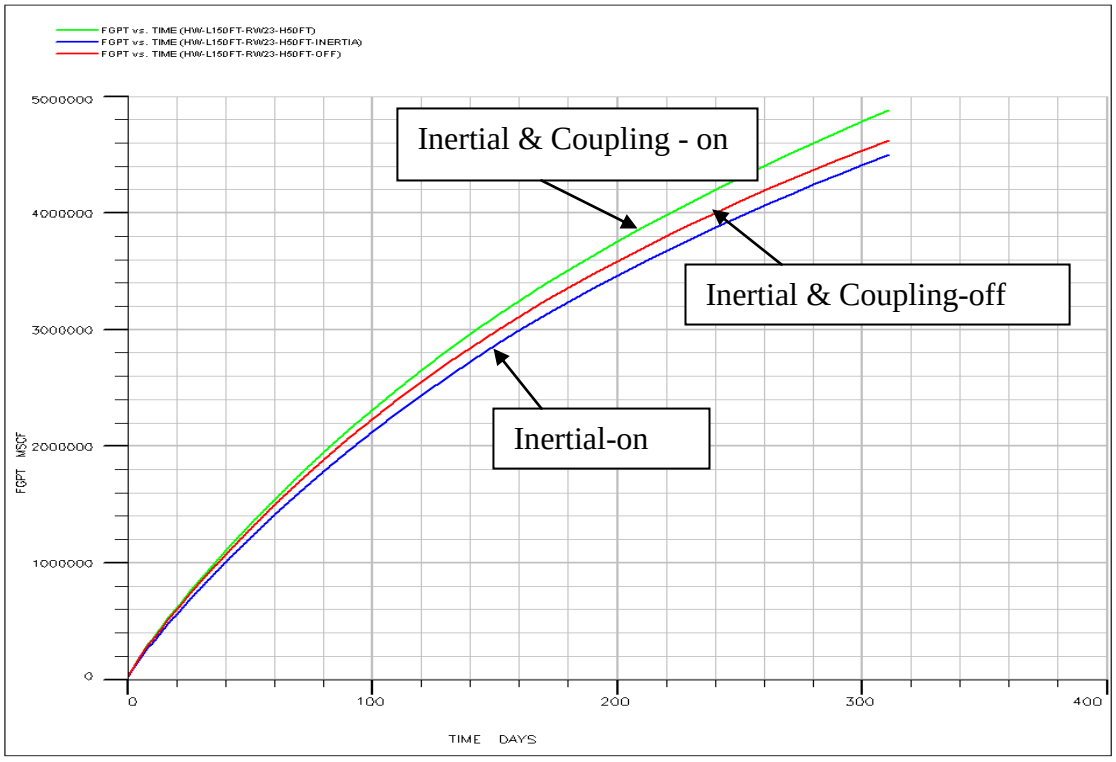

Figure 3.6: Total gas production vs. time, with and without considering coupling and inertial effects, Model B (Table 3.2), Lhw=300 ft, Texas Cream core properties.

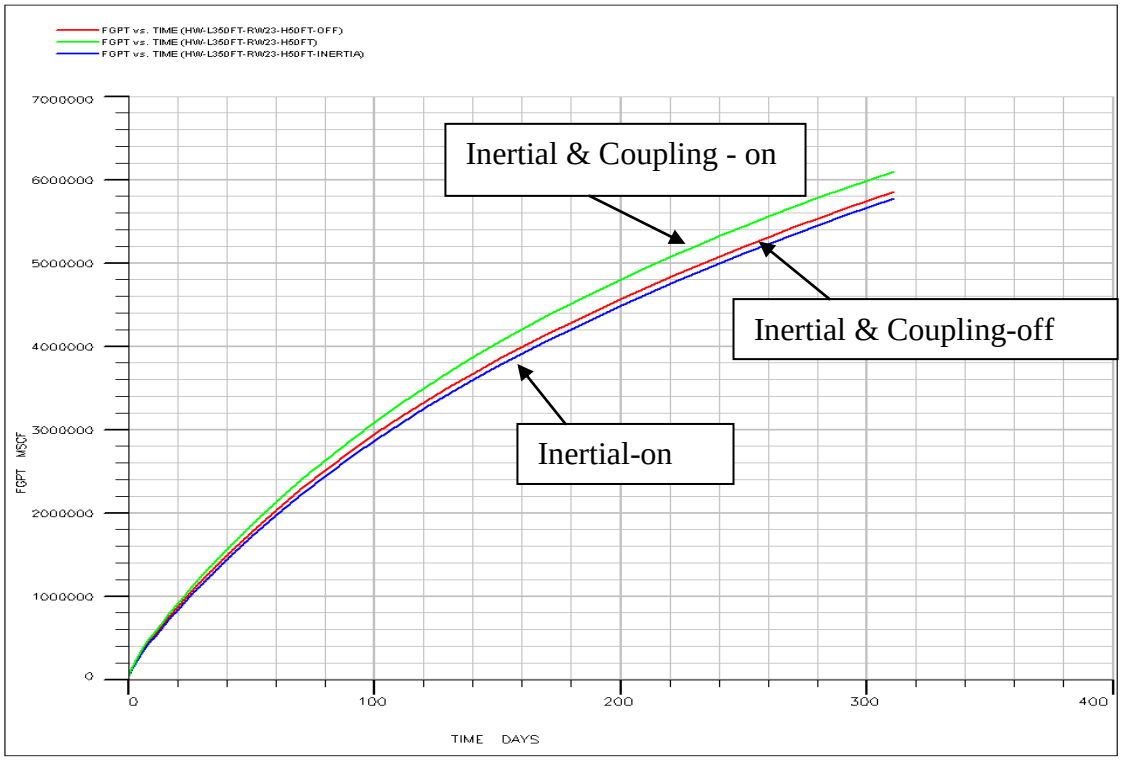

Figure 3.7: Total gas production vs. time, with and without considering coupling and inertial effects, Model B (Table 3.2), Lhw=700 ft, Texas Cream core properties.

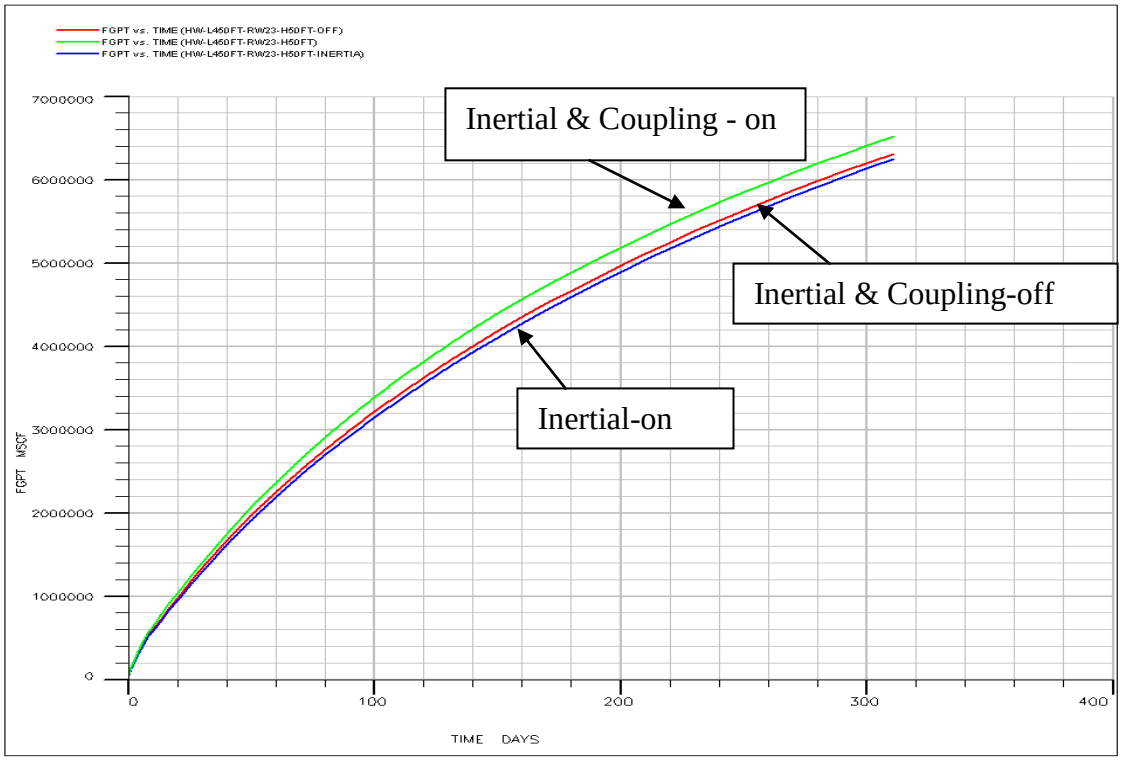

Figure 3.8: Total gas production vs. time, with and without considering coupling and inertial effects, Model B (Table 3.2), Lhw=900 ft, Texas Cream core properties.

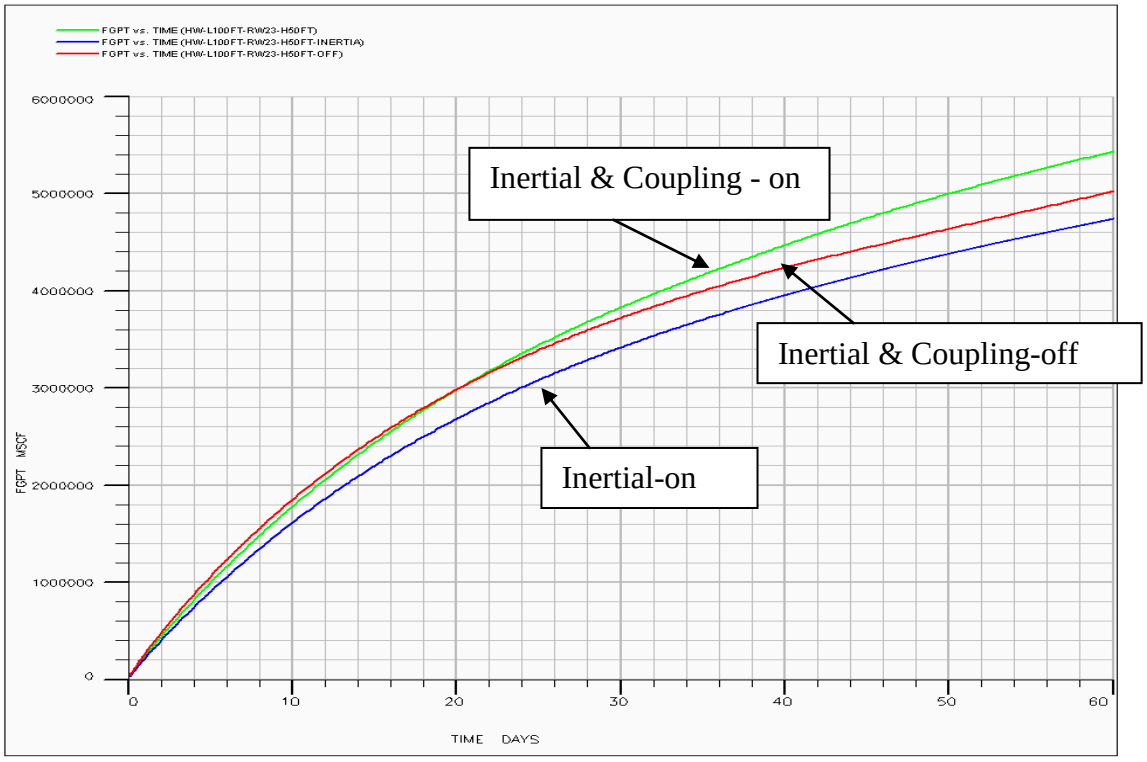

Figure 3.9: Total gas production vs. time, with and without considering coupling and inertial effects, Model B (Table 3.2), Lhw=200 ft, Berea core properties.

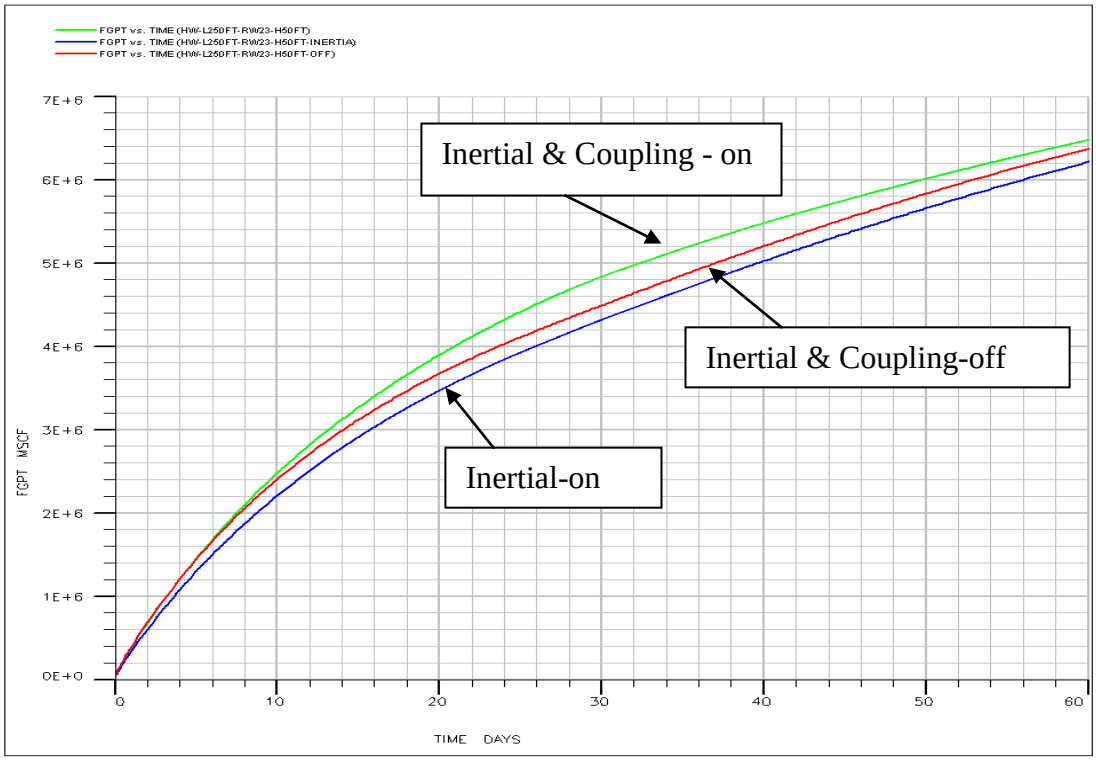

Figure 3.10: Total gas production vs. time, with and without considering coupling and inertial effects, Model B (Table 3.2), Lhw=500 ft, Berea core properties.

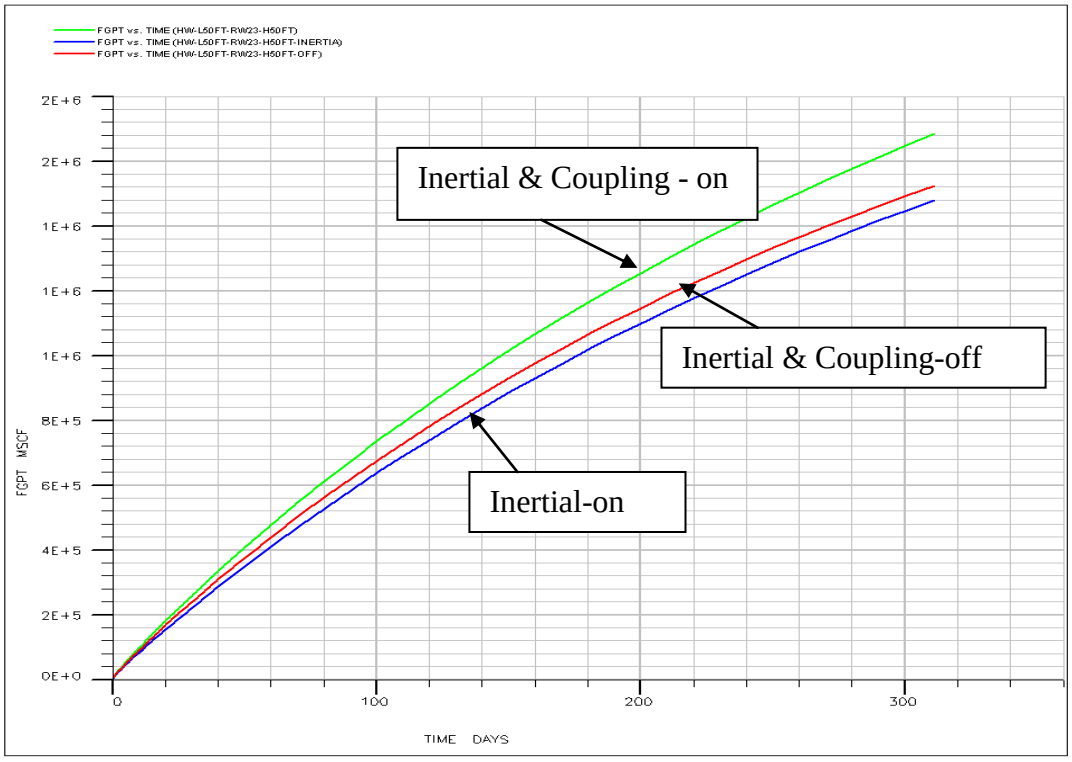

Figure 3.11: Total gas production vs. time, with and without considering coupling and inertial effects, Model B (Table 3.2), Lhw=100 ft, RC1b core properties.

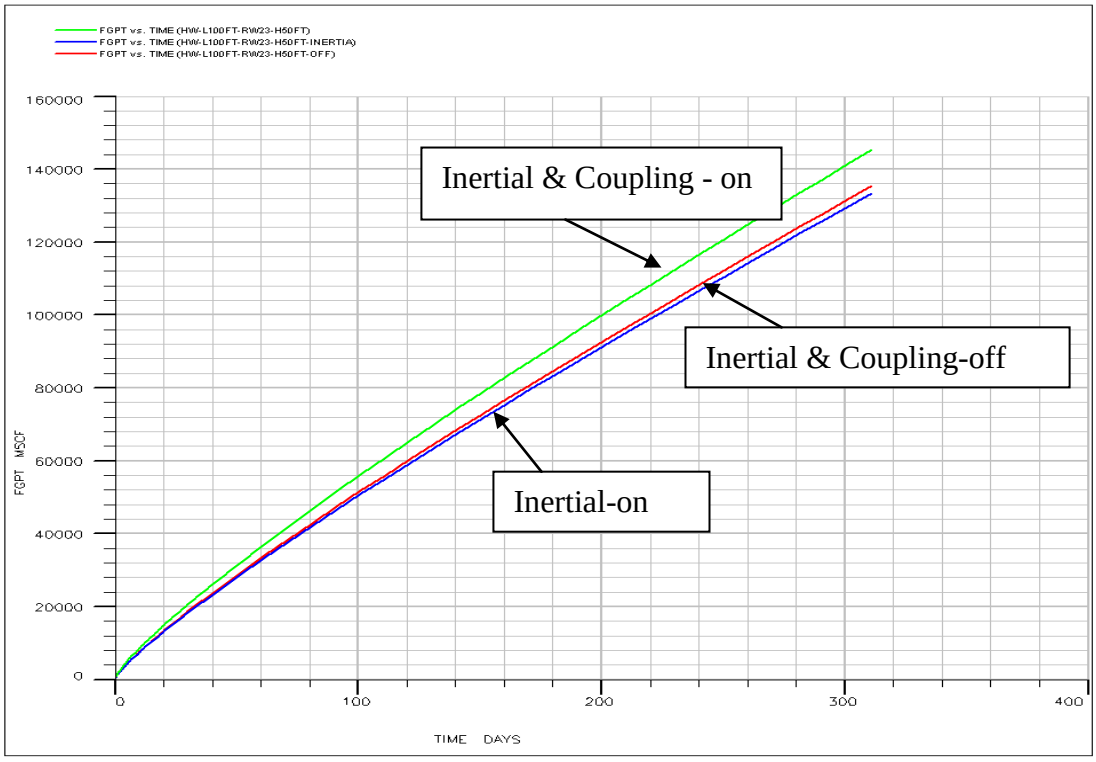

Figure 3.12: Total gas production vs. time, with and without considering coupling and inertial effects, Model B (Table 3.2), Lhw=200 ft, RC1b core properties.

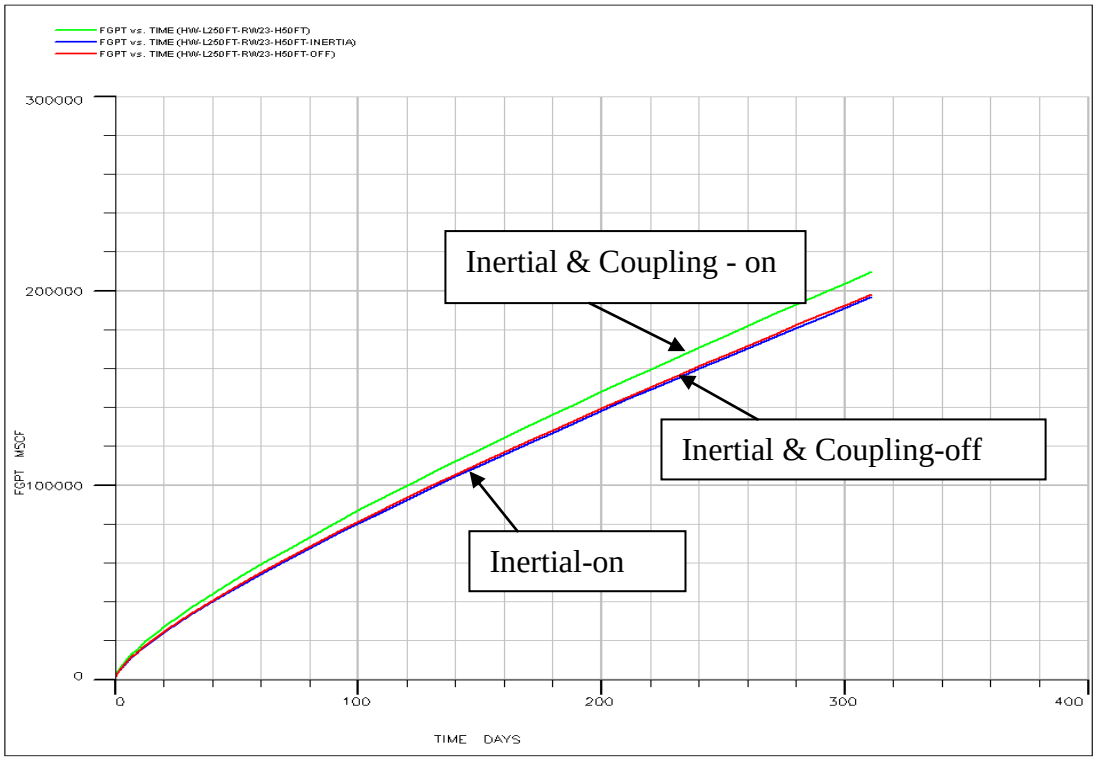

Figure 3.13: The total gas production vs. time, , with and without considering coupling and inertial effects, Model B (Table 3.2) ,Lhw=500 ft, RC1b core properties.

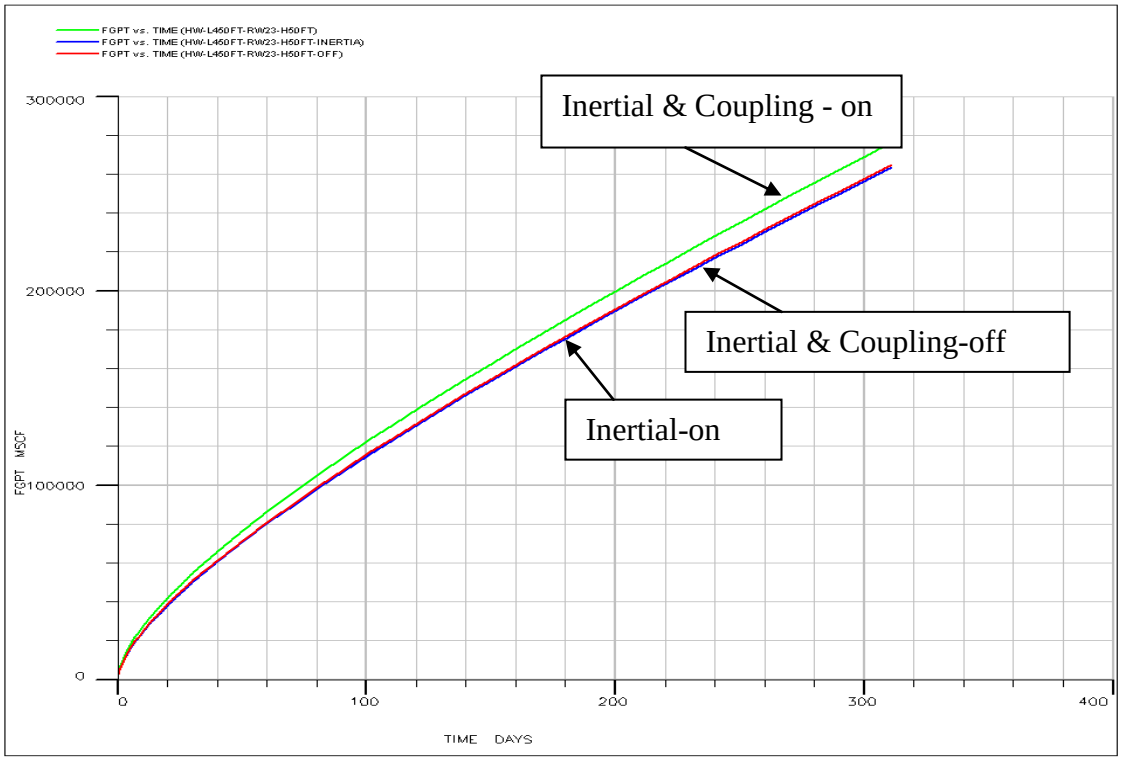

Figure 3.14: The total gas production vs. time, with and without considering coupling and inertial effects, Model B (Table 3.2), Lhw=900 ft, RC1b core properties.

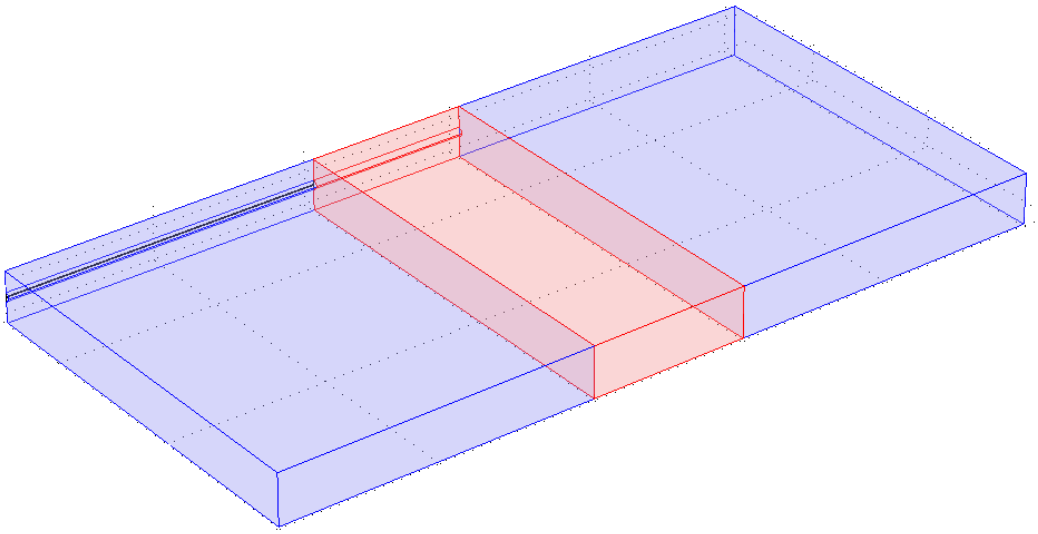

Figure 3.15: 3-D Geometry of the horizontal well in this study.

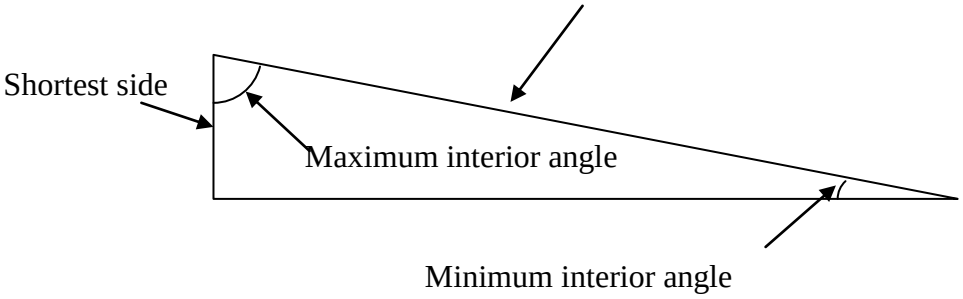

Figure 3.16: Triangular mesh element showing the longest side, shortest side, maximum interior angle and the minimum interior angle, (Mesh quality tutorials (rocksceince)).

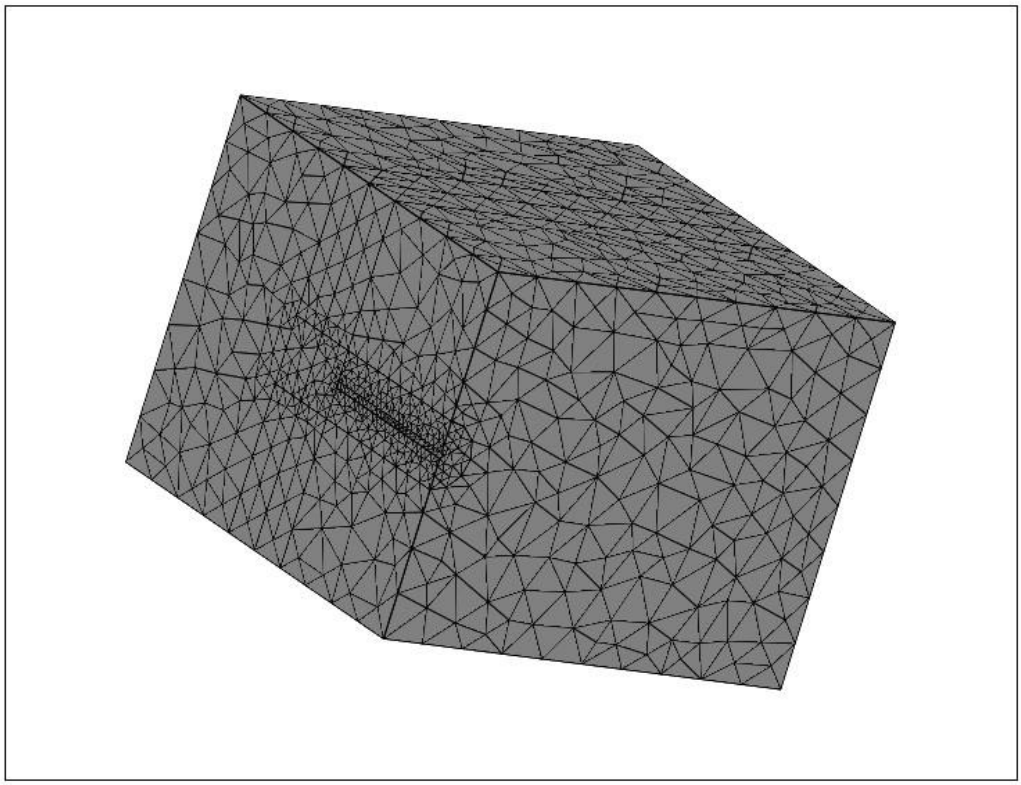

(a)

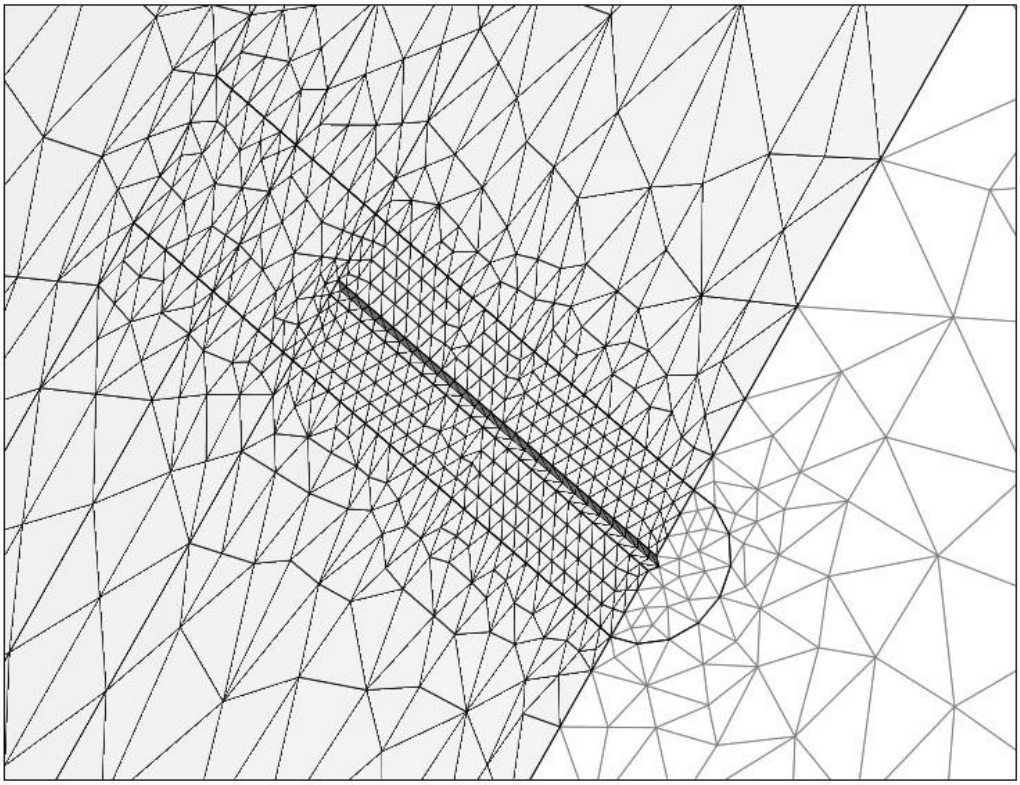

(b)

Figure 3.17: a) En example of the defined mesh the reservoir model (object) for one of the cases studied here b) the refined and specified elements around the horizontal well.

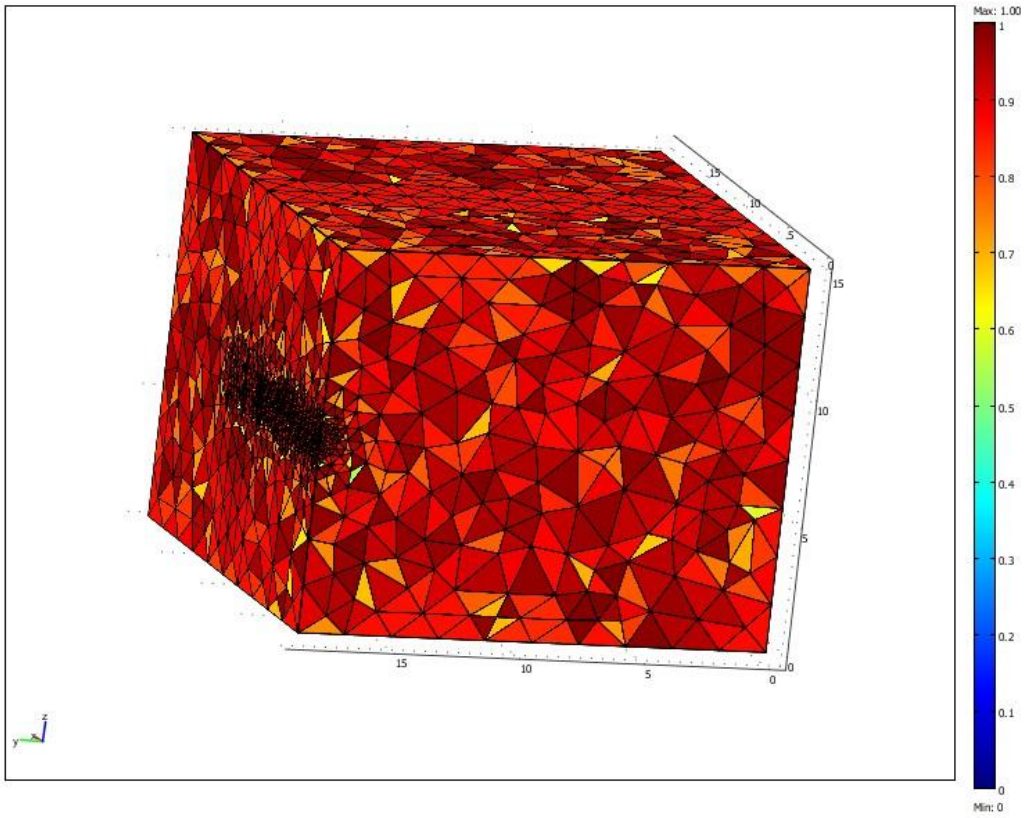

Figure 3.18: The mesh quality of the reservoir model of Figure 3.17.

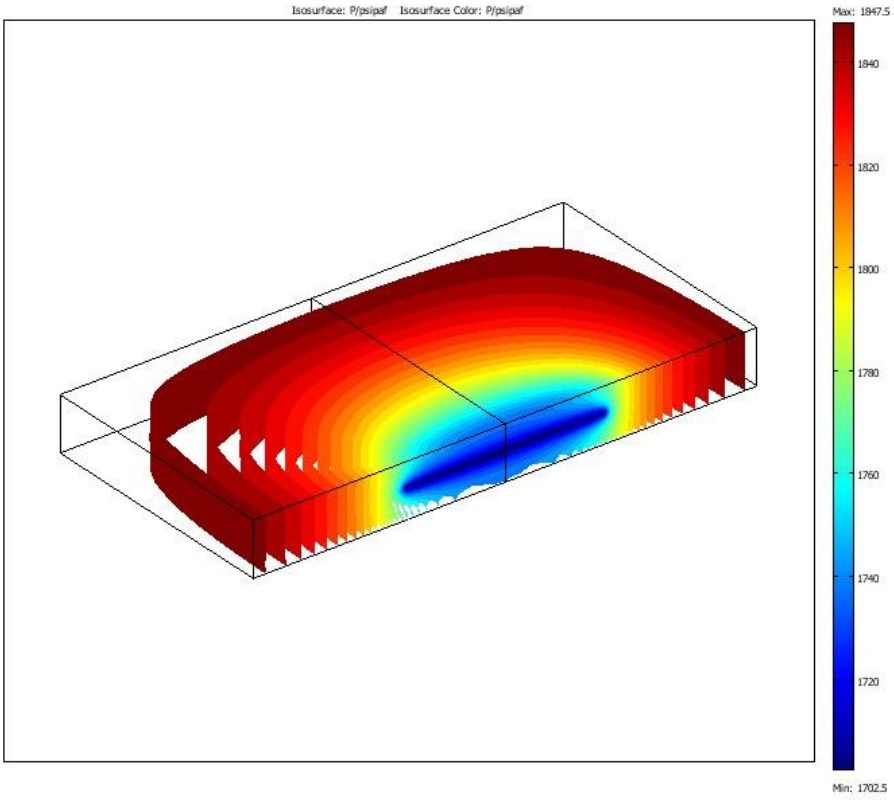

Figure 3.19: The pressure distribution around the HW for the selected model shown in Tables 3.17 and 3.18.

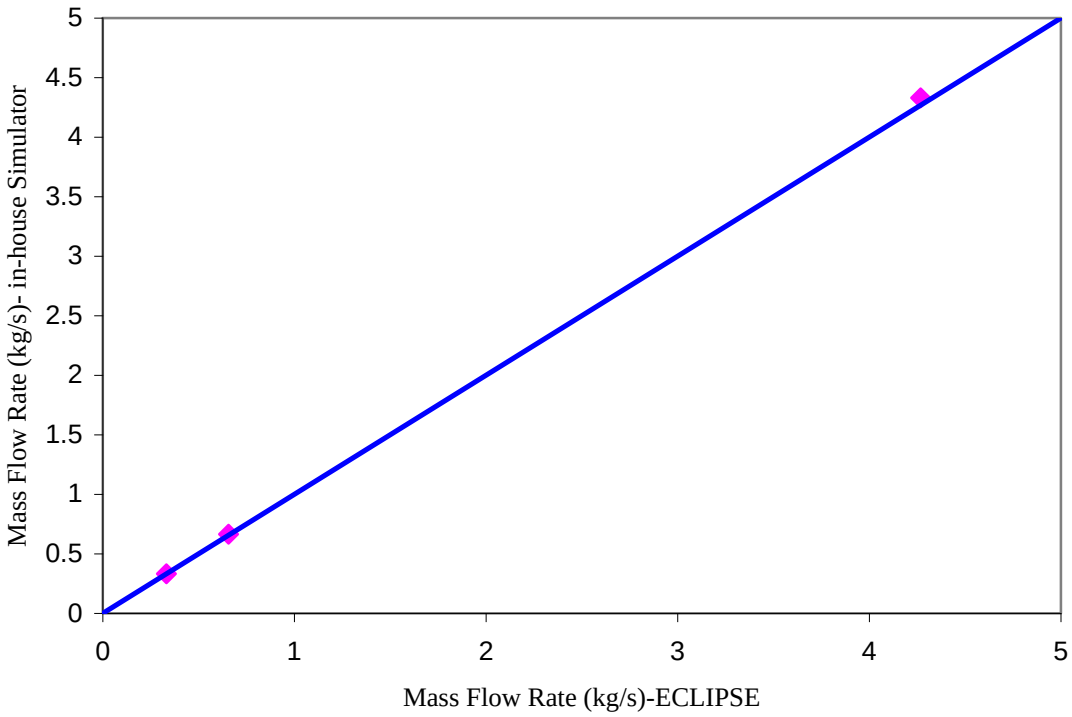

Figure 3.20: Comparison between the mass flow rates estimated using the in-house and ECLIPSE simulators.

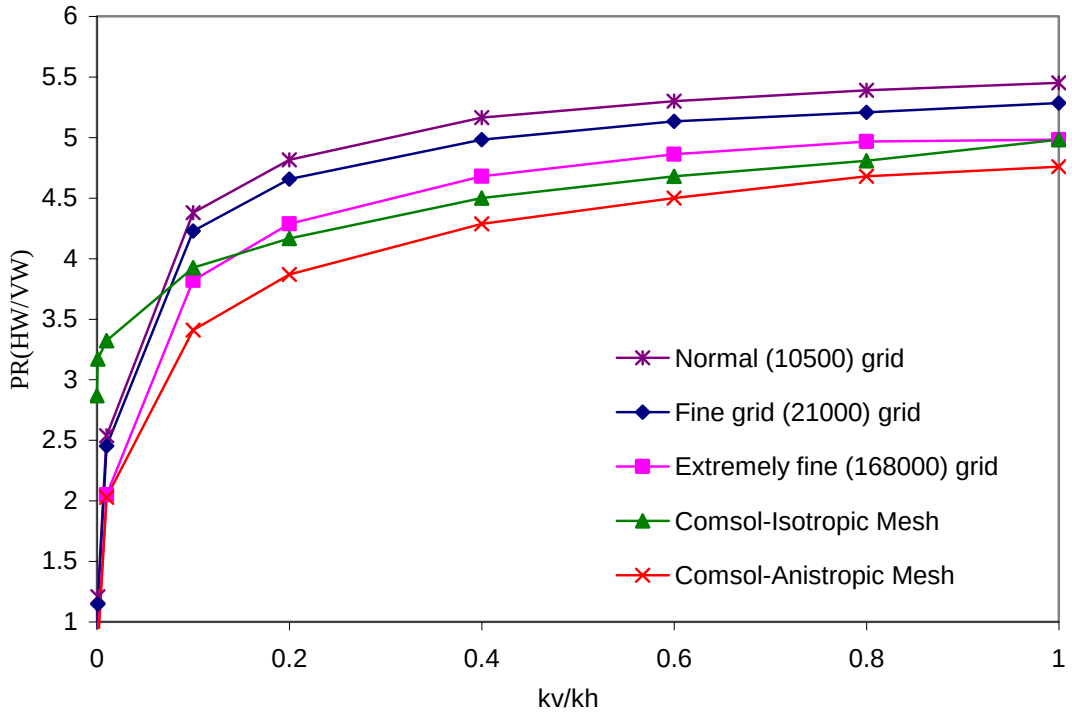

(a)

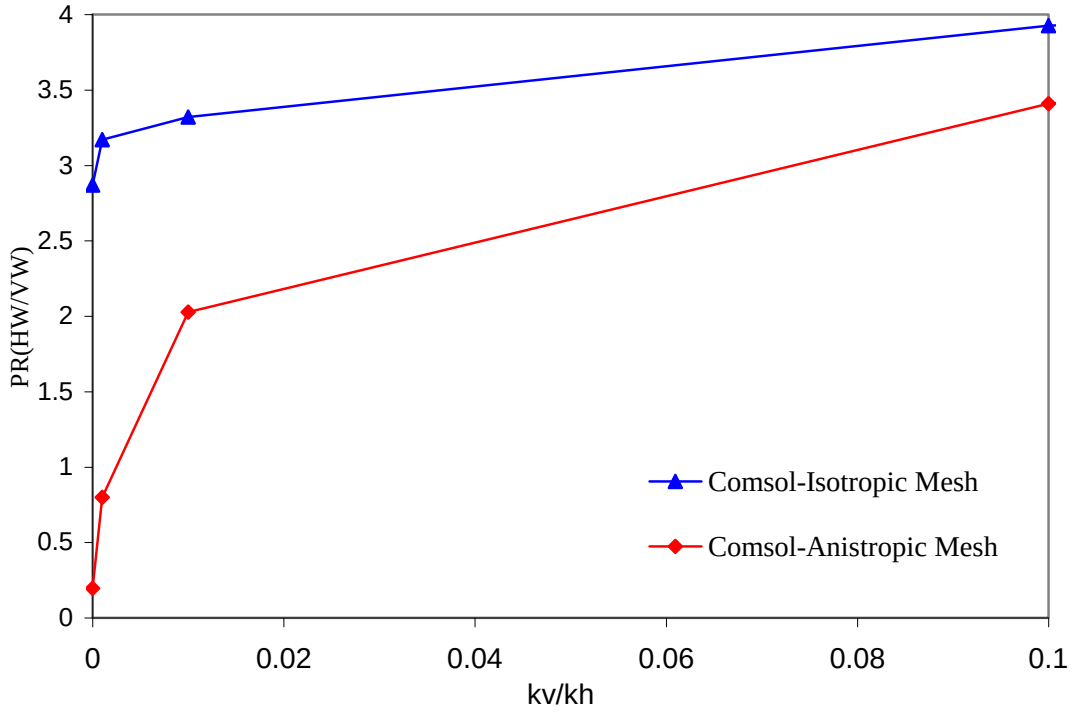

(b)

Figure 3.21: The productivity ratio (horizontal well to vertical well) versus the permeability anisotropy index.

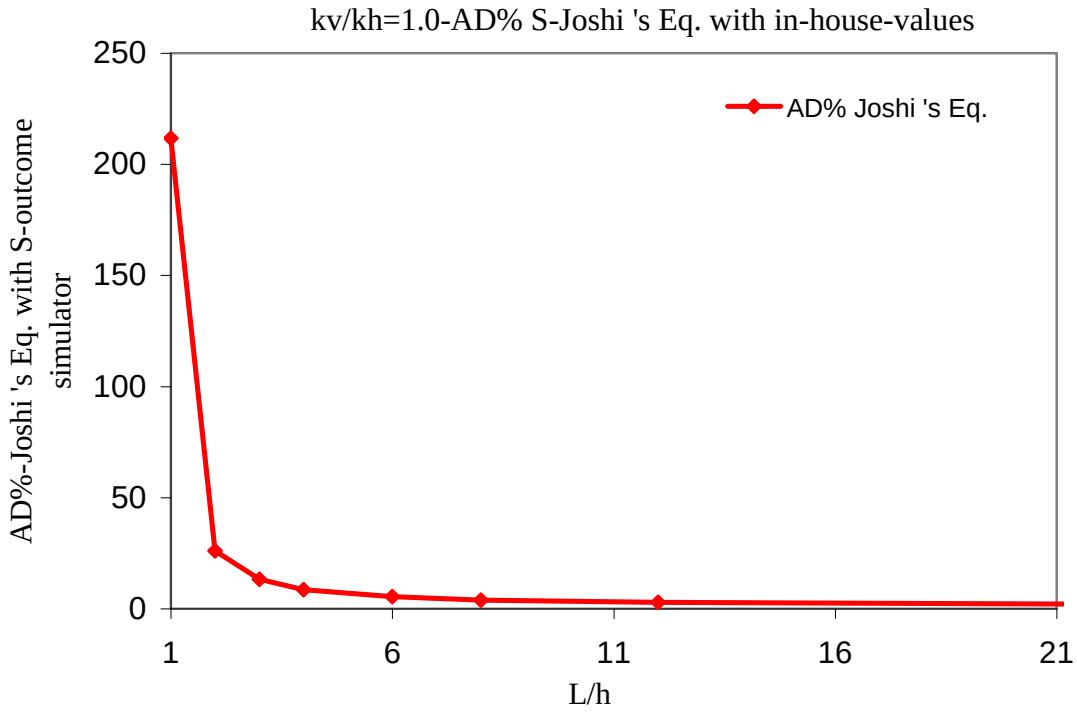

(a)

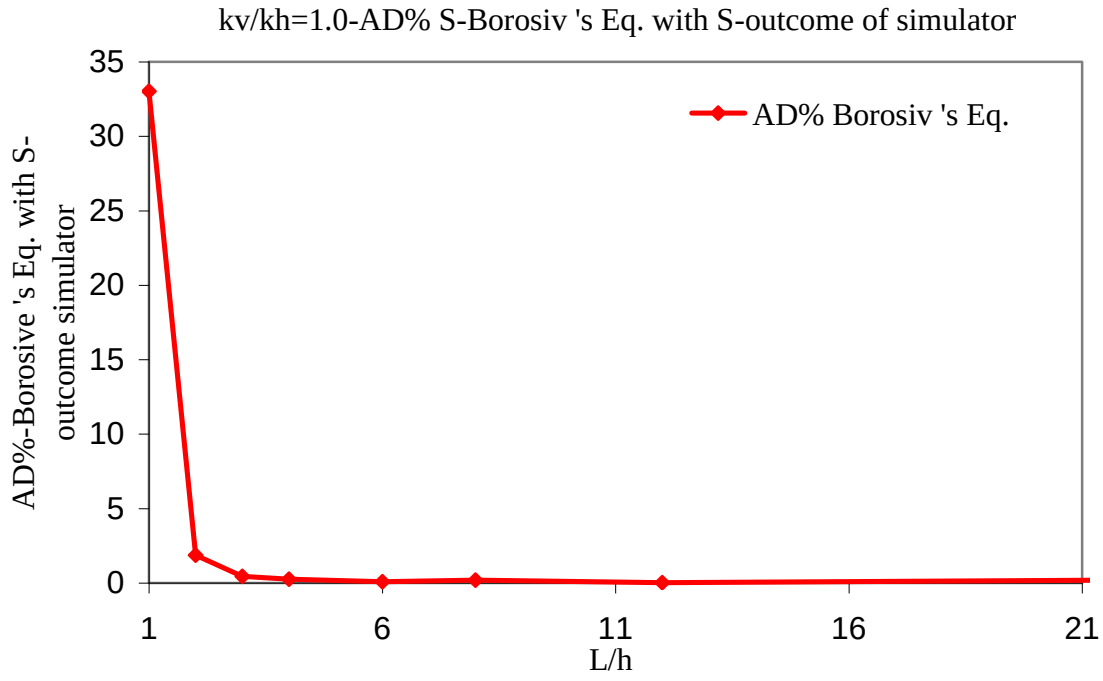

(b)

Figure 3.22: Absolute deviation error skin values calculated using a) Joshi‘s and b) Borosiv‘s equation and those obtained by applying the calculated in-house simulator mass flow rates into Equation 3.8.

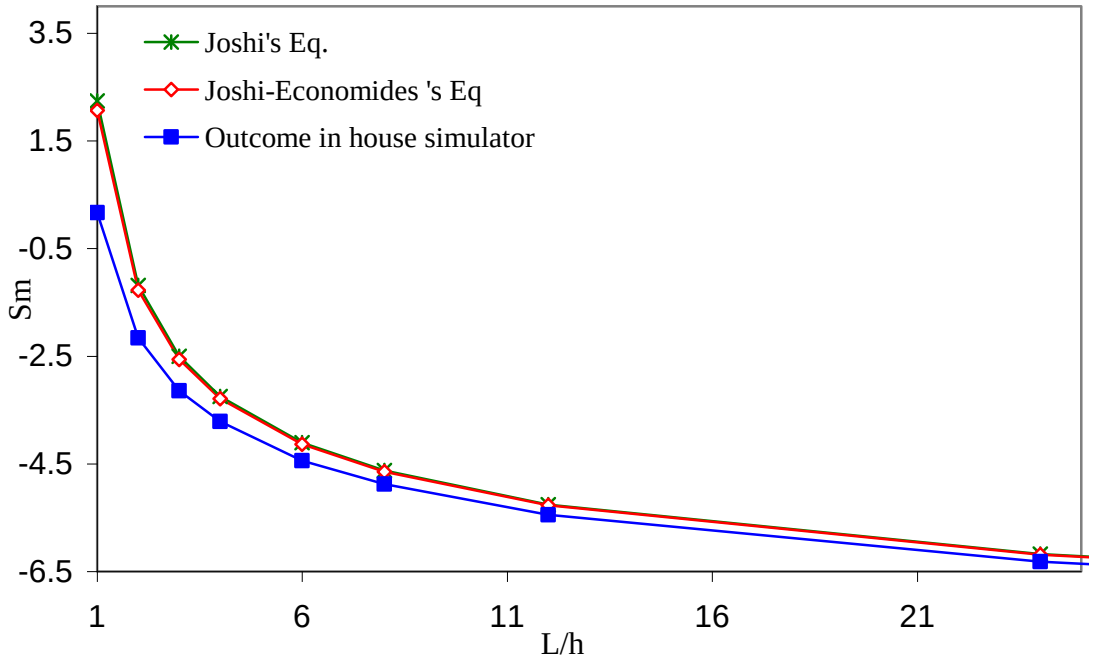

(a)

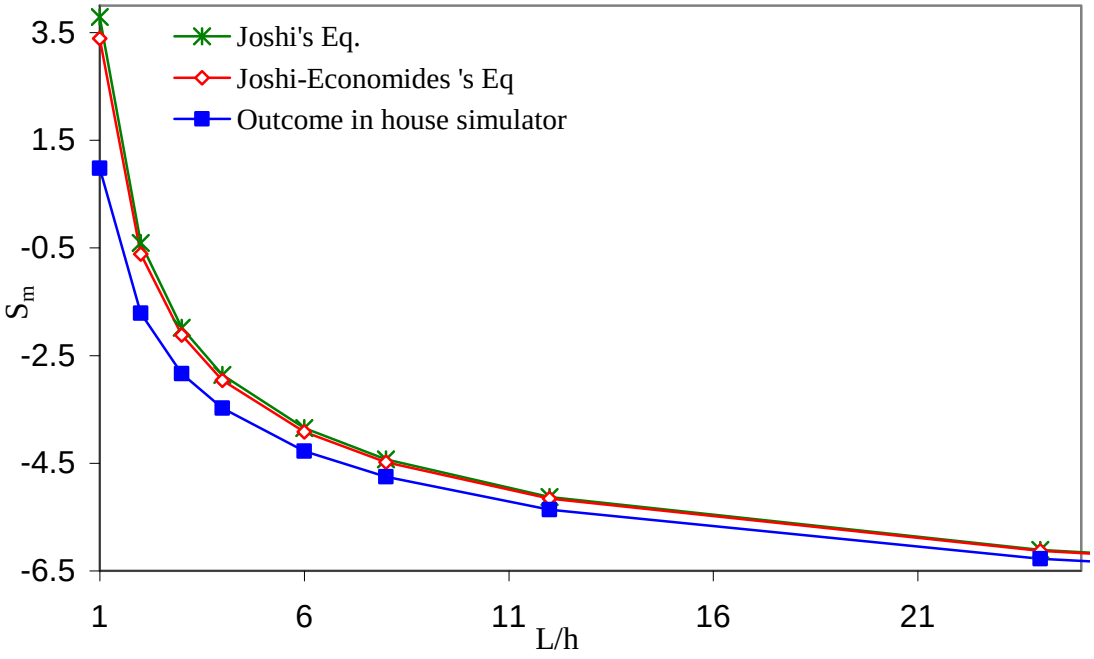

(b)

Figure 3.23: Comparison of the calculated skin using Joshi's and Joshi-Economides's equations with those obtained by applying the calculated in-house simulator mass flow rates into Equation 3.8, anisotropic reservoir, kvkh= [0.6 0.4].

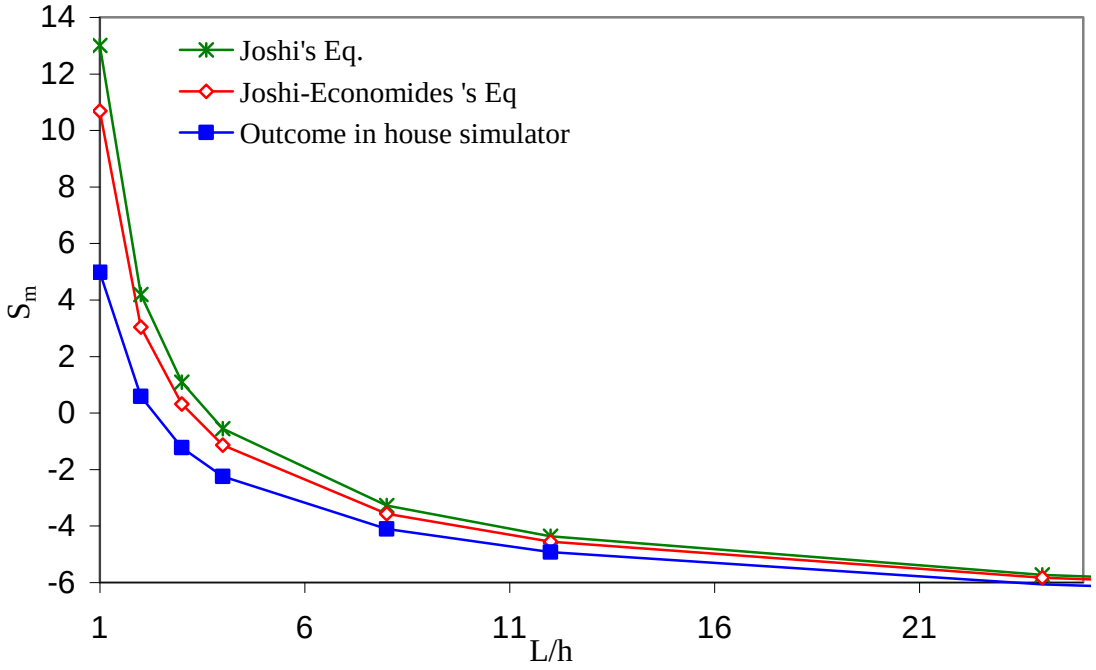

(a)

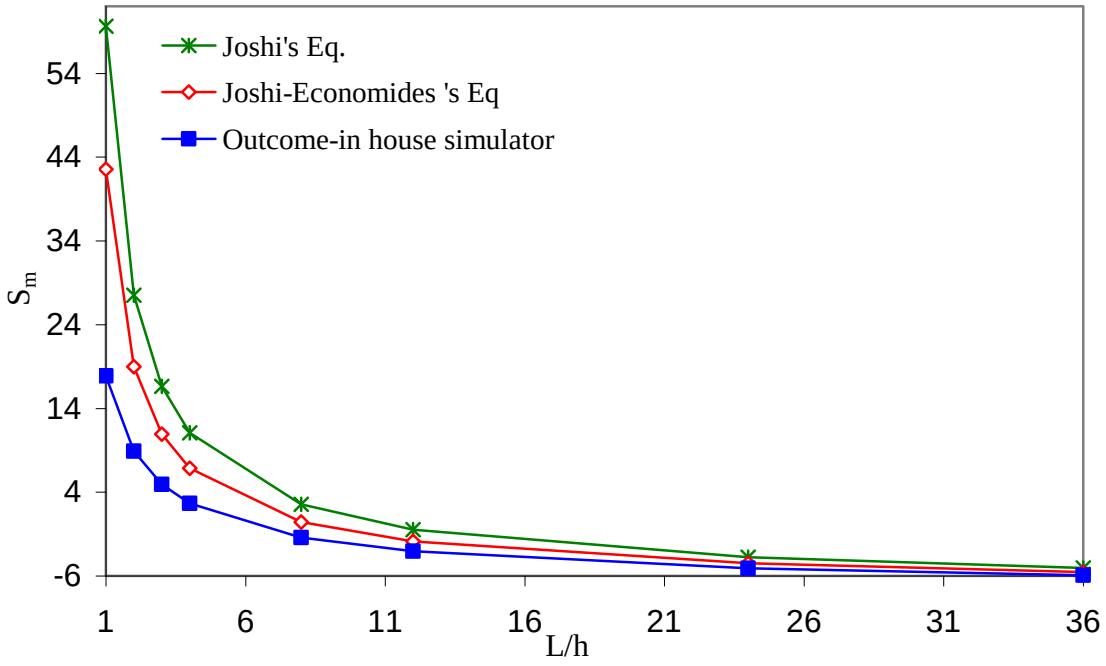

(b)

Figure 3.24: Comparison of the calculated skin using Joshi's and Joshi-Economides's equations with those obtained by applying the calculated in-house simulator mass flow rates into Equation 3.8, anisotropic reservoir, kvkh= [0.1 0.01].

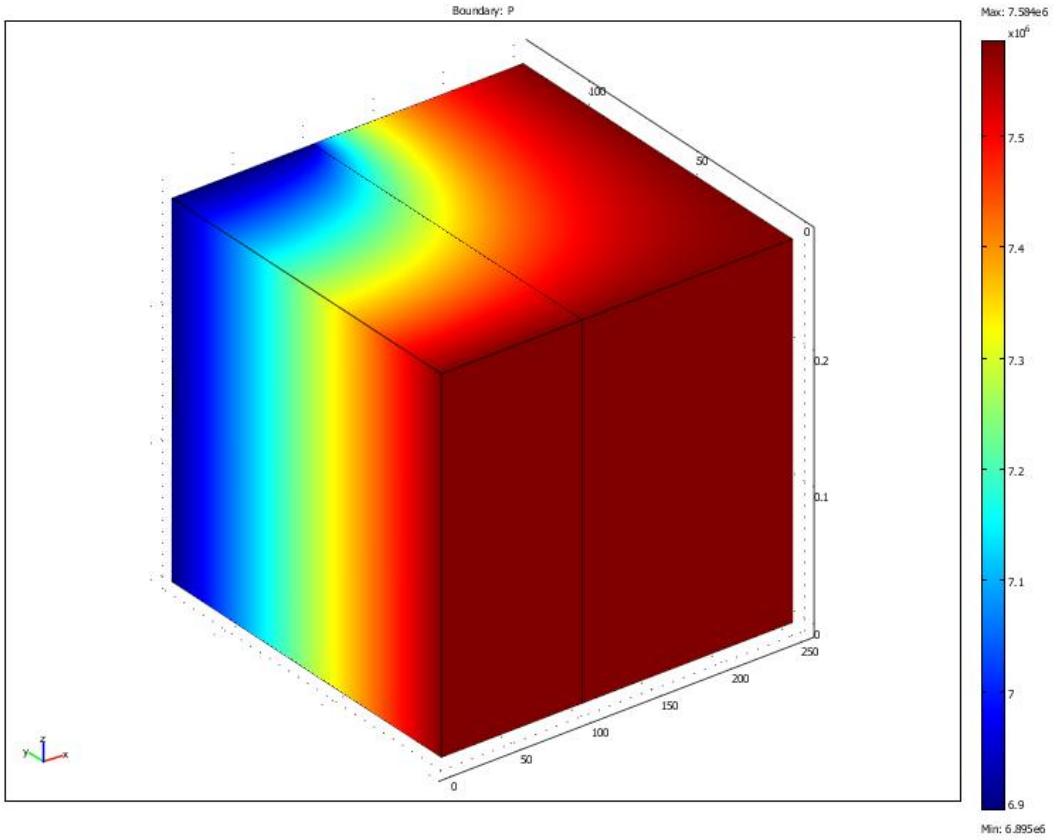

(a)

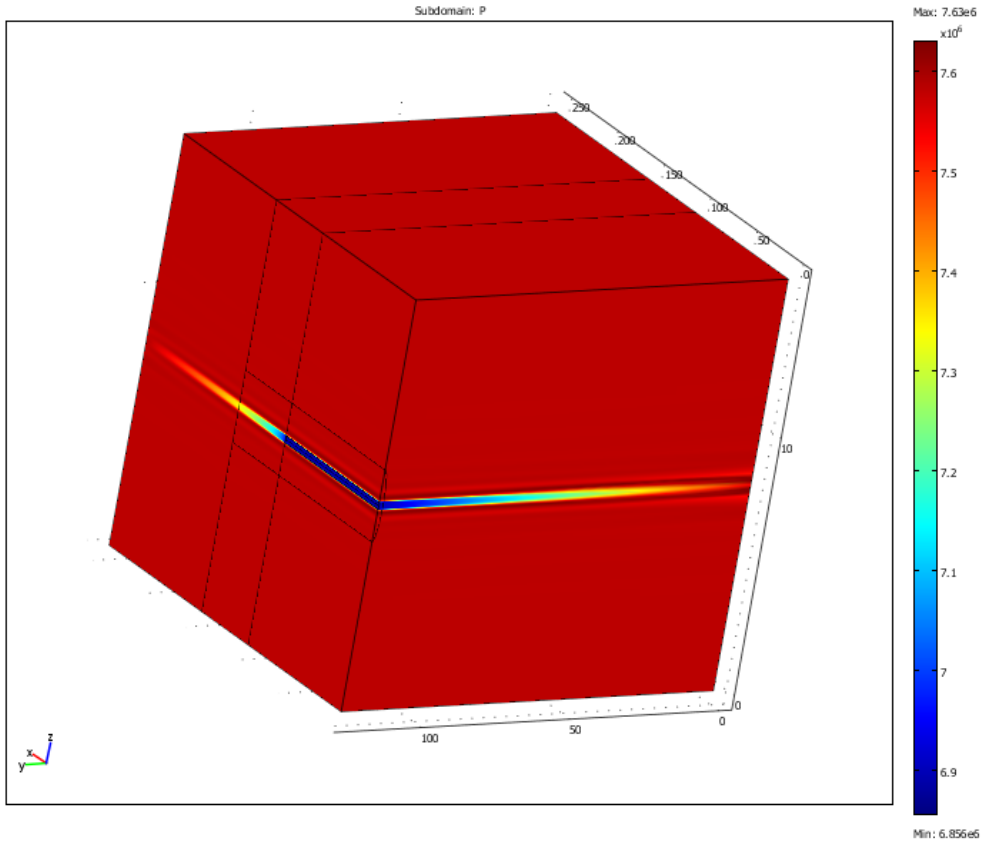

(b)

Figure 3.25: a) A schematic image of thin layer model; b) The pressure profile across the reservoir for the extreme anisotropic case of k_v=0.

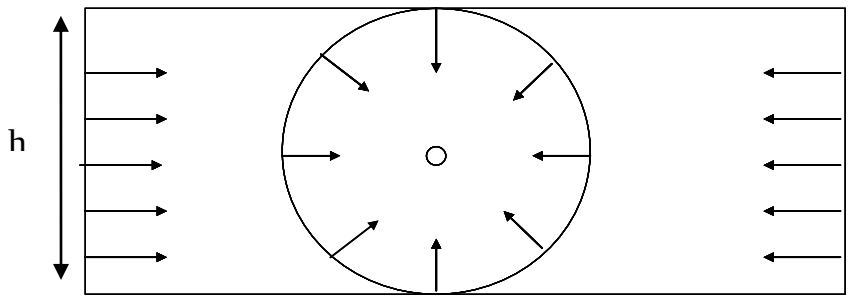

Figure 3.26: The schematic flow diagram of a fully penetrating HW in an isotropic reservoir.

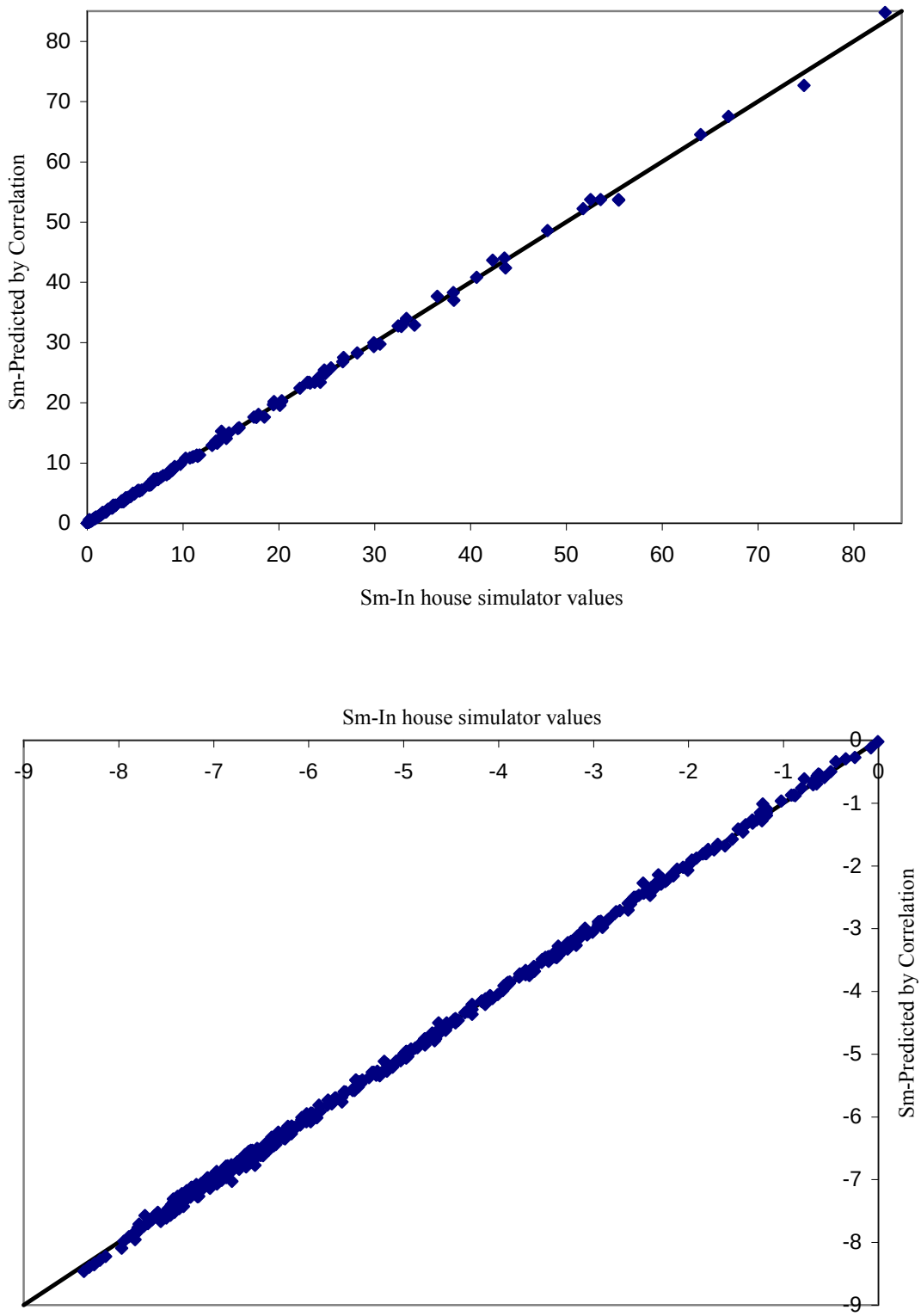

Figure 3.27: Comparison of geometric skin values calculated using the proposed S_m correlation with those obtained by applying the calculated HW in-house simulator mass flow rates into Equation 3.8.

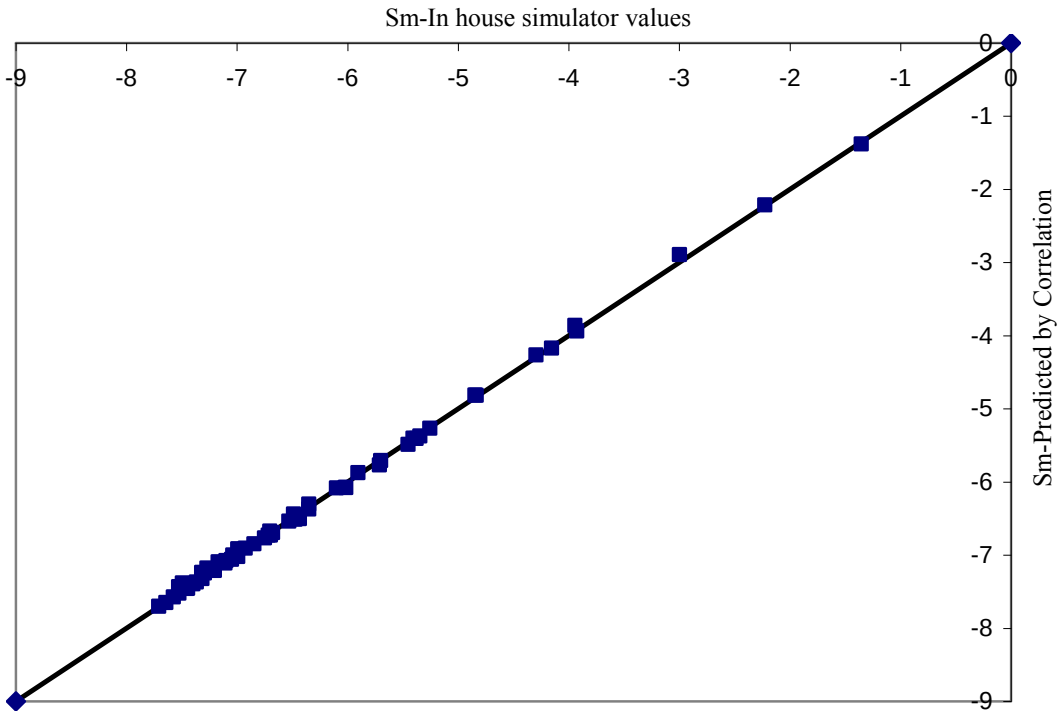

Figure 3.28: Comparison of the geometric skin values calculated using the author's proposed correlation and the corresponding values from the in-house simulator, new data points not used in the development of the correlation.

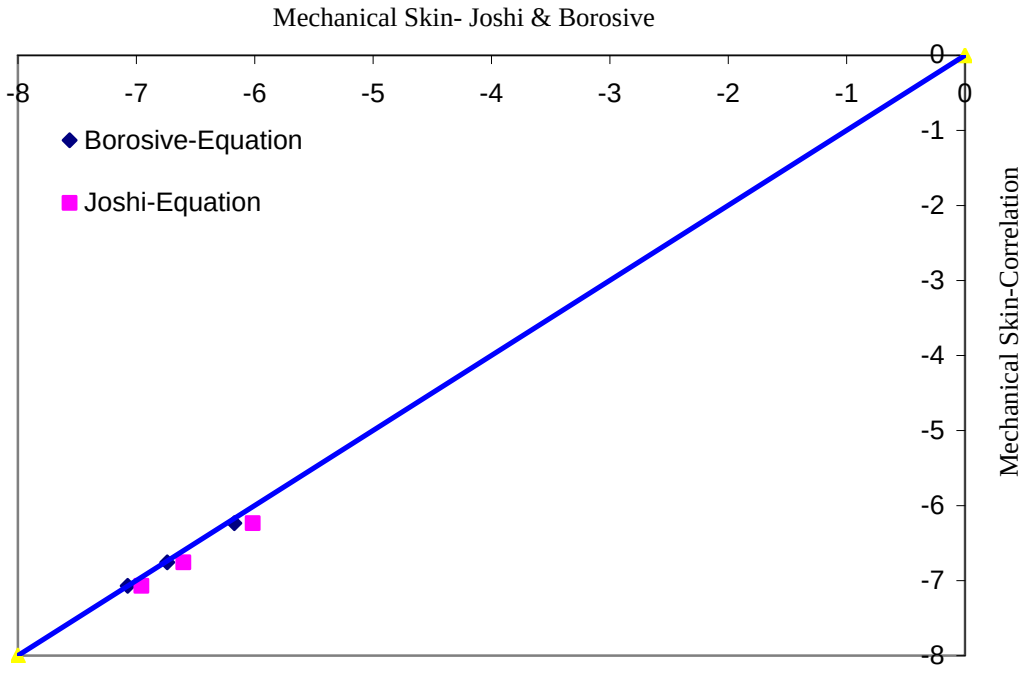

Figure 3.29: Comparison between geometric skin values calculated using the author's proposed correlation and the corresponding values using Joshi's (1991) and Borosiv's (1984) semi-analytical equations.

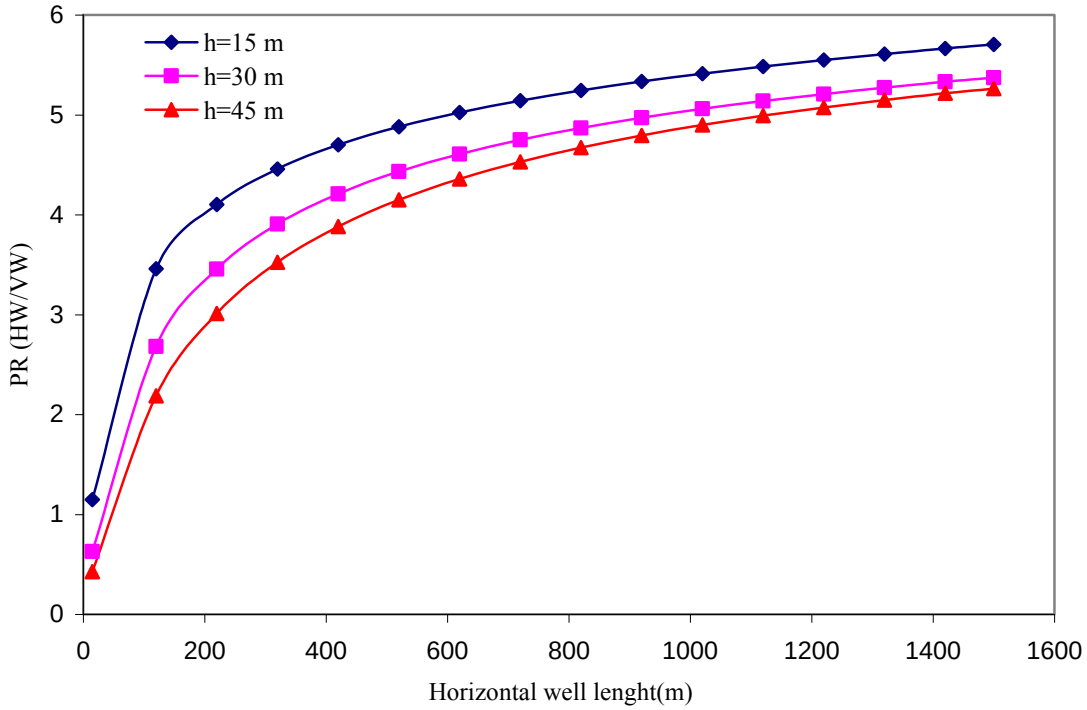

Figure 3.30: Productivity ratios of a HW to a VW versus HW length, effect of reservoir thickness.

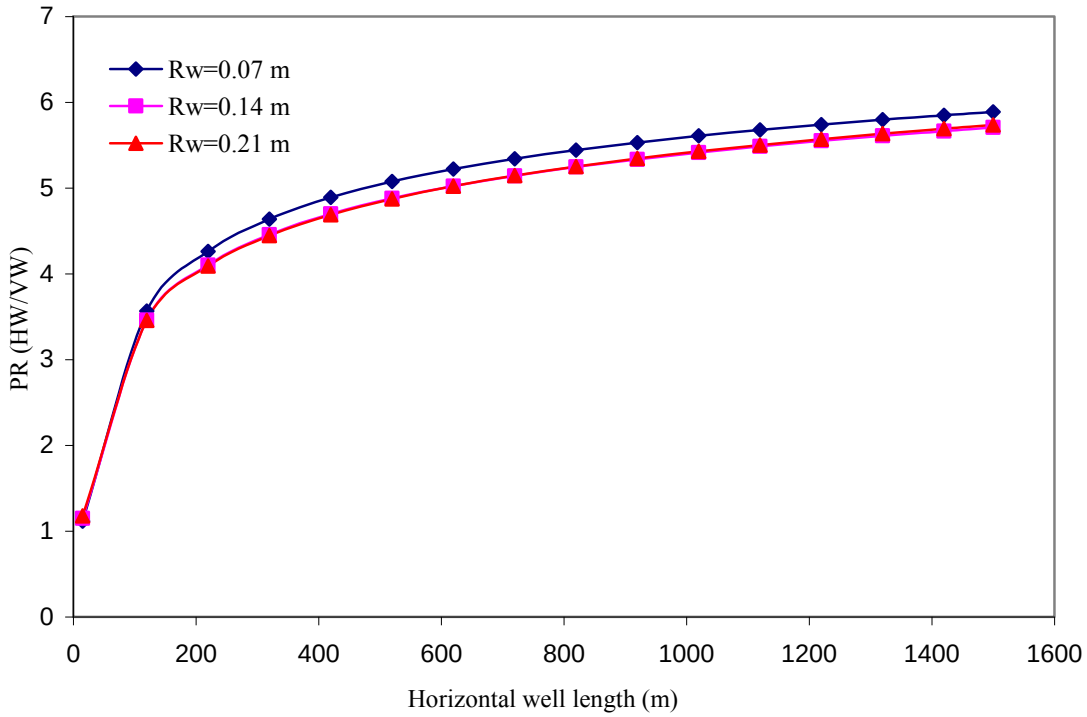

Figure 3.31: Productivity ratio of a HW to a VW versus length, effect of wellbore radius.

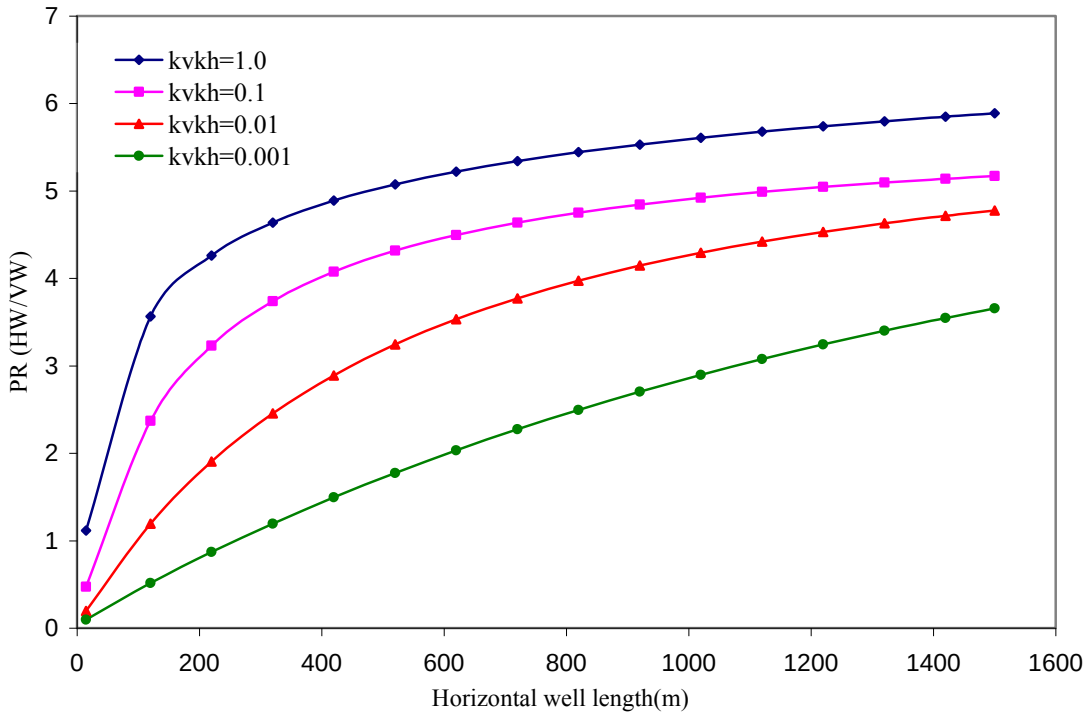

Figure 3.32: Productivity ratio of a HW to a VW versus length, effect of anisotropy.

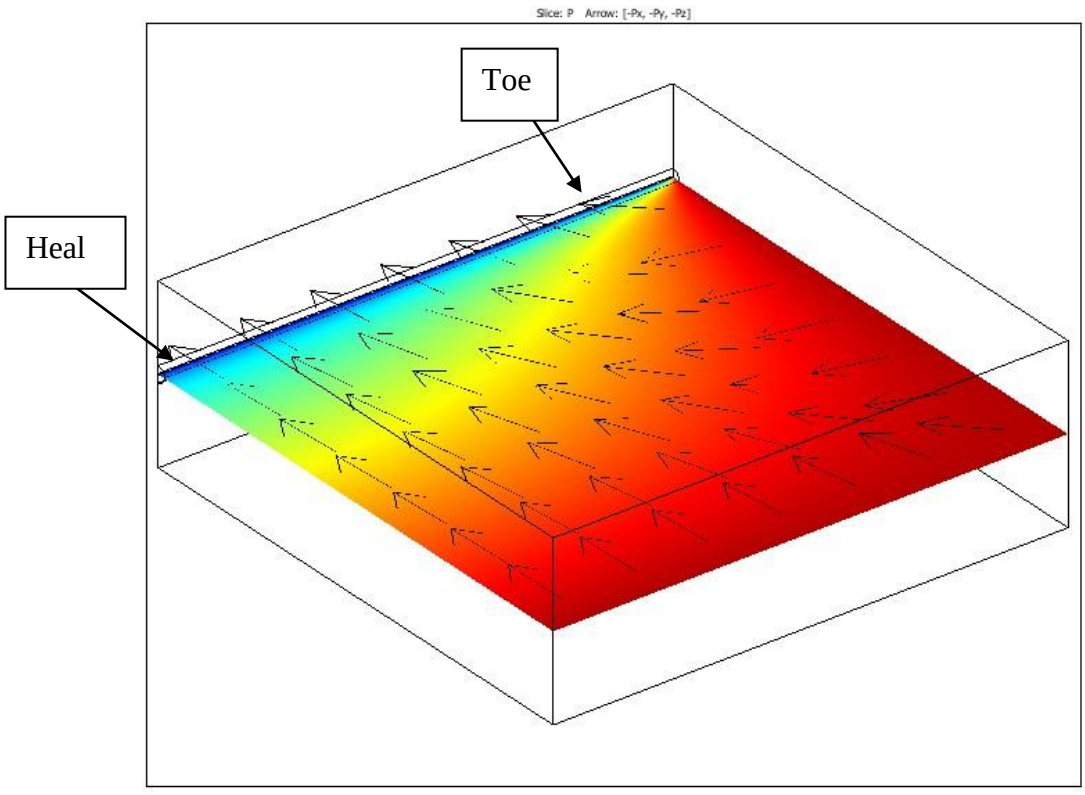

Figure 3.33: Flow pattern and pressure distribution of a fully horizontal well.

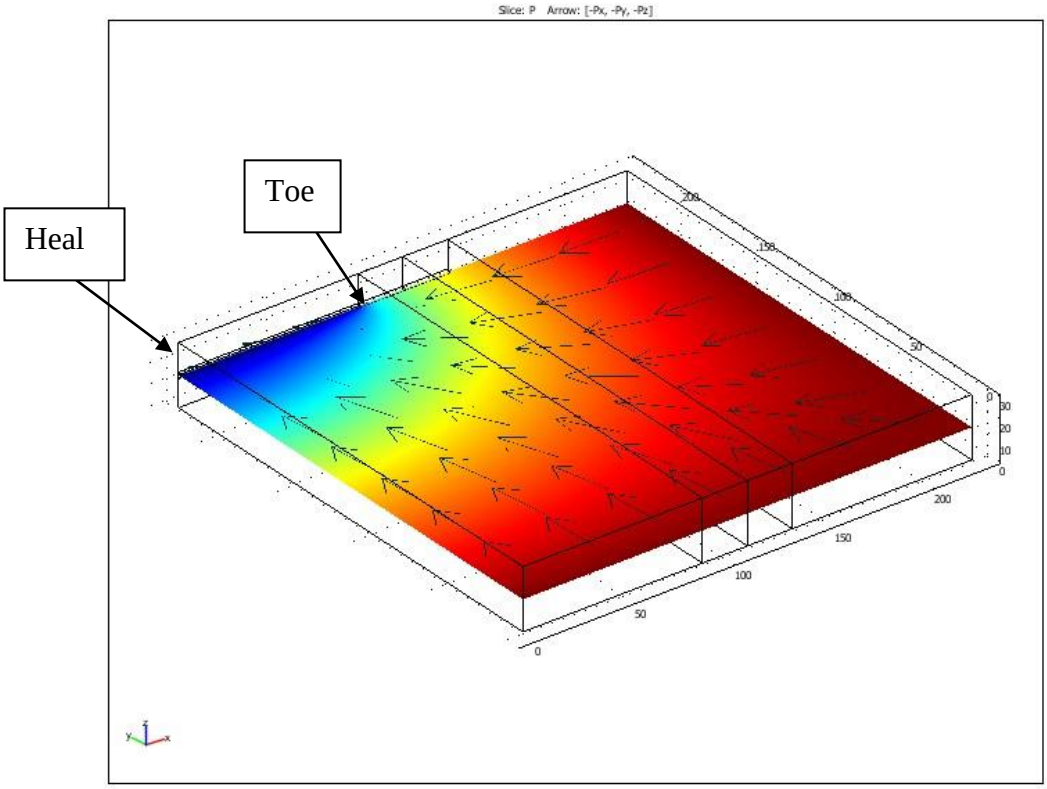

Figure 3.34: Flow pattern and pressure distribution of a partially horizontal well.

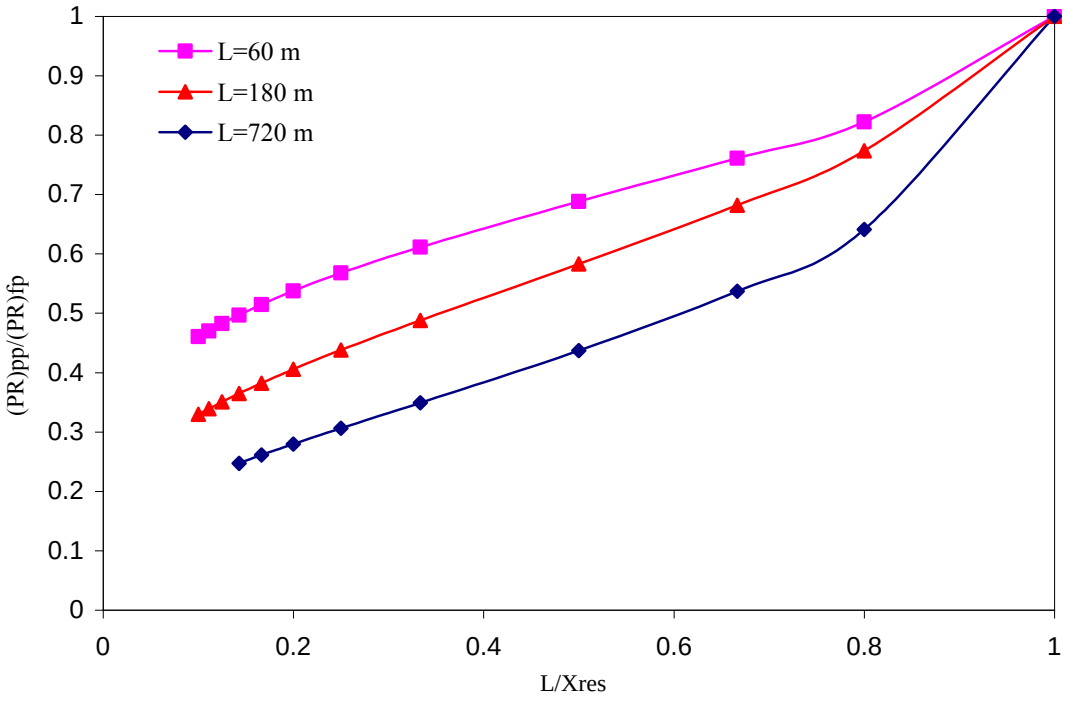

Figure 3.35: Productivity ratio of partially to fully penetrating horizontal wells versus penetration ratio at three different horizontal well lengths, r_w=0.14 m, h=30 m.

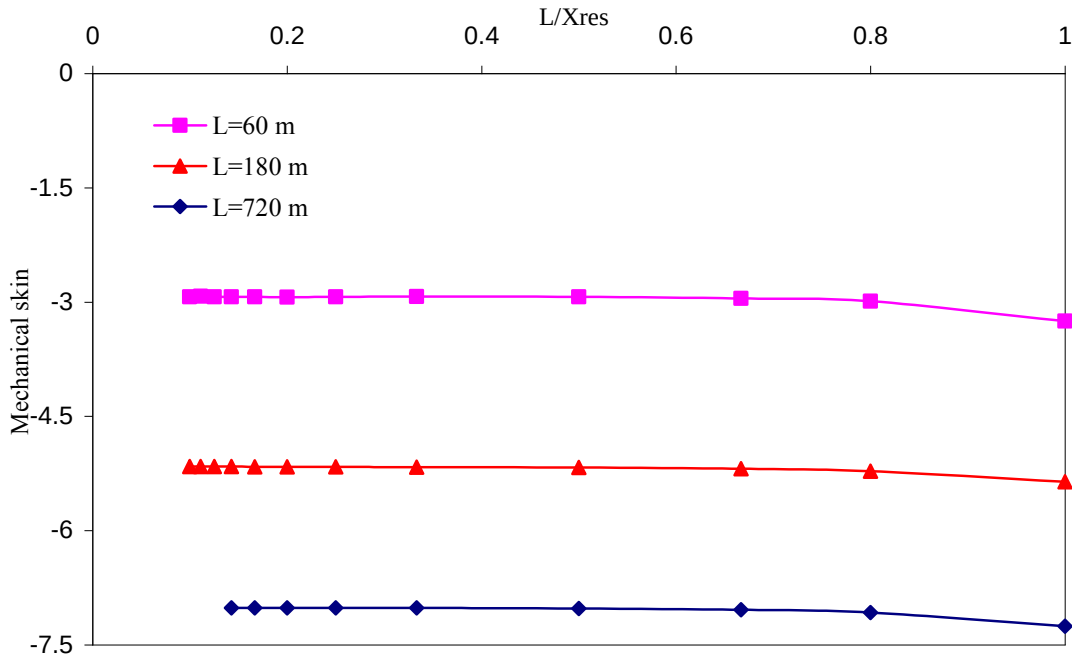

Figure 3.36: Variation of geometric skin with partial penetration ratio at three different horizontal well lengths, h=30 m and r_w=0.14 m.

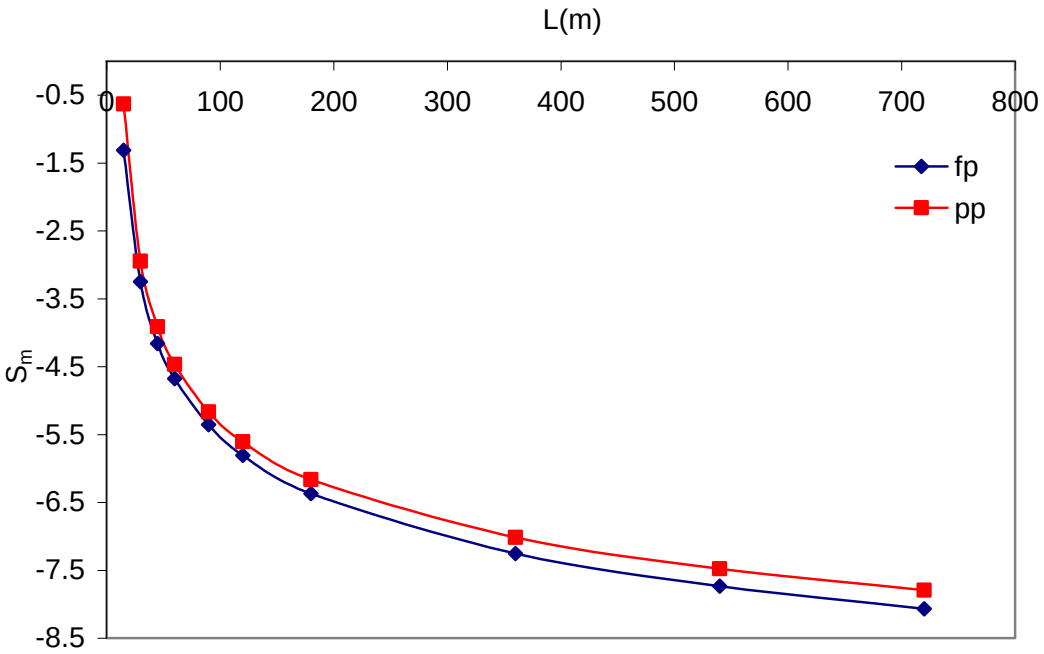

(a)

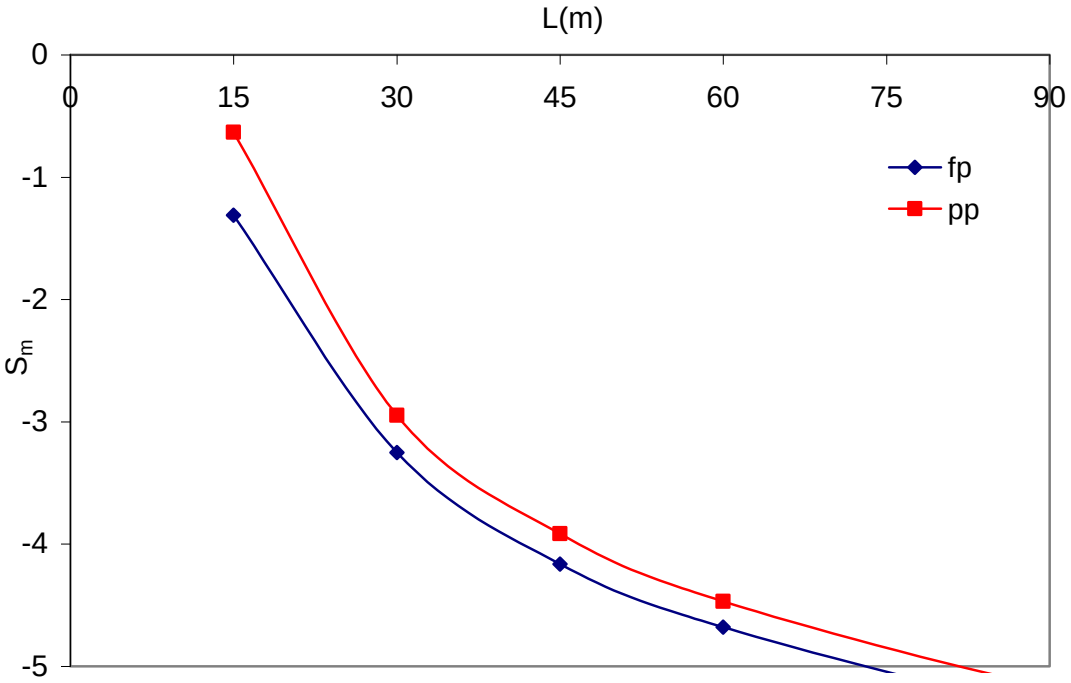

(b)

Figure 3.37: Variation of S_m versus HW length for fully (fp) and partially (pp) penetrating HWs, r_w=0.07 m and h=15 m.

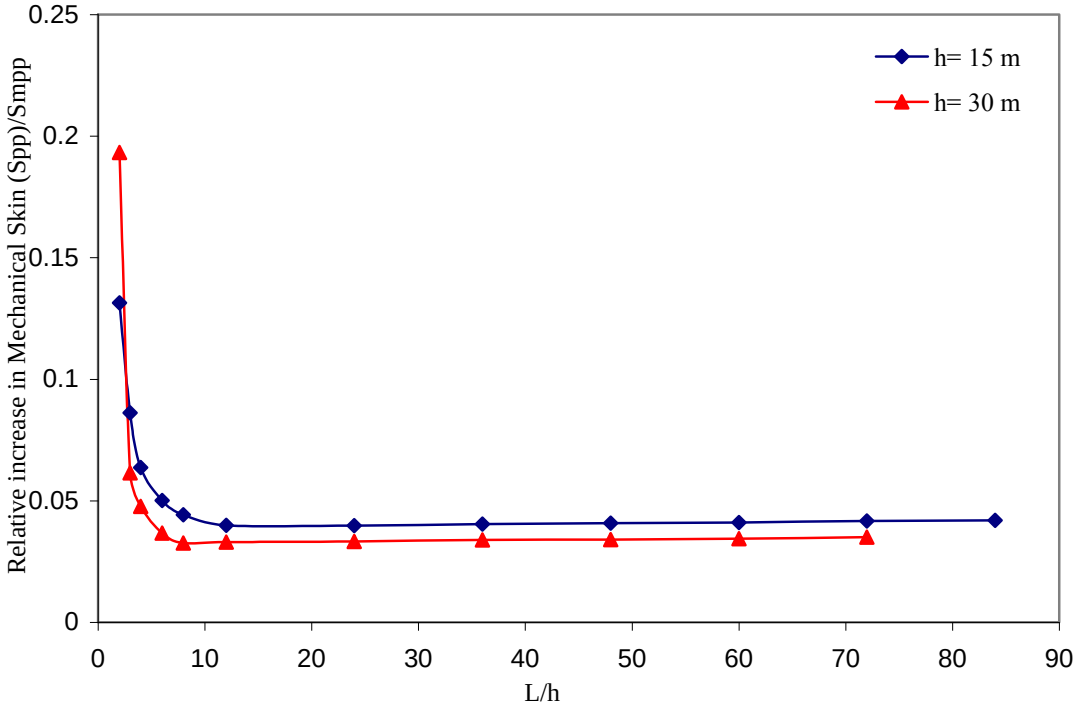

Figure 3.38: Variation of relative increase in geometric skin versus length to thickness ratio, r_w=0.14 m.

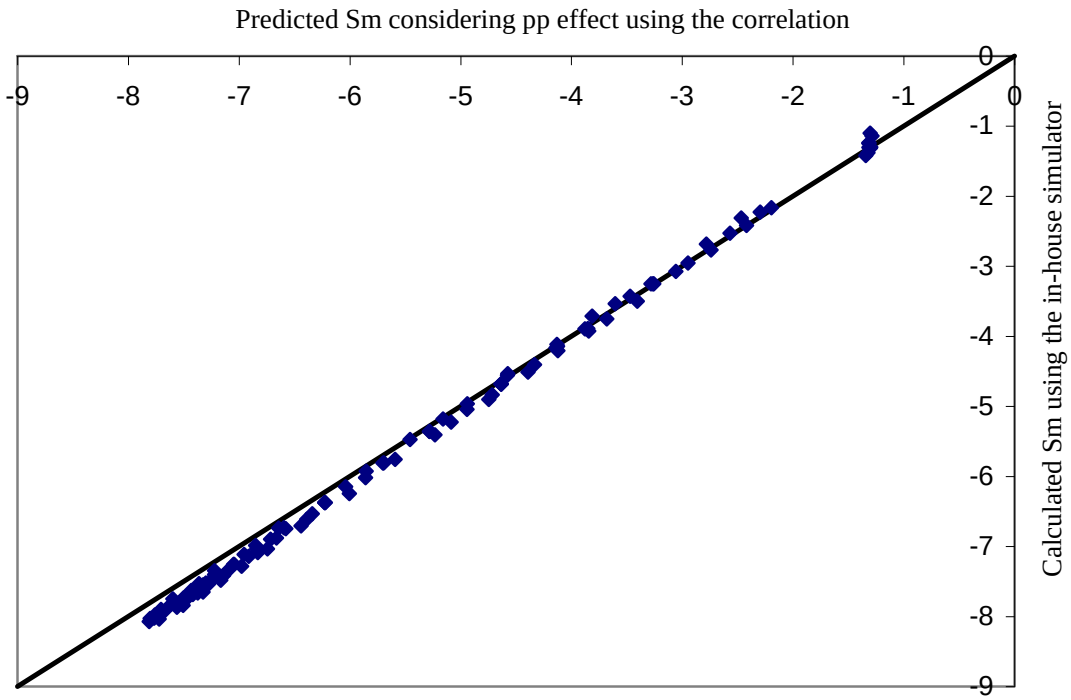

(a)

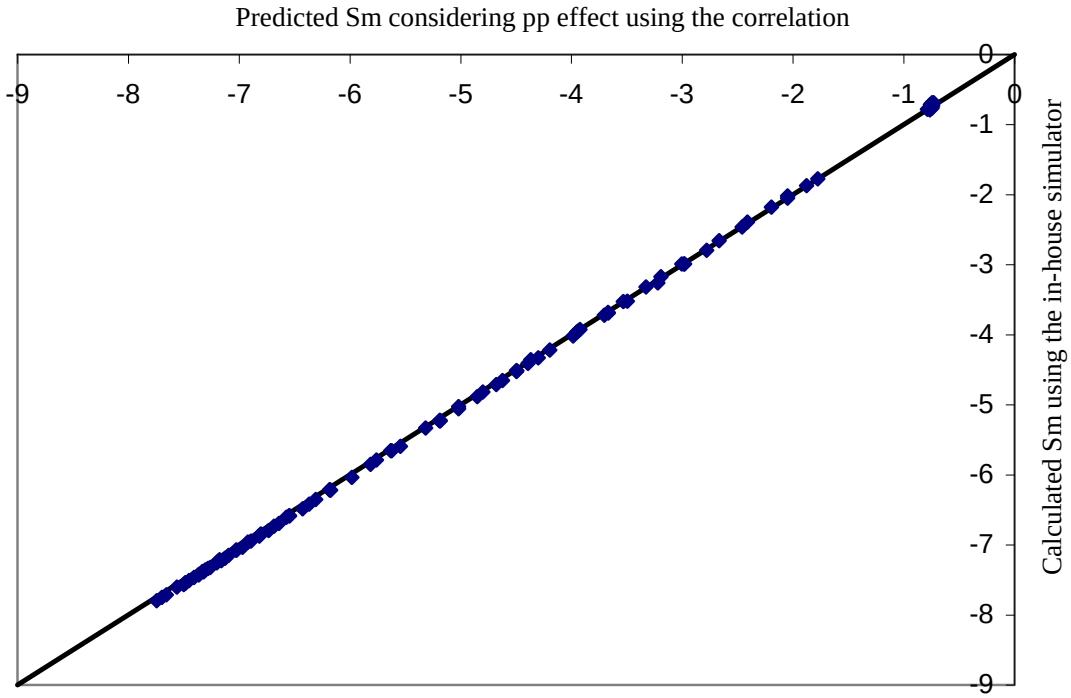

(b)

Figure 3.39: The predicted $S_{m,}$ including partial penetration effect using the author's proposed correlation (Equation 3.40 and 3.41), versus the corresponding values obtained using the in-house simulator, a) $\frac{L}{X_{res}} = 1$ b) $\frac{L}{X_{res}} = 0.8$.

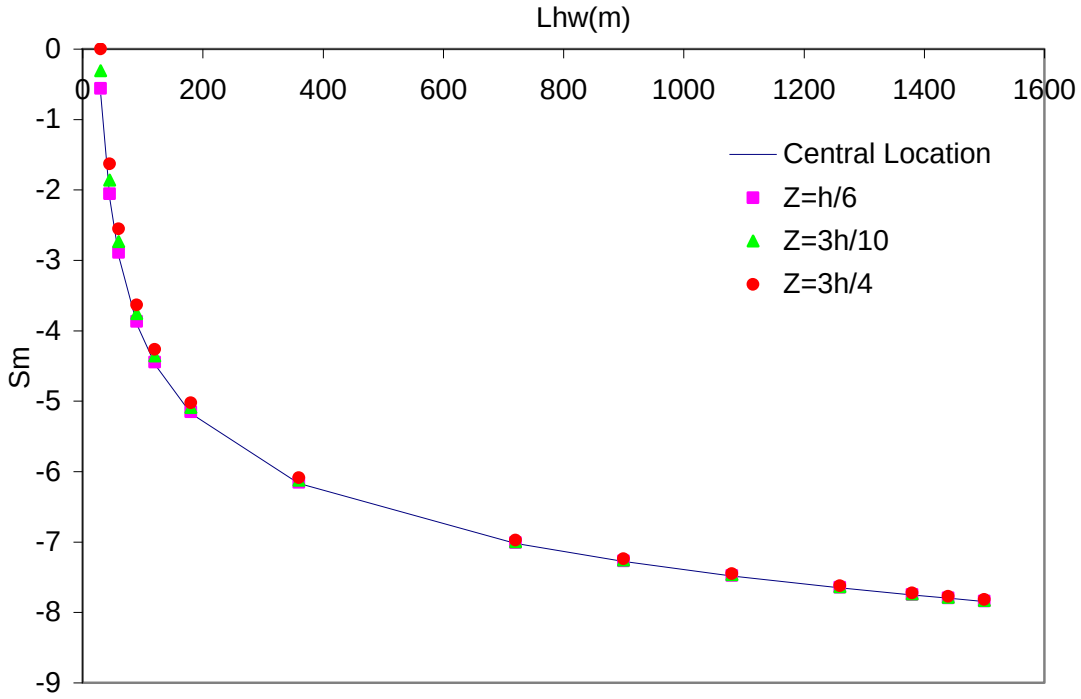

(a)

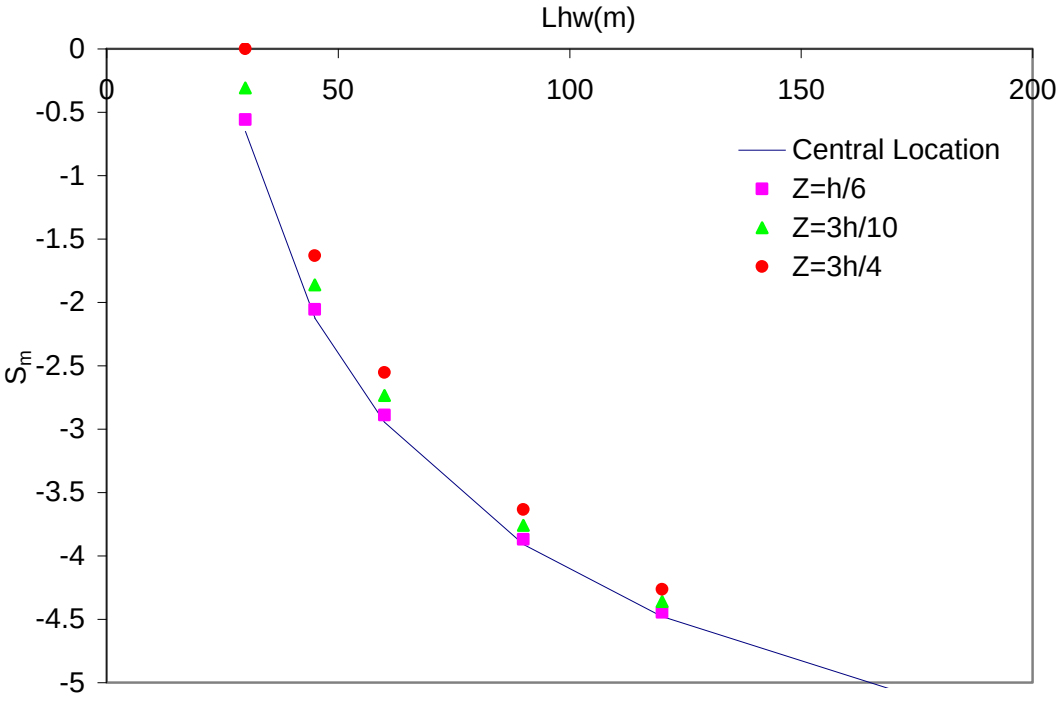

(b)

Figure 3.40: Variation of geometric skin versus the HW length for a HW located a distance from the formation centre, h/2, in the z direction.

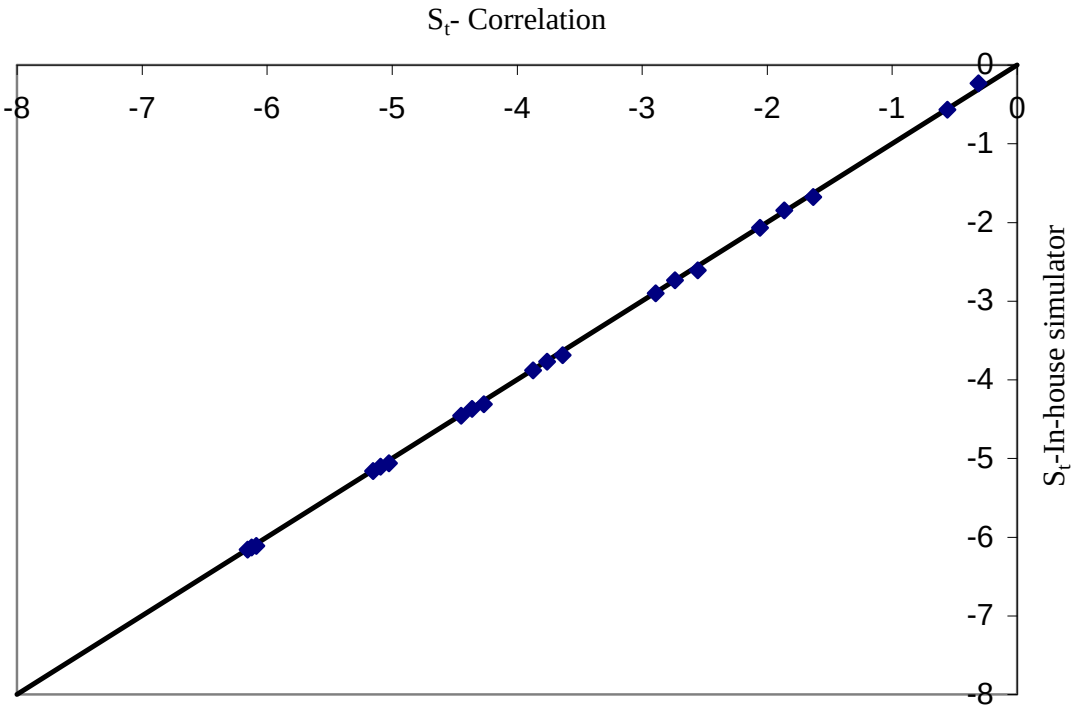

Figure 3.41: Comparing $S_t = S_m + S_z$ calculated by the author's proposed correlation, Equation 3.45, against those obtained by the HW in-house simulator.

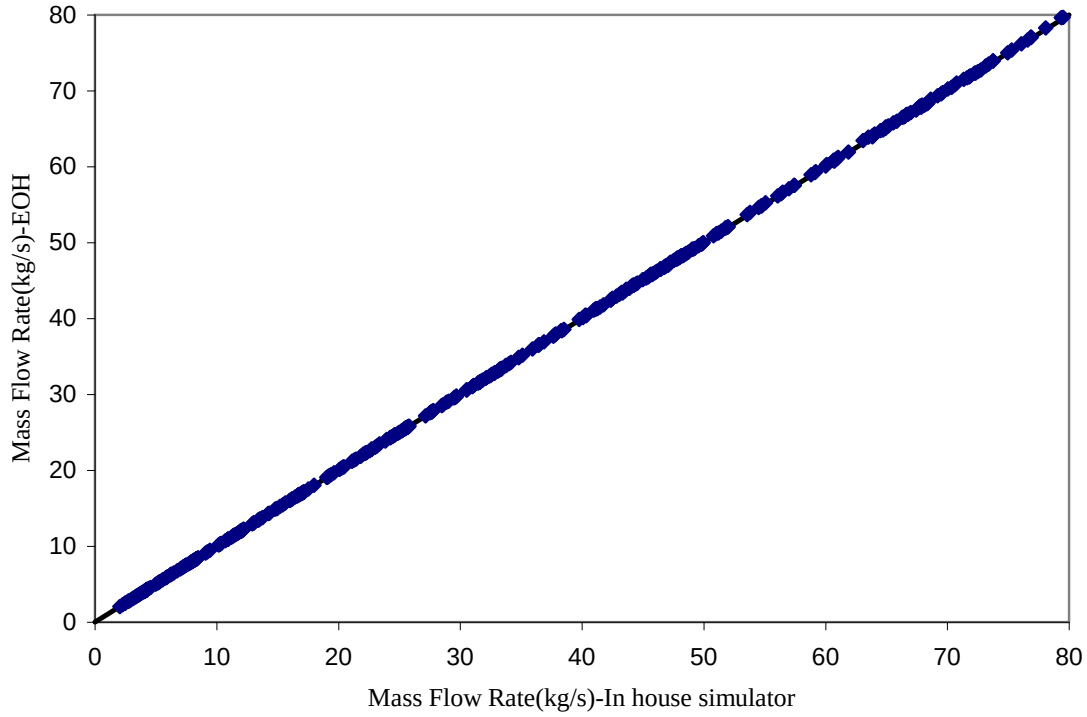

Figure 3.42: Comparison of mass flow rate of a HW calculated using in-house simulator with predicted mass flow rate by the equivalent open hole (EOH) model, using the effective wellbore radius, HW-1 data set of Table 3.6.

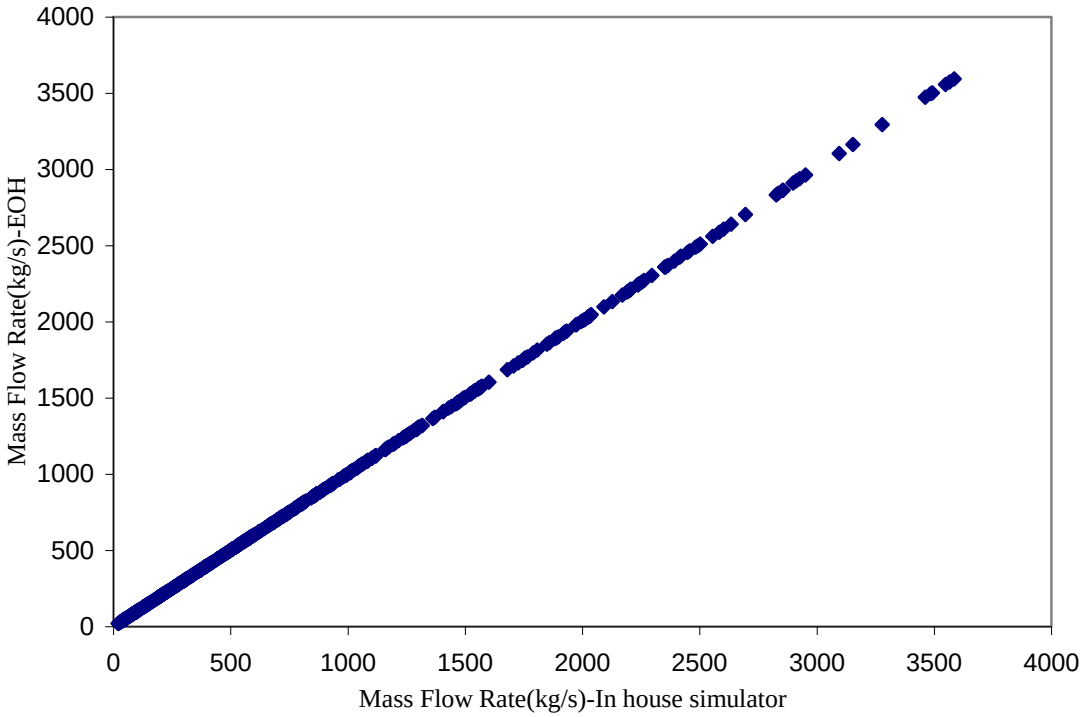

Figure 3.43: Comparison of mass flow rate calculated using the HW in-house simulator with predicted mass flow rate by the equivalent open hole (EOH) model with the effective wellbore radius, HW-2 data set of Table 3.6.

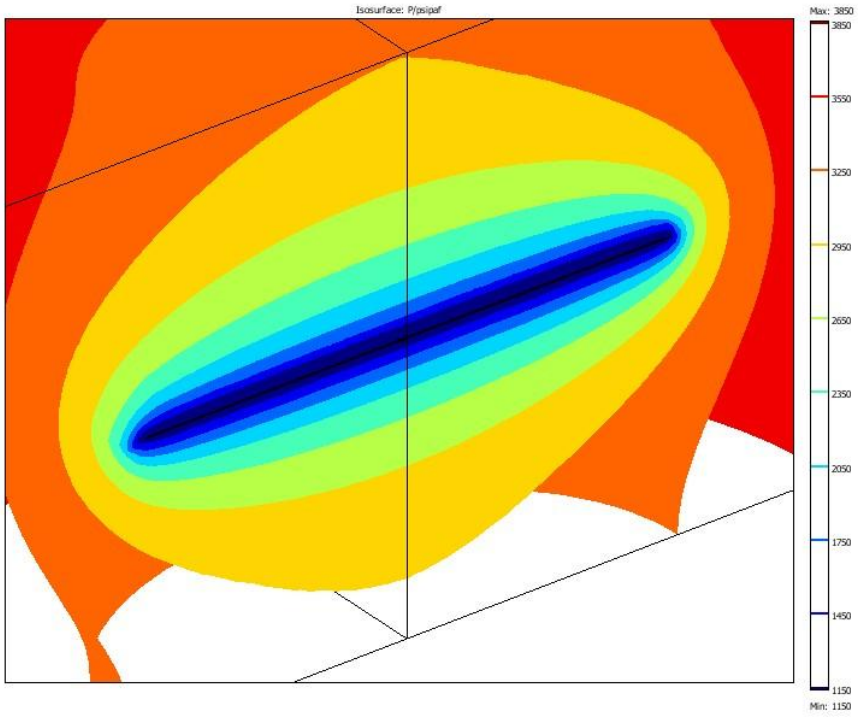

(a)

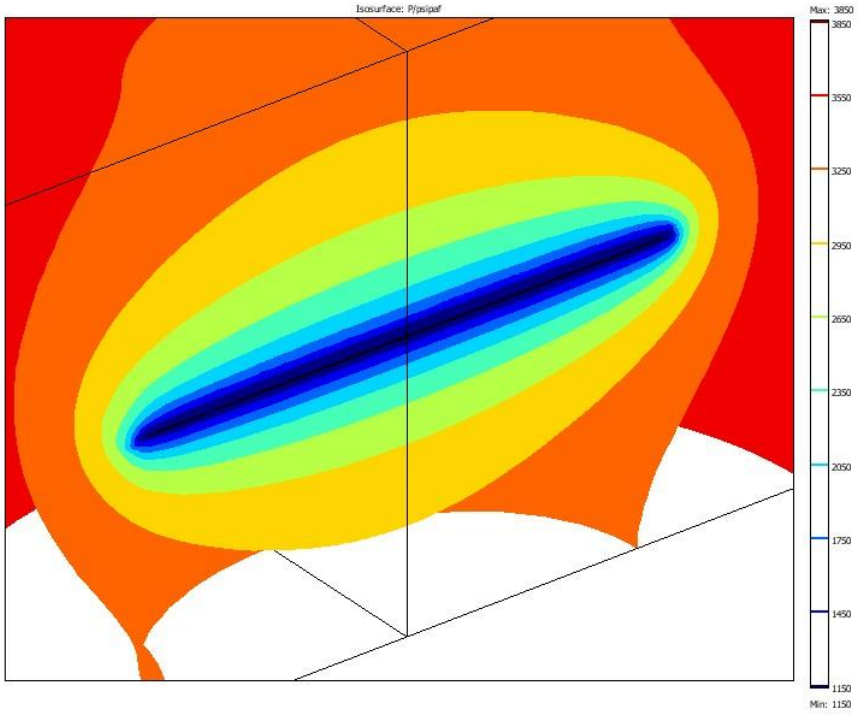

(b)

3.44: Isobar curves around a horizontal well a) without and b) with inertia (non-Darcy).

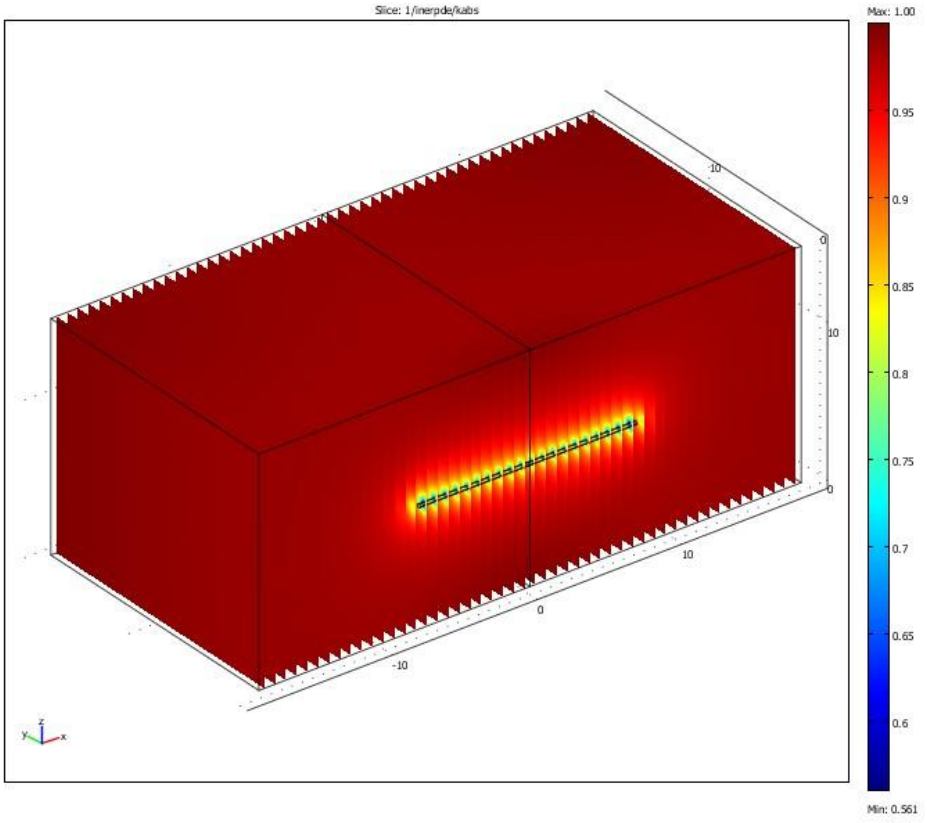

Figure 3.45: k_r distribution for non-Darcy flow around a horizontal well.

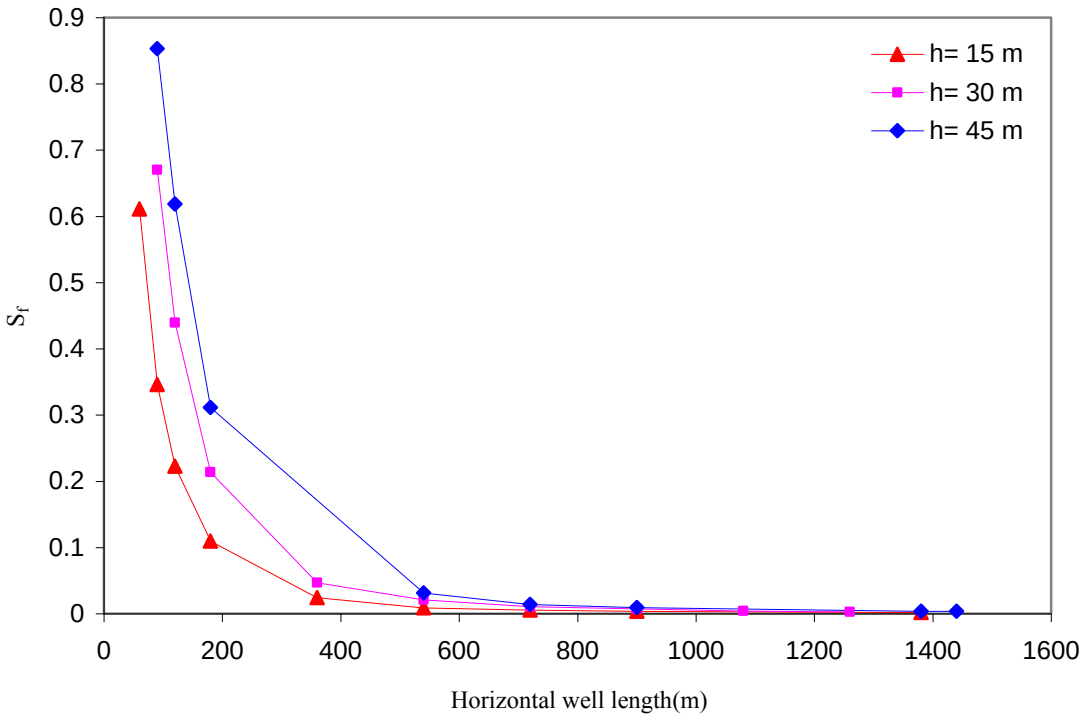

Figure 3.46: Variation of the flow skin S_f versus horizontal well length at three different reservoir thicknesses, HW-2 data set of Table 3.6, r_w= 0.14 m.

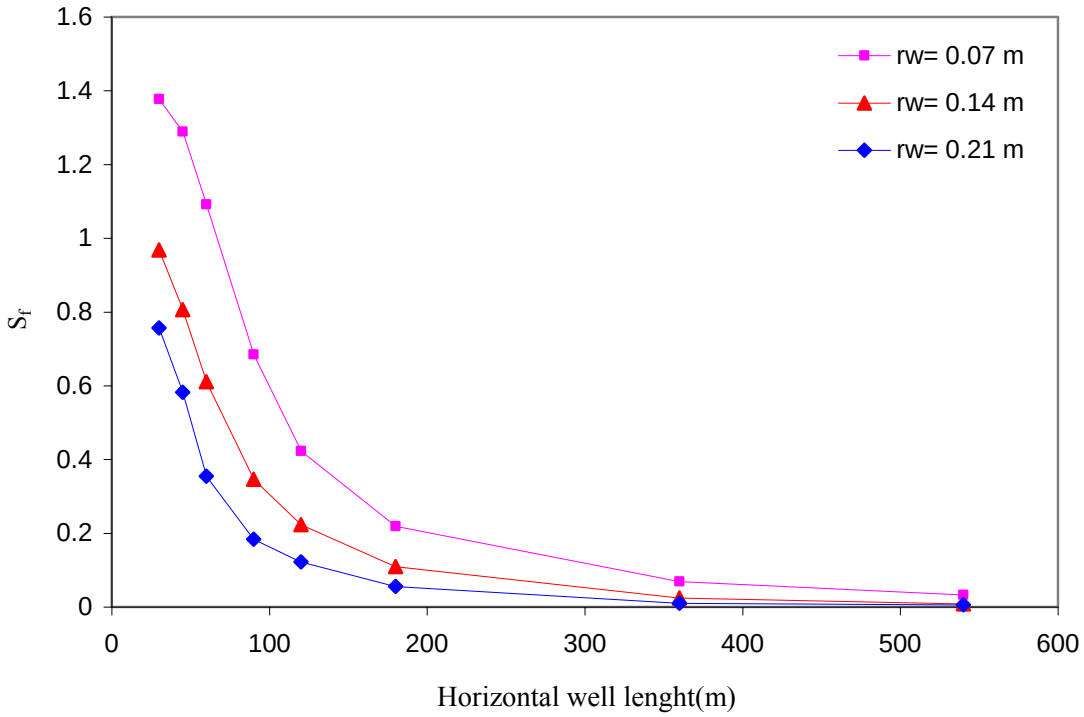

Figure 3.47: Variation of the flow skin S_f versus horizontal well length at three different wellbore radii, HW-2 data set of Table 3.6, h= 15 m.

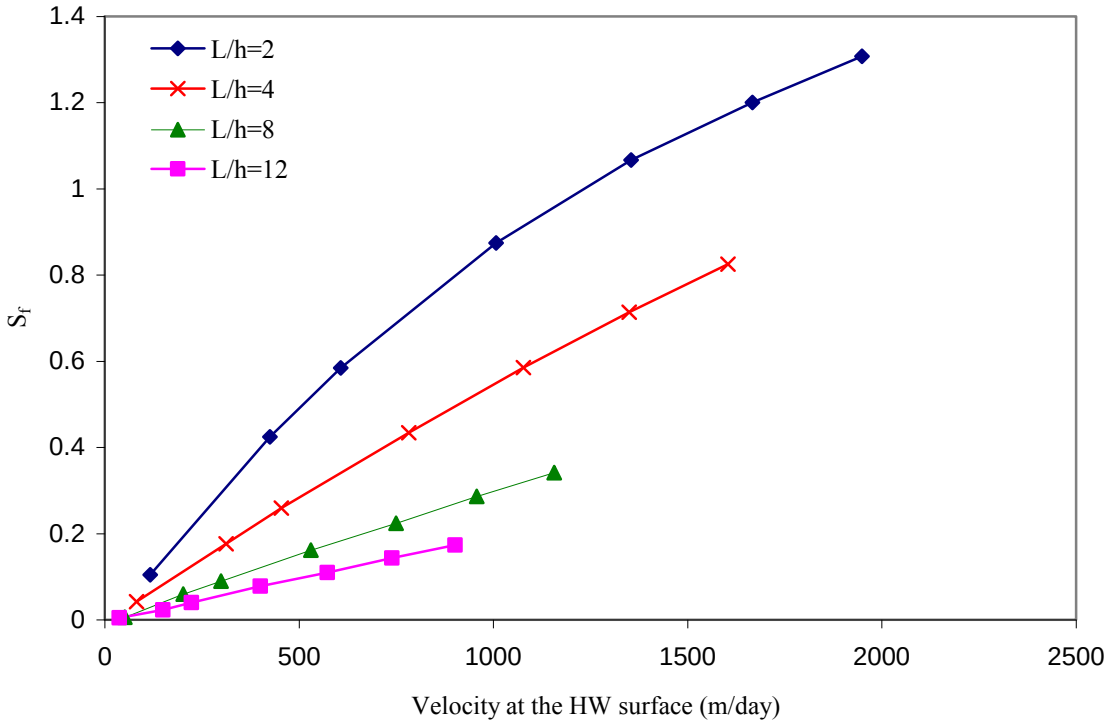

Figure 3.48: Variation of the flow skin (S_f) versus velocity at different HW lengths to the reservoir thickness, HW-1 data set of Table 3.6, h=45 m.

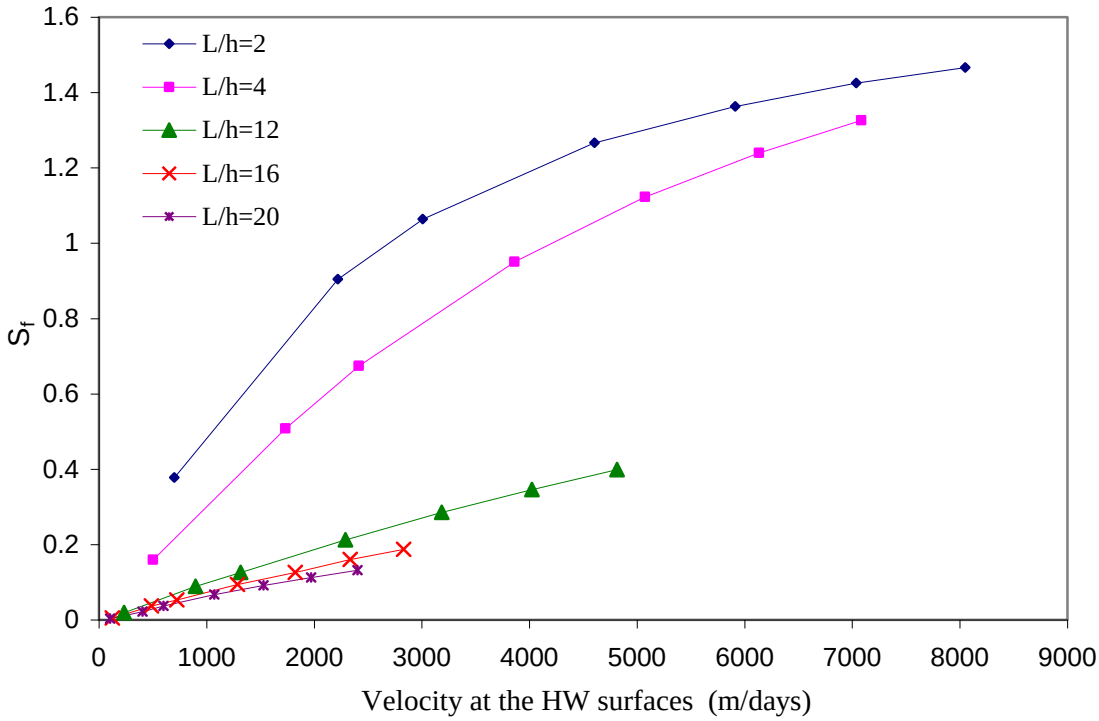

Figure 3.49: Variation of the flow skin S_f versus velocity at different HW lengths to the reservoir thickness, HW-2 data set of Table 3.6, h=45 m.

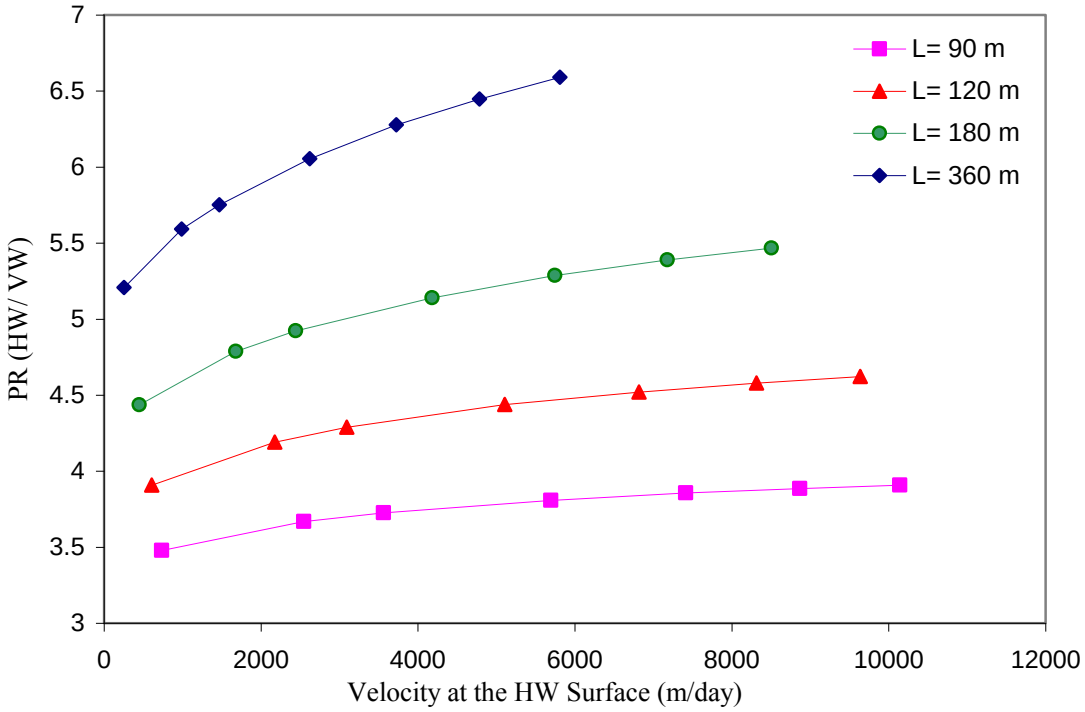

(a)

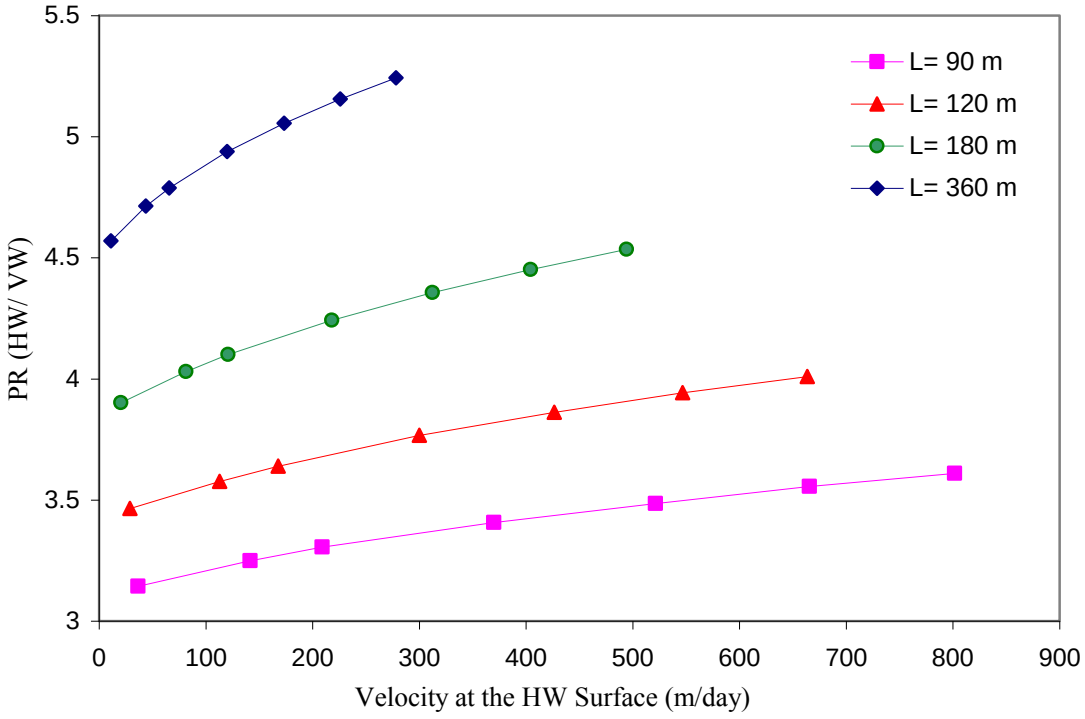

(b)

Figure 3.50: Productivity ratio (horizontal to vertical well) versus velocity at four different HW lengths, r_w=0.14 m, h=15 m , P_w=1000 psi a) Berea b)Texas Cream core properties .

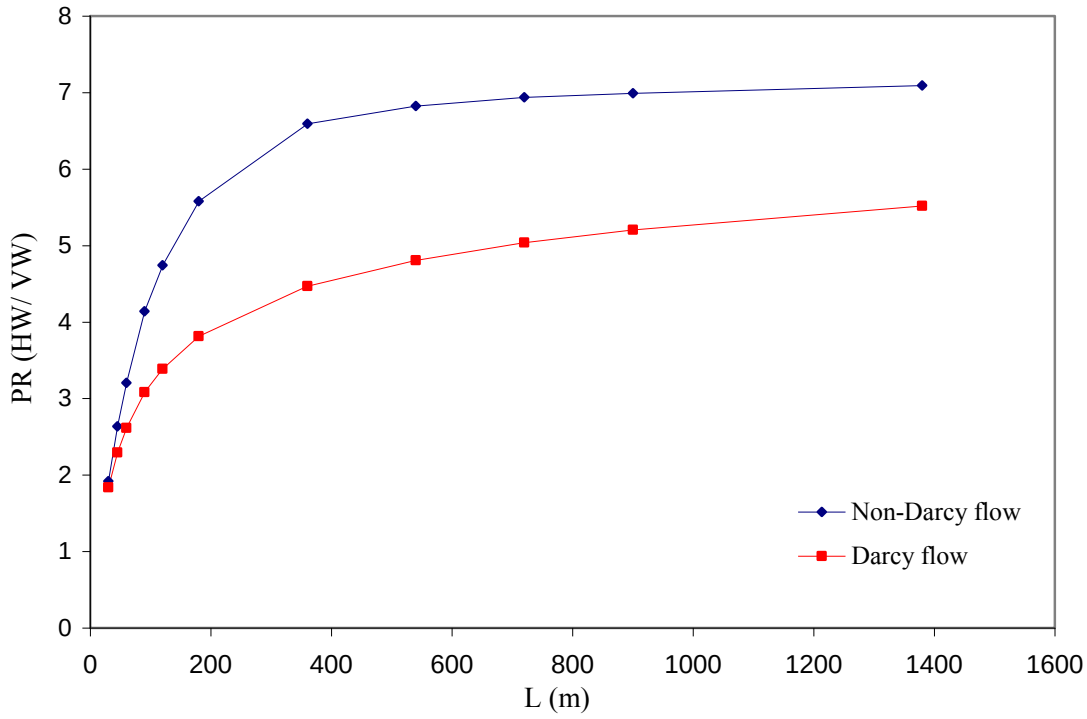

(a)

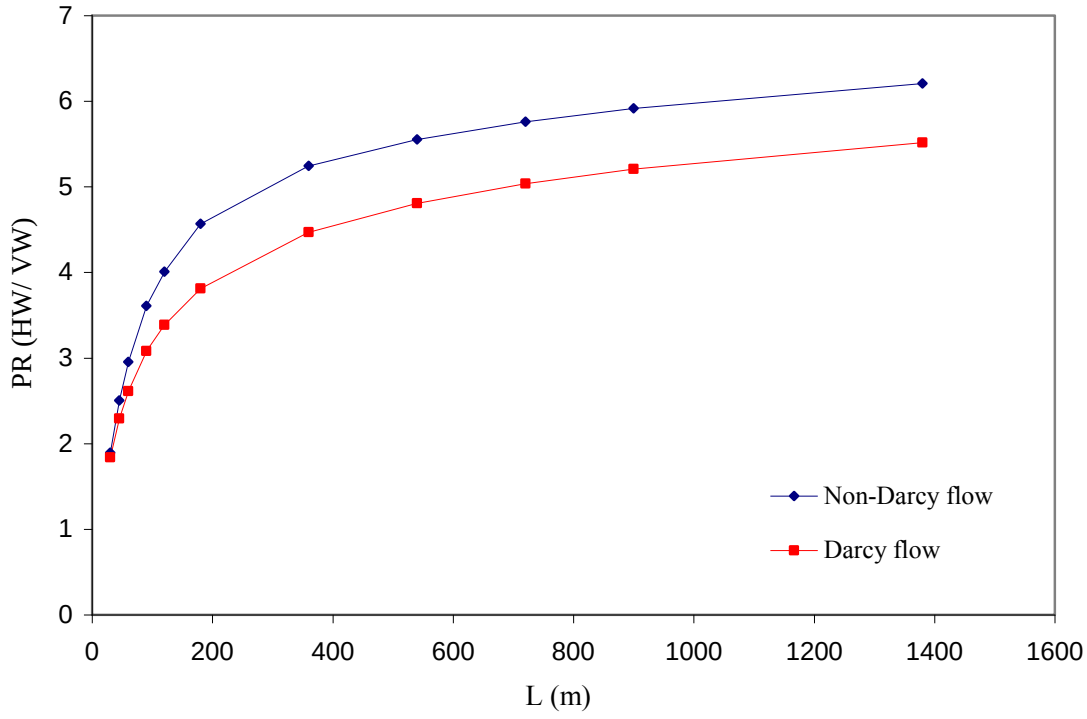

(b)

Figure 3.51: Productivity ratio (horizontal to vertical well) versus horizontal well length for Darcy and non Darcy flow regimes, r_w=0.14 m, h=15 m, P_w=1000 psi and P_{res}= 6200 psi a) Berea b)Texas Cream core properties.

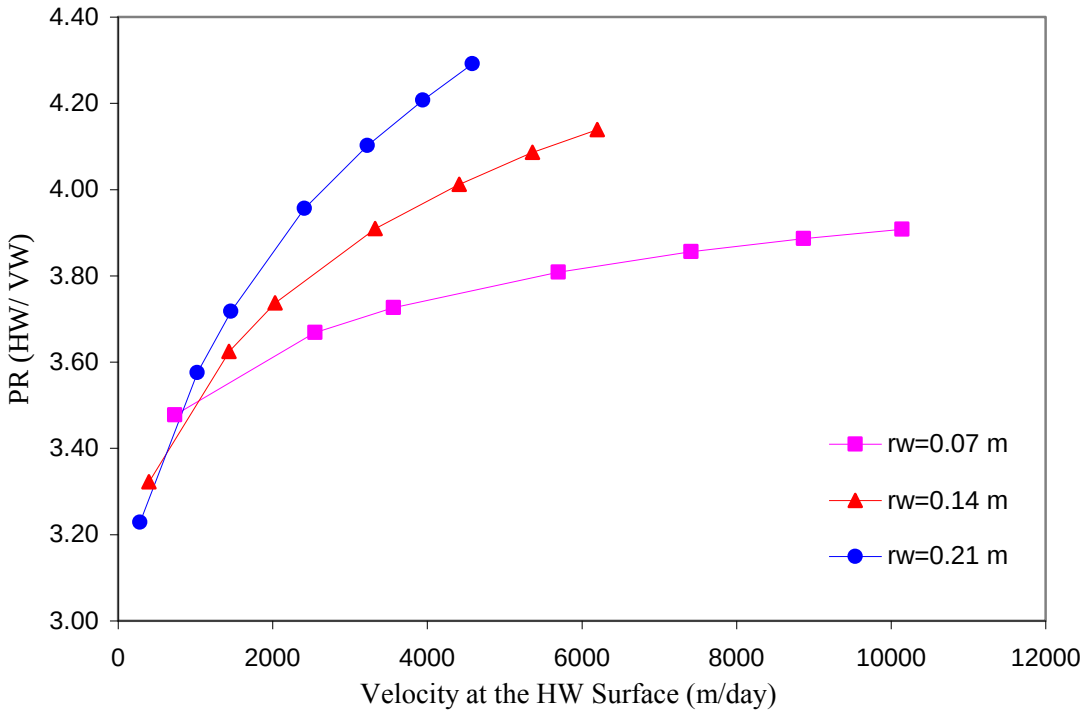

(a)

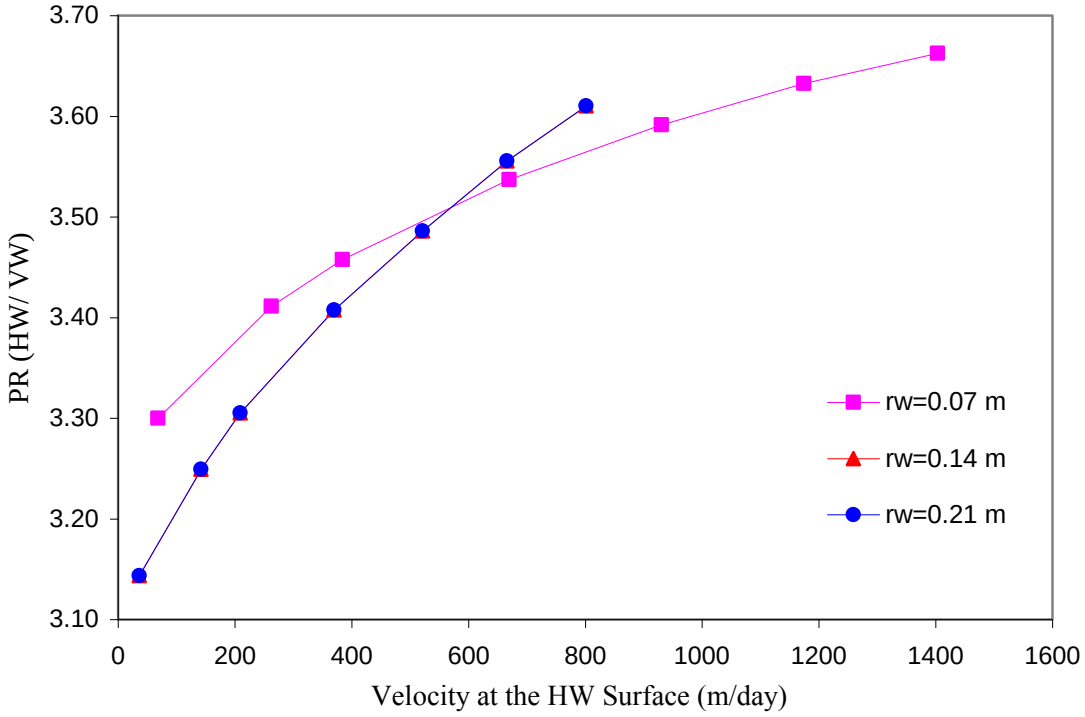

(b)

Figure 3.52: Productivity ratio (horizontal to vertical well) versus velocity for three wellbore radii, L=90 m, h=15 m, P_w=1000 psi, a) Berea b) Texas Cream core properties.

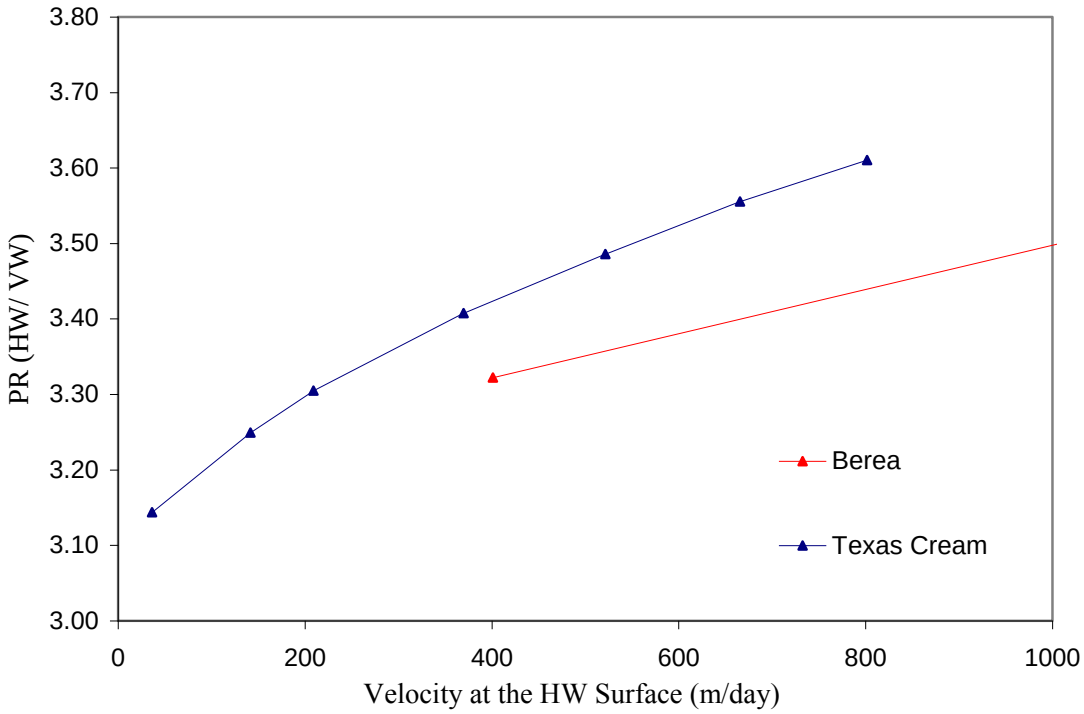

Figure 3.53: Productivity ratio (horizontal to vertical well) versus velocity, L=90 m, h=15 m, P_w=1000 psi, r_w=0.14 m for Berea and Texas Cream core properties.

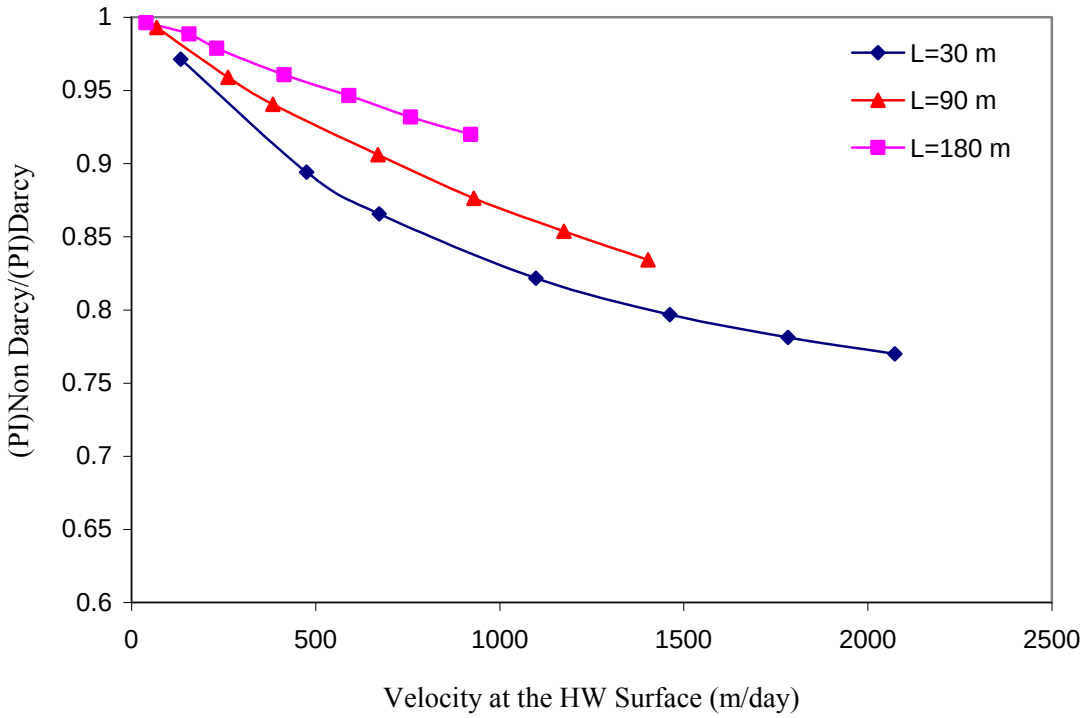

Figure 3.54: Productivity ratio (Non Darcy to Darcy flow) versus velocity for the different HW lengths, h=15 m, P_w=1000 psi, r_w=0.14 m for Texas Cream core properties.

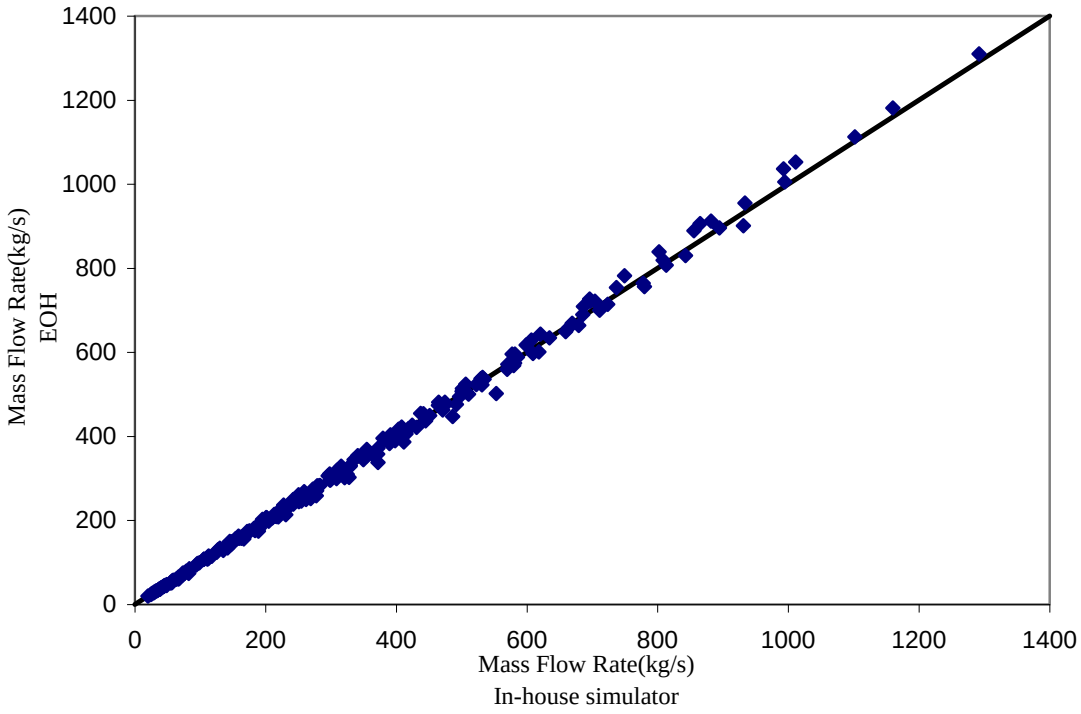

Figure 3.55: The mass flow rate calculated using the author‘s proposed effective equivalent wellbore radius correlation based on the equivalent radius concept versus the corresponding values obtained by the in-house simulator, Berea core properties.

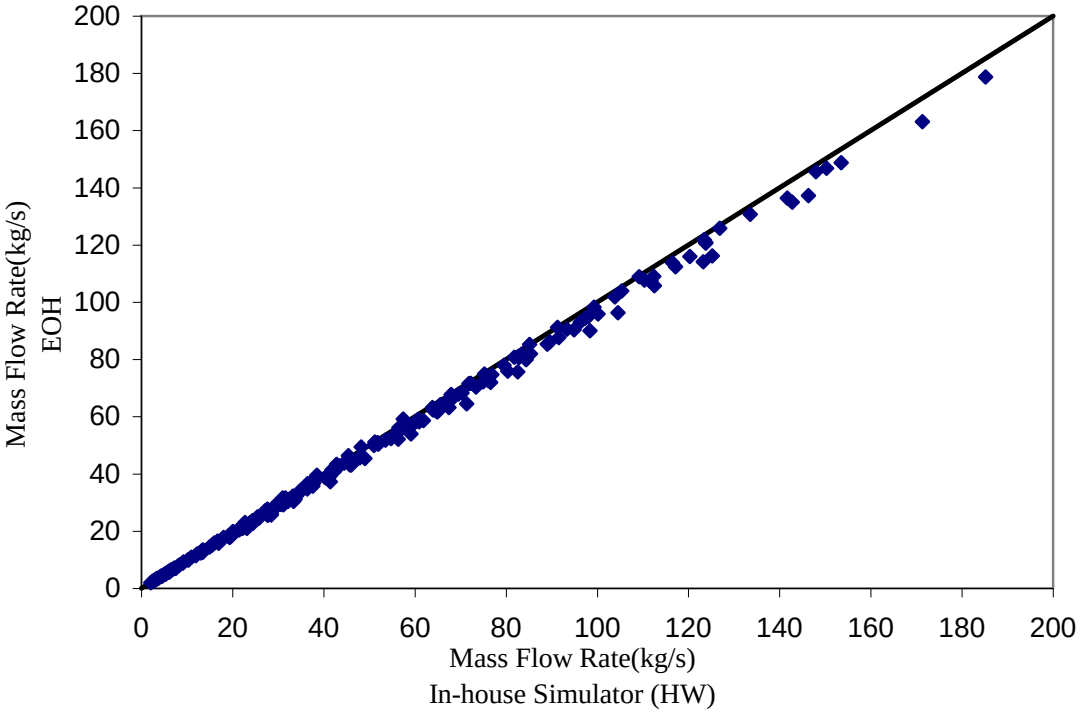

Figure 3.56: The mass flow rate calculated using the author‘s proposed effective equivalent wellbore radius correlation based on the equivalent radius concept versus the corresponding values obtained by the in-house simulator, Texas Cream core properties.

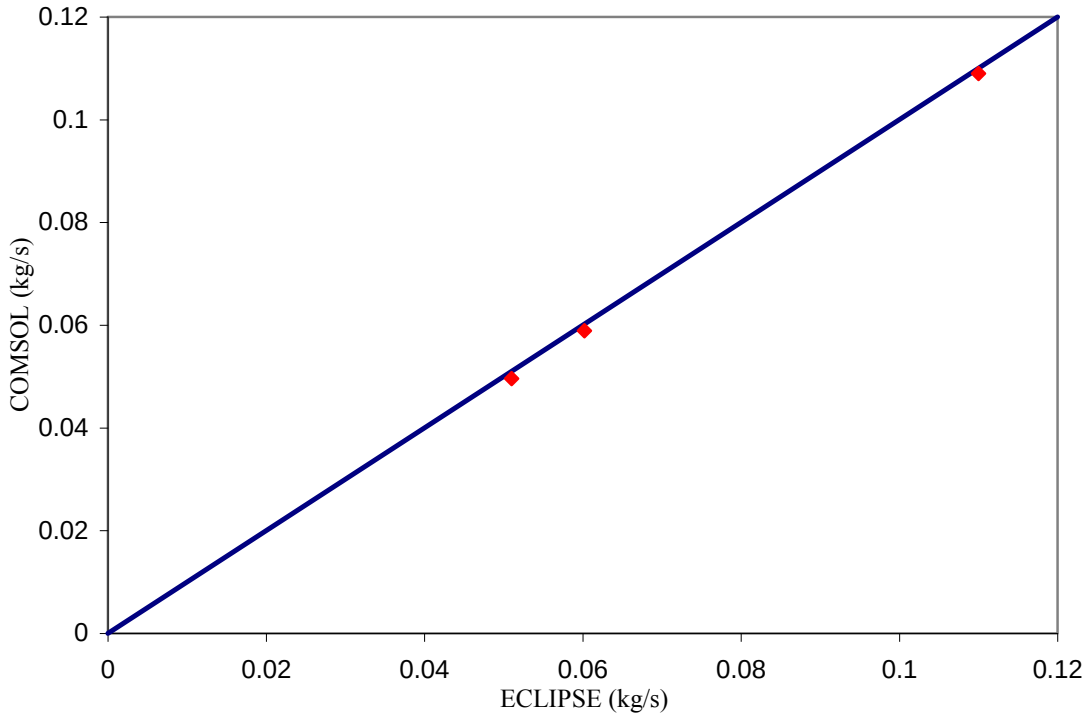

Figure 3.57: Comparison of the results of ECLIPSE two-phase model (gas and condensate) with those of the in-house simulator at three different pressure drops and fractional flow.

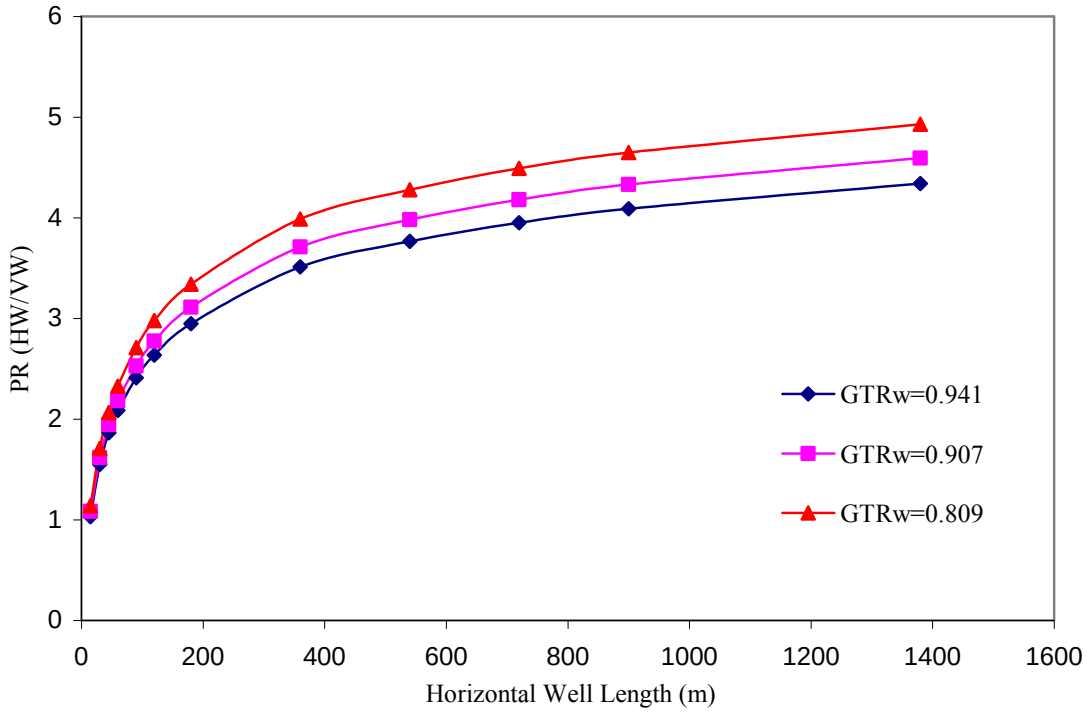

(a)

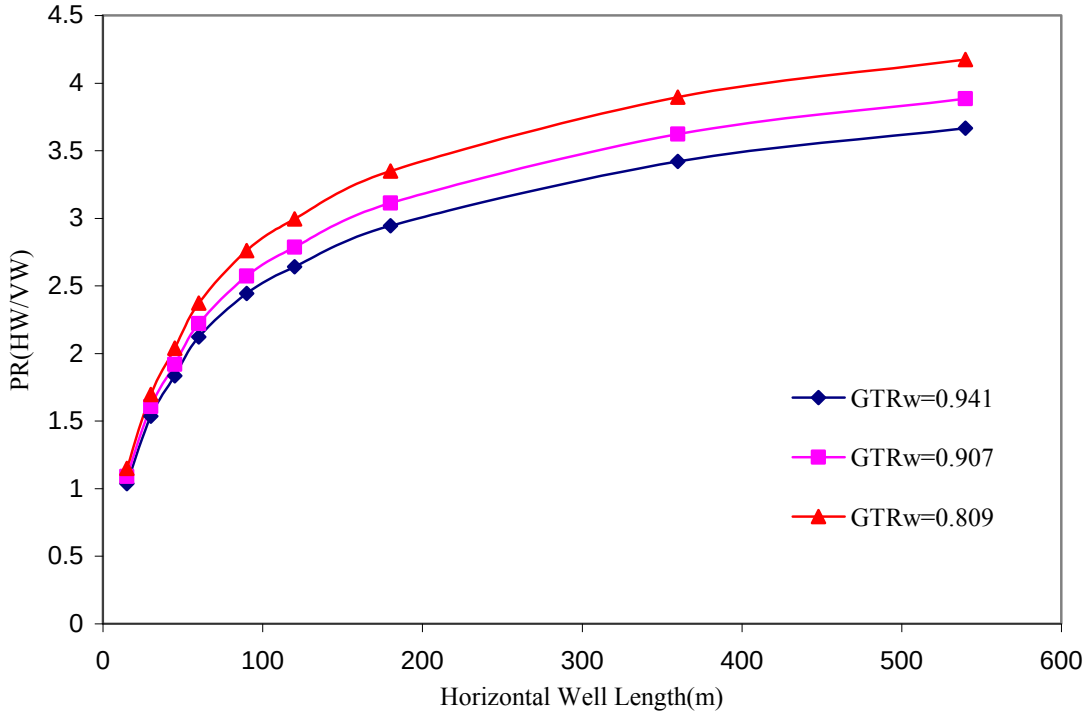

(b)

Figure 3.58: Productivity ratio (horizontal to vertical well) versus horizontal well length at three different gas fractional flows, h= 15 m, P_{res}=1800 psi, P_w= 1300 psi, a) r_w=0.14 m b) r_w=0.21 m, Berea core properties.

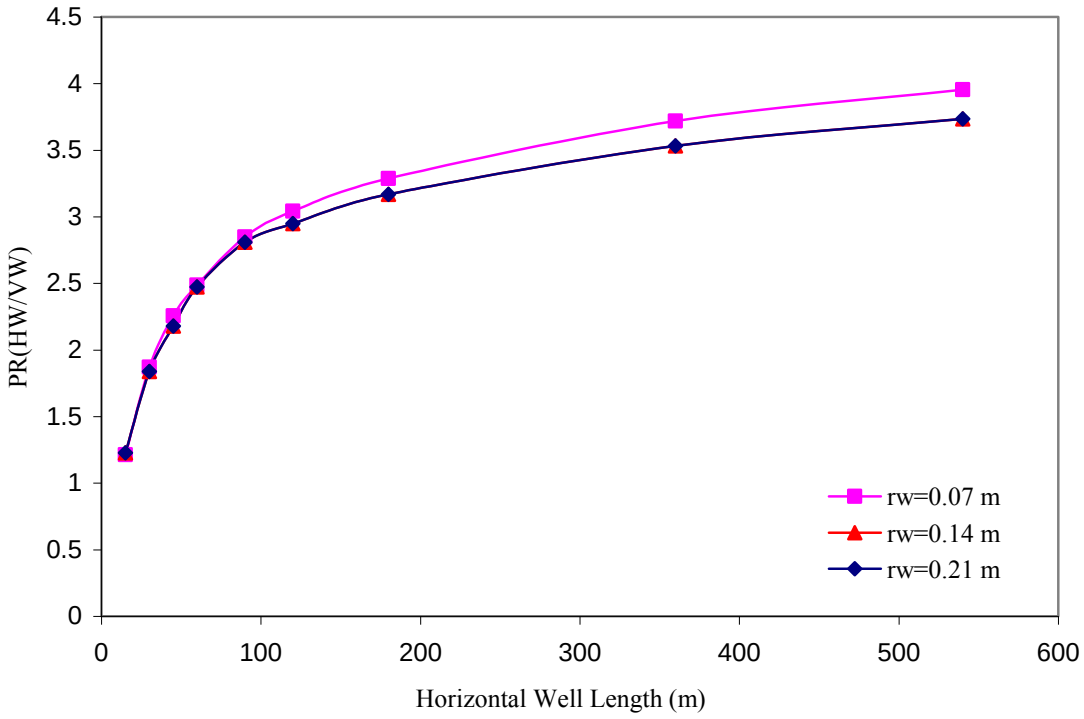

Figure 3.59: Productivity ratio versus horizontal well length at the wellbore radii of 0.07 m, 0.14 m and 0.21 m, GTR=0.809, h= 15 m, P_{res}=1800 psi, P_w= 1300 psi.

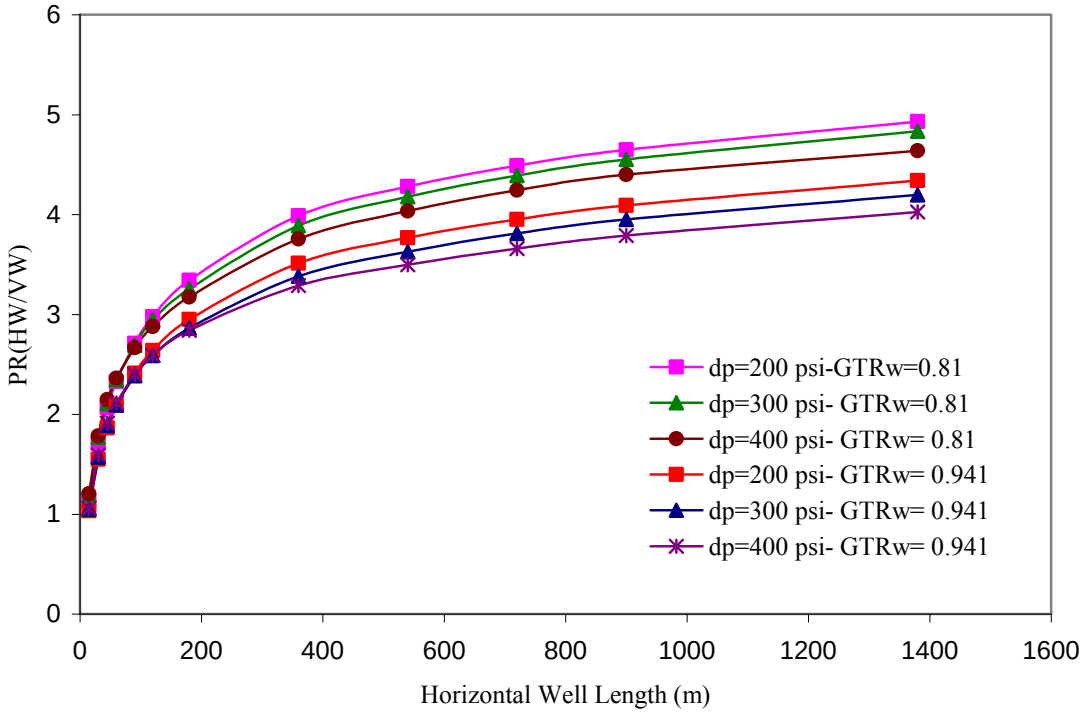

Figure 3.60: Productivity ratio versus horizontal well length, r_w=0.14 m, GTR_w=0.941 & 0.809, h= 15 m, P_w= 1300 psi, pressure drops of 200, 300 and 400 psi.

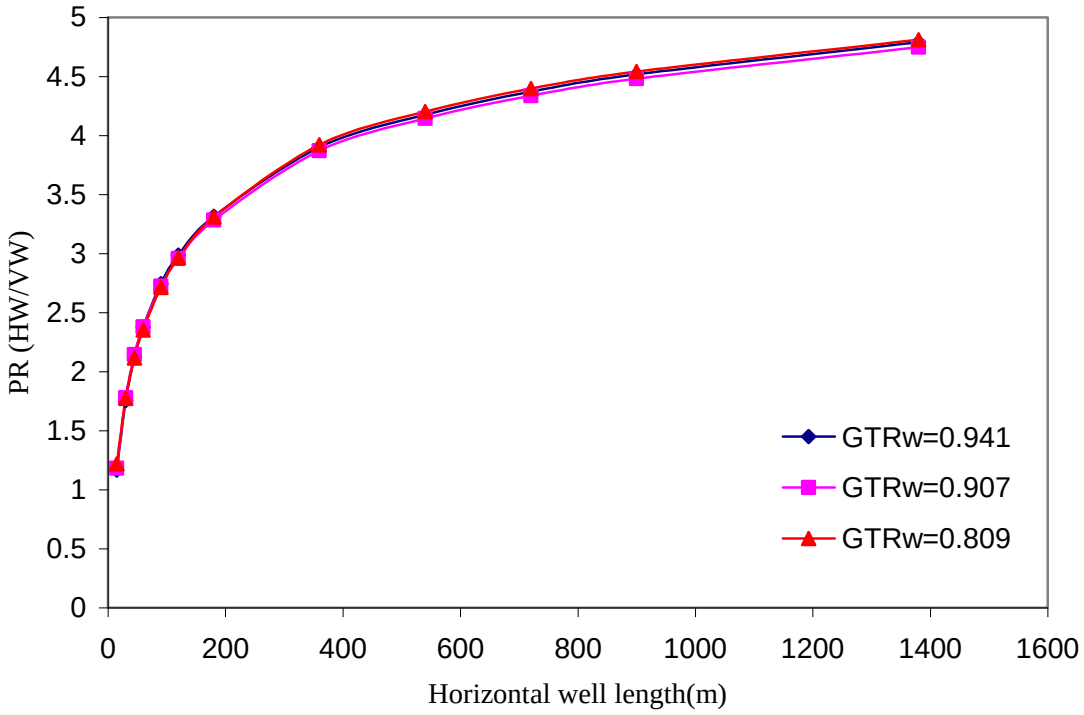

(a)

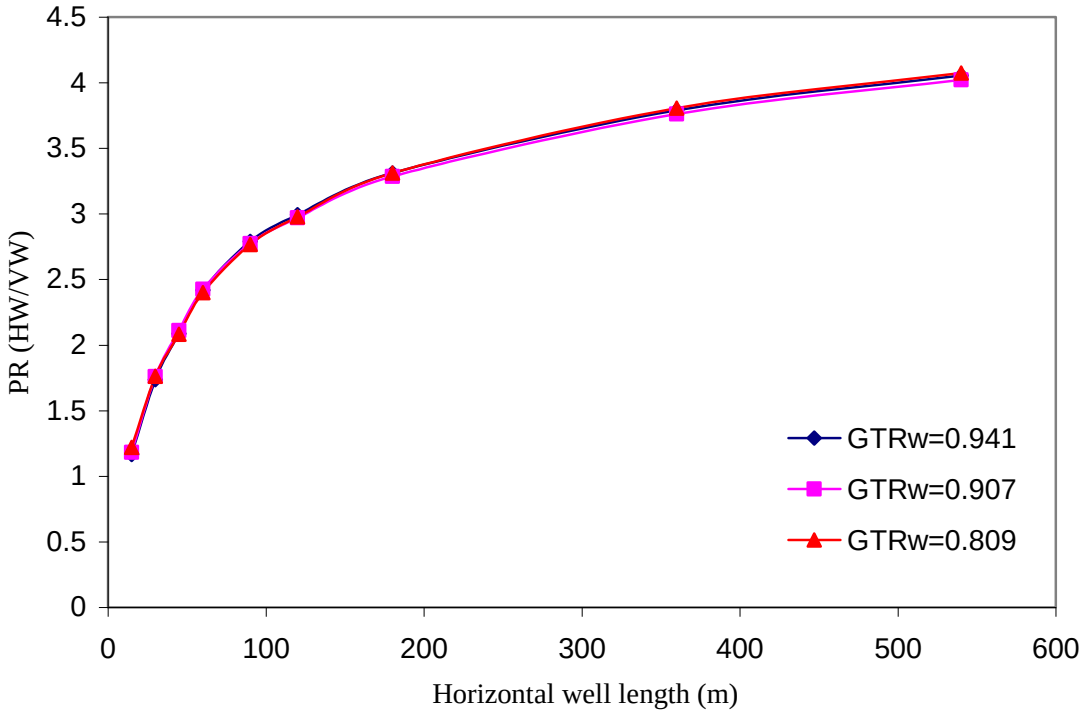

(b)

Figure 3.61: Productivity ratio versus horizontal well length at three different gas fractional flows, h= 15 m, P_{res}=1800 psi, P_w= 1300 psi, a) r_w=0.14 m b) r_w=0.21 m, Texas cream core properties.

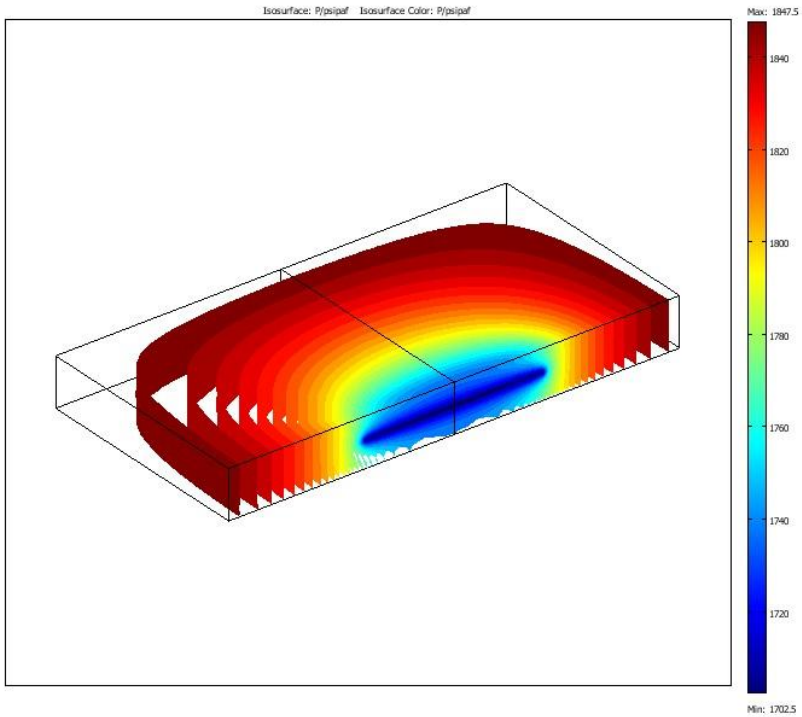

(a)

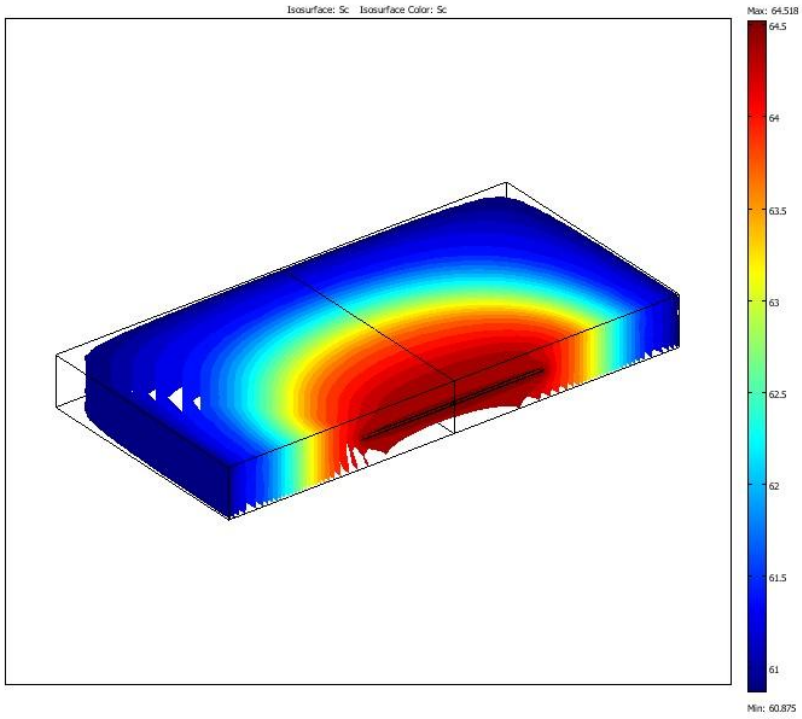

(b)

Figure 3.62: a) Iso-pressure map b) Iso-condensate saturation map around a HW.

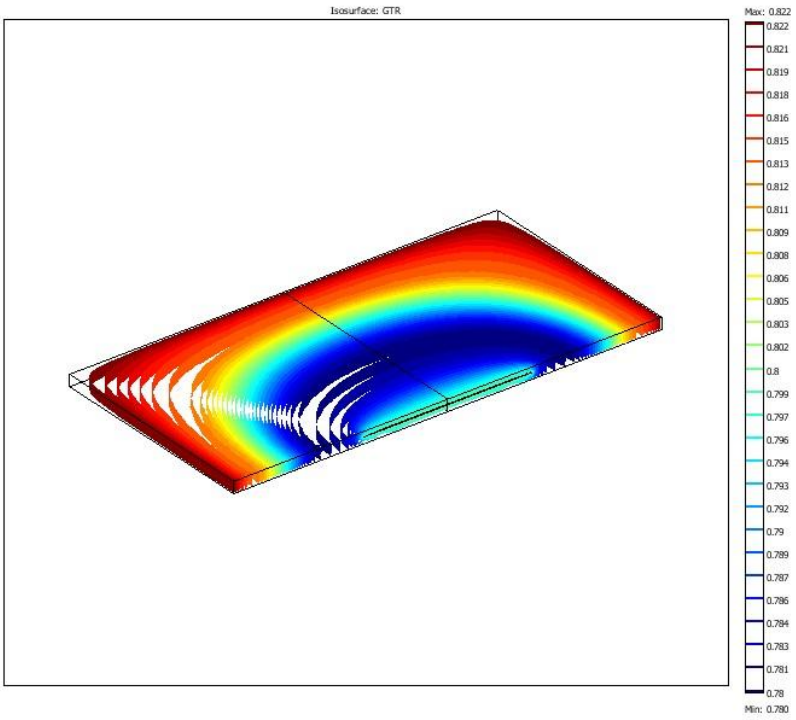

(a)

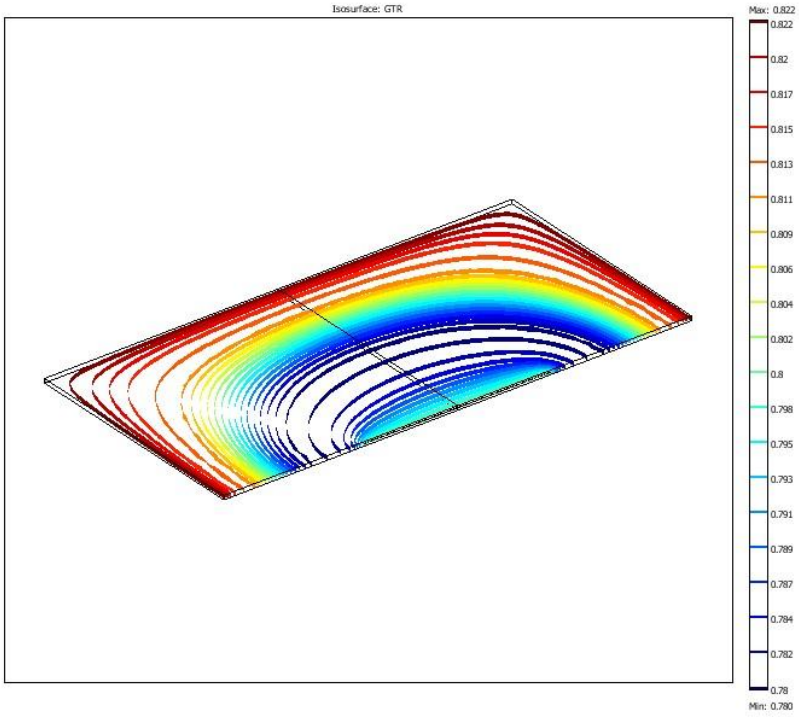

(b)

Figure 3.63: Iso GTR map a) Short and b) long HW, HW-1 and HW-2 in Table 3.9, respectively.

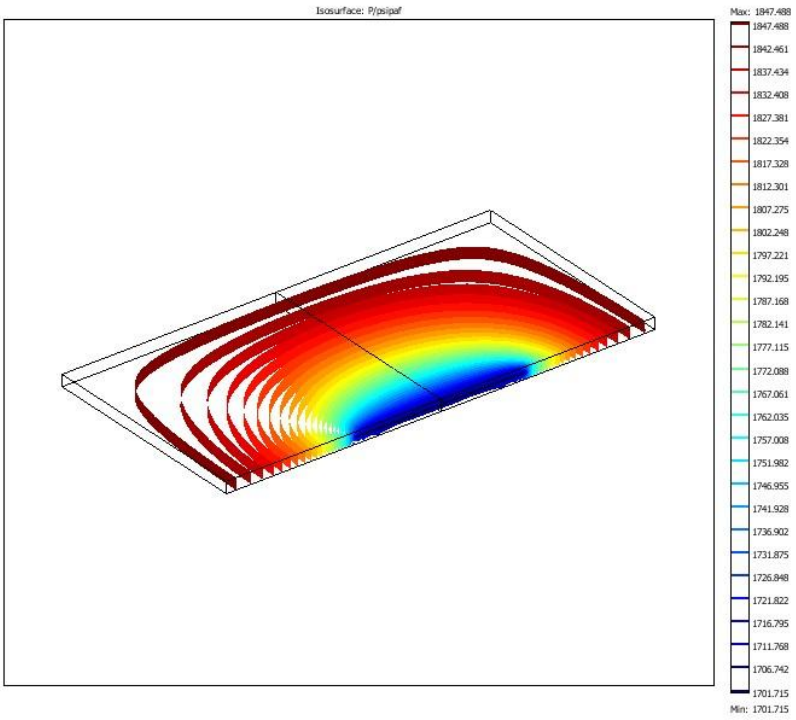

(a)

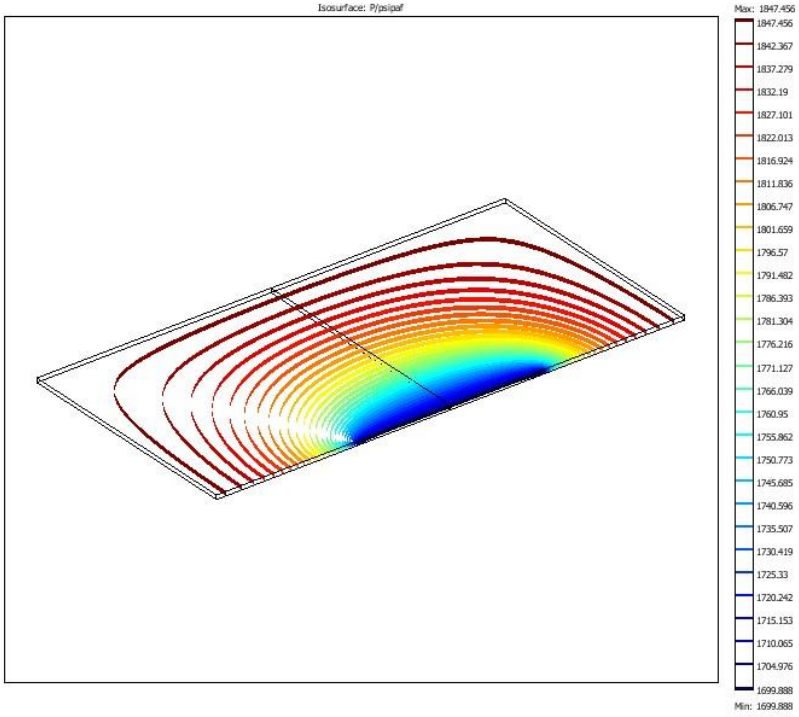

(b)

Figure 3.64: Iso-pressure map a) Short and b) Long HW, HW-1 and HW2 in Table 3.9, respectively.

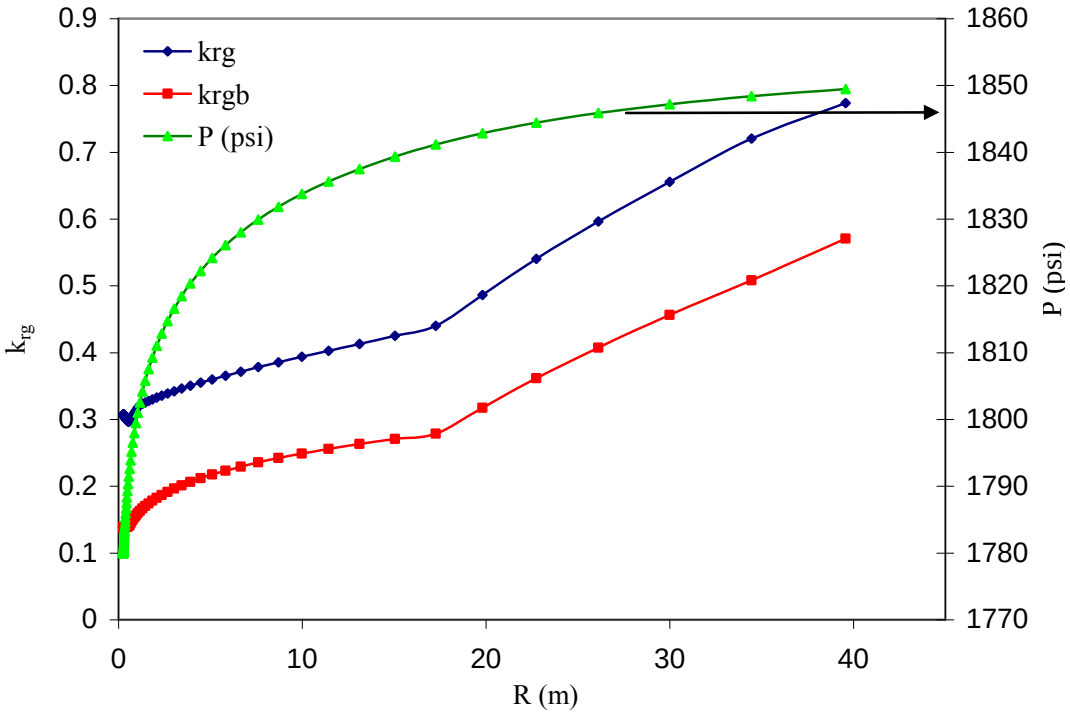

(a)

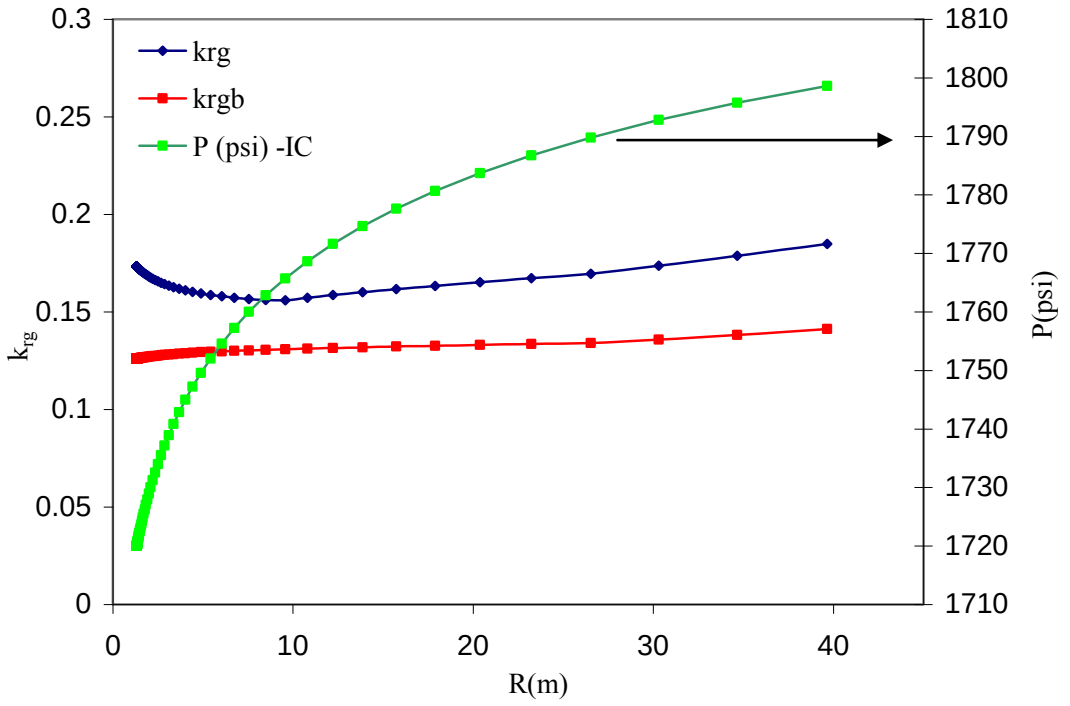

(b)

Figure 3.65: Variation of affected (by coupling and inertia) gas relative permeability and base relative permeability for EOH of a) HW-3 b) HW-4, listed in Table 3.9.

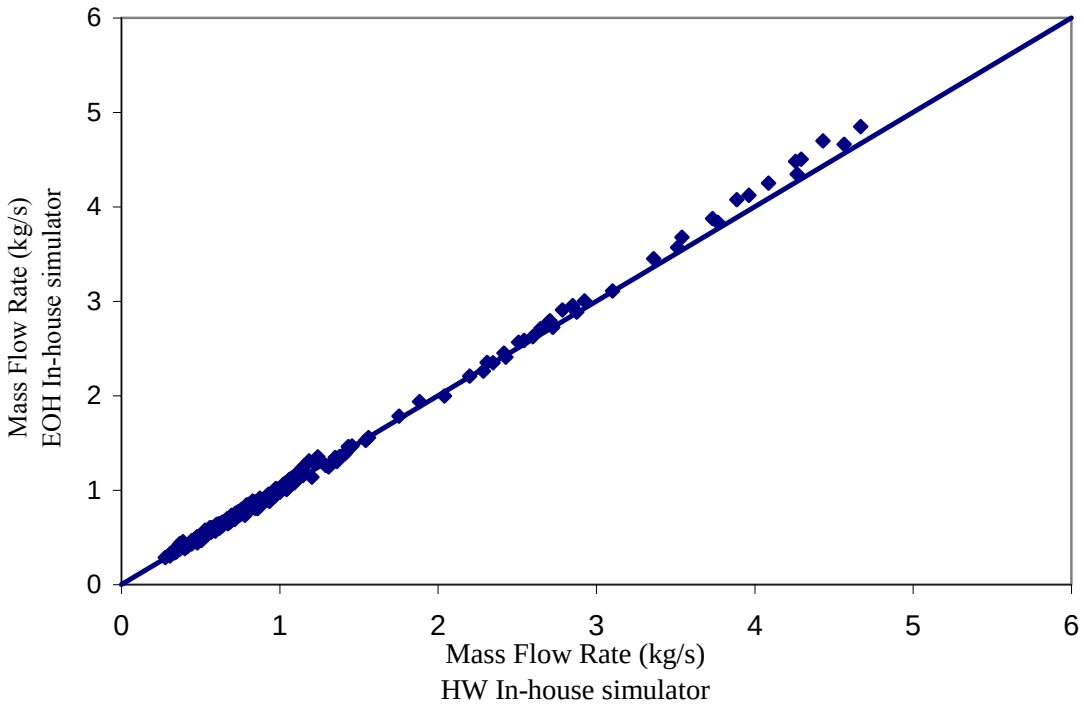

Figure 3.66: Mass flow rates calculated using the proposed two-phase flow skin correlation based on the equivalent radius concept versus the corresponding values obtained using the in-house simulator for HWS-5-HWS-16, listed in Table 3.9.

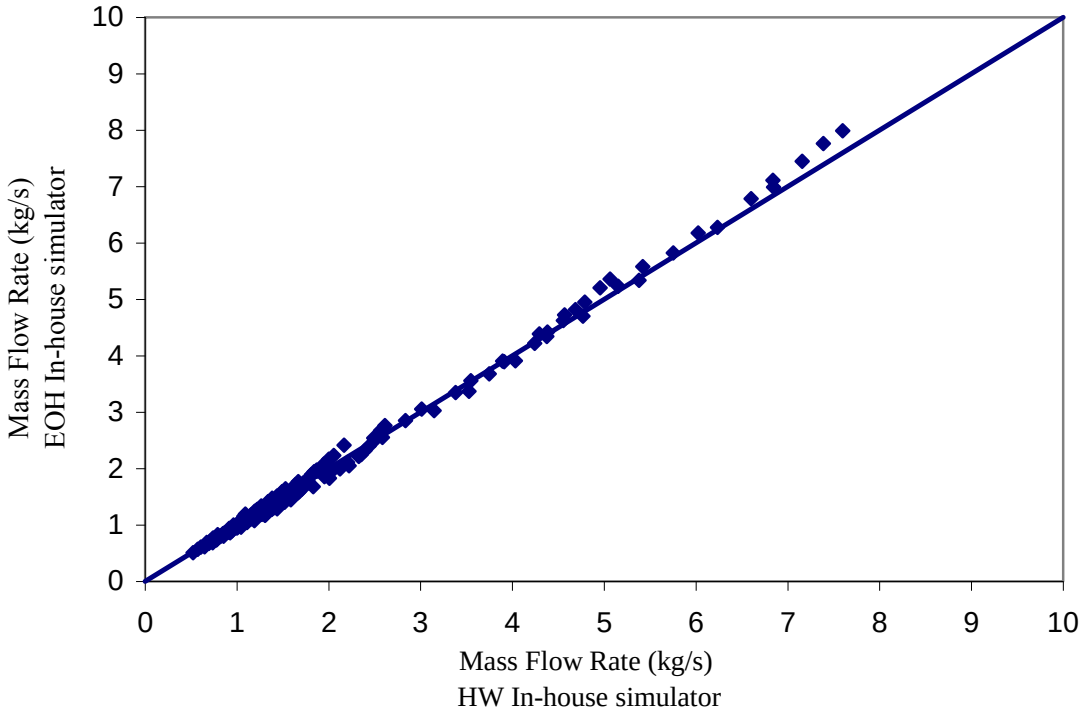

Figure 3.67: Mass flow rates calculated using the proposed two-phase flow skin correlation, based on the equivalent radius concept, versus the corresponding values obtained using the in-house simulator for HWS-17-HWS-22, listed in Table 3.9.

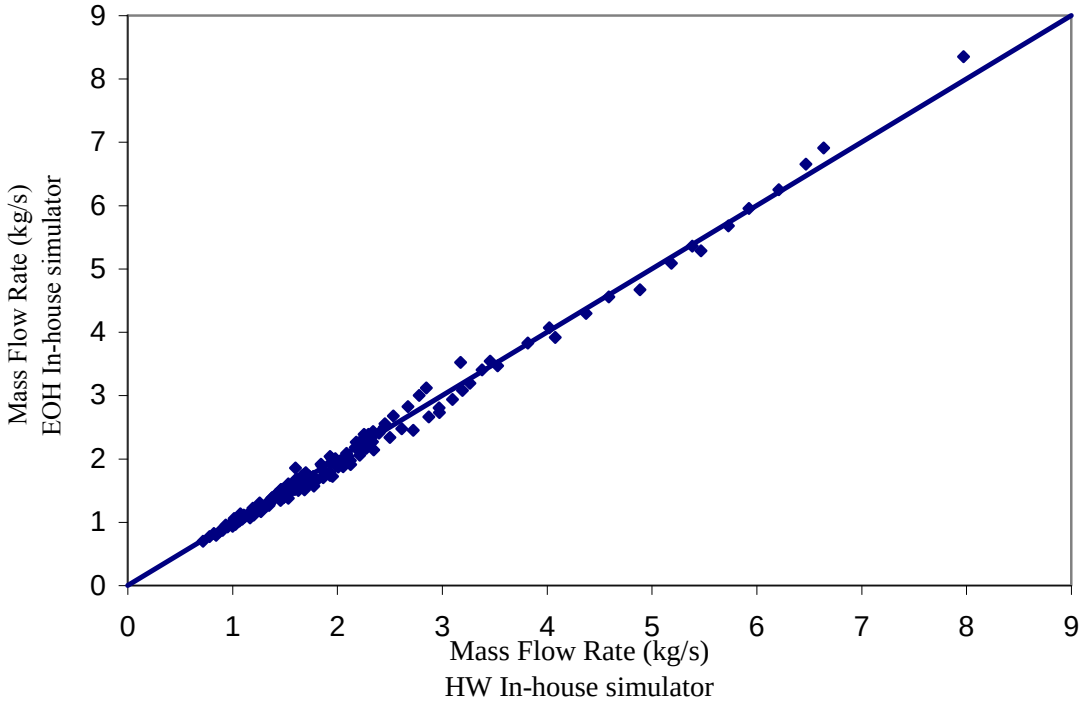

Figure 3.68: Mass flow rate calculated using the proposed two-phase flow skin correlation, based on the equivalent radius concept, versus the corresponding values obtained using the in-house simulator for HWS-23-HWS-34, listed in Table 3.9.

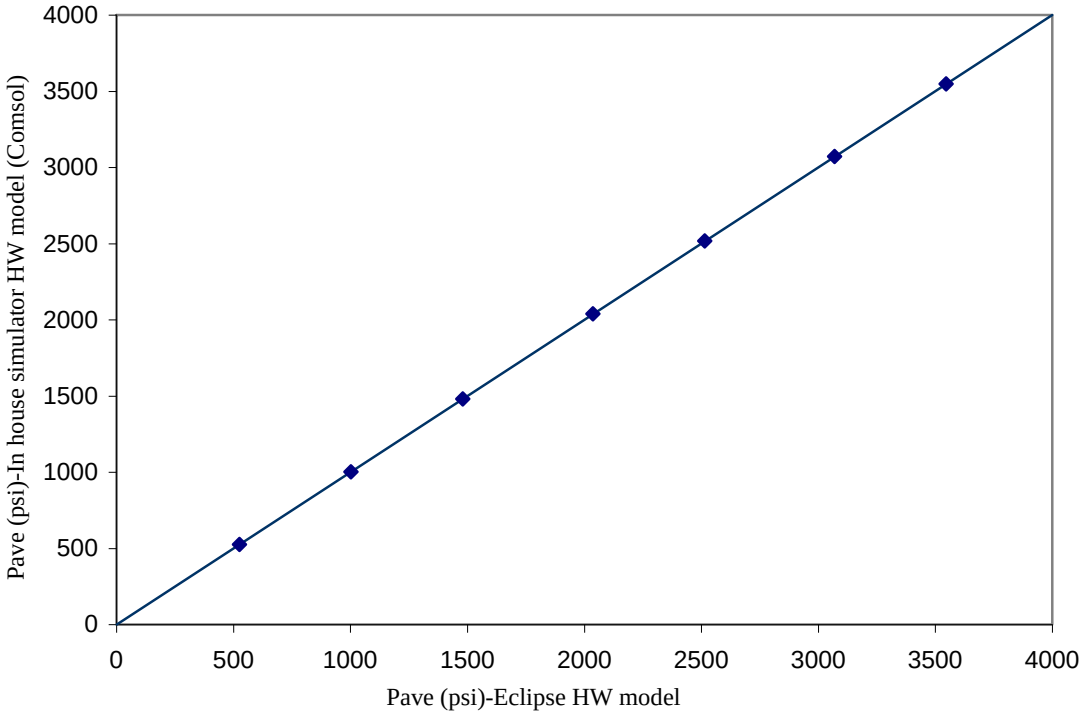

Figure 3.69: Comparison between the average pressures estimated using the in-house simulator and ECLIPSE simulators, both operating under pseudo steady state conditions, AAD% 1.

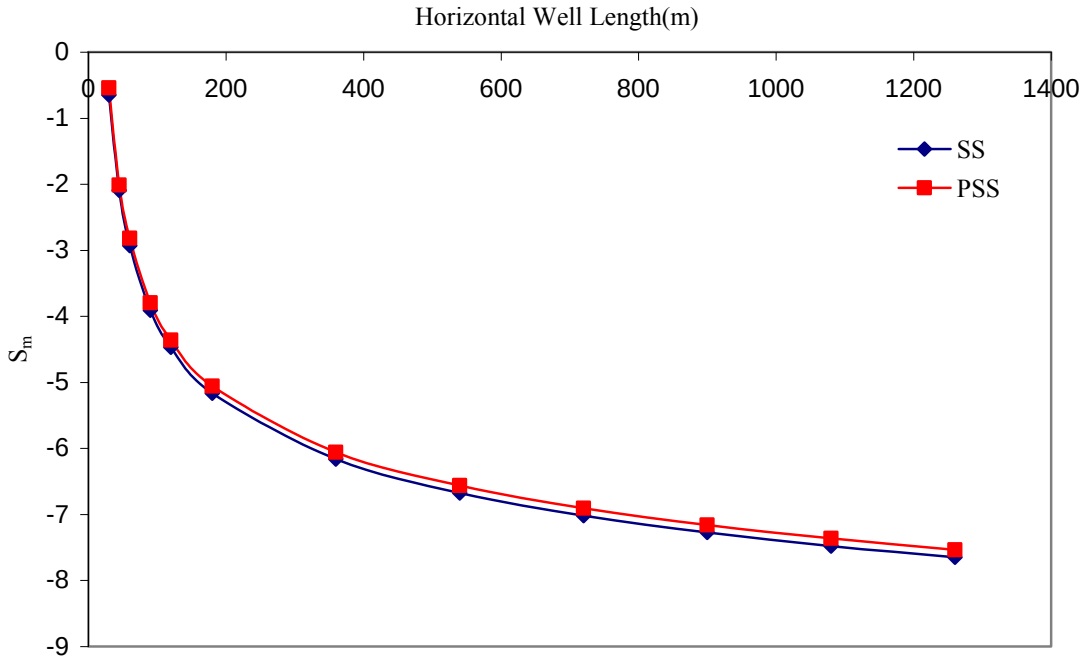

(a)

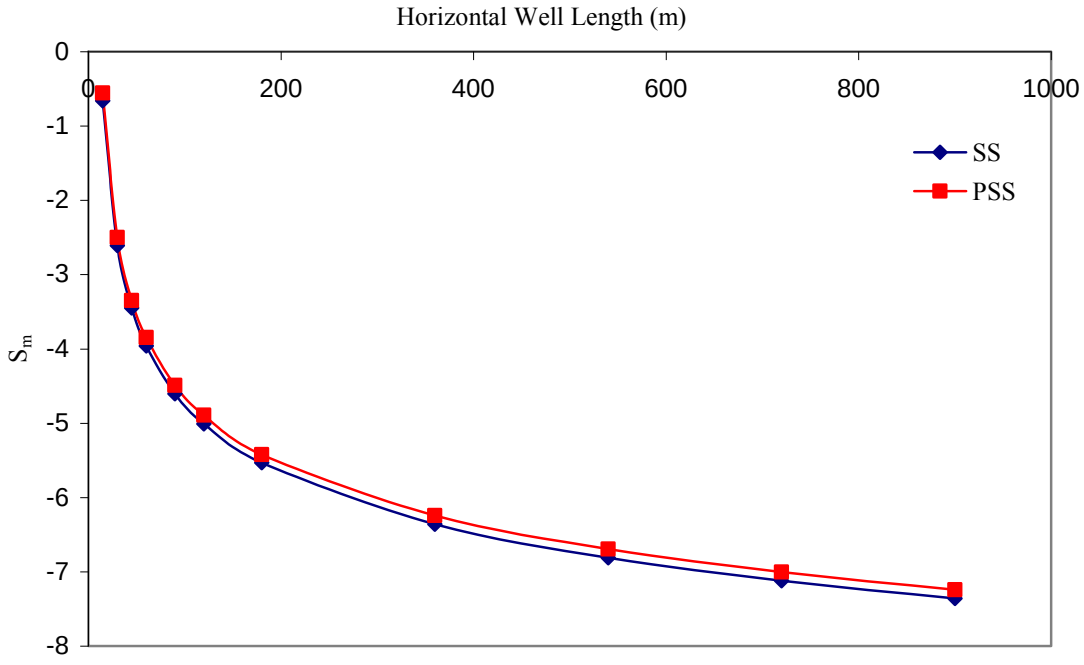

(b)

Figure 3.70: Geometric skin calculated by the HW pseudo steady and steady state in-house simulators versus HW length a) h=15 m b) h=30 m.

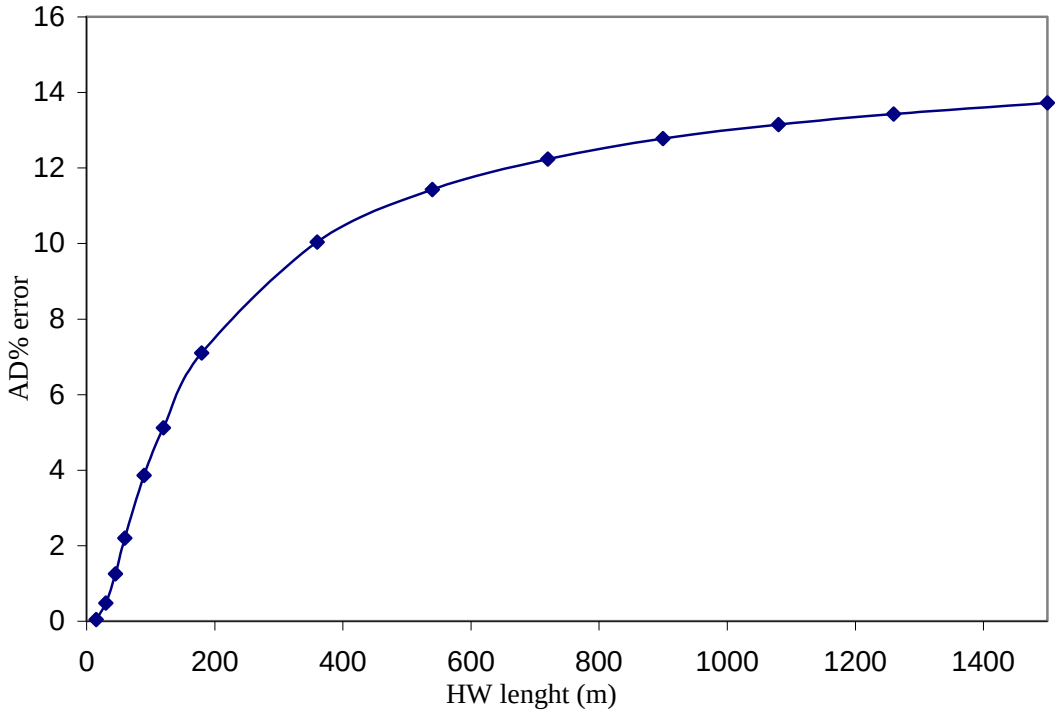

Figure 3.71: Variation of error on the pseudo-steady state horizontal well productivity index (J_D) obtained by ignoring the last two terms in the denominator of J_D, Equation 3.102, versus HW lengths.

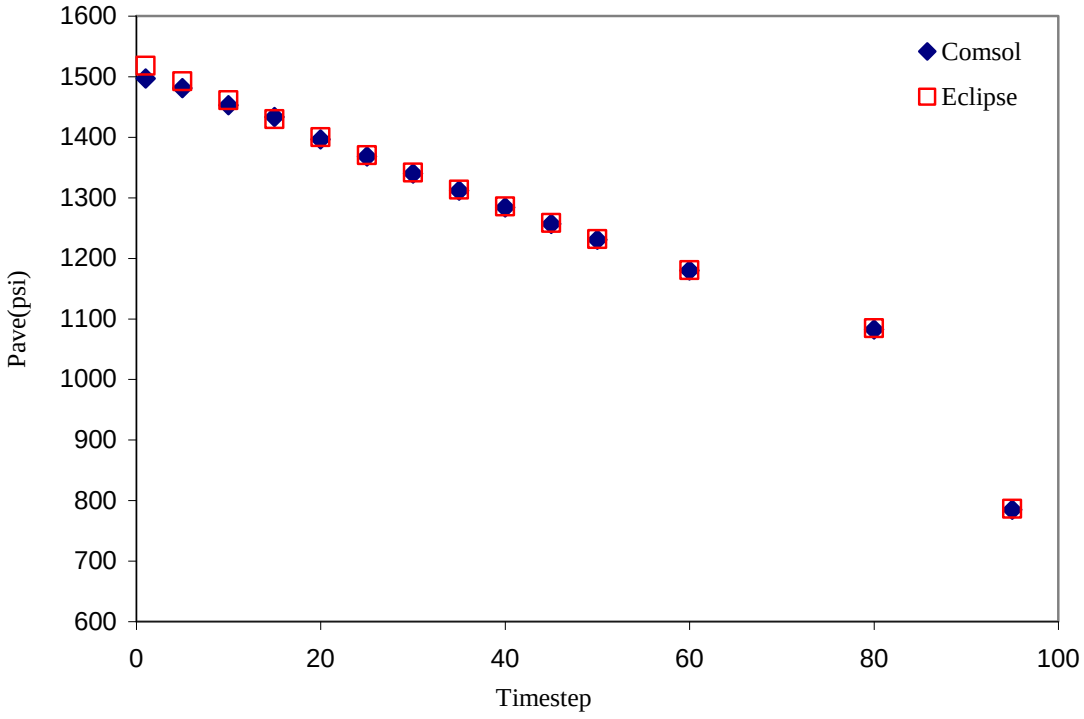

Figure 3.72: The calculated average pressure at the pseudo steady condition versus timestep, obtained by the in-house simulator (Comsol) and the model constructed by E300, Case A.

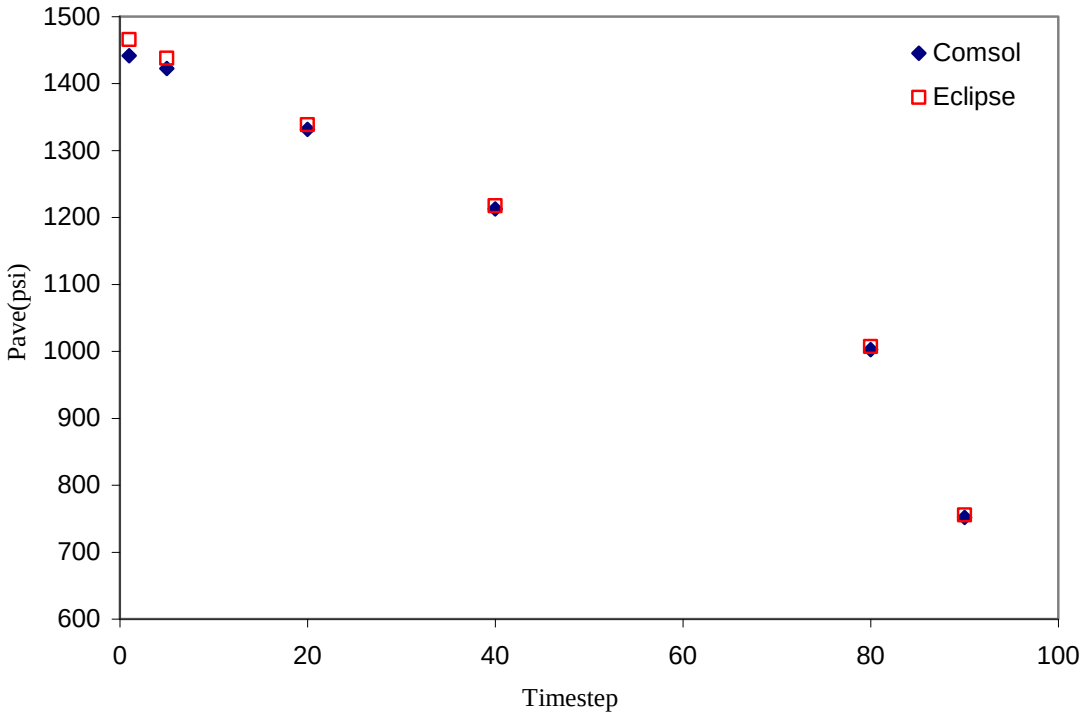

Figure 3.73: The calculated average pressure at the pseudo steady condition versus timestep obtained by the in-house simulator (Comsol) and the model constructed by E300, Case B.

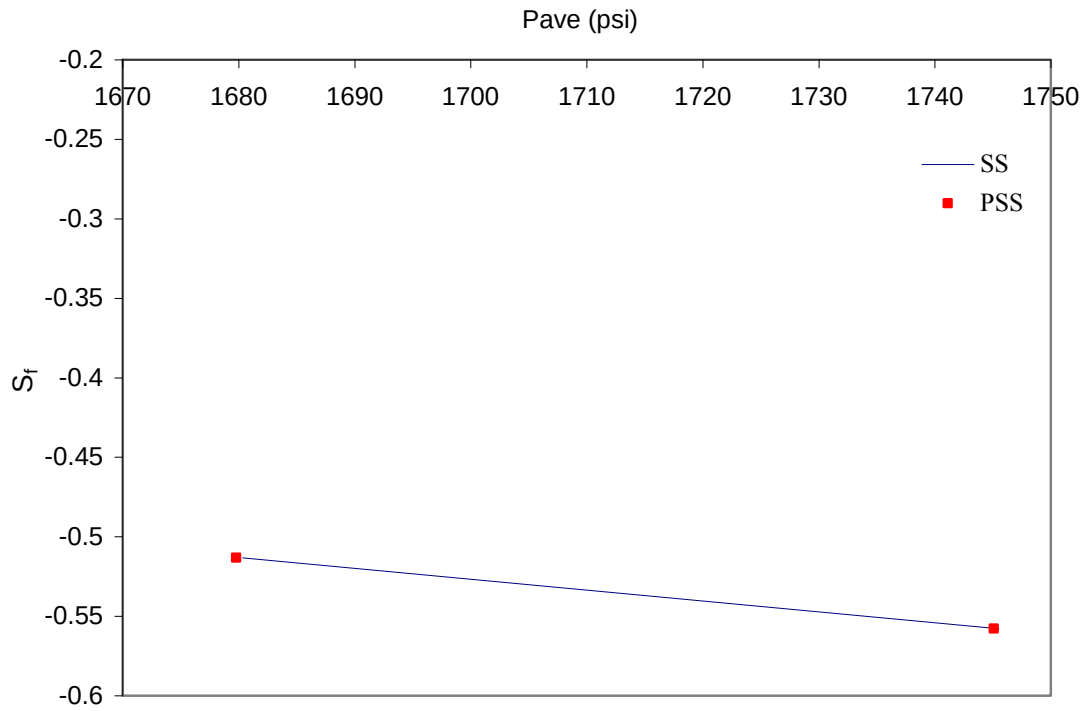

Figure 3.74: Comparing the flow skins calculated using PSS and SS HW in house simulators and EOH for HW1 Table3.11.

FLOW AROUND DEVIATED WELLS

4.1 INTRODUCTION

In the last two decades, drilling horizontal (HWs) and deviated (DWs) wells has become a common practice around the world. The major purpose of drilling such wells is to achieve greater wellbore exposure to the reservoir, which results in improving the well productivity.

Drilling a HW is more expensive than a vertical well and involves more operational risk. It is well documented that the productivity of HWs is significantly affected by the reservoir anisotropy. These facts imply that drilling highly deviated and deviated wells rather than HWs is more attractive for many practical cases. Moreover, in reality, many wells are not exactly vertical or horizontal wells, and deviate from the vertical and horizontal axis.

Nowadays in the oil industry, many deviated ($30 \le \theta \le 60$), θ being the angle between the wellbore axis and a line normal to the horizontal formation plane, and highly deviated ($60 \le \theta < 90$) wells are drilled to increase wellbore exposure of the reservoir and improve the well productivity. In this study, no distinction will be made between deviated and highly deviated wells and the term deviated wells is used to cover the deviation angles corresponding to both DWs and highly deviated wells (HDWs), i.e. any well with $30 \le \theta < 90$.

Many studies have been devoted to predicting the productivity of DWs for single-phase flow conditions. However, due to the complexity of the flow behaviour around the wellbore, including the impact of anisotropy, the existence of thin layer reservoirs, inertial and multiphase flow issues, the study of flow around DWs is still a subject of interest.

The effect of well deviation for single-phase Darcy flow conditions is generally expressed by the radial flow equation for a vertical well (VW) with a geometric skin.

$$q_{DW} = \frac{2\pi k h \Delta P}{\mu\left(Ln\left(\frac{r_e}{r_w}\right) + S_\theta \right)}, \tag{4.1}$$

where q_{DW} is the deviated well flow rate, ΔP is the pressure drawdown in the reservoir, r_e and r_w are the external and wellbore radius, respectively and S_θ is the deviated well geometric skin.

Cinco-lay et al. (1975) were the first to study the unsteady state flow of slightly incompressible fluid around deviated wells (DWs) in an isotropic, homogeneous reservoir. They developed a formulation, Equation 4.1, for the skin factor of the fully penetrating DWs. The skin factor was obtained analytically by subtracting the dimensionless pressure created by a fully penetrating DW from that created by a fully penetrating VW. It should be noted that this correlation is only applicable to those fully penetrating DWs with an angle less than 75^0 in an isotropic formation:

$$S_\theta = -\left(\frac{\theta_w^{'}}{41}\right)^{2.06} - \left(\frac{\theta_w^{'}}{56}\right)^{1.865} \times \log\left(\frac{h_D}{100}\right), \tag{4.2}$$

where

$$h_D = \frac{h}{r_w}, \tag{4.3}$$

and h, θ_w and r_w are the reservoir thickness, the well deviation angle and the wellbore radius, respectively.

Besson (1990) developed an improved semi-analytical correlation, Equation 4.4, for the geometrical skin factor of a fully penetrating DW in an isotropic formation. The results of a simulator which replicated the flow around DWs and skin factor values for HWs, as proposed by Giger (1985), were used in this analysis.

$$S_\theta = Ln\left(\frac{4r_w}{L}\right) + \frac{h}{L} Ln\left(\frac{\sqrt{Lh}}{4r_w}\right), \tag{4.4}$$

or, in another form

$$S_\theta = Ln\left(\frac{4r_w \times Cos(\theta)}{h}\right) + Cos(\theta) \times Ln\left(\frac{h}{4r_w \times \sqrt{Cos(\theta)}}\right) \tag{4.5}$$

where L is the length of the fully penetrating DW.

He also adopted the common transformation method of replacing h with $h\sqrt{\frac{k_h}{k_v}}$, in his analysis to obtain an expression that accounts for the effect of anisotropy on the DW performance, as follows:

$$S_\theta = Ln\left(\frac{4r_w}{L}\frac{1}{I_{ani}\gamma}\right) + \frac{h}{\gamma L} Ln\left(\frac{\sqrt{Lh}}{4r_w}\frac{2I_{ani}\sqrt{\gamma}}{1+1/\gamma}\right), \tag{4.6}$$

$$I_{ani} = \sqrt{\frac{k_h}{k_v}}, \tag{4.7}$$

$$\gamma = \sqrt{\frac{1}{\alpha^2} + \frac{h^2}{L^2}\left(1 - \frac{1}{\alpha^2}\right)}. \qquad (4.8)$$

In this later exercise, anisotropic formations were not simulated and therefore, later investigations by Chen (1995) and Tehrani & Peden (1992) demonstrated that the adopted transformation is not sufficient to give accurate results for anisotropic reservoirs.

Rogers et al. (1996) proposed another correlation, Equations 4.9-4.11, for the skin of the fully penetrating DWs in anisotropic reservoirs. They used the semi analytical Economides (1996) productivity index model for HWs to account for the effect of well deviation. To express the anisotropy effect, the same transformation as that adopted by Besson (1990) was applied.

$$S_\theta = -1.64 \frac{Sin\theta^{1.77} {h_D}^{0.164}}{I_{ani}^{0.821}}, \quad \text{for } I_{ani} < 1 \qquad (4.9)$$

$$S_\theta = -1.64 \frac{Sin\theta^{5.87} {h_D}^{0.152}}{I_{ani}^{0.964}}, \quad \text{for } I_{ani} \geq 1 \qquad (4.10)$$

where $I_{ani} = \sqrt{\frac{k_h}{k_v}}$. (4.11)

In a sensitivity exercise, which is reported in this Chapter, it was noted that the skin values obtained using Equations 4.9-4.11 were underestimated and significantly different from those predicted by equations proposed by Besson (1990) and Cinco-ley et al. (1975) using the same transformation.

Sul Kyoon Choi et al. (2008) conducted a series of sensitivity studies to evaluate the available analytical correlations for the DWs' productivity calculation. They concluded that these semi-analytical correlations are not appropriate for wells with a deviation angle of more than 75^0. Furthermore, as mentioned above, their validity for anisotropic formations is open to question. They are also not appropriate when used for partially penetrating DWs.

For gas condensate systems, when the pressure falls below dew point, condensate drops out around the wellbore, which reduces well productivity. The flow behaviour around such systems is even more complex because of phase change and the combined effects of inertia (a reduction of relative permeability (k_r) due to an increase in velocity) and coupling (an increase in k_r due to a reduction in IFT and or increase in velocity). Therefore, in addition to the limitations mentioned above, the application of these

equations for prediction of the productivity of deviated wells in gas condensate reservoirs would be inappropriate.

This study, therefore, aimed to investigate the well performance of DWs (both partially and fully penetrating) in gas and gas condensate reservoirs. A comprehensive sensitivity study was conducted to evaluate the impact of pertinent parameters including inertia and coupling on the performance of such wells.

In a systematic approach, first the steady state single-phase flow around DWs was simulated using the Comsol mathematical package, which is based on finite element methods. Then the integrity of this in-house simulator was verified by checking the consistency of its results with those obtained by the ECLIPSE commercial reservoir simulator, using a very fine grid, under the same prevailing flow conditions. The results of the in-house simulator and ECLIPSE with the predicted values using the available formulations in the literature for the productivity of DWs are compared in a separate sensitivity study. This indicates that these equations might not be suitable candidates for the productivity calculation of such wells, especially in anisotropic reservoirs. Finally, the proposed formulations for calculation of mechanical and single-phase non-Darcy flow skins for such well geometries which were developed based on the results of the developed in-house simulators, are presented. Similarly to the approach proposed for HWs in the previous chapter, the skin is converted into an effective wellbore radius, before being applied in the pseudo-pressure calculation of the equivalent open hole system. In the second part of this study, a similar approach is followed for the two-phase flow of gas and condensate.

4.2 SINGLE PHASE DW MODEL: ISOTROPIC FORMATION

At this stage of the study the flow of a single-phase compressible fluid around the wellbore of a deviated well (DW) has been simulated. As mentioned earlier, the objective of this study is to extend the mathematical modelling approach to two-phase flow of gas and condensate.

It should be noticed that the developed single-phase flow simulator has an option to account for the effects of inertia and change in fluid property with pressure. Initially, these effects have been ignored in developing the DW geometric skin, which is independent of flow rate and fluid property. Next flow skin, which accounts for the effects of non-Darcy flow and a change in fluid property with pressure, is developed.

This part of the study consists of two sections. The first section describes the in-house simulator. Next the integrity of the constructed 3-D model is confirmed by comparing some of its results with those of the ECLIPSE simulator for the same prevailing flow conditions.

4.2.1 In-house Mathematical Single Phase DW Model

The aim of the present study is to develop a 3-D in-house simulator that can be used to create a large bank of data covering the impact of pertinent parameters on the productivity of many DWs (either partially or fully penetrating) with different lengths, angles, and wellbore radii, drilled in a formation with different dimensions and thicknesses.

The 3-D system considered in this study consists of a DW with radius of R_w and length of L in a single layer cubic reservoir, as shown in Figure 4.1. This homogenous porous medium has an absolute permeability k and formation thickness h. The anisotropy effect has also been investigated, as described later in Section 4.3. The length of the formation is assumed to be 1.5 times the DW length. It should be noted that a partial penetration ratio of 1.5 was chosen based on the results of the study of the effect of partial penetration on the HWs productivity and geometric skin, demonstrating that the impact of partial penetration for penetration ratio larger than 1.25 is negligible. Due to the existing symmetry, only a half of the model has been considered.

Governing Equations

The equations employed in this study are similar to those described for the single-phase flow of gas around HWs. These equations are:

1) The continuity equation for a compressible fluid:

$$\nabla.(\rho v) = 0 . \tag{4.12}$$

2) The 3-D form of the Forchheimer equation:

$$\nabla P = \frac{\mu}{k} V + \beta \rho |V| V . \tag{4.13}$$

Combining the continuity and 3-D form of the Forchheimer equation, after some mathematical manipulation, gives:

$$\nabla.\left[2\left[\frac{k}{\mu}\right].\frac{\rho \nabla P}{1+\sqrt{1+4\beta\left(\frac{k}{\mu}\right)^2 |\nabla P|}} \right] = 0 . \tag{4.14}$$

Mathematical Solution Technique

The governing non-linear partial differential equation (PDE), Equation 4.14, is solved using Comsol multi-physic software (Version 4.4, 2007), which uses the finite element method. The main dependent variable in this equation is P (pressure).

The boundary conditions applied to this system are:

1) Infinite conductivity within the deviated wellbore (the pressure gradient in the wellbore is ignored),
2) The pressure at the outer boundary (external radius) is known,
3) The pressure at the inner boundary (wellbore radius) is known.

Due to the large difference between the DW radius and length and dimensions of the reservoir, considerable attempts have been made to generate a consistent mesh file for the constructed 3-D geometry. Similarly to HW models, initially a 2-D geometry was created, benefiting from the symmetry of the system, , which was then extruded to a complete 3-D system. Here, the 3-D system is also divided into two regions, 1) the inner shell, which starts from the wellbore and extends a certain distance (10 times that of the wellbore radius) into the reservoir, and 2) the second region starts from the outer boundary of the first region and ends at the outer dimension of the reservoir. Moreover, the mesh is refined in the inner region in order to improve the accuracy of the results around the wellbore.

As noted in the HWs chapter, the mesh quality plays an important role in the finite element analysis, as it affects the accuracy of the results and also convergence problems, which could occur during the mathematical solution. Here considerable attempts were made to generate a consistent mesh file with very high quality values for the constructed 3-D geometry. All DW models were meshed manually according to the author's basic knowledge of the flow behaviour for the different prevailing conditions. The majority of the elements of each DW in this study have a quality value more than 0.8. Furthermore the minimum mesh quality is higher than 0.6, which ensures the accuracy of the results under different flow conditions. Here, the accuracy of the in-house simulator is also modified, in the case of anisotropic formations, using the quadratic Lagrange function.

4.2.2 ECLIPSE Well Model

In order to confirm the integrity of the in-house single-phase mathematical simulator, similar single-phase DWs with the deviation angles of 45^0, 65^0 and 80^0 were constructed using ECLIPSE 100.

The core properties of Texas Cream with porosity 0.21 and permeability 9.1 mD were used to describe the reservoir in this model. The PVT tables were set up in a similar way to those for the HW model described in Section 3.3.2 of Chapter 3: that is, with single phase gas with specific gravity of 0.7, viscosity of 0.0352 cp and the formation volume factor of 0.0103 Rm^3/Sm^3. The reservoir was 18.75 m in the x and y directions and 15 m in the z direction. The DW length and wellbore radius were 15 and 0.14 m, respectively. The external reservoir pressure values for the cases studied were 75.84, 103.42, 137.89 or 172.37 bar and the controlled bottom hole pressure of the wellbore was 68.9476 bar. The fine grid option was used to capture the abrupt changes in the flow parameters near the wellbore.

Thirty four injection wells were located in the boundary of the reservoir to maintain the reservoir pressure at the drainage boundary constant.

The results of the in-house mathematical simulator were compared with those of similar simulations that were conducted using the ECLIPSE simulator. Figure 4.2 shows the good agreement between the two results. The arithmetic average absolute percentage deviations (AAD %), which is the absolute deviation error divided by a true value was computed to quantify the error, Here the true value is the PR (productivity ratio defined as the ratio of the flow rate of the DW to that of the VW for the same pressure drop) calculated by the in-house simulator. ADD % of the PR values predicted by the ECLIPSE simulator compared to those estimated by the DW simulator, was 1.94 %.

4.3 SINGLE PHASE DW MODELS: ANISOTROPIC FORMATION

In this section, the effect of anisotropy on the performance of DWs is investigated by comparing the in-house simulator results with the corresponding ECLIPSE very fine DW model results. Next the comparison between the results of the in-house simulator and three correlations, which are available in the literature, were made to evaluate the accuracy of these equations and also limitations on the range of their applications. This section also includes a sensitivity study to evaluate the effect of anisotropy on the performance of DWs.

4.3.1 In-House Simulator versus ECLIPSE

In the previous section, the integrity of the mathematical in-house simulator was validated by comparing its results with those obtained using the ECLIPSE simulator for an isotropic formation. Here, the results of the in-house simulator are compared with those of the ECLIPSE DW model for an anisotropic reservoir. It was discussed previously (HW Chapter) that even a fine grid model of the ECLIPSE simulator produces erroneous results for anisotropic horizontal well (HW) models. The error increased gradually as the anisotropy decreased to 0.1 and then it increased sharply for lower anisotropy values. It was also shown that the error was reduced by refining the grid cell in the z direction. The same trend was also observed for the case of the DW model created using the ECLIPSE, as shown in Figure 4.3a. In this figure productivity ratio (PR), defined as the ratio of the flow rate of the DW to that of the VW for the same pressure drop, has been plotted versus the anisotropy ratio, k_v/k_h. The ECLIPSE DW model used in this study, the same in terms of well dimensions and reservoir properties, is as the one that was used in Section 4.2.2. The deviation angle is 45^0. As was discussed for the HW study, when the permeability anisotropy index decreases, a sharp pressure drop develops around the wellbore region in the vertical flow direction. Consequently, a very fine grid in this direction is required to model accurately the pressure distribution around the wellbore.

As can be seen in Figure 4.3a, in the ECLIPSE model, decreasing the anisotropy value does not affect the PR. Chen (1995) demonstrated that with the ECLIPSE simulator, the use of the peacman's equivalent well block radius obtained for the VWs for calculating equivalent well block radius of DWs and HWs, which are not parallel to the grid line, could result in enormous errors. The conclusions of the previous investigations, and such limitations of the ECLIPSE highlighted by a number of researchers, explain the discrepancy between the results of the in-house simulator and the ECLIPSE DW model for the anisotropy values below 0.4. It should be mentioned that the results of the same ECLIPSE DW model were in good agreement with those of the DW in-house simulator for an isotropic formation as shown in Figure 4.2.

4.3.2 In-House Simulator Versus Cinco-Ley (1975), Besson (1990) and Rogers (1996) Equations

As mentioned earlier, three correlations available in the literature are widely used in the petroleum industry to calculate the productivity of DWs. This section is devoted to evaluating the accuracy of these three correlations for different prevailing conditions.

Cinco et al. (1975) were the first to express the effect of the well deviation on productivity of an open-hole vertical well by a negative geometric skin. Their skin correlation (Equation 4.2) was obtained by solving an unsteady state flow of slightly incompressible fluid. As discussed earlier, their correlation is only valid for fully penetrating DWs with a deviation angle less than 75^0 in isotropic reservoir formations. Besson (1990) developed another correlation for skin (Equation 4.4 and 4.5), to cover the whole range of deviation angles between 90^0 and 0^0. They also presented another formulation for anisotropic formations (Equations 4.6-4.8). Rogers (1996) developed another expression to calculate skin due to the deviation angle of such wells in anisotropic reservoir formations (Equations 4.9 and 4.11).

The DW model considered here is the one which was used in the previous section. The length of well, the reservoir dimensions in the X and Y directions and reservoir thickness are 15, 18.75 m, 15 m, respectively. The well deviation angle is 45^0.

The productivity ratio (PR) of the DW to VW (ratio of the flow rates for the same pressure drop) can be calculated using the following equation:

$$PR = \left(\frac{q_{DW}}{q_{VW}} \right) = \frac{1}{1 + S_\theta / Ln(r_e / r_w)} . \qquad (4.15)$$

where S_θ is the skin factor.

Figure 4.3b presents PR calculated by Equation 4.15, using three available skin correlations and those obtained using flow rates estimated by the in-house simulator versus the anisotropy ratio, kv/kh. PR calculated using the expression introduced by Rogers (1996) is always lower than that obtained using Cinco et al. (1975) and Besson (1990) equations, for the whole range of variation of anisotropy values from 1 to 0.01. PRs predicted by Rogers' equation are constant at kv/kh> 0.6, decrease slightly, and then remain almost constant for kv/kh varying between 0.4 and 0.01. The only data point where the difference between the productivity ratio values obtained using Rogers' equation and the in-house simulator is small is at the anisotropy value of 0.6. PRs calculated using Cinco et al. (1975) and Besson (1990) are almost the same for the whole range of anisotropy variations. Based on these two Equations, PR slightly decreases as the anisotropy value decreases. Where the anisotropy values are more than 0.4, they are in relatively good agreement with the in-house simulator. However, based on these results, it can be concluded that these equations are not good candidates to estimate the well productivity of DWs for anisotropic values less than 0.4. It should be noticed that the effect of anisotropy on the DW productivity increases as the deviation

angle increases. Therefore, it is expected that the difference between the results of these two expressions and those of the in-house simulator will increases gradually as the deviation angle increases.

4.4 Geometric skin: Single Phase Darcy Flow

As mentioned previously, the effect of well deviation is generally expressed by the vertical well flow equation with a geometric skin (Equation 4.1).

In this study, the following assumptions have been made to calculate the geometric skin.

1) There is an incompressible single phase flow under steady state conditions.
2) The gravity effect is ignored.
3) The wellbore deviates at different angles between 0^0 and 90^0 in the uniform anisotropic porous formation, $\frac{k_v}{k_h}\langle 1$.
4) The pressure drop inside the well bore is assumed to be negligible.
5) The deviated well is located in the centre of the reservoir model with no significant formation damage.

Isotropic Formation

Figures 4.4 (a & b) and 4.5 show the pressure counter map around deviated ($\theta = 45^0, 80^0$) and horizontal wells, respectively. Comparing these three figures shows that the 3-D flow behaviour around a DW is similar to that around a HW. In Figures 4.4a and 4.5, the pressure counter map is an almost confocal ellipse around the wellbore. However as the deviated angle decreases to 45^0 in Figure 4.4b, the pressure contour map approaches that of a radial VW. That is, the flow pattern around the DW changes from radial to completely elliptical as the deviation well angle increases from 0^0 to 90^0. In the other words, as the angle of the DW increases from 0^0 to 90^0, its well productivity changes from that of a VW to that of a HW with the same well radius and length. Hence, the DW productivity can be related to that of a HW. It should be mentioned that the HW productivity is represented by an equivalent open-hole vertical well representing the effect of the well orientation by a negative geometric skin. Thus, due to the similarity of the flow behaviour around the HWs and DWs, the DW geometric skin can be written by:

$$S_{DW} = f(S_{HW}), \tag{4.16}$$

where, S_{DW} and S_{HW} are the deviated and horizontal geometric skin values respectively. In this approach the DW length, which is similar to that of a HW, is projected to the horizontal XY plane simply by $L_{hw} \times Sin\theta$. It should be noted that in this study, a DW is a HW rotated from the horizontal plane by an angle, θ. Therefore, the key parameters that affect the DWs's productivity are those affecting the HW productivity (i.e. well radius, length and their relative magnitude to the dimensions of drainage area) and the deviation angle (θ).

To look more closely at the flow regime around DWs, the flow region around a DW can be divided into two regions. The first region describes the flow regime close to the DW, with the confocal elliptical pressure counter map. This region is mainly affected by geometrical parameters, such as the DW length, the reservoir thickness, the deviation angle and wellbore radius. However, in the second region, which is not significantly affected by the geometrical parameters, the flow regime is mainly radial. Therefore, Equation 4.1 can be rearranged to take the following form:

$$Q_{DW} = \frac{2\pi kh\Delta P}{\mu\left(Ln\left(\frac{r_e}{r_w + L_{DW} \times Sin\theta} \right) + Ln\left(\frac{r_w + L_{DW} \times Sin\theta}{r_w} \right) + S_\theta \right)}, \tag{4.17}$$

$$Q_{DW} = \frac{2\pi kh\Delta P}{\mu\left(Ln\left(\frac{r_e}{r_w + L_{DW} \times Sin\theta} \right) + Ln\left(\frac{r_w + L_{DW} \times Sin\theta}{r_{eff}} \right) \right)} \tag{4.18}$$

with $r_{eff} = r_w \times e^{-S_\theta}$,

or

$$Q_{DW} = \frac{2\pi kh\Delta P}{\mu(R_1 + R_2)}. \tag{4.19}$$

In Equation 4.18, the first term in the dominator describes the flow resistance in a radial open hole, with inner radius of ($r_w + L_{DW} \times Sin\theta$) and drainage radius, r_e. The second term describes the flow resistance around an equivalent open hole with drainage radius, R_{EOH} = ($r_w + L_{DW} \times Sin\theta$) and inner effective wellbore radius of r_{eff}.

Equation 4.18 can be written as follows:

$$Q_{DW} = \frac{2\pi kh\Delta P}{\mu\left(Ln\left(\frac{r_e}{r_w + L_{DW} \times Sin\theta} \right) + S_{DW} \right)} \tag{4.21}$$

Equation 4.21 is not only more consistent with the physics of the flow but also it gives a more efficient correlation for geometric skin of DWs, which is always positive.

In the case of HWs, $r_w + L_{hw} \times Sin\theta$ reduces to $r_w + L_{hw}$. It should be noticed that the value of the wellbore radius, r_w, is so small compared to that of the HW length, that $r_w + L_{hw}$ can be simplified to L_{hw}. Similarly for DWs, $r_w + L_{DW} \times Sin\theta$ is simplified to $L_{DW} \times Sin\theta$, respectively.

The similarities between the characteristic length of HWs and DWs can also be extended to the geometric skin values of DW and HWs. That is, the deviated geometric skin can be given approximately by:

$$S_{DW} = f\left(S_{HW} \times Sin^a(\theta)\right), \tag{4.22}$$

Considering that the pertinent parameters which affect the DW geometric skin are similar to those affecting the HW geometric skin, it was noted that the following equation provides a very good approximation for the geometric skin of DWs:

$$S_{DW} = S_{HW} \times Sin\ (\theta). \tag{4.24}$$

In other words, Equation 4.24 states that the first term, S_{HW} represent the impact of key pertinent parameters and the effect of deviation angle on the geometric skin is expressed simply by the second term, $Sin(\theta)$.

Figure 4.6 is a plot of the DW geometric skin obtained directly from the results of the in-house simulator versus those obtained by Equation 4.24. The latter values were calculated using the geometric skin of the corresponding HW again estimated directly from the in-house simulator. It should be noted that these S_m values have been calculated using Equation 4.19 and the estimated flow rates by the in-house simulator. The average absolute deviation error for 267 data points is only 1.2%, confirming the consistency of the proposed approach expressed by Equation 4.24. The data points shown in Figure 4.6 cover a wide range of variation of pertinent parameters as shown in Table 4.1. Here, two cores from the laboratory, Texas Cream and Berea, with permeability of 11 and 110 mD, respectively, were used to describe the reservoir rock. The reservoir fluid was the one used for the study of the flow around the HWs in Section 3.6, with density of 87.85 kg/m^3 and viscosity of 0.0131 cp.

Equation 2.24 is also valid for deviation angles of 0^0 (VW) and 90^0 (HW). That is, the zero value for the geometric skin corresponds to DW with a deviation angle of zero, i.e VW. Furthermore, the HW geometric skin is obtained when the deviation angle is 90^0; i.e. a DW is converted to a HW. Another advantage of this equation is its simplicity. That is, using the skin formulation of Equation 4.24, it is easy to compare the productivity of vertical, horizontal and deviated wells.

Anisotropic Formation

One of the most important parameters which affects the productivity of DWs is anisotropy. All geometric skin formulations available in the literature, Cinco-Ley et al. (1974), Besson (1990) and Rogers (1996) were developed for isotropic reservoirs. They have been extended to anisotropic reservoirs by using a coordinate transformation technique. The limitations of these formulations were discussed in Section 4.3.2. It should be noted that a decrease in the vertical to horizontal permeability, the anisotropy index, decreases the performance of DWs. Furthermore, as the deviation angle decreases, i.e. approaching VW, the importance of this effect on the DW performance decreases gradually, i.e in the case of a VW, anisotropy does not affect the resultant of the 1-D radial flow pattern. In other words, the performance of DWs in anisotropic reservoirs is greatly controlled by the deviation angle. Figure 4.7a shows the impact of anisotropy on the productivity ratio for two DWs with deviation angles of 45^0 and 80^0. Here, the DW model with the deviation angle of 45^0 is the one used in the Section 4.4.1, where these results were compared with those of ECLIPSE. The only difference between the DW models with an angle 80^0 and 45^0 is the deviation angle. The performance of the DW with the higher deviation angle of 80^0 is better than that with a 45^0 deviation angle for the isotropic formation, kv/kh=1. As anisotropy is decreased, PR reduces for both DW models. However, the trend is very steep for the DW with the higher deviation angle, 80^0. This results in a better performance for the DW with the lower angle 45^0, at kv/kh <0.6.

As explained earlier, the proposed formulation for the calculation of the DW geometric skin, Equation 4.24, consists of only two components. The first term is the HW geometric skin and the second term, which transforms this value to that of the DW geometric skin, is Sin(θ). In this equation, the effect of anisotropy can be taken into account by transforming the anisotropic formation into an equivalent isotropic case. According to Muskat's transformation, the reservoir thickness should be changed from h to $h\sqrt{\frac{k_h}{k_v}}$, as shown in Figure 4.7b. Therefore, the deviation angle in the equivalent isotropic reservoir can be given by:

$$\tan\left(\theta^{'}\right)=\left(\frac{k_v}{k_h}\right)^{0.5}\times\tan\left(\theta\right)\Rightarrow\theta^{'}=Arc\tan\left(\left(\frac{k_v}{k_h}\right)^{0.5}\times\tan\left(\theta\right)\right) \tag{4.25}$$

As discussed extensively in the study of the flow around HWs, the above transformation is only valid for anisotropy values above 0.4. That is, it was shown that

the contrast of the geometric skin calculated using the in-house simulator and the corresponding values obtained by the equations (Joshi (1985) and Joshi-Economides (1996)) using this transformation increases for lower anisotropy values. The same observation was noted for the DWs with the equivalent deviation angle calculated by Equation 4.25.

Figure 4.8 shows that the geometric skin values predicted by the in-house simulator and Equations 4.24 and 4.25 are in good agreement for anisotropy values more than 0.1. The AAD is only 1.3% for 480 data points (Table 4.1). However, as can be seen in Figure 4.9, the transformation of the deviated angles using Equation 4.25 does not result in a good approximation of the DW performance for anisotropy values lower than 0.1. To improve this transformation Equation 4.25 was rewritten as follows:

$$\theta' = Arc\tan\left(\left(\frac{k_v}{k_h}\right)^a \times \tan(\theta)\right), \tag{4.26}$$

where a is a constant.

Analysis of a large number of cases showed that a should be 0.25. Thus Equation 4.25 can be written as follows:

$$\theta' = Arc\tan\left(\left(\frac{k_v}{k_h}\right)^{0.25} \times \tan(\theta)\right). \tag{4.27}$$

Figures 4.10, 4.11 and 4.12 show that the results of the in-house simulator are in good agreement with those obtained using Equations 4.24 and 4.27: for more than 800 data points, AAD% is only 2% (Table 4.1), , which confirms the integrity of the proposed geometric skin correlation.

Comparing the data in Figure 4.10 with those in Figure 4.8 (with a=0.25) demonstrates that changing the constant a does not have any effect on the DW geometric skin for anisotropy values of above 0.4.

For the extreme case when anisotropy is zero, the flow to the wellbore is purely in the horizontal direction (Figure 4.13), and the above set of equations (Equations 4.27, 4.24 and 4.19) correctly predicts a zero geometric skin, i.e. flow is similar to that of a vertical well.

On the other hand, the productivity of a fully penetrating DW in a reservoir with zero vertical permeability can be analytically given by a VW equation as follows:

$$Q_{DW} = \frac{2\pi kL \times Cos(\theta)\Delta P}{\mu\left(Ln\left(\frac{r_e}{r_w}\right)\right)}, \tag{4.28}$$

For the fully penetrating DWs, it can be written:

$$h = L \times Cos(\theta), \tag{4.29}$$

Substitution of the above equation into Equation 4.28 gives:

$$Q_{DW} = \frac{2\pi k h \Delta P}{\mu\left(\ln\left(\frac{r_e}{r_w}\right)\right)}. \tag{4.30}$$

Therefore, from both Equations 4.30 and 4.24, the geometric skin is zero, which confirms the accuracy of the results even for the extremely highly anisotropic reservoirs.

It should be noted that when the DW penetrates the reservoir partially, the results of the proposed approach could be overestimated for extreme case of k_v=0, if the total formation thickness is used. That is, in this case, as vertical permeability is zero and the flow pattern is horizontal, the projected DW is converted to a partially VW with zero skin, which is incorrect. However, if instead of the total formation thickness, the projected length of DW, i.e. $L \times Cos(\theta)$, is used for the VW flow calculation, the result is correct. In this case, the effect of flow convergence, due to limited entry, is negligible, as the flow is only horizontal. Therefore, reducing the formation thickness to the projected length of the DW is valid.

4.5 SINGLE PHASE NON-DARCY FLOW

According to Darcy's law, Equation 4.31, the pressure drop inside a porous medium is a linear function of velocity.

$$V = -\frac{k}{\mu}\nabla P. \tag{4.31}$$

However, this linear function is not valid for high volumetric flow rates. Forchheimer (1914) added a quadratic term to this flow equation to express the nonlinear part of the flow as given by:

$$-\nabla P = \frac{\mu}{k}V + \rho\beta|v|v, \tag{4.32}$$

From Equation 4.32, the inertial effect could be defined by a relative permeability term, in the Darcy equation, as follows:

$$k_r = \frac{1}{1+R_e} \Rightarrow -\nabla P = \frac{\mu}{k k_r}V, \tag{4.33}$$

where R_e is Reynolds number and given by:

$$R_e = \frac{\rho |V| k\beta}{\mu}. \tag{4.34}$$

As discussed in the previous section, the flow of a DW can be defined by the flow equation of a VW with a skin (Equation 4.1). In the case of non-Darcy flow. the total skin is a summation of mechanical and flow skins. It should be noted that damaged skin has not been considered in this study. Therefore, Equation 4.1 can be rewritten as follows:

$$m = \frac{2\pi kh\Delta\psi}{Ln\left(\frac{r_e}{r_w}\right) + S_t}, \tag{4.35}$$

where ψ is the pseudo pressure and S_t is the total skin effect that can be expressed mathematically as follows:

$$S_t = S_\theta + S_f. \tag{4.36}$$

In this equation, S_θ and S_f are the mechanical and flow skins, respectively. Here, the flow skin S_f represents the effect of inertia on the productivity of DWs. It should be noticed that S_f, like S_f for the HWs, depends on the fluid properties and flow rates in addition to geometrical parameters. As ψ and S_f are both functions of the volumetric flow rate and fluid properties, obtaining S_f is not a straight forward task. After conducting a comprehensive sensitivity study it was noted that similarly to the flow around HWs, the concept of the effective wellbore radius is the more appropriate method to evaluate the flow skin. Hence, the concept of effective wellbore radius is extended here to the DWs using Equation 4.37:

$$r_w^{'} = r_w \times e^{-S_t}, \tag{4.37}$$

where $r_w^{'}$ is the effective well bore radius, and S_t is the total skin factor.

Rearranging Equation 4.35 using the effective wellbore radius gives:

$$m = \frac{2\pi kh\Delta\psi}{Ln\left(\frac{r_e}{r_w^{'}}\right)}. \tag{4.38}$$

4.5.1 Effective Well Bore Radius Calculation by In-House Simulator

The 1-D open hole simulator developed previously for the study of flow around the HWs has been used to evaluate the effective wellbore radius of an equivalent open hole.

In the 1-D in-house simulator, similarly to in the 3-D in-house simulators, the flow is steady state under the constant pressure boundary conditions at both the external and wellbore radius. The external radius of the 1-D VW in-house simulator is that of the 3-D DW model.

As noted earlier, the flow skin and pseudo pressure calculation are both functions of fluid properties and flow rates. Consequently, the in-house simulator follows an iterative procedure to estimate $r_w^{'}$. The details of this procedure have been explained in the HW Chapter, Section 3.7.

The pertinent parameters, such as geometrical parameters (the DW length, wellbore radius, reservoir thickness and the deviation angle) are those used for developing the geometric skin in Section 4.4, Table 4.1. Velocities were varied from 100 to 11000 m/day, to generate a large data bank required to develop a general flow skin correlation. Two cores from the laboratory, Texas Cream and Berea cores, were used to describe the reservoir rock. The rock properties of these two cores are listed in Table 4.2. The reservoir fluid properties were those used for developing the geometric skin correlation in Section 4.4. Figure 4.14, shows a good agreement between the results of the equivalent open hole in-house simulator (EOH) with $r_w^{'}$, calculated by Equations 4.37 and 4.38, and those of the HW 3-D in-house simulator. AAD% for 1350 data points is 0.1. These $r_w^{'}$ values are then converted to S_f using Equation 4.37, to develop a skin formulation as described in the next section.

4.5.2 Flow Skin Correlation

As noted earlier, in Section 4.5, the author benefited from the similarity of the Darcy flow behaviour around DWs with that around HWs. Here, it is proposed to extend the same approach adopted for modelling the flow around DWs in the case of Darcy flow to that in the case of non-Darcy flow. Figures 4.15 and 4.16 show the isobar counter maps around a DW with an angle 45^0 and a HW for the Darcy and non-Darcy flow cases, respectively. The fluid and reservoir properties for both well models are the same. It should be noted that a HW can be defined as a DW with a deviation angle of 90^0. It is clear that for the non-Darcy flow case, as the flow approaches to the wellbore, the velocity is increased. This results in an extra pressure drop in this region compared to the case of Darcy flow. Therefore, the isobar counters for the non-Darcy flow are closer to each other than those for the Darcy flow. Based on Equation 4.33, inertia affects the single-phase gas relative permeability (k_{rg}). Figure 4.17 shows the variation of this k_{rg}

for both horizontal and deviated wells. It is noted that k_{rg} is less than 1 near the well bore and it reaches 1 far from the wellbore for both the HWs (Figure 4.17a) and the DWs (Figure 4.17b).

Figure 4.18 shows the variation of the flow skin versus the deviation angle, θ. Here, the reservoir thickness and the DW lengths are both 15 m. The pressure drop across the flow models is 200 psi for the same drainage area. It seems that as the deviation angle, θ, increases from 45^0 to 75^0, the flow skin increases gradually. This is mainly due to the fact that flow rate increases as the deviation angle increases. Then it reaches a plateau as the highly deviated well is converted to a HW.

These results suggest that the pertinent parameters of the flow skin of the DWs are the same as those of the HWs. These parameters are the well length, wellbore radius, reservoir thickness and velocity (Reynolds number). Further data analysis showed that the same relationship reported between the geometric skin of DWs and HWs can be extended to their flow skins. That is, the DW flow skin can be written as follows:

$$S_{f_{DW}} = S_{f_{HW}} \times Sin^{\alpha}(\theta), \tag{4.39}$$

where $S_{f_{HW}}$ is the HW flow skin, which can be calculated using the proposed formulation (Equation 4.40) for calculation of effective wellbore radius of the equivalent open hole system in the HWs study in Chapter 3. It should be noted that $r_w^{'}$ and total (mechanical plus flow) skin are related by Equation 4.37. After calculation of S_t, S_m is deducted from S_t to obtain S_f required in Equation 4.39.

$$[\, r_w^{'} = \frac{r_w \times e^{-Sm}}{1 + a \times \left(\frac{\mathrm{Re} \times h_D}{L_D} \right)^b} \,]_{\mathrm{HW}}. \tag{4.40}$$

with $a = 0.04$ and $b = 0.6$.

A closer look at the data revealed that α in Equation 4.39 is equal to 1.0 for all the deviation angles.

It is noted that, based on Equation 4.39, to obtain the flow skin of a DW, first the flow skin of a HW at the same flow conditions (the same well length, wellbore radius, pressure drop, and reservoir characteristics) should be calculated. As discussed in the previous Chapter, the proposed HW flow skin equation (Equation 4.40) requires an iterative procedure as follows:

1) First, the flow skin is assumed to be zero and the effective wellbore radius is estimated as follows:

$$r_w^{'} = r_w \times e^{-Sm}. \tag{4.41}$$

2) Based on the effective wellbore radius, the pressure profile and flow rate are calculated. It should be noted that the pseudo pressure calculation is a function of the velocity; therefore an iterative procedure is required to estimate the pressure profile and mass flow rate.
3) Using Equation 4.40, a new effective wellbore radius is estimated, and then the flow skin is calculated using Equation 4.37.
4) If the difference between S_f calculated with the one calculated previous step is not negligible, the calculation is repeated from step 2, otherwise the calculated effective well bore radius and mass flow rate are considered as the correct answers, representing flow performance of a HW. The calculated flow skin of the HW is then converted to that of a DW using Equation 4.39. Finally, the DW effective radius is then calculated using Equation 4.37.
5) Based on the effective wellbore radius, the pressure profile and flow rate is calculated.

4.5.3 Verification

Figure 4.19 shows the calculated mass flow rate obtained using Equation 4.39 and the iterative procedure described in the previous section versus the corresponding values obtained using the DW 3-D in-house simulator. The close agreement between these two mass flow rates confirms the integrity of the proposed formulation and approach. In this study AAD% average absolute deviation error for 100 data point is only 1%.

4.5.4 Application of Flow Skin

Figure 4.20 shows the productivity ratio (PR) of a DW to a VW at different deviation angles versus velocity, which is calculated at the DW surface assuming uniform flow along the DW surface. In order to obtain higher velocity, the wellbore pressure was 1000 psi and pressure at the external boundary was 4200 psi. The reservoir thickness was 15 m and equal to the DW length. The Berea and Texas Cream core properties were used to describe the reservoir rock for Figure 4.20a and 4.20b, respectively. It is noted that for the DW with a 45^0 angle, PR is less than 1 at velocities above 500 m/day. At low velocities, Darcy flow regime, the well deviation results in an improved performance. This is more pronounced for larger well deviation angles. However, an increase in the velocity decreases the performance of the DW, especially for smaller well deviation angles. This indicates that when the deviated length is equal to the reservoir thickness, the negative impact of inertia on the DW performance is more

pronounced than that on the VW performance. This can be explained by comparing pressure profile distribution around the DW with 45^0 deviation angle and around the HW (Figures 4.15 and 4.16). It is noted that as the deviation angle increases, the isobar counters around the wellbore become closer, which results in decreasing the affected area by the high velocity inertial effect, thus reducing its negative impact. It was demonstrated earlier in the HW study that the flow convergence towards the wellbore caused an extra pressure drop around the tip of the wellbore, resulting in decreased productivity for HWs. The same conclusion can be made here for DWs. It is noted that the magnitude of this pressure loss decreases as the deviation angle increases. That is, as the distance between the tip of wellbore and the reservoir boundary decreases, the flow pattern is more linear around the tip of the wellbore, resulting in an improved DW productivity. This observation has also been reported in the study of partial penetration HWs. The same observation was noticed when Texas cream core properties were used for the reservoir model description (Figure 4.20 b).

Figure 4.21 shows a comparison of the calculated PR using Berea or Texas cream properties. It seems that the adverse effect of inertia on the DW productivity became more pronounced compared to that on the VW productivity, when the Texas cream core properties were used for reservoir descriptions. It is clear that the contribution of the inertial effect depends on the term (βk), which is higher for Texas Cream core (Figure 4.21).

Figure 4.22 shows that the effect of the wellbore radius on PR is negligible. When the DW length is equal to the reservoir thickness, PR decreases with velocity (Figure 4.22 a) to almost the same extent at three different wellbore radii. That is, for each of these three cases the inertial effect is more pronounced for DW compared to VW, to the same extent. It is interesting to note that as the DW length increases, the observed trend changes and becomes similar to that noted for the HW Figure 4.22 b.

Figure 4.23 compares PR of Non Darcy flow with Darcy flow cases, at different deviation angles. Here, the pressure drop across the reservoir models for all DWs, with different deviation angles, and the VW was 3200 psi. The velocity at the DW surface varied from 10047 to 11511 md^{-1}. As expected, at the lower DW length, Figure 4.23 a, the inertial effect is more pronounced for DWs compared to VWs. That is, the PR curve of Darcy flow is always above that of non Darcy flow. However, an increase in the DW length changes this trend, as confirmed in Figure 4.23 b. That is, in the latter case, the performance of DWs is better for the case of non Darcy flow, similarly to what was

observed for HWs. This is due to the fact that the increase in the surface of the wellbore significantly reduces the negative impact of inertia on DW performance.

The effect of the reservoir thickness was investigated by comparing the PR of a DW with the deviated length of 45 m versus velocity at two reservoir thicknesses. As can be seen in Figure 4.24, increasing the velocity decreases the PR. This is similar to the observation for the DW in the reservoir model with thickness of 15 m, reported above. It is clear that PR is always higher for the low reservoir thickness, 30 m here, because of higher L/h, i.e. greater reservoir exposure. It is worth citing that for the case of the reservoir thickness 45 m, because the DW length is equal to the reservoir thickness, the PR values are close to one, i.e. deviation has minimal impact on PR. The same observation was made for DWs with the length equal to the reservoir thickness of 15 m.

The effect of the reservoir thickness was investigated by comparing the PR of a DW versus velocity at two reservoir thicknesses, Figure 4.25. Here, DW length is equal to the reservoir thickness. As noted in this Figure, increasing the velocity decreases the PR. It seems that the impact of inertia on DW productivity compared to that on VW is more pronounced for thicker reservoirs.

4.6 GAS CONDENSATE FLOW

As mentioned earlier, the aim was to extend the single-phase mathematical modelling approach to study two-phase flow of gas and condensate around DWs. To achieve this objective, an in-house simulator was developed, simulating a steady state flow of gas and condensate around a single DW. In the in-house simulator, the generalised relative permeability correlation (Jamiolahmady et al. 2009) was employed, which accounts for the combined effects of positive coupling and negative inertia on k_r. To confirm the integrity of the structure of the in-house simulator, some of the simulations conducted using the in-house simulator were also performed using the fine grid option of the ECLIPSE 300 commercial software. Next, an extensive bank of data was generated using the in-house simulator. This data bank was then used to propose a general method for modelling the two-phase flow of gas and condensate around DWs, using an equivalent open hole approach.

4.6.1 In-House 3-D Two-Phase Deviated Well Model

The 3-D geometry which is used to simulate the gas condensate flow around a DW is the same as that for the single phase flow case (Figure 4.1). However, the governing equations are those describing two-phase flow of gas and condensate.

Governing Equations

As mentioned earlier, the two equations describing the two-phase flow of gas and condensate around a DW are similar to those described for gas condensate flow around a HW:

The continuity equation for gas and condensate flow at steady state conditions

$$\nabla.\left((\rho v)_g + (\rho v)_c\right) = 0, \tag{4.42}$$

where g and c represent the gas and condensate phases, respectively.

1) The flow equation for each phase:

$$v_i = \frac{k k_{ri}}{\mu_i} \nabla P \text{ . i=g,c} \tag{4.43}$$

Combining the continuity and flow equations, after some mathematical manipulation, gives:

$$\nabla.\left(\left\{\left[\frac{\rho k_r}{\mu}\right]_g + \left[\frac{\rho k_r}{\mu}\right]_c\right\} k \nabla P\right) = 0 . \tag{4.44}$$

As the fluids flow through the porous media, there is a mass transfer between the two phases but the total fluid composition (z_j) is constant (Fevang &Whitson (1996)), as expressed by the following equation.

$$z_j = \frac{\rho_g y_j GTR + \rho_c x_j (1 - GTR)}{\rho_g GTR + \rho_c (1 - GTR)} = cons., \tag{4.45}$$

where GTR is the total gas fractional flow. A binary mixture of C1 (methane) and n-C4 (normal butane) has been used as the gas-condensate fluid model. The values of composition, density (ρ□□), viscosity (μ□) and interfacial tension (IFT) of C1-nC4 binary gas condensate model mixture as a function of pressure are those measured in the hydrocarbon carbon recovery group's laboratory as well as in literature data (Sage et. al, 1940; SUPERTRAPP User's Guide, 1992; Weinaug and Katz, 1943) at 311 K over a wide pressure range, which were implemented in the model in a tabular form.

Mathematical Solution Technique

Similarly to the single-phase modelling approach, the governing non-linear partial differential equation (PDE), Equation 4.44, and the auxiliary equation, Equation 4.45, are solved using Comsol multi-physic software (Version 3.5, 2008), which uses the

finite element method. The main dependent variable in this equation is P (pressure) but the equations are solved for both pressure and GTR.

The boundary conditions applied to this system are:

1) The pressure at the outer boundary (external radius) is known.
2) The pressure at the inner boundary (wellbore radius) is known.
3) The pressure gradient in the wellbore has been ignored, i.e. infinite conductivity for the flow through DW wellbore.

3) As noted earlier, the total composition is constant, Equation 4.45. Therefore, either the total composition fluid is given or GTR at a particular point in the drainage area, normally at the wellbore, should be known and used in Equation 4.45 to calculate the total composition.

4.6.2 ECLIPSE 3-D Two-Phase Deviated Well Model

The accuracy of the two-phase mathematical in-house simulator was confirmed by comparing its results with those of ECLIPSE300 under the same prevailing flow conditions.

The reservoir model in this exercise has the core properties of Texas Cream with porosity 0.21 and permeability 9.1 mD. The reservoir fluid is a binary mixture of C1 (methane) and n-C4 (normal butane) described in the previous section. The reservoir is 38 m in the x and y directions and 4 m in the z direction. The length of the DW is 15 m. Many different cases were simulated using both ECLIPSE300 with a fine grid option and the in-house simulator. The fractional flow at average reservoir pressure was the same in both simulators. As the k_r correlations used in these two models (i.e. Comsol and ECLIPSE300 models) are different, the base curve relative permeability has been used to describe the flow around a DW in these simulations.

In ECLIPSE 300, seventy injection wells were placed at the boundary of the reservoir to keep the reservoir pressure at the drainage boundary constant.

Figure 4.26 shows the good agreement between the results of two simulators. The arithmetic average absolute percentage deviation (AAD%) of the predicted mass flow rates values by the ECLIPSE300 simulator compared to those estimated by the DW simulator was 2 %. The wellbore pressure was constant and equal to 1365 psi in these simulations. The only difference between runs 1 and 2 corresponding to each DW was the reservoir pressure, with the corresponding values being 1765 and 1565 psi, respectively.

4.6.3 In-House 1-D Two-Phase Open-Hole Well Model

The 1-D two-phase open-hole in-house simulator is the one, which was developed to simulate the steady state two-phase flow of gas and condensate around a single VW in the HW study, Chapter 3. As noted in the previous chapter, the model features are similar to those of the single-phase flow model, but instead, the governing equations of the two-phase flow of gas and condensate, as described above, are solved.

4.6.4 Effective Wellbore Radius

The total (gas and condensate) mass flow rate of DWs can be calculated using an equivalent open-hole (EOH) vertical well as follows:

$$m^0 = \frac{2\pi kh \int_{Pw}^{Pe} \left(\frac{\rho_l k_{rl}}{\mu_l} + \frac{\rho_g k_{rg}}{\mu_g} \right) dp}{Ln\left(\frac{r_e}{r_w^{'}} \right)}, \qquad (4.46)$$

where $r_w^{'}$ is the effective wellbore radius calculated by Equation 4.37. As noted earlier, S_t, total skin, given by Equation 4.36 is the summation of mechanical and flow skins, neglecting damage skin. S_m depends on the geometrical parameters and anisotropy. S_f is defined as the difference between the effect of two-phase flow behaviour around DW and EOH VW systems. Here, the author intends to introduce an EOH system which produces the same flow performance, gas and condensate production rate, as that of a DW system. An approach similar to that used for the single-phase flow system described in Section 4.5.1 has been followed. That is, the mass flow rates of the 1-D open-hole simulator and that of the 3-D in-house simulators are matched iteratively by varying $r_w^{'}$. $r_w^{'}$ is then converted to S_f using Equation 4.37.

Using the in-house simulators, a large bank of data was generated to obtain two phase flow skin for different flow conditions. For this part of study, the Texas Cream core properties described the reservoir rock. The fluid was a binary mixture of C1 (methane) and n-C4 (normal butane). The reservoir and wellbore pressures were varied between 1800 psi to 1750 psi and 700 psi to 400 psi, respectively. GTR was changed from 0.846 to 0.999.

In the previous section, the non-Darcy and Darcy flow study, it was demonstrated that the mechanical and single-phase flow skin of a DW could be estimated by using a simple relation between the corresponding skin values calculated for a HW and the

deviation angle (Equations 4.24 and 4.39). Here a similar formulation is proposed for the two-phase flow skin:

$$S_{f\,DW} = S_{f\,HW} \times Sin^{\alpha}(\theta), \tag{4.49}$$

The results of the data analysis showed that the constant α in Equation 4.49 should be 1. In other words, the transformation of the two-phase flow skin formulation of HWs to that of DWs is similar to that for the single-phase flow and geometric skin cases.

Figure 4.27 shows the mass flow rate calculated using the two-phase flow skin correlation based on the effective radius concept (Equation 4.49) versus the corresponding values obtained by using the in-house simulator. It is noted that the results of the DW matches exactly those of EOH, using the two-phase flow skin correlation, Equation 4.49. AAD% for 40 data points is 1%, which confirms the accuracy of the proposed formulation and method.

4.6.5 Application of Effective Wellbore Radius

As mentioned before, the impact of inclination can be quantified by introducing a skin factor. The geometric skin value is negative, as the performance of a DW is better than that of a VW. In the case of single-phase non-Darcy flow, the flow skin expresses the difference between the inertial effect on the DW and EOH VW systems, based on the geometric skin. It should be mentioned that this flow skin is always positive, that is, the impact of inertia is always more pronounced for a DW compared to an EOH VW system. Here, the velocity around the EOH is decreased significantly as the surface is increasing significantly compared to DWs. The gas condensate flow behaviour around DWs is more complex because the relative permeability of gas and condensate is a function of velocity as well as IFT. That is, inertia decreases the relative permeability, whilst coupling increases it.

Figure 4.28 shows the variation of the two-phase skin versus the deviation angle at three different gas fractional flows at the wellbore (GTR_{well}). The formation thickness, the wellbore length and the wellbore radius are 15, 15, and 0.07 m, respectively. The rock properties were those of the Texas Cream core, Table 4.2. The reservoir pressure is constant for all different cases considered here while the wellbore pressure is varied to obtain different GTR_{well} and velocity. It is noted that the absolute value of the two-phase flow skin decreases as the inclination angle decreases. For the same pressure drop, as the deviation angle decreases the DW flow rate decreases, which at lower GTR_{well} values, in turn, could also result in reducing the positive impact of coupling for the DW. At higher GTR_{well} values, the impact of inertia on the relative permeability is more

pronounced, i.e. increasing GTR decreases the absolute value of the-two phase flow skin.

Figures 4.29 to 4.31 show PR, ratio of flow rates for the given pressure drop of a deviated to a vertical well versus deviation angle. In this exercise, the DW and VW had the same L, r_w ,with k_r varying due to coupling and inertia. For the set of simulation runs shown in these figures, the pressure drop across the reservoir and wellbore pressure were either 50 or 1800 psi. The DWs length and reservoir thickness were both 15 m, and the Texas Cream core properties (Table 4.2) were used unless otherwise stated.

Figure 4.29 compares PR versus the deviation angle at three different GTR_w. It is noted, as expected, that the PR increases by increasing the deviation angle. Decreasing GTR_w, improves the PR for all DWs considerably. This is mainly due to the more pronounced impact of positive coupling in DWs compared to that in VWs.

Figure 4.30 presents the effect of the wellbore radius on PR versus the deviation angle. Here, GTR_w was 0.7. As can be seen the impact of the wellbore radius on the DW performance is minimal. The small increase in PR as r_w increases is due to the higher surface flow area in the HW model at this low GTR value.

The impact of the reservoir thickness on the PR is shown in Figure 4.31. Here again, GTR_w was 0.7. The same conclusion that has been drawn for the HWs study can be made here: that is, the performance of DWs is better for thin reservoirs.

Figure 4.32 examines the effects of the rock properties on the PR versus the deviation angle. Two different rocks, Berea and Texas Cream, were used here. The rock properties of theses two cores are listed in Table 4.2. The wellbore pressure and the differential pressure across the reservoir models were 1565 and 200 psi. The velocities for the DW models with Texas Cream and Berea core properties were varied from 17, 156 to 134, 1400 md^{-1}, respectively. The observed trends for both models are the same, i.e. increasing GTR_w decreases the PR significantly because of dominant impact of inertia for DWs or, in other words, there is a more pronounced coupling effect for VW at lower GTR_w. It should be noted that in these simulations, the DW lengths were equal to the reservoir thickness. The observed trends here are in the opposite direction to those reported for the HWs, where velocity at the HWs surface decreased significantly, resulting on a decrease in the pronounced impact of inertia on the HWs productivity. As will be shown here, Figure 4.36, for the DWs with a length longer than the reservoir thickness, the observed trend is similar to that for HWs .It should be noted that for the same pressure drop, higher velocity in Berea results in a more pronounced effect of inertia in VWs, slightly increasing the PR for this rock compared to that for Texas

Cream. It should be noted that $k\beta$ of Texas Cream is higher than that of Berea, which at same velocity would results in a more pronounced impact of inertia in Texas Cream compared to that in Berea.

Figure 4.33 shows the PR versus the deviation angle at three different Δp of 100, 200 and 400 psi. The wellbore pressure was either 1365 (Figure 4.22 a) or 1450 (Figure 4.22 b) psi. GTR_w was 0.7. The corresponding VW velocity values for the three drawdown pressure of Figure 4.33a, were 6, 11, and 27 $md^{-1.}$, respectively. The corresponding values for the data in Figure 4.33b were 6, 13, and $39md^{-1}$, respectively. It should be noted that increasing the velocity results in an increase of the negative inertial effect on the productivity of VW. That is, the PR increases as the velocity is increased.

Figure 4.34 shows PR versus GTR_w for a DW with 15 m length, at different deviation angles, in the reservoir model with thickness 15 m. The well and reservoir pressures were 1725 and 1775 psi, respectively. The velocity at VW surface varied from 3.6 to 33 md^{-1}. It is noted that, as the deviation angle increases, the PR increases for all GTR_w. Furthermore, the PR remains almost constant when GTR_w varies between 0.7 to 0.85. However, PR decreases at higher GTR_w values (greater than 0.95) where the negative inertial effect is more pronounced for the DW compared to the VW.

The impact of DW length on PR is displayed in Figure 4.35. For this set of data, GTR_w was 0.7. The rate of increase of the PR with increase in the deviation angle is more or less similar for all DW lengths. It is interesting to point out that increasing the DWs length significantly improved the PR. For example, if the DWs length increased from 30 to 60 m, the PR increased considerably, i.e. by a factor of 2. It should be noted that in these simulations, the DW length can be increased until the DW fully penetrates the whole 15 m thickness of the formation.

The PR of a DW with deviation angle of 87^0 versus the DW lengths at different GTR_w is shown in Figure 4.36. In these simulations, the wellbore and differential pressures were 1725 and 40 psi. The velocity of the VW varied from 0.28 to 3.9 m/day. As expected, increasing the DW length significantly improves the performance of the DW. Moreover, the performance of DWs is better at high GTR_w values compared to that for low GTR_w values. This is mainly due to the more pronounced adverse effect of inertia on the productivity of VWs, compared to that of DWs, at higher GTR_w values. It should be noted that, as the DW length increases, the velocity decreases, which in turn decreases the negative impact of inertia on the productivity of DWs compared to that of

VWs. It is also important to point out that as GTR_w approaches 1, the gas fractional flow and flow rate increases significantly due to the high mobility of gas.

A comparison of data in Figures 4.34 and 4.36 demonstrates that the PR strongly depends on the DW lengths. It is noted that the trends of PRs for long and short DWs are in the opposite direction. That is, in the former, an increase in GTR_w has increased the negative impact of inertia on the DW performance more, compared to that of the VW, (PR decreases at higher GTR_w). This results in the latter the velocity of long DWs decreases significantly compared to that of a VW e.g. this results in a decrease in the negative impact of inertia on the DW performance, compared to that of the VW, (PR increases at higher GTR_w).

4.7 SUMMARY AND CONCLUSIONS

A number of in-house simulators were developed to study the well performance of deviated wells (DWs) in gas and gas condensate reservoirs. The integrity of the results of the in-house simulators was confirmed by comparing some of their results with those obtained using ECLIPSE with fine grid for the same prevailing flow conditions.

1. It was confirmed that at low velocities, Darcy flow regime, any well deviation from vertical results in an improved performance, i.e. there is a negative geometric skin.
2. A comprehensive study for some of equations for DWs available in the literature has been conducted and the range of their application has been determined. The results indicated that these equations cannot accurately predict DWs productivity in an anisotropic formation with anisotropy values less than 0.6.
3. It was shown that the DWs geometric skin depends on the same pertinent parameters as those for horizontal wells (HWs), i.e., length of horizontal well, radius of the well, reservoir thickness, and anisotropy. Therefore, an easy to use formulation for geometric skin of DWs was developed, which correlated the HWs geometric skin to that of DWs, using the deviation angle. The integrity of the geometric skin formulation was validated by comparing its results for data points not used in its development.
4. Similarly to that of geometric skin, the single-phase flow skin formulation for DWs was developed, which is related to that for HWs. Based on this formulation, first an effective wellbore radius of an equivalent open-hole system should be estimated for the HW with the same well length. Then, this effective wellbore

radius is converted to the HW flow skin to be included in the proposed formulation to calculate the DW flow skin. This flow skin is then converted to an effective radius to be used in an open-hole well model replicating flow around the corresponding DW. The integrity of the flow skin formulation was validated by comparing its predictions with the corresponding estimated values using the in-house simulator, thereby confirming the integrity of the proposed approach.

5. A comprehensive sensitivity study has been also conducted on the impact of important parameters on PR of DW to (vertical well) VW for single phase. From these results the following conclusions can be made:

6. For the same DW length, as that of a VW (i) an increase in velocity decreases the PR (of the DW to the VW), due to the more pronounced effect of inertia for the DW compared to that for the VW, especially for smaller well deviation angles; (ii) the PR is always higher for low reservoir thickness values: (iii) the negative impact of inertia on DW productivity compared to that on VW productivity is more pronounced for thicker reservoirs, due to the higher production rate.

7. Similarly to the HW findings at higher DW length, the negative impact of inertia is less for DWs compared to that for VW, thus improving the PR, especially at higher velocities.

8. In the case of a two-phase flow of gas and condensate, a similar approach to that for the single-phase non-Darcy flow skin has been followed to develop the two-phase flow skin for the DWs. The integrity of the proposed procedure has been confirmed by comparing its predictions with the corresponding estimated values using the in-house simulator .

9. The results of a comprehensive sensitive study on the impact of parameters on the PR of DWs to VWs for two-phase gas condensate demonstrated that:

10. For the same DW length, as that of the VW (i) as the deviation angle increases, PR increases for all GTR_w (gas fractional flow at the wellbore), due to higher negative geometric skin, (ii) decreasing GTR_w below 0.95 improves the PR because of the more pronounced effect of positive coupling in DWs compared to that in VWs, but the extent of this improvement is almost constant when GTR_w varies between 0.7 to 0.85 (iii) the PR decreases at GTR_w values greater than 0.95, where the negative impact of inertia is more pronounced for a DW compared to that for a VW (iv) the DW performance is better for thinner reservoirs.

11. Similarly to the HW cases, (i) PR strongly depends on the DW lengths: higher L means higher PR, (ii) at higher DW lengths, the negative impact of inertia is less for

DWs compared to that for VWs, improving the PR, especially at higher velocities (iii) wellbore radius has minimal impact on DW performance.

12. At higher GTR_w, the trends of variation of PR for long and short DWs are in opposite directions. That is, in the former, an increase in GTR_w increases the negative impact of inertia on the DW performance more than in the case of a VW, where PR decreases at higher GTR_w. However in the latter, the velocity of long DWs decreases significantly compared to that of a VW, resulting in a decrease in the negative impact of inertia on the DW performance compared to that of VW where the PR increases at higher GTR_w.

References

Besson, J., 22-24 Oct. 1990: Performance of Slanted and Horizontal Wells on Anisotropic Medium, SPE 20965, Presented at Europec 90, The Hague, the Netherlands.

Chen G., Tehrani D.H. and Peden J., 12-15 February 1995: Calculation of Well Productivity in a Reservoir Simulator I, SPE29121, Presented at the 1995 SPE Symposium on Reservoir Simulation in San Antonio, Texas.

Cinco-Lay H., Ramey H. J. Jr. and Miller, F. G. , 28 Sept-1 Oct. 1975: Pseudo Skin Factors for Partially Penetrating Directionally-Drilled Wells, SPE 5589, Presented at the 50th Annual Fall Meeting of the SPE of AIME, Dallas, Texas.

Cinco-Lay H., Ramey H. J. Jr. and Miller F. G., 1975: Unsteady State Pressure Distribution Created by a Directional Drilled Well, p 1392-1400, JPT.

Comsol Multiphysics Reference Manuals http://www.comsol.com, version 3.4, 2008, by COMSOL, Inc.

Economides M.J., Deimbacher F. X., Clement W. B. and Heinmann E. Z. , Dec 1991: Comprehensive Simulation of Horizontal Well Performance, SPE 20717.

Economides M.J., Brand C.W. and Frick, T.P., Dec. 1996: Well Configurations in Anisotropic Reservoirs, SPEFE (Dec. 1996), 257-262. (Also Paper SPE 27980, 1994.)

Fevang Ø. And Whitson C.H., 1996: Modeling Gas-Condensate Well Deliverability, SPE reservoir engineering.

Forchheimer P., 1914: Hydraulik, Chapter15, pp. 116-8, Leipzik and Berlin.

'Gas Condensate Recovery Project', Progress Report, Sep 2008-Feb 2009, Heriot-Watt University, Institute of Petroleum Engineering.

'Gas Condensate Recovery Project', Final Report FTPM/02/2-2, July 2005-2008, Heriot-Watt University, Institute of Petroleum Engineering.

Giger, F., May 1985: Reduction du nombre de puits pm I'tilisation de forages horizontals, Reveue de L'institute Gancais du Petrole, 38.

Jamiolahmady M., Sohrabi M., Ireland S., and Ghahri P., 2009: A Generalized Correlation for Predicting Gas-Condensate Relative Permeability at near the Wellbore Conditions, Journal of Petroleum Science and Engineering.

Joshi S.D., 1991: Horizontal Well Technology, PennWell, Tulsa, Oklahoma.

Rogers, E. and Economides M., Nov. 1996: The Skin due to Slant of Deviated Wells in Permeability- Anisotropic Reservoirs, SPE37068.

Sage B.H, Hick B.L. and Lacey W.N. , 1940: Phase Equilibria in hydrocarbon system-the methane-n-butane systems in the two-phase region, Ind. Eng. Chem. 32, 1058-1092.

SUPERTRAPP (NIST Thermophysical Properties of Hydrocarbon Mixture Database) User‘s Guide by National Institute of Standards and Technology (NIST), NIST Standard Reference Database 4, July 1992, Version 1.0.

Suk Kynoon Choi, Liang-Biao Ouyang, and Wann-Sheng Huang, 21-24 Sep. 2008: A Comprehensive Comparative Study on Analytical PI/PR Correlations, SPE 116580, Presented SPE Annual Technical Conference and Exhibition held in Denver, Colorado, USA.

Tehrani D.H., Chen G. and Peden, J. M., 10-12 December 1995: Effect Absolute Permeability of a Heterogeneous Reservoir for Calculating Well Pressure, Presented at the SPE & UAE University Regional Symposium on Improved Oil Recovery, in Al-Ain, UAE.

Weinage C.F. and Katz D.L., 1943: Surface Tension of Methane-Propane Mixtures, Industrial Engineering Chem. 35(2), 239-246.

Table 4.1: Parameters of deviated well models in this study.

Length of deviated well (DW)	15-720 m	15-720 m
Deviation angle	0-87 ^{0}	0-87 ^{0}
Reservoir thickness	15-45 m	15-45 m
Wellbore radius	0.07-0.21 m	0.07-0.21 m
Anisotropy $\left(\frac{k_v}{k_h}\right)$	0.01-1.0	0.01-1.0

Table 4.2: Basic core properties.

Type core	**Porosity**	**Permeability (mD)**	**Single-phase inertia factor (1/m)**
Texas Cream	0.21	11.1	3.93E+9
Berea	0.185	100	1.08E+8

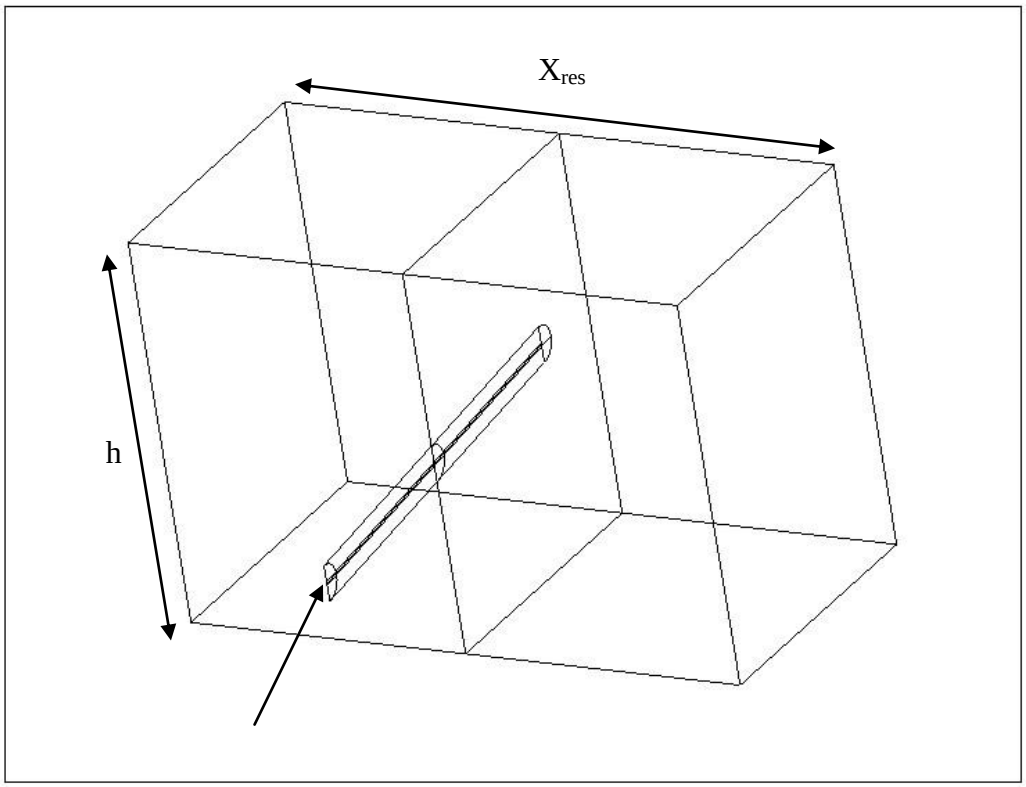

Figure 4.1: A schematic diagram of the deviated well model in this study.

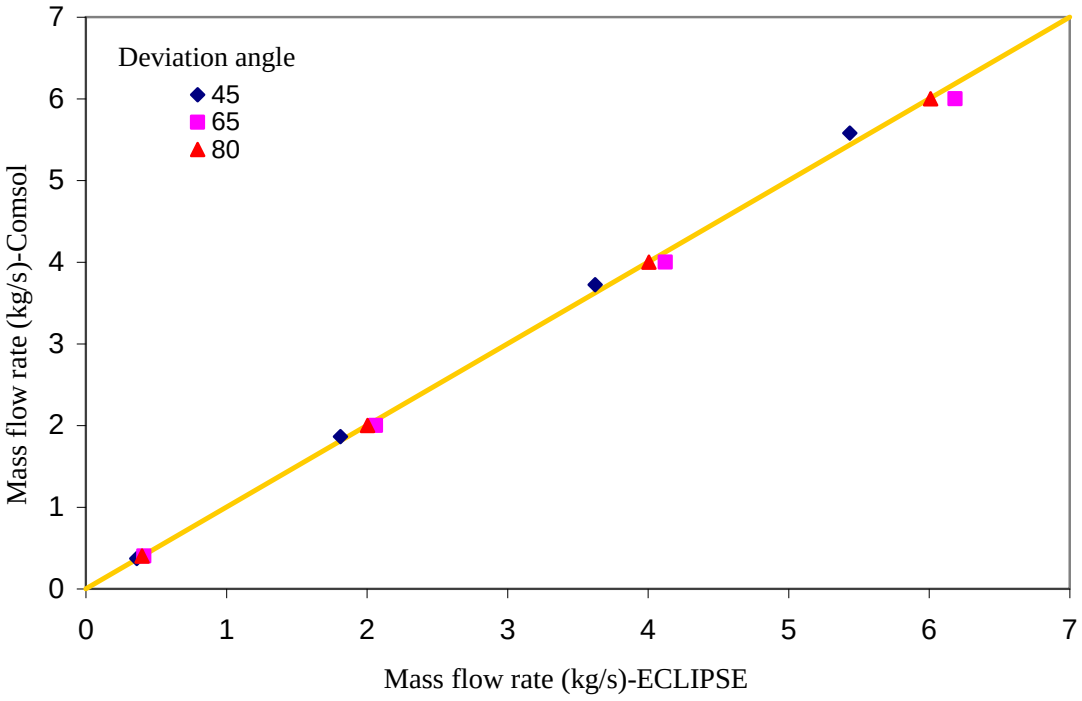

Figure 4.2: Comparison of the results of ECLIPSE single phase deviated well models with deviation angles of 45^0, 65^0, and 80^0 at three different pressure drops with those of the in-house simulator under the same prevailing conditions.

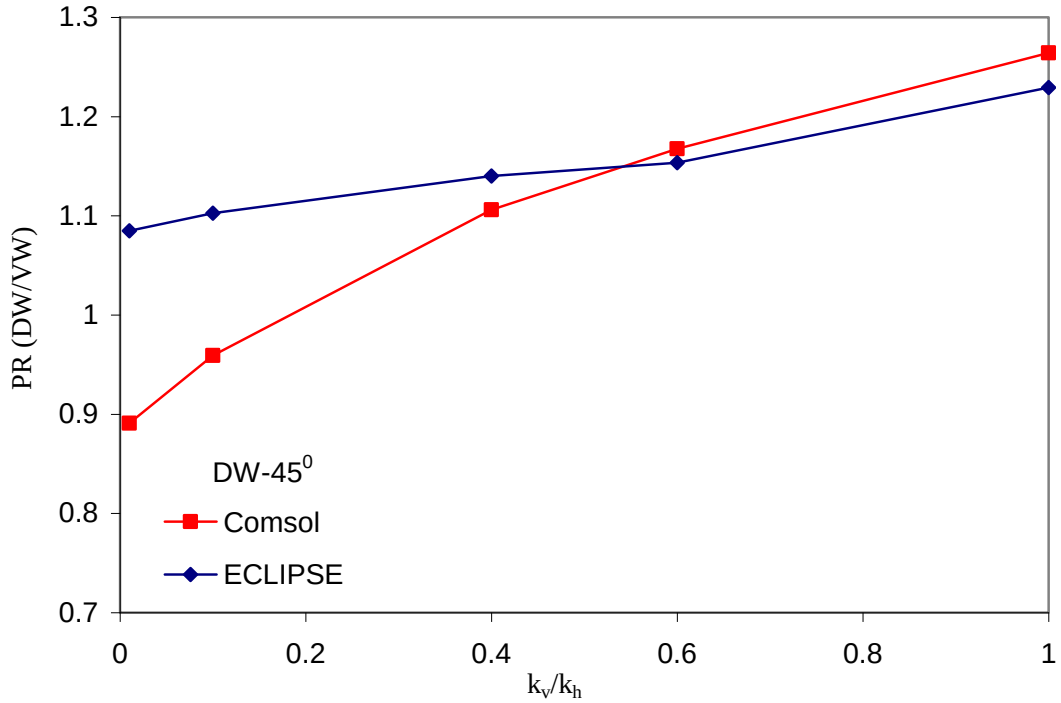

Figure 4.3a: Ratio of deviated to vertical well flow rates, for the same pressure drop, estimated by the in-house and ECLIPSE single deviated well models, 45^0 well deviation angle.

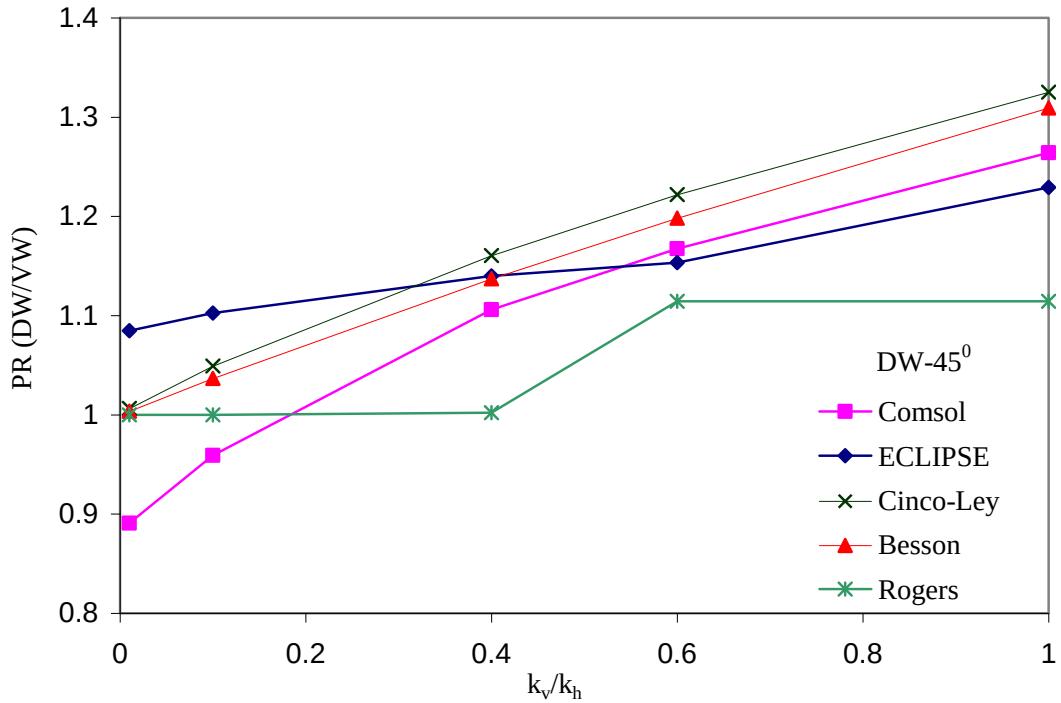

Figure 4.3b: Ratio of deviated to vertical well flow rates, for the same pressure drop, estimated by the in-house simulator (single phase deviated well model) and those obtained by the Cinco et. al, (1975), Besson (1990) and Rogers et. al (1996) correlations versus formation anisotropy, 45^0 well deviation angle.

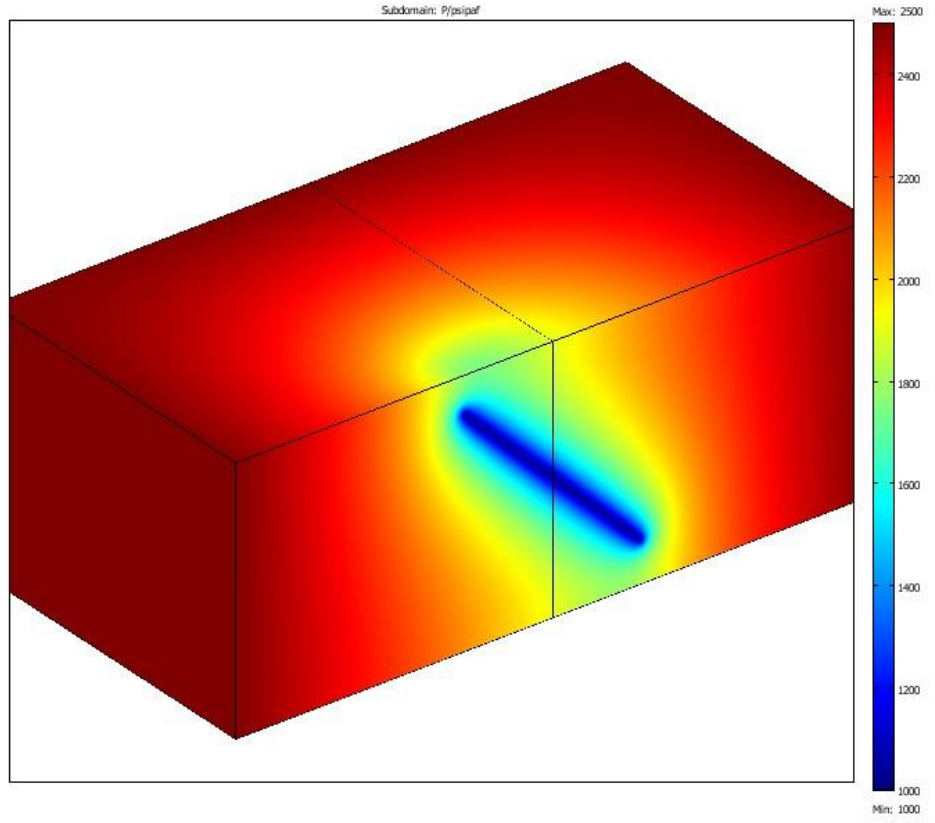

(a)

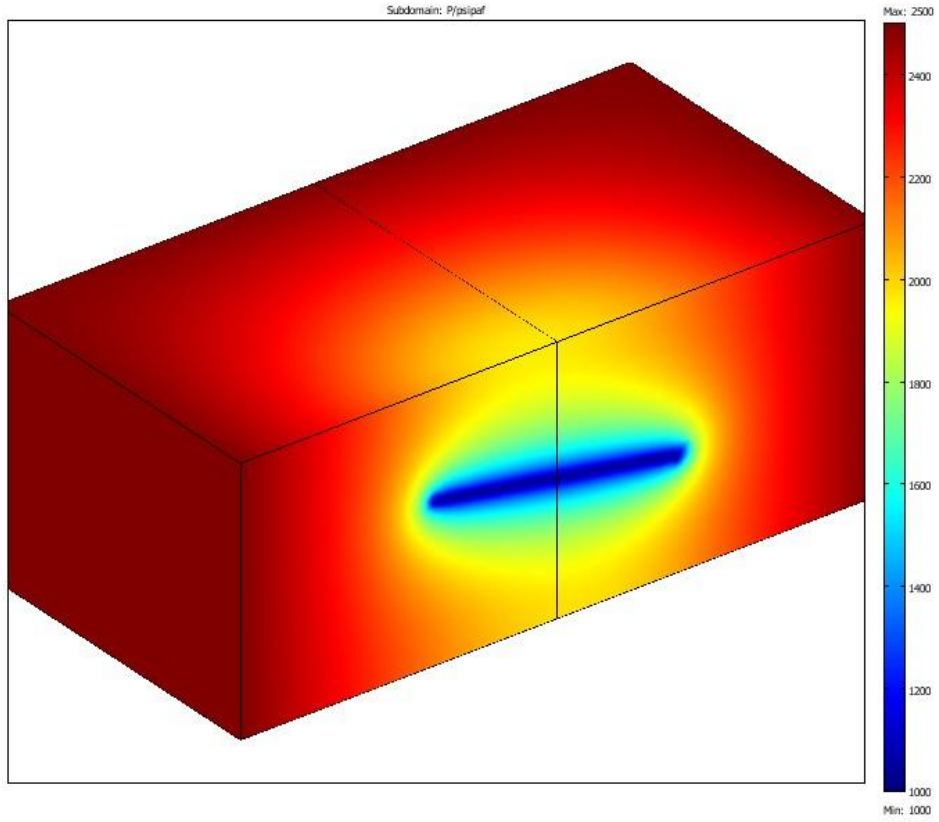

(b)

Figure 4.4: Pressure counter maps around two deviated wells; a) $\theta = 45^0$; b) $\theta = 80^0$.

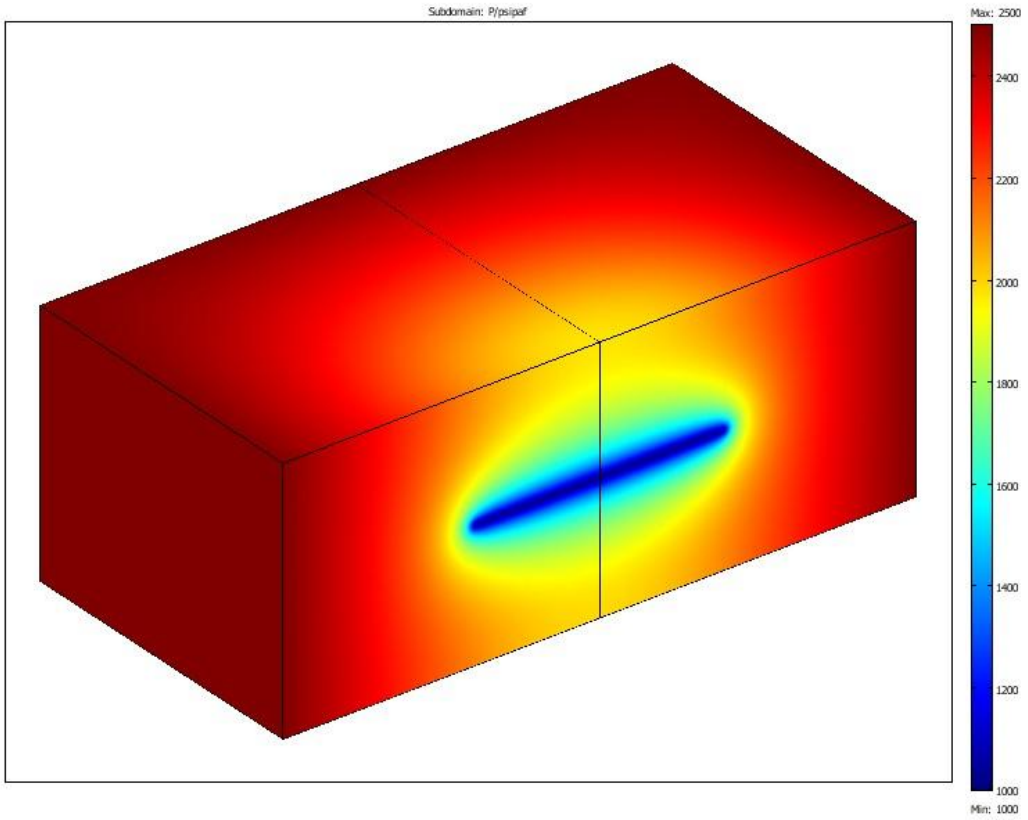

Figure 4.5: Pressure counter map around a horizontal well.

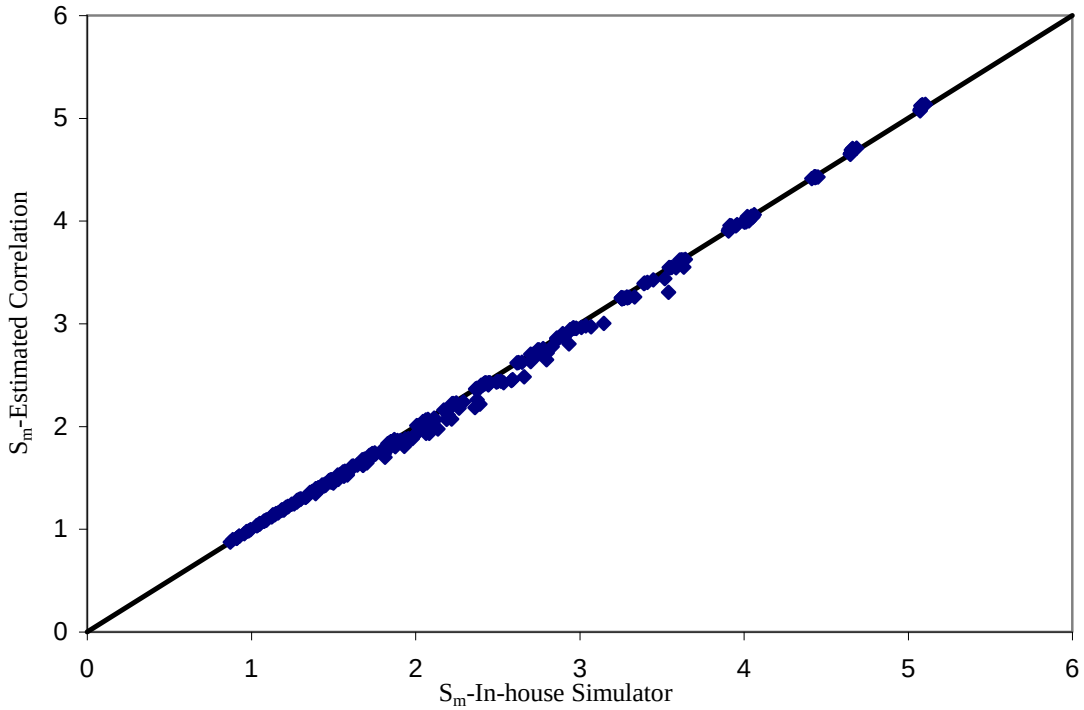

Figure 4.6: Geometric skin of deviated wells (with parameters described in Table 4.1), calculated using Equation 4.24, versus the corresponding values obtained by applying the calculated in-house simulator mass flow rates into Equation 4.19, isotropic formation.

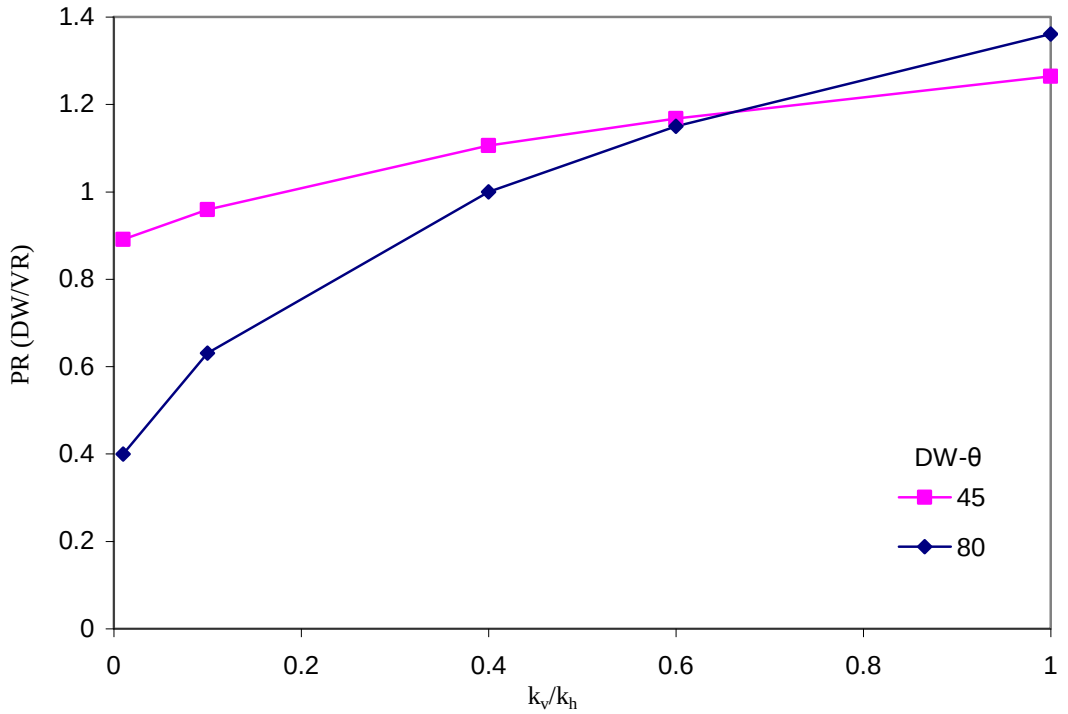

Figure 4.7a: Ratio of deviated to vertical well flow rates, for the same pressure drop, estimated by the in-house simulator (single phase deviated well model) versus formation anisotropy for two deviation angles of 45^0 and 80^0.

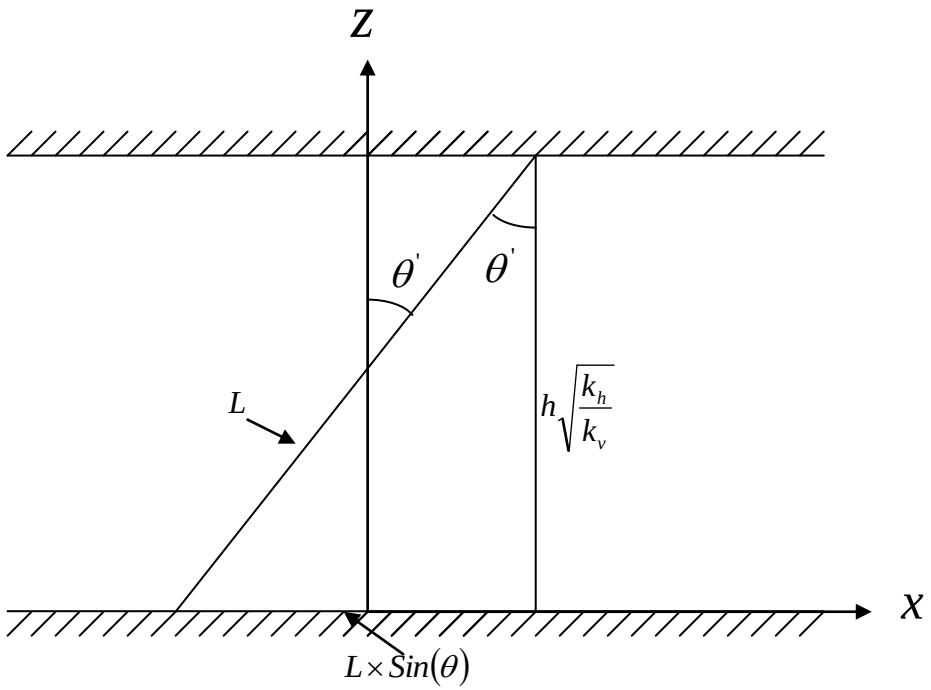

Figure 4.7b: A schematic diagram of the deviated well in the equivalent isotropic reservoir.

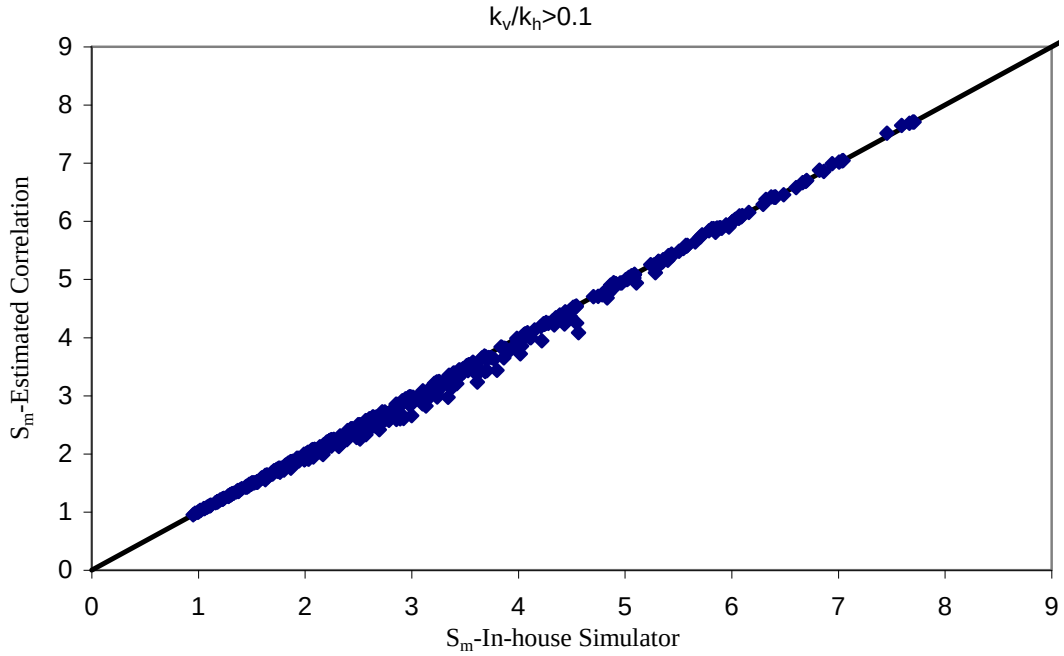

Figure 4.8: Geometric skin of deviated wells (with parameters described in Table 4.1) calculated using Equations 4.24 and 4.25 versus the corresponding values obtained by applying the calculated in-house simulator mass flow rates into Equation 4.19, k_v/k_h>0.1.

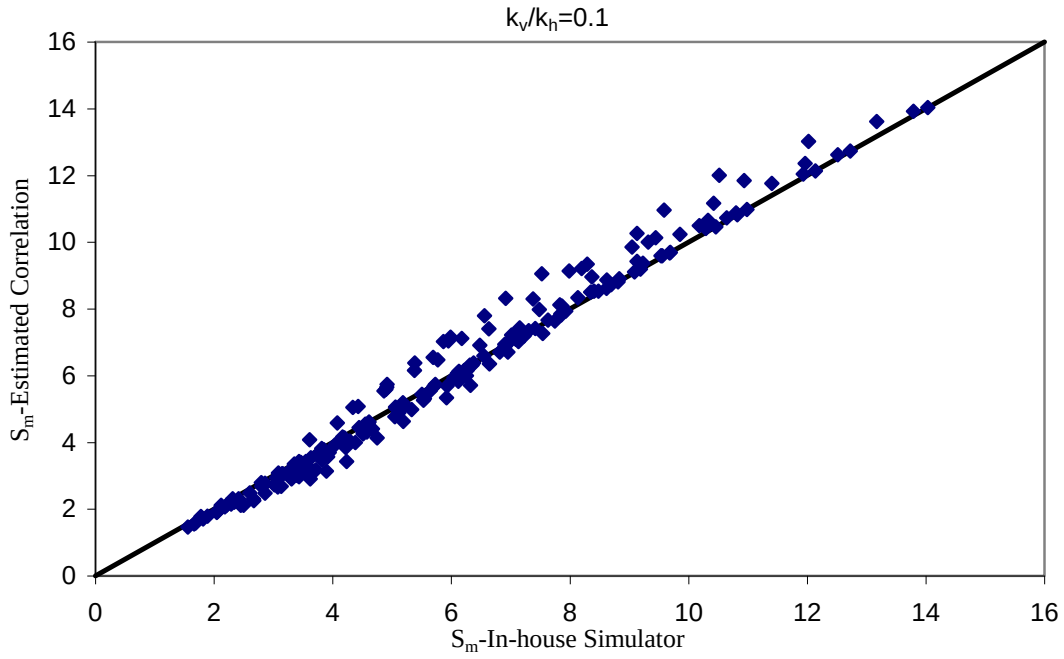

Figure 4.9: Geometric skin of deviated wells (with parameters described in Table 4.1) calculated using Equations 4.24 and 4.25 versus the corresponding values obtained by applying the calculated in-house simulator mass flow rates into Equation 4.19, k_v/k_h=0.1.

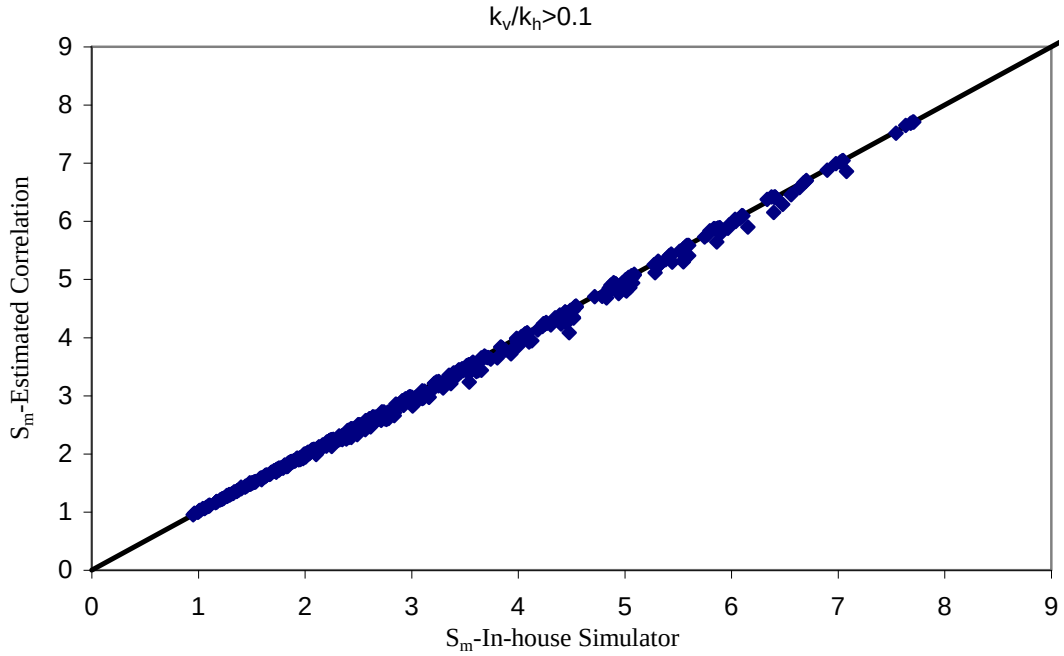

Figure 4.10: Geometric skin of deviated wells (with parameters described in Table 4.1) calculated using Equations 4.24 and 4.27 versus the corresponding values obtained by applying the calculated in-house simulator mass flow rates into Equation 4.19, k_v/k_h>0.1.

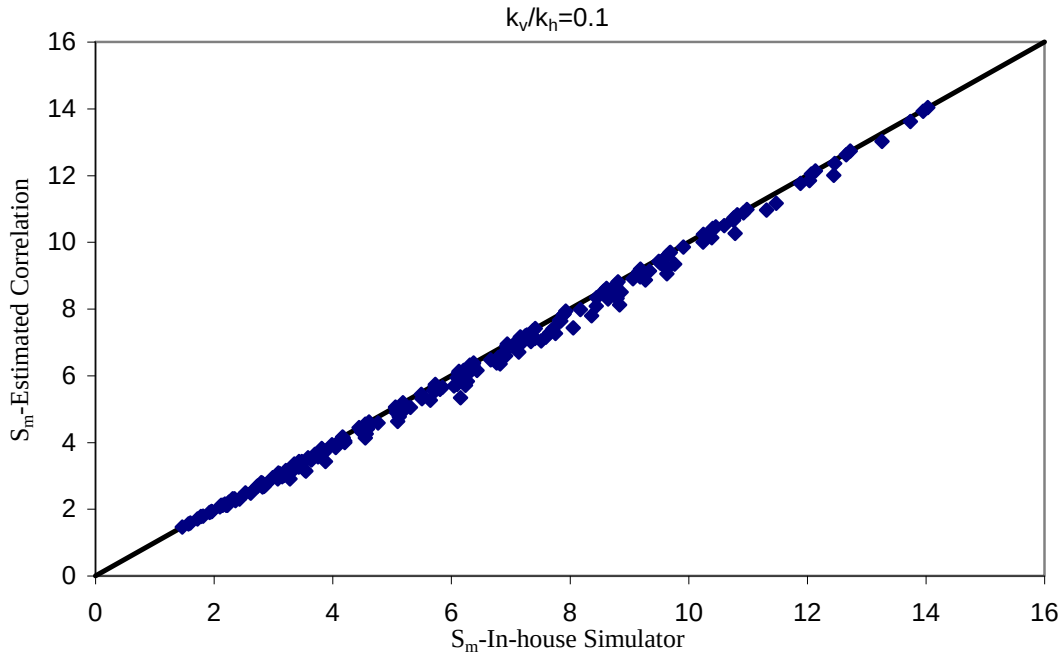

Figure 4.11: Geometric skin of deviated wells (with parameters described in Table 4.1) calculated using Equations 4.24 and 4.27 versus the corresponding values obtained by applying the calculated in-house simulator mass flow rates into Equation 4.19, k_v/k_h=0.1.

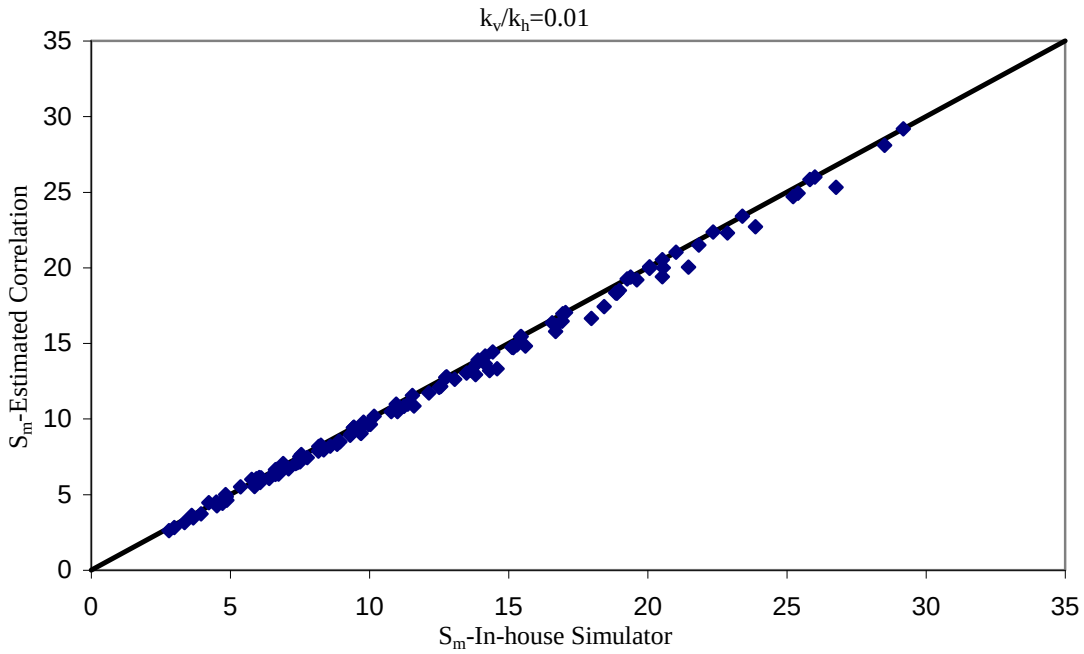

Figure 4.12: Geometric skin of deviated wells (with parameters described in Table 4.1) calculated using Equations 4.24 and 4.27 versus the corresponding values obtained by applying the calculated in-house simulator mass flow rates into Equation 4.19, k_v/k_h=0.01.

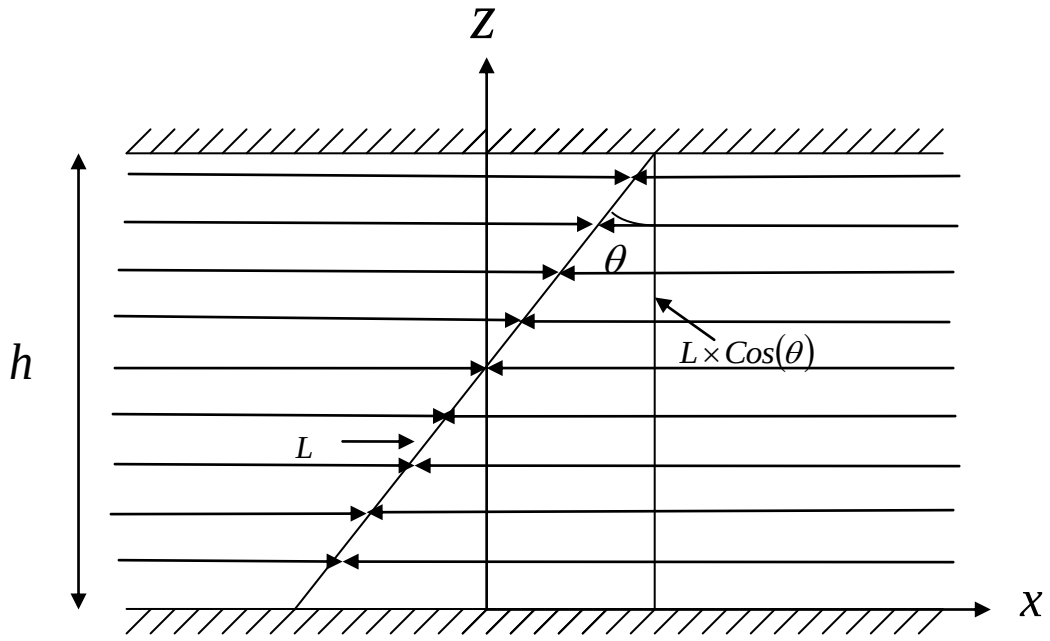

Figure 4.13: Flow pattern around a deviated well in the reservoir with a zero vertical permeability, k_v=0 .

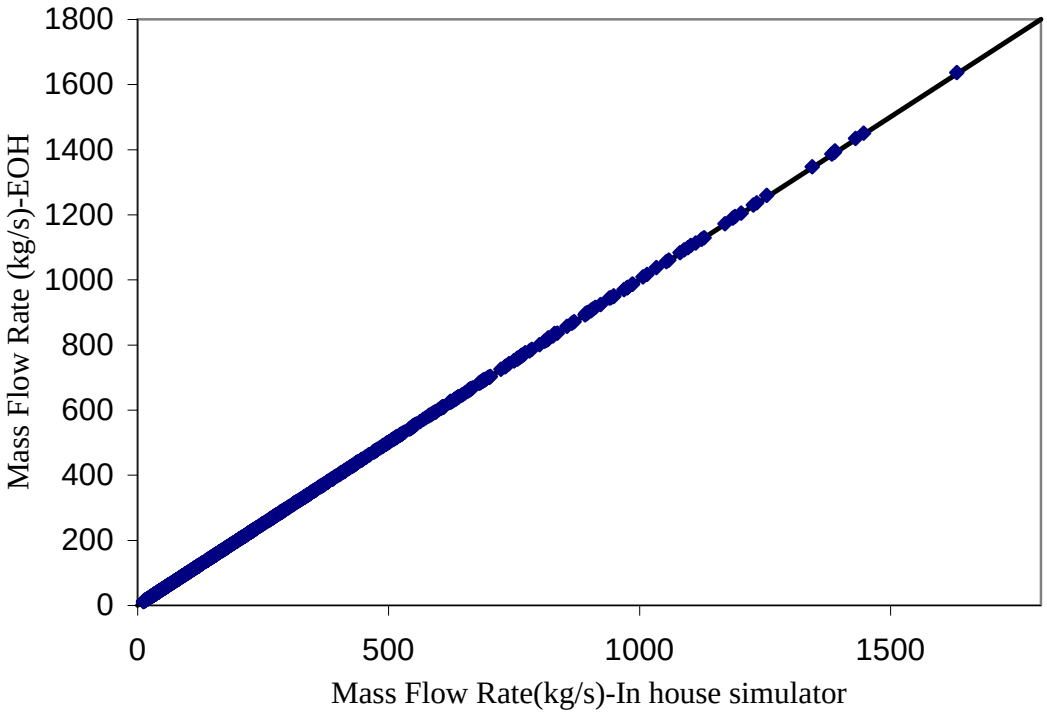

(a)

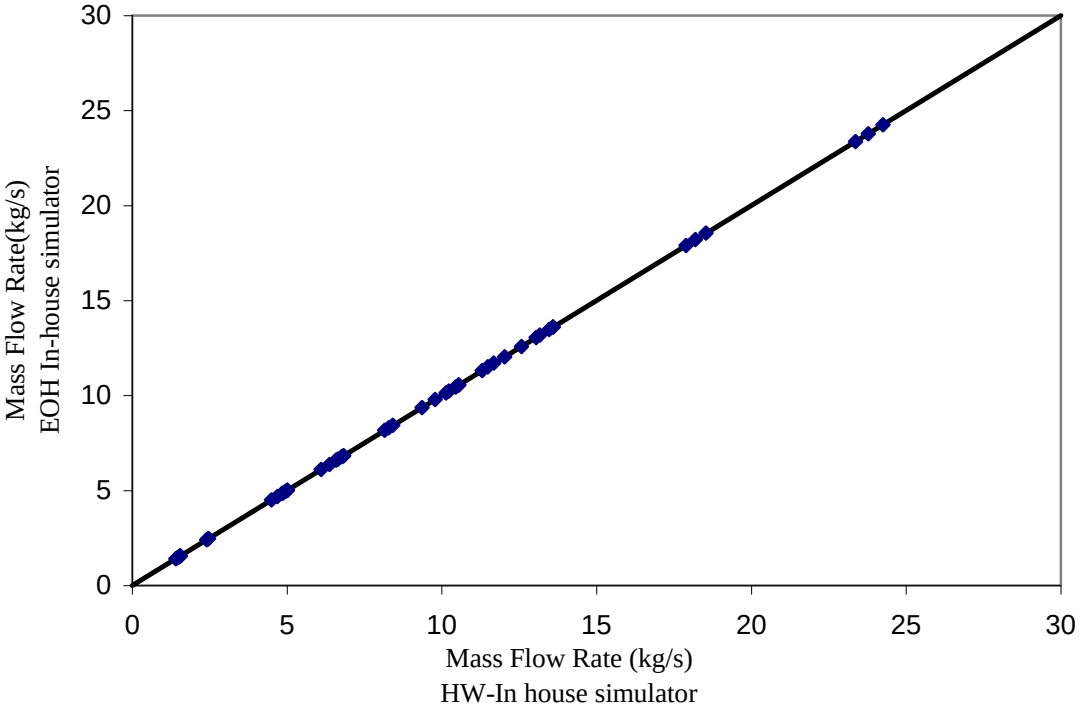

(b)

Figure 4.14: Calculated mass flow rates using EOH model with equivalent radius versus the corresponding values estimated by the DW-in house simulator, (a) Berea (b) Texas Cream core properties (listed in Table 4.2).

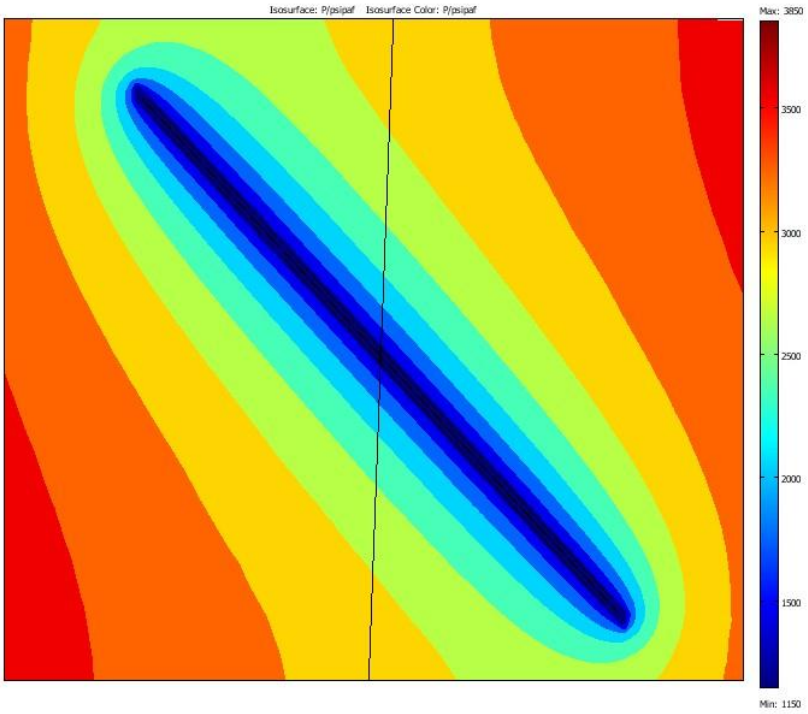

(a)

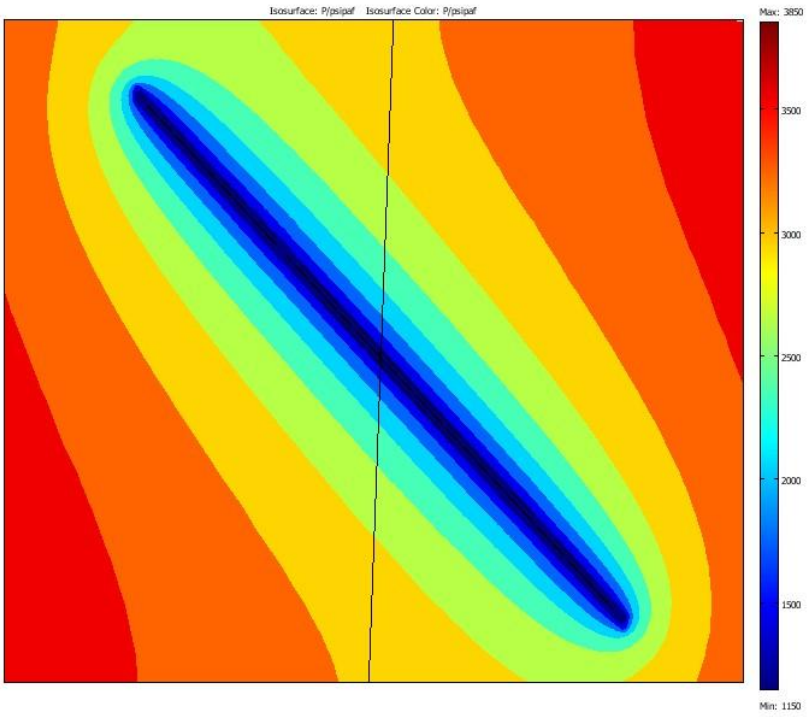

(b)

Figure 4.15: Isobar curves around a deviated well with a 45^0 angle a) without (Darcy flow) b) with inertia (Non-Darcy flow)

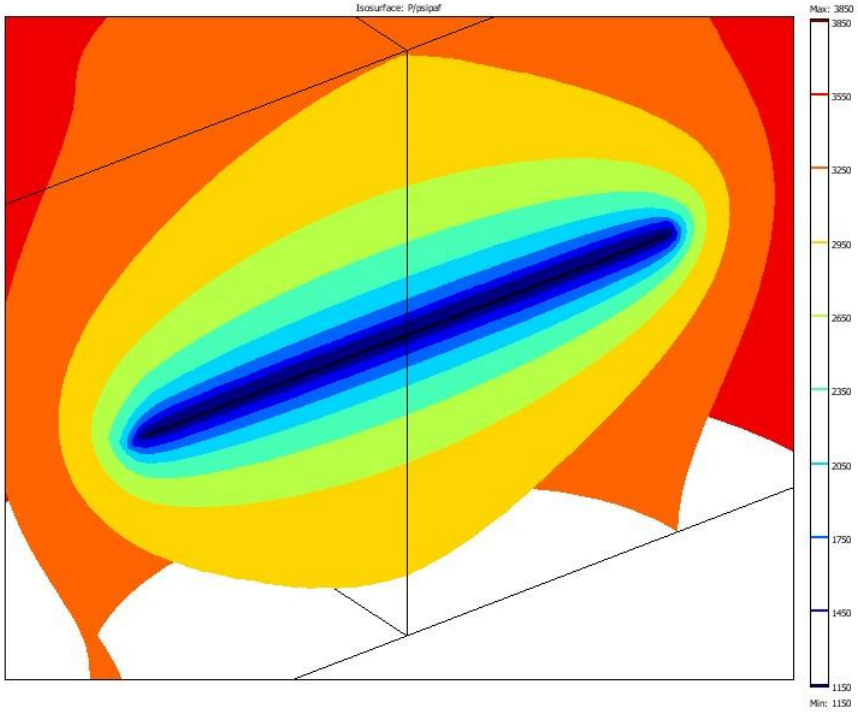

(a)

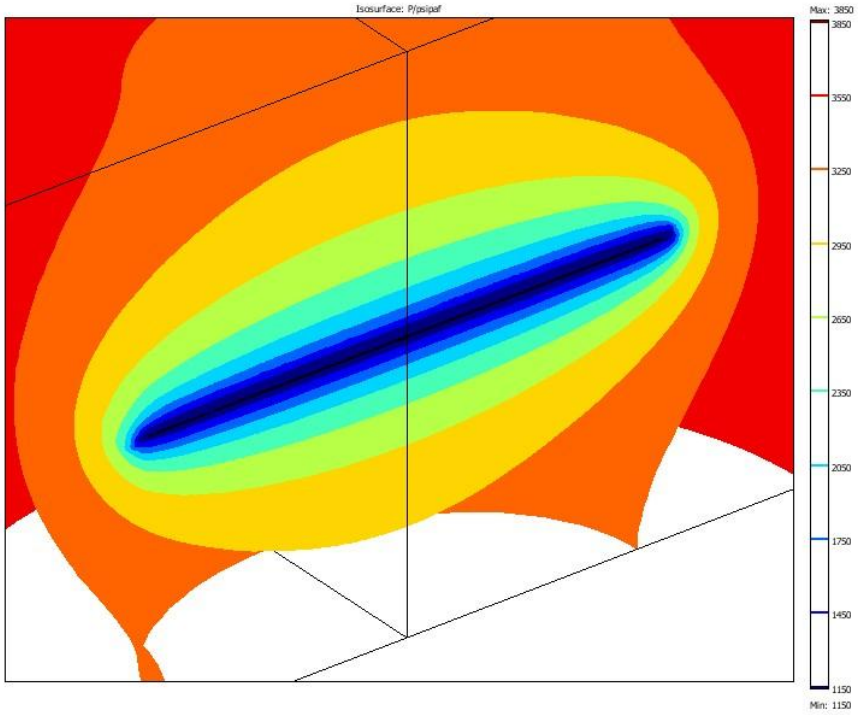

(b)

Figure 4.16: Isobar curves around a horizontal well a) without (Darcy flow) and b) with inertia (Non-Darcy flow).

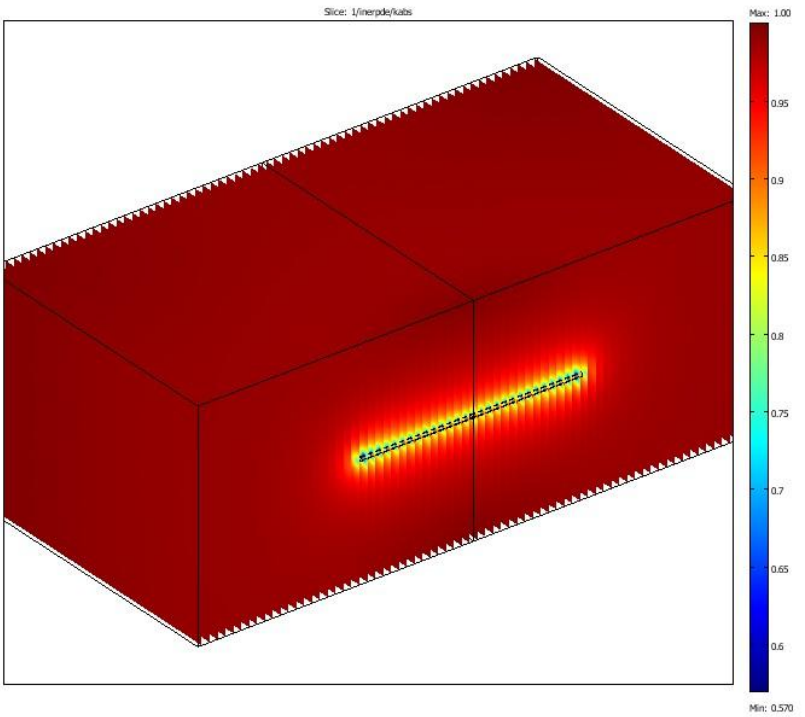

(a)

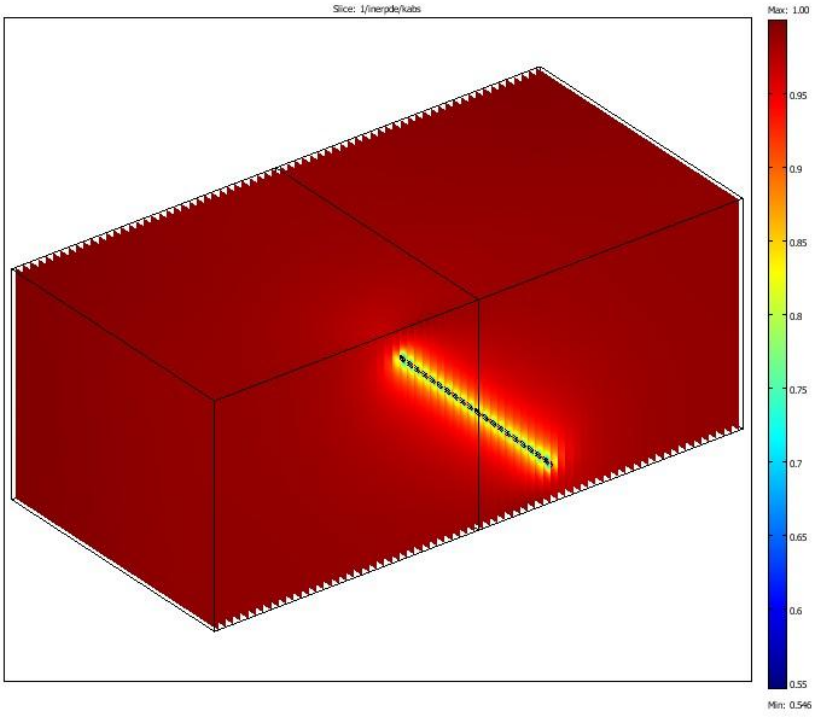

(b)

Figure 4.17: k_r profiles for non-Darcy (inertial) flow around a) horizontal well and b) deviated well (with 45^0 angles).

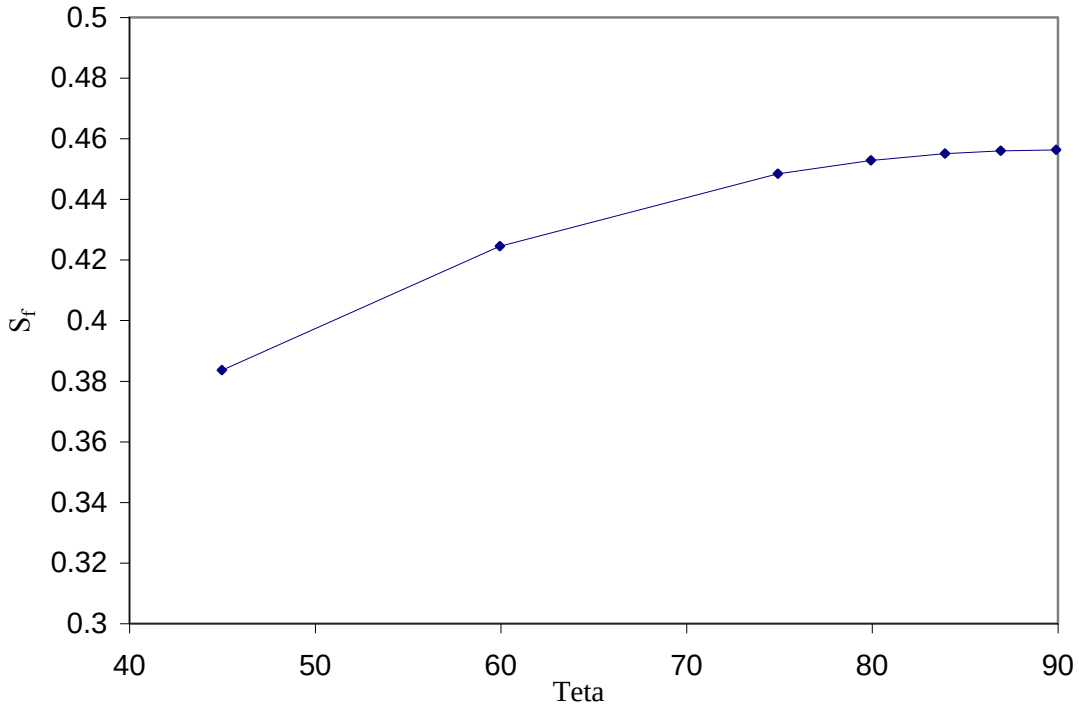

Figure 4.18: Variation of flow skin versus Theta (θ), the pressure drop across the flow domain is 200 psi, h=L_{DW}=15 m, r_w= 0.07 m.

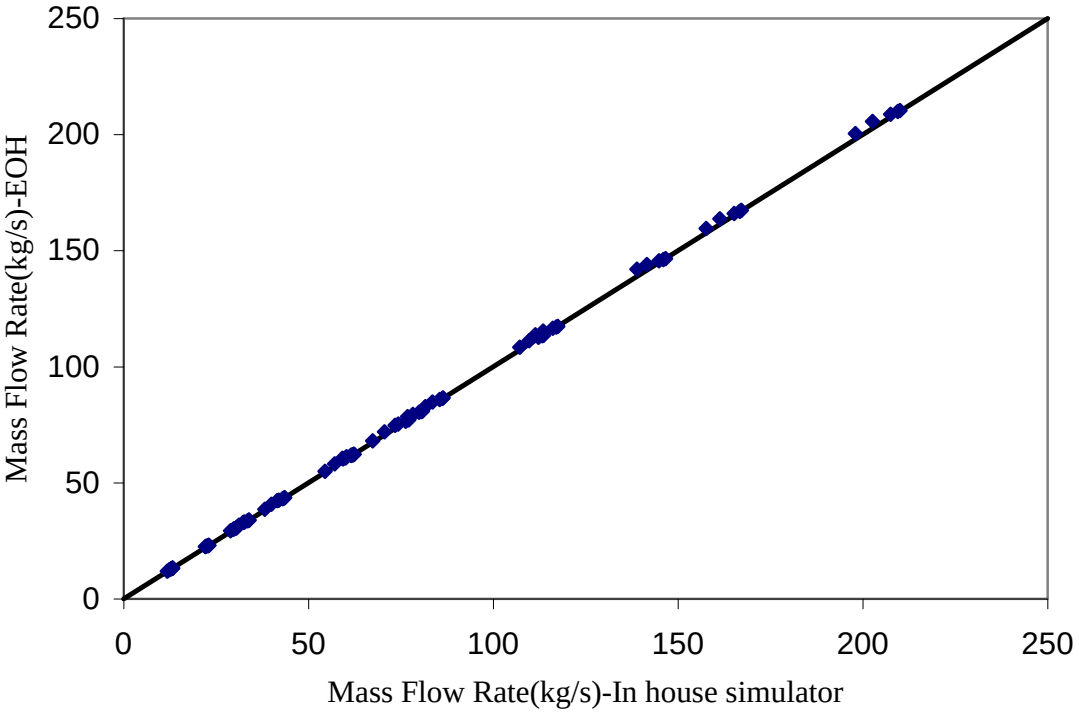

Figure 4.19: Mass flow rates calculated using the flow skin correlation based on the author‘s proposed the effective wellbore radius correlation versus the corresponding values obtained by the in-house simulator, single-phase non-Darcy flow.

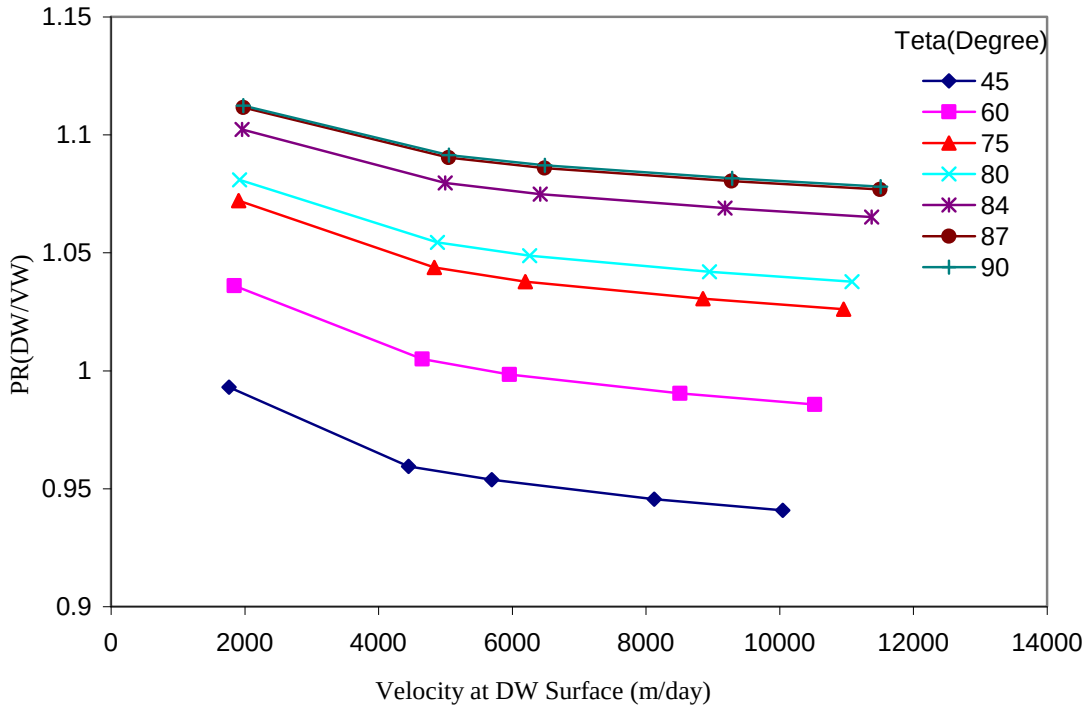

(a)

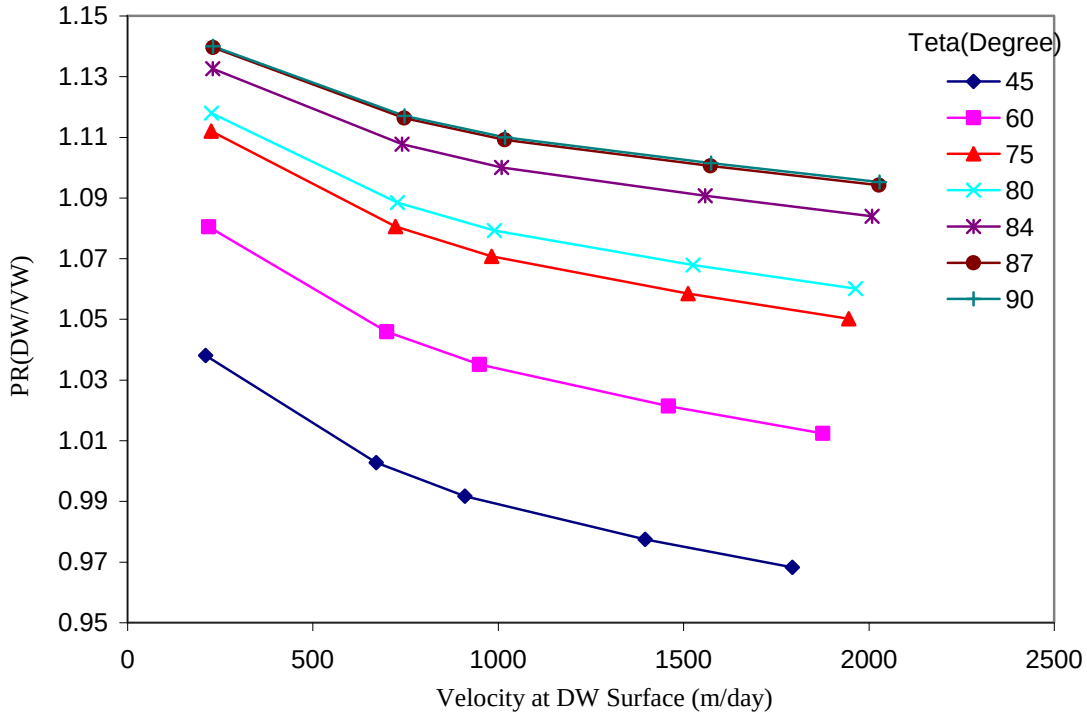

(b)

Figure 4.20: Productivity ratio (deviated to vertical well) (PR) versus velocity at different deviation angles, r_w=0.07 m, h=15 m , P_w=1000 psi a) Berea b)Texas Cream (core properties listed in Table 4.2).

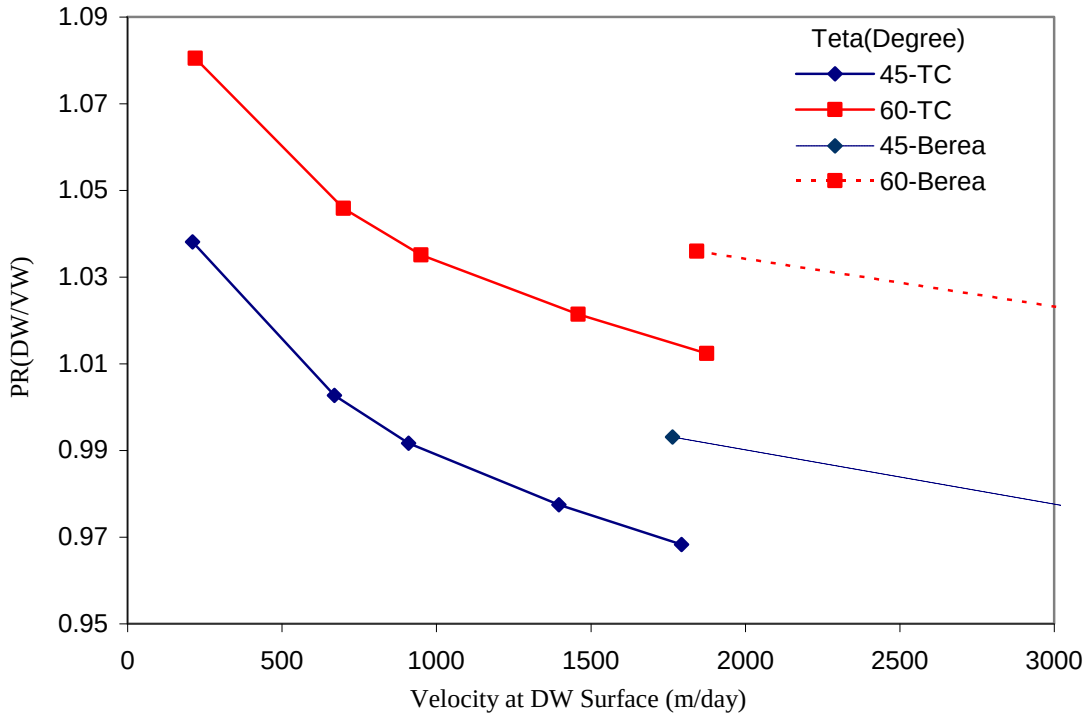

(a)

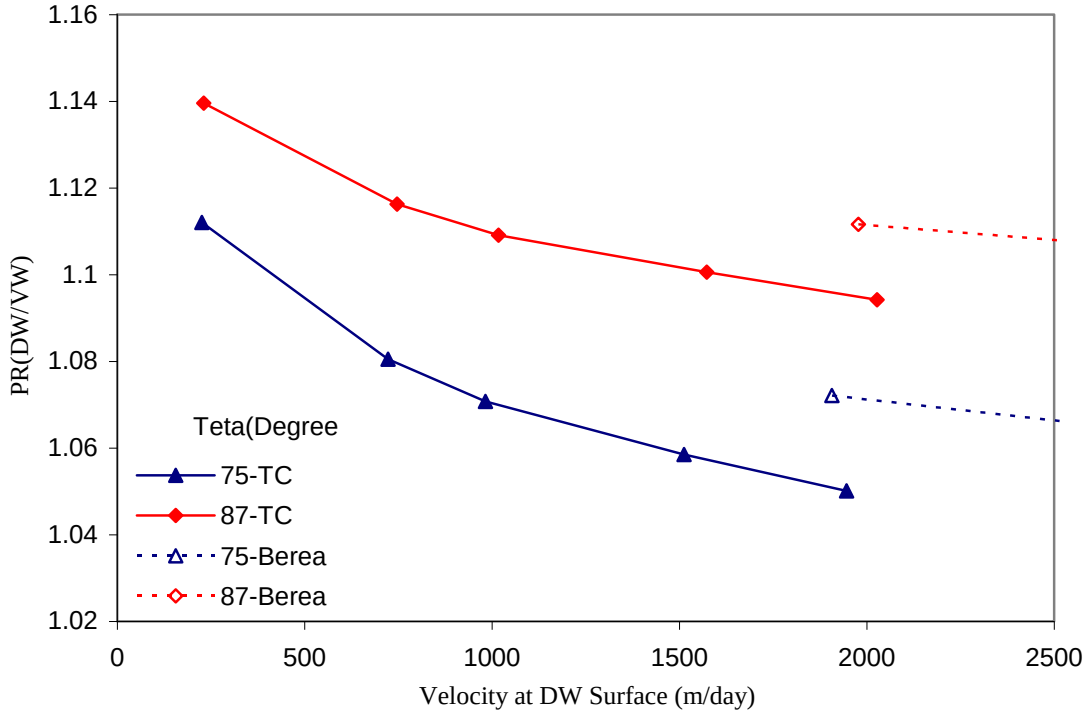

(b)

Figure 4.21: Comparison of PR versus velocity at different deviation angles, r_w=0.07 m, h=15 m , P_w=1000 psi using two core properties, Berea and Texas Cream , (listed in Table 4.2).

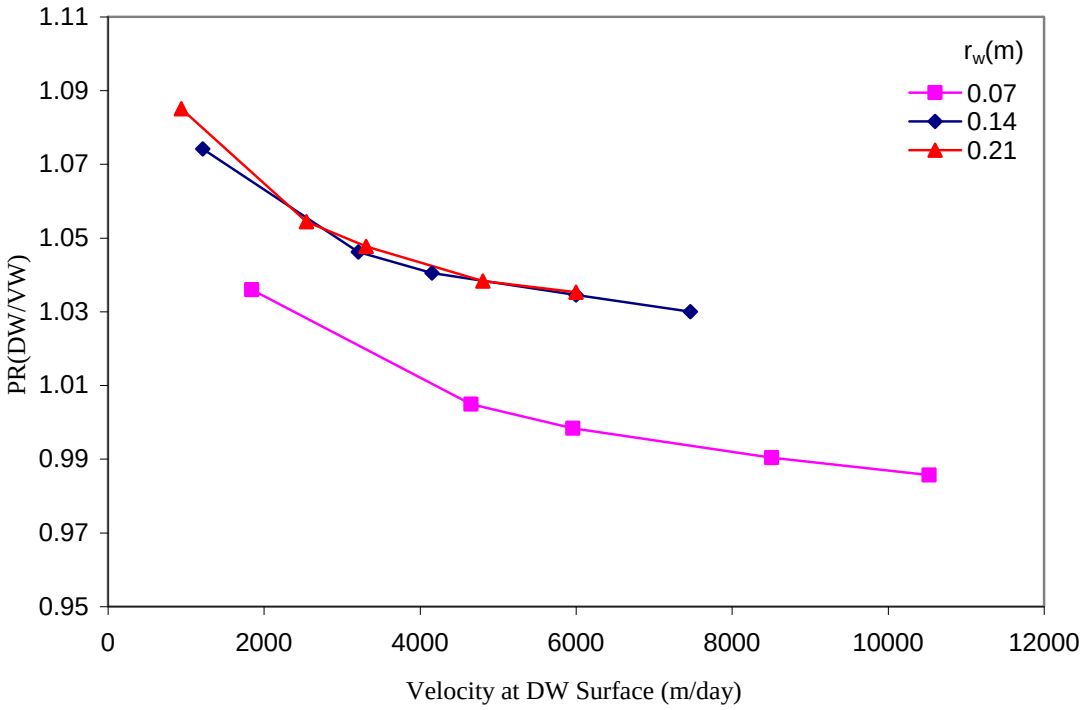

(a)

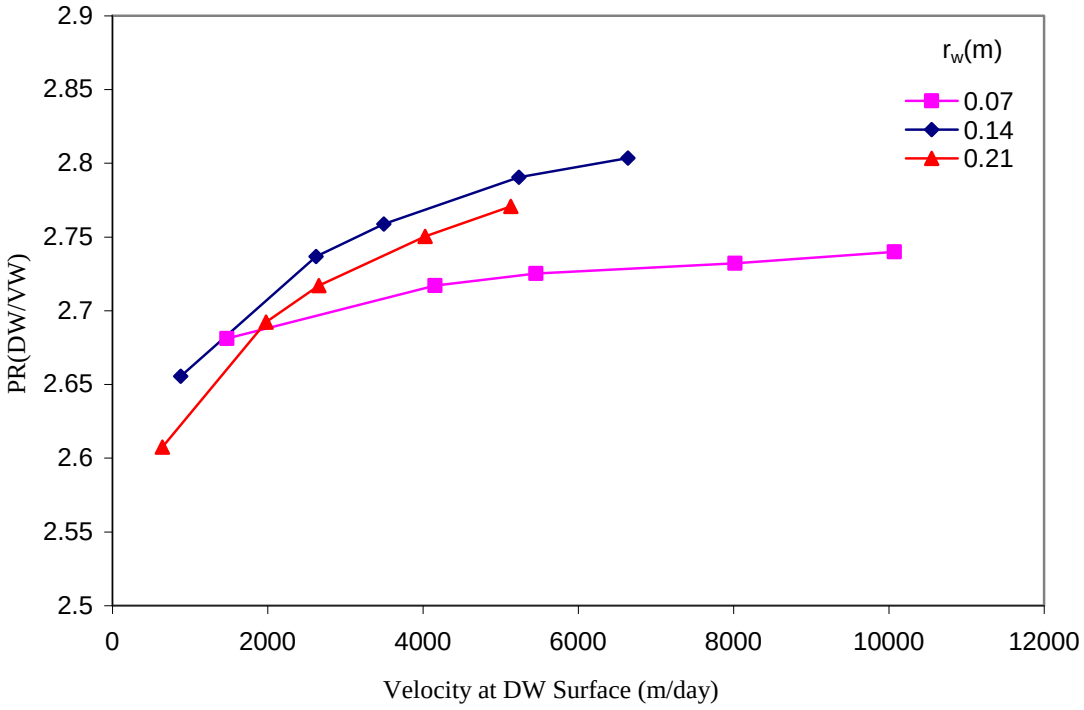

(b)

Figure 4.22: Productivity ratio (deviated to vertical well) versus velocity (at the DW surface) at three wellbore radii, h=15 m, P_w=1000 psi, Teta= 60^0 a) L=15 m and b) L=45 m.

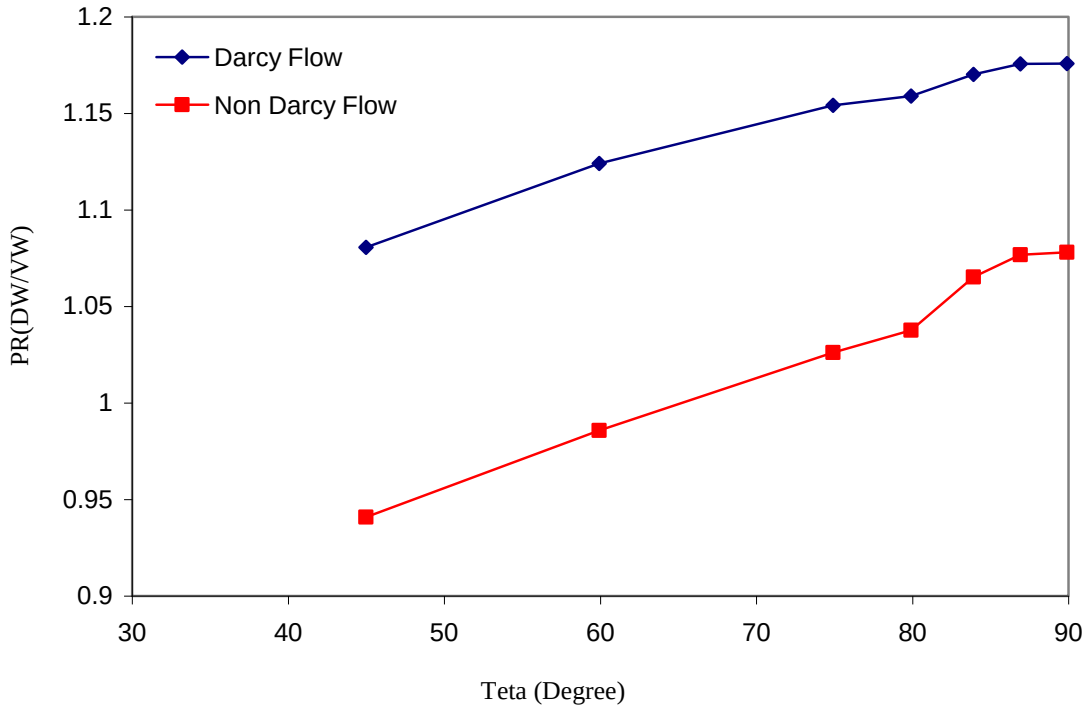

(a)

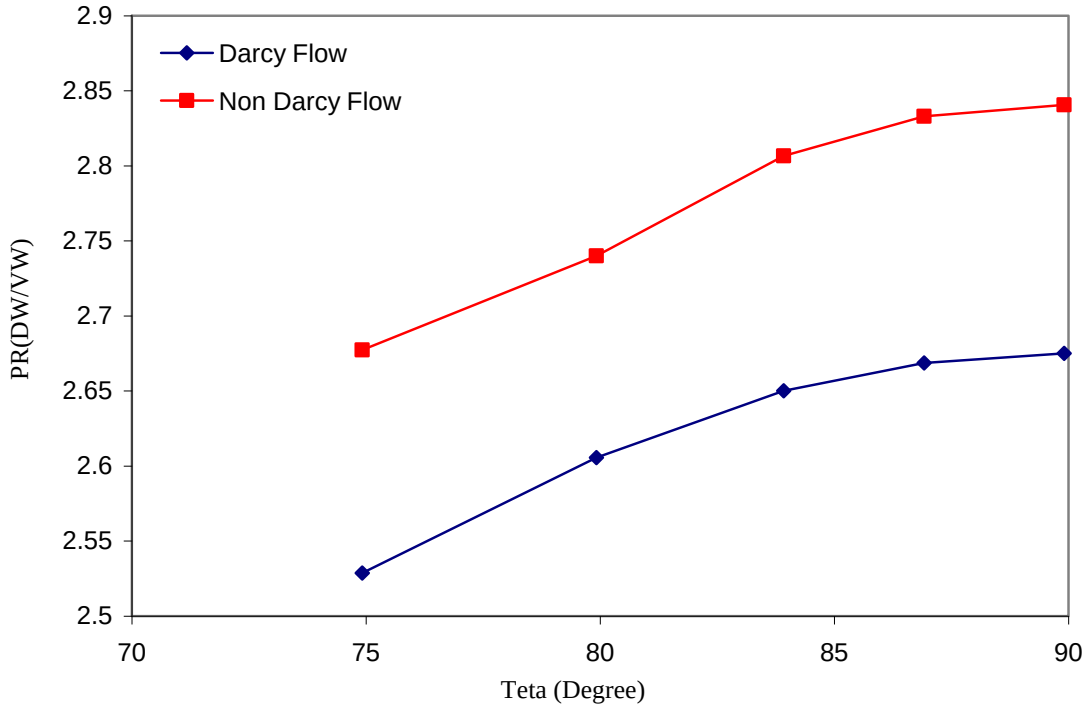

(b)

Figure 4.23: Productivity ratio (deviated to vertical well) versus the deviation angle for Darcy and non Darcy flow regimes, r_w=0.07 m, h=15 m, P_w=1000 psi and P_{res}= 4200 psi a) L_{DW}=15 m b) L_{DW}=45 m, Berea core properties, listed in Table 4.2.

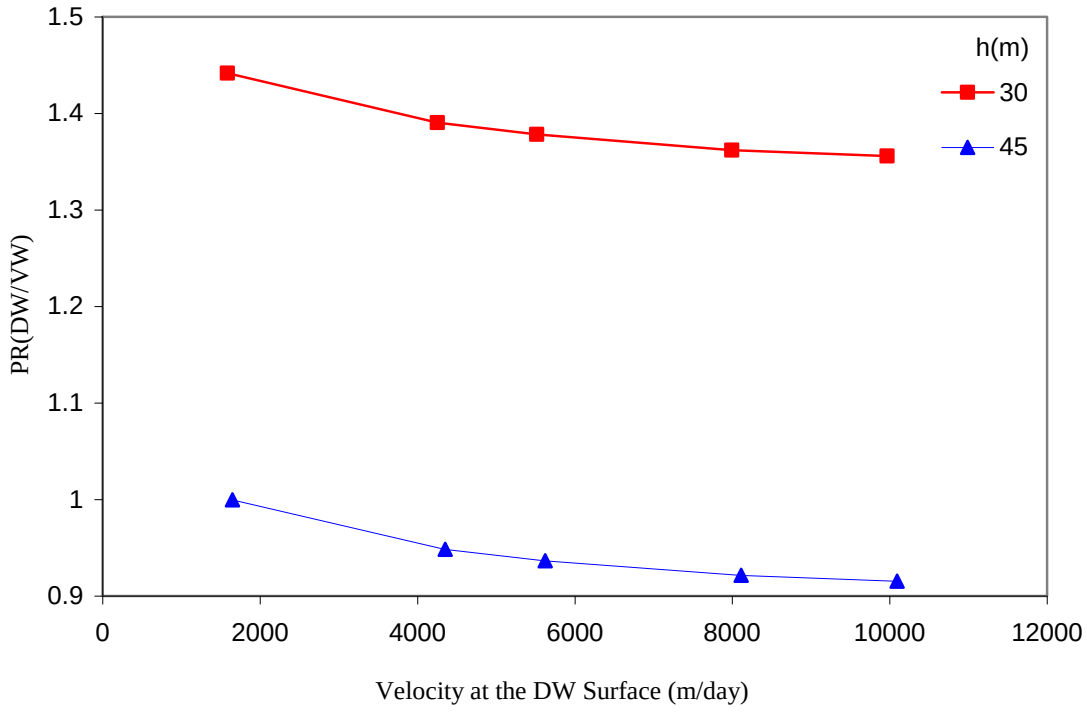

(a)

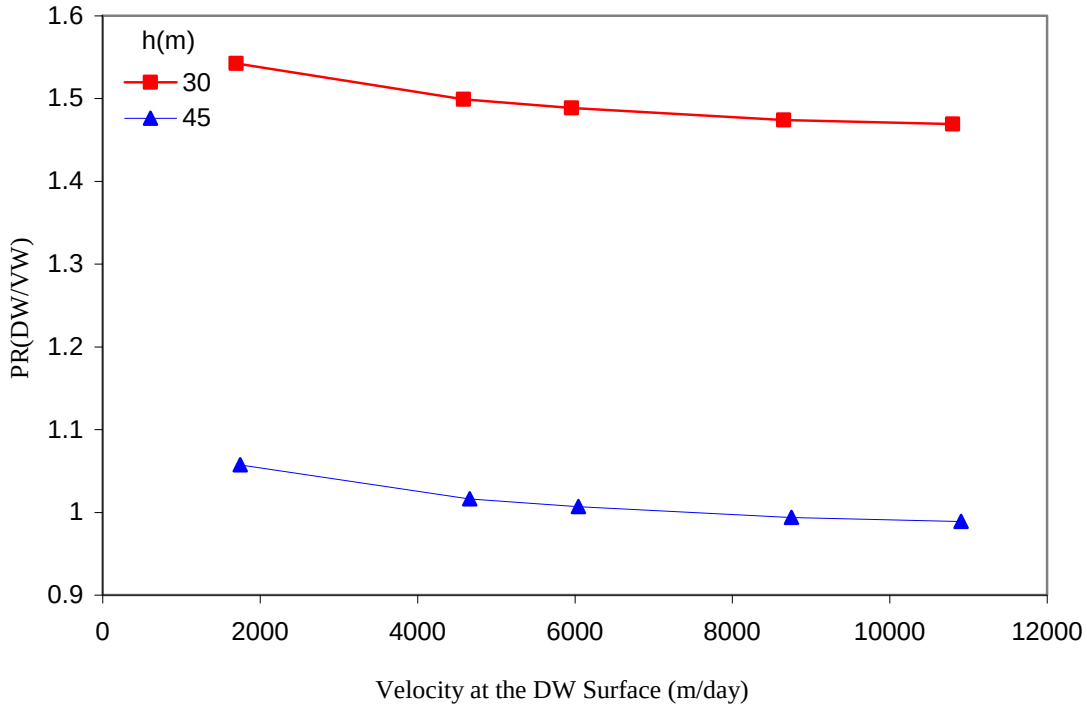

(b)

Figure 4.24: Productivity ratio (deviated to vertical well) versus velocity (at the DW surface) two formation thicknesses, P_w=1000 psi, L_{DW}=45 m a) Theta= 60^0 b) Theta= 84^0.

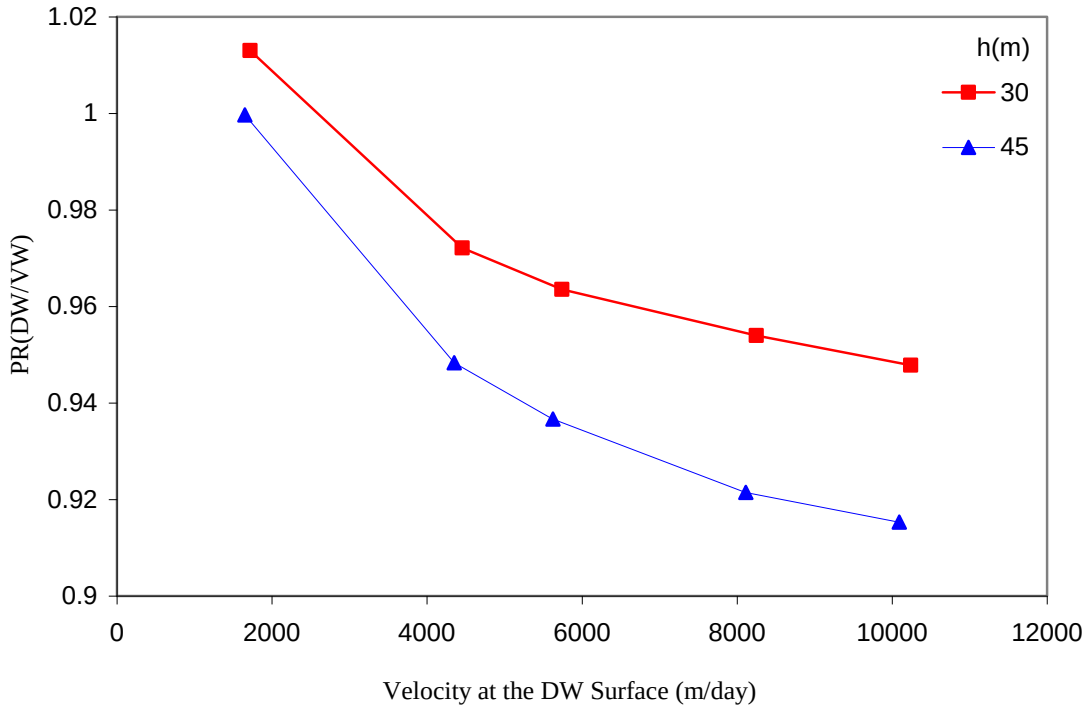

(a)

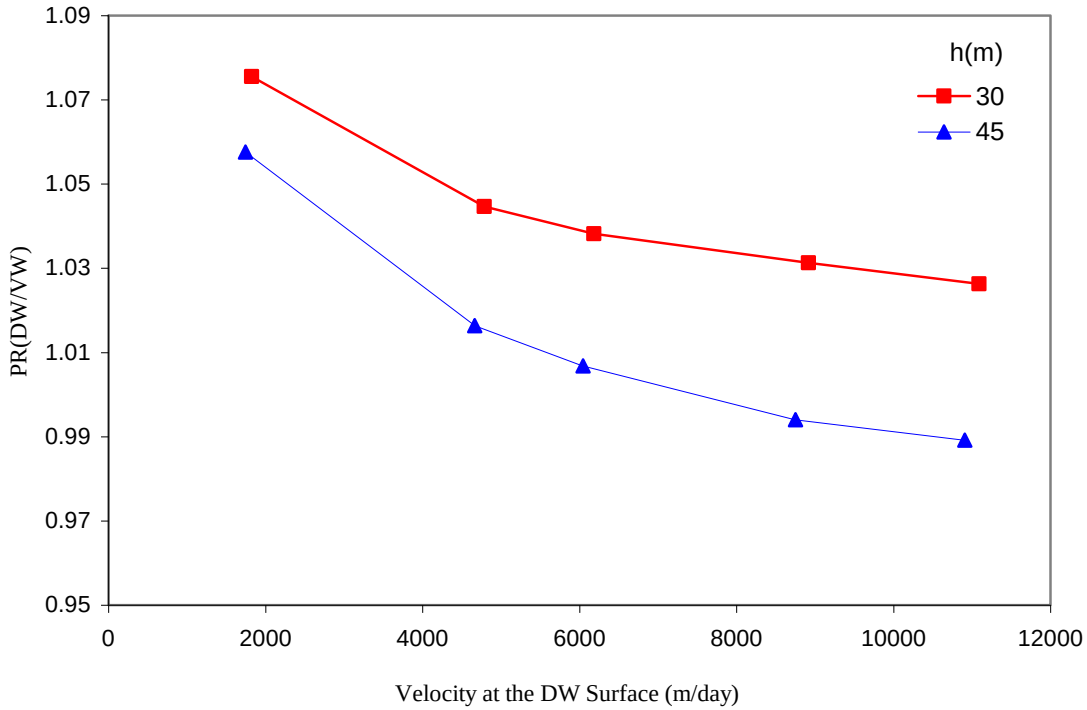

(b)

Figure 4.25: Productivity ratio (deviated to vertical well) versus velocity for two different reservoir thickness values, P_w=1000 psi, L_{DW} =h a) Theta= 60^0 b) Theta= 84^0.

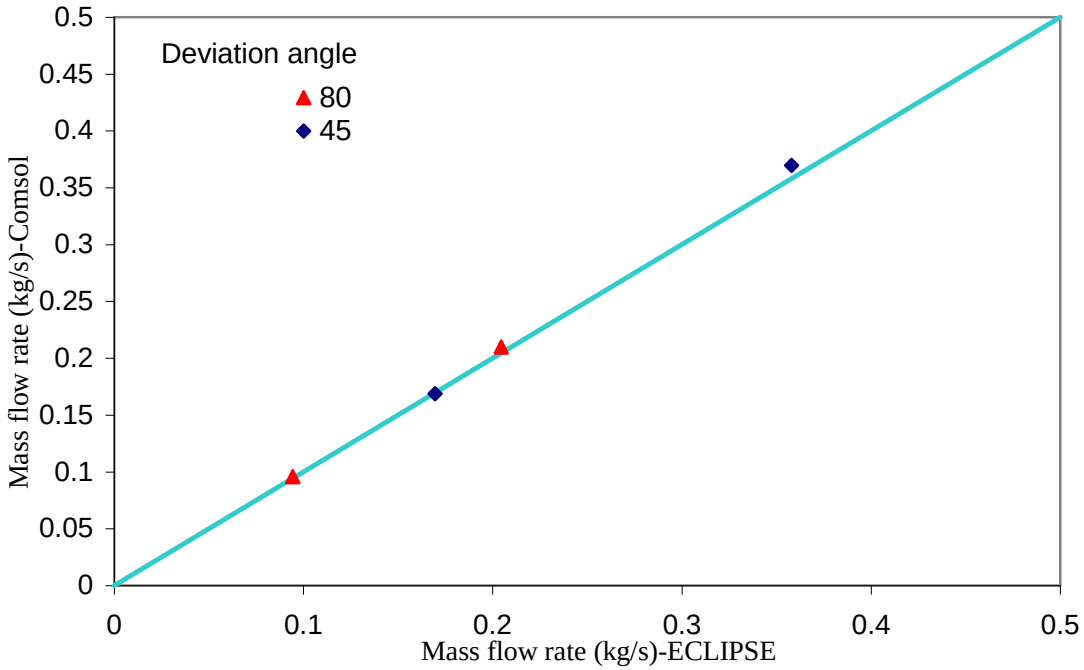

Figure 4.26: Comparison of the results of ECLIPSE two-phase deviated well models with deviation angles of 80^0 and 45^0 with those of the in-house simulator at two different pressure drops of 200 and 400 psi.

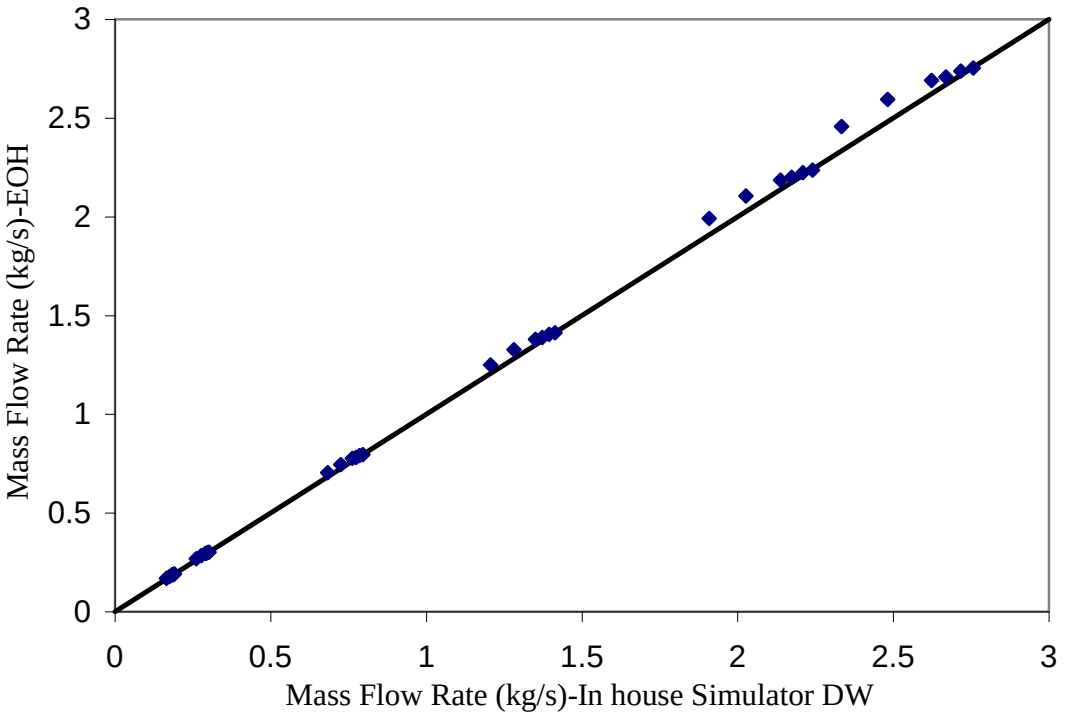

Figure 4.27: Mass flow rate calculated using the two phase flow skin correlation based on the author‘s proposed effective wellbore radius correlation versus the corresponding values obtained by the in-house simulator.

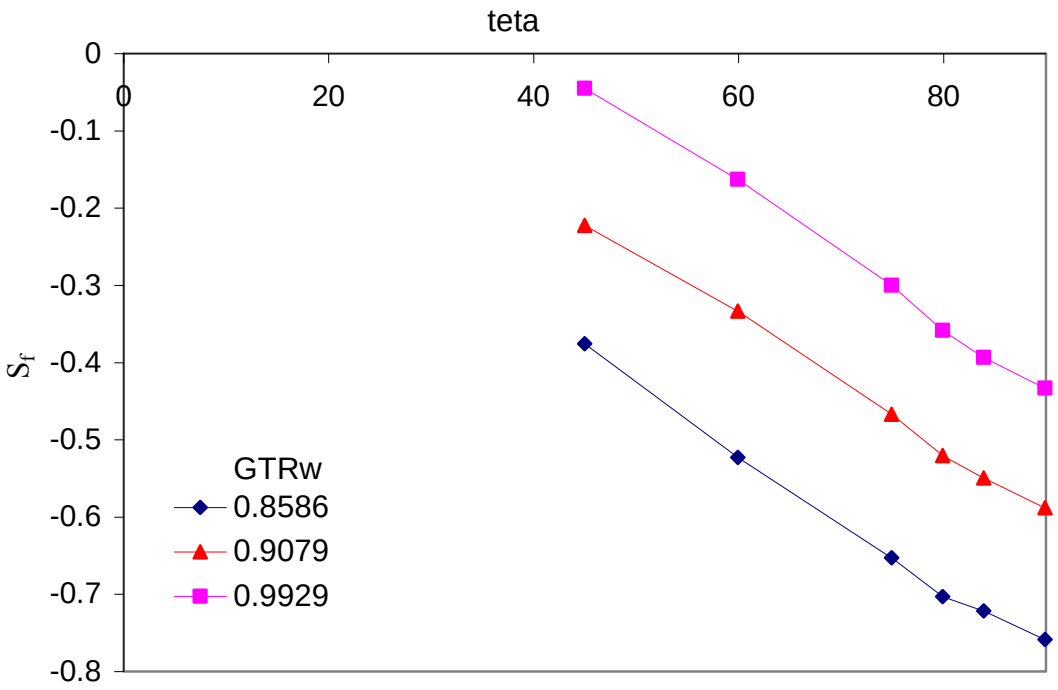

Figure 4.28: Two-phase flow skin versus the deviation angle at three different $GTR_{well.}$. The reservoir thickness, wellbore length and the wellbore radius are 15, 15, and 0.07 m, respectively.

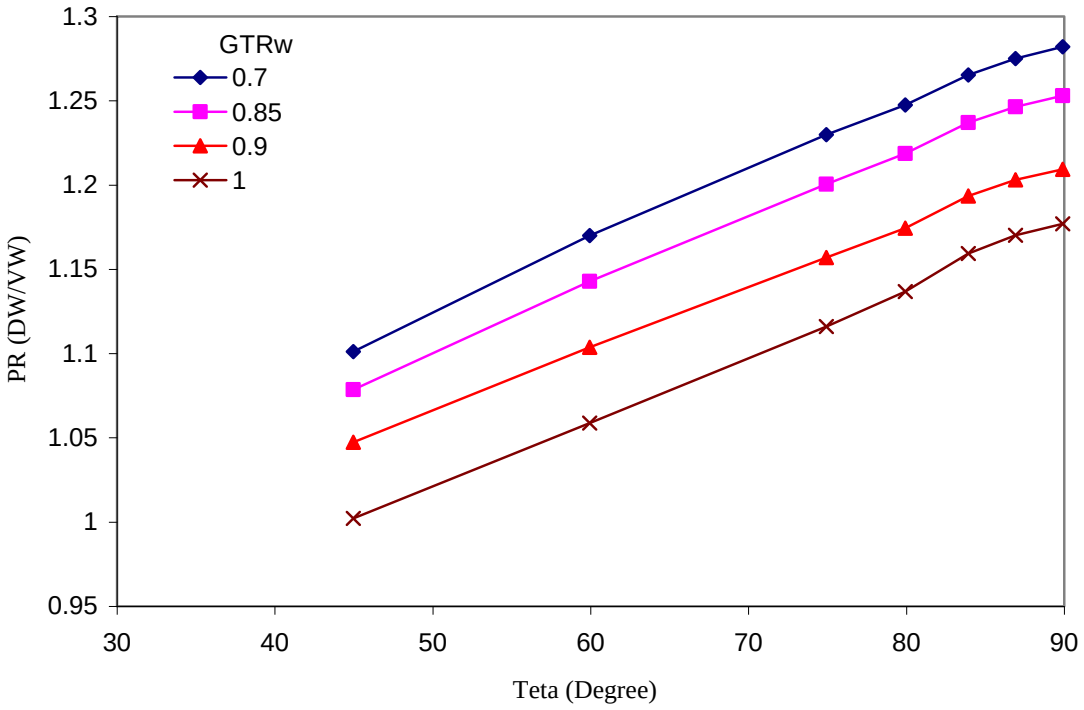

Figure 4.29: Productivity ratio (deviated to vertical well) versus deviation angle at different gas fractional flow (GTR_w), $\Delta p = 50$ psi, $P_w = 1800$ psi, $L_{DW} = 15\,\text{m}, r_w = 0.07$ m and $h = 15$ m.

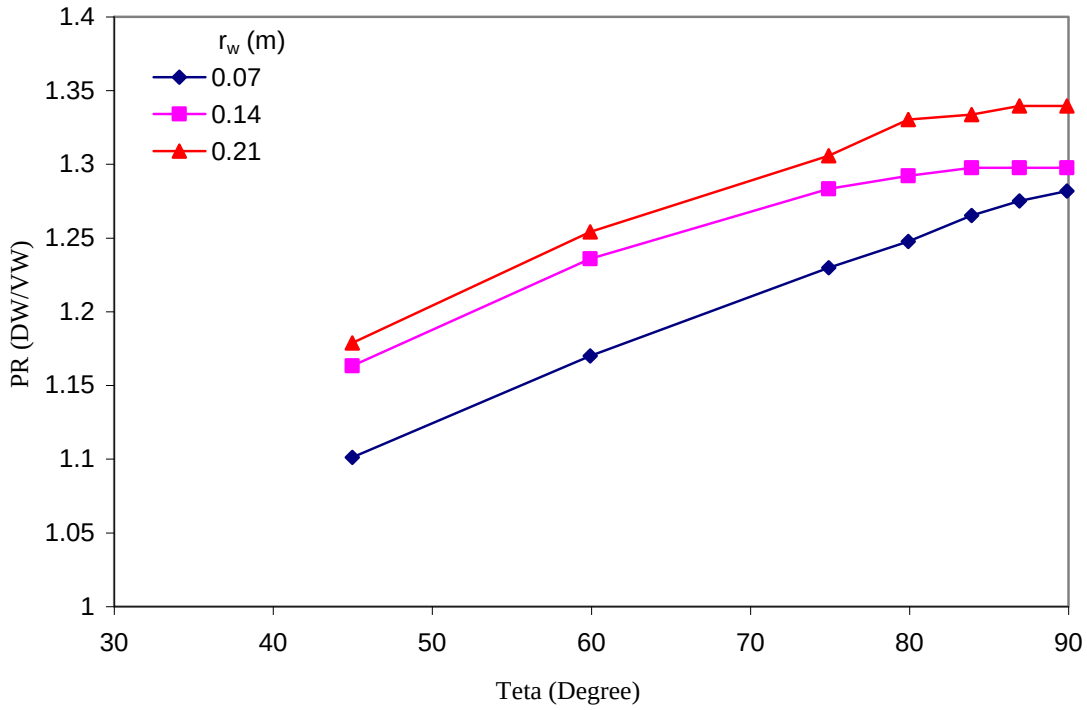

Figure 4.30: Productivity ratio (deviated to vertical well) versus deviation angle at different wellbore radii, GTR_w=0.7, $\Delta p = 50$ psi, $L_{DW} = 15$ m, $P_w = 1800$ psi, $r_w = 0.07$ m and $h = 15$ m.

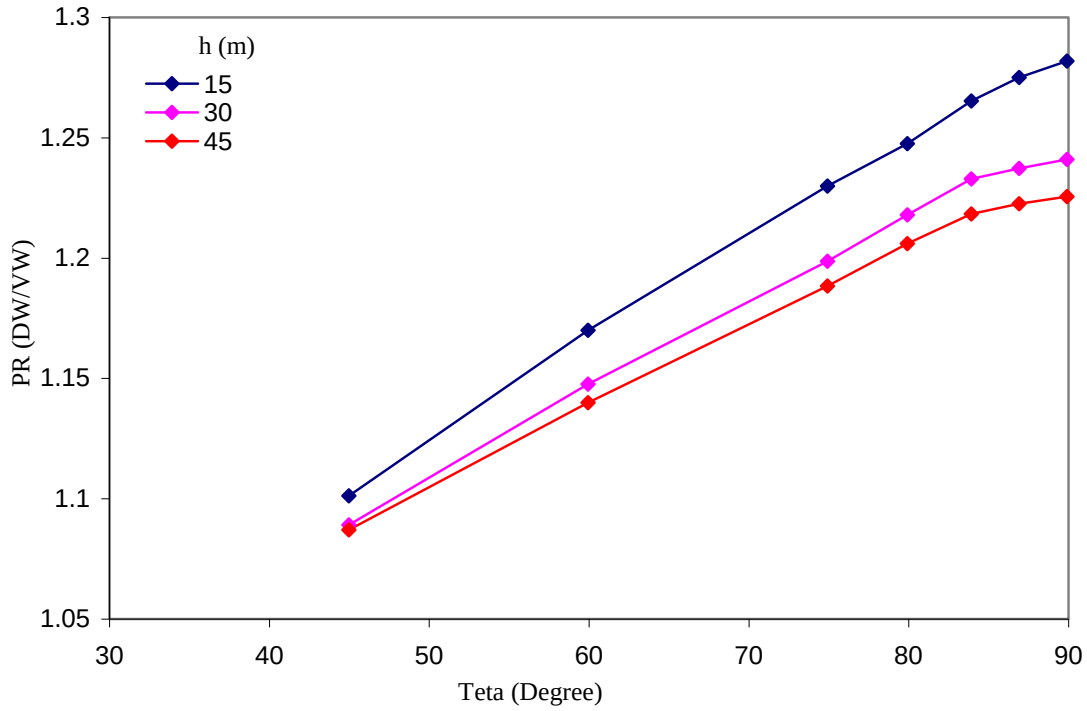

Figure 4.31: Productivity ratio (deviated to vertical well) versus deviation angle for a deviated well at three different reservoir thicknesses, GTR_w=0.7, $\Delta p = 50$ psi, $L = 15$ m, $P_w = 1800$ psi, $r_w = 0.07$ m.

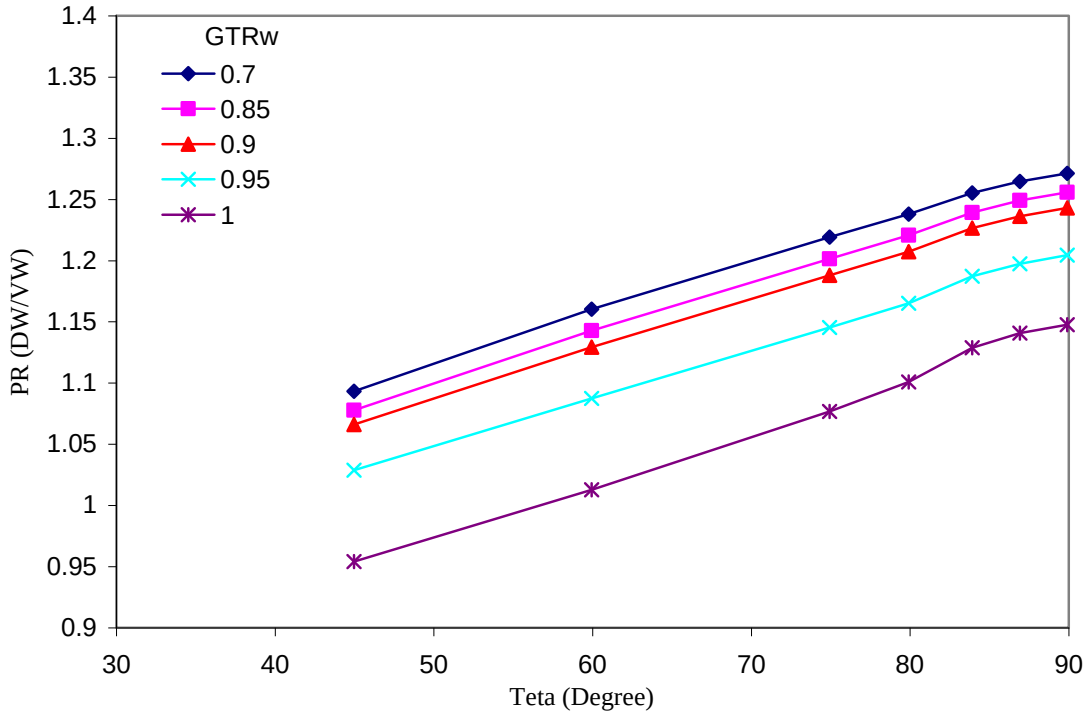

(a)

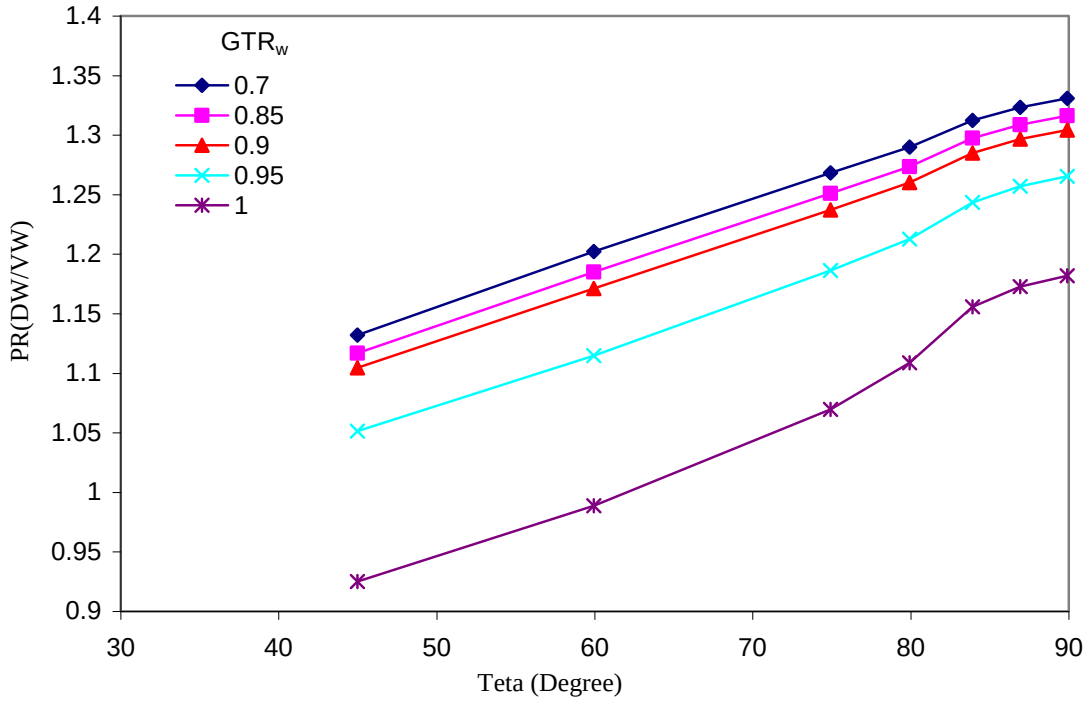

(b)

Figure 4.32: Productivity ratio (deviated to vertical well) versus deviation angle at different the total gas fractional flows (GTR), $\Delta p = 200$ psi, $P_w = 1565$ psi, $L_{DW} = 15$ m, $r_w = 0.07$ m and $h = 15$ m. a) Texas Cream, b) Berea properties (listed in Table 4.2).

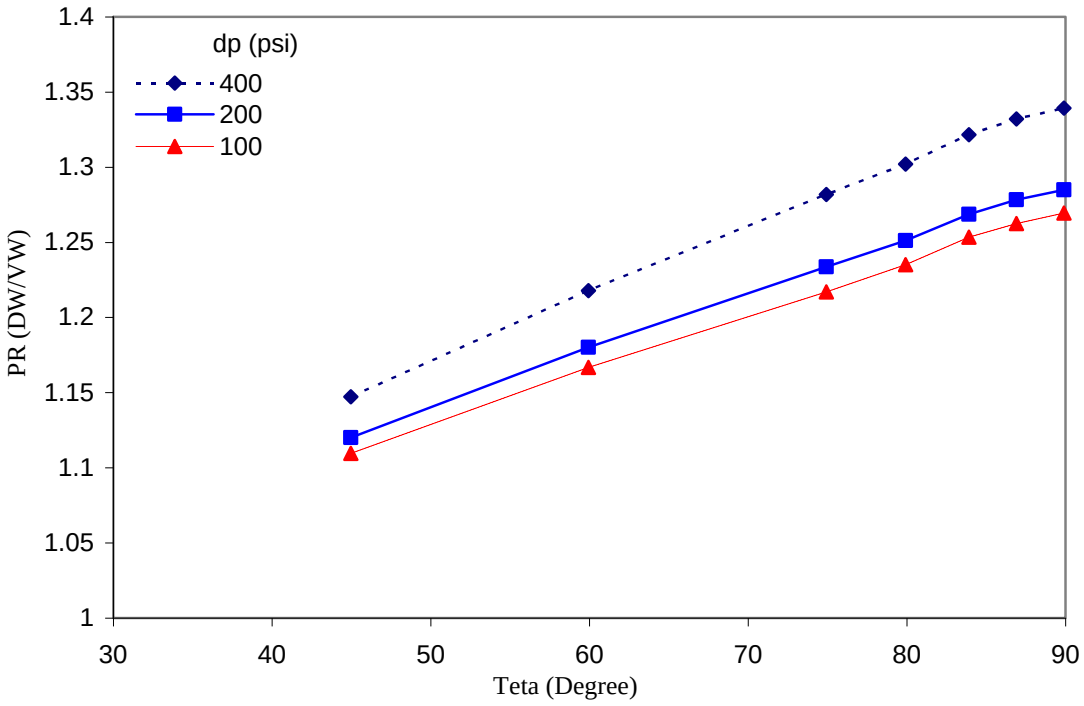

(a)

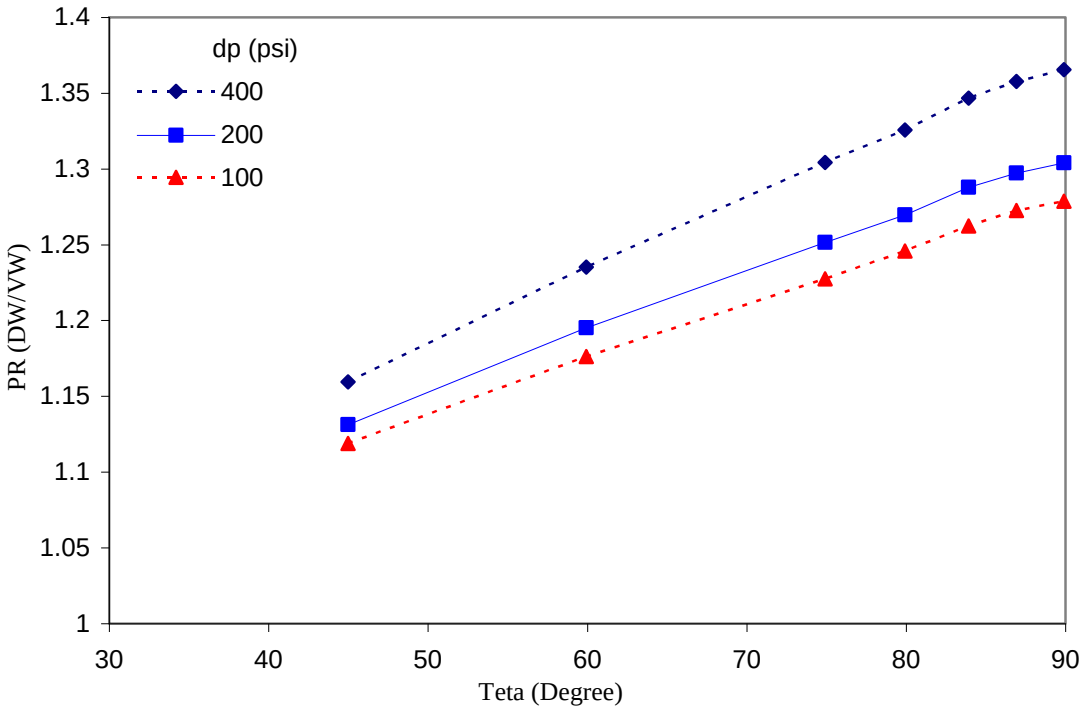

Figure 4.33: Productivity ratio (deviated to vertical well) versus deviation angle at three pressure drawdown values (Δp) of 400, 200 and 100 psi and GTR_w=0.7 a) P_w=1365 psi b) P_w=1450 psi.

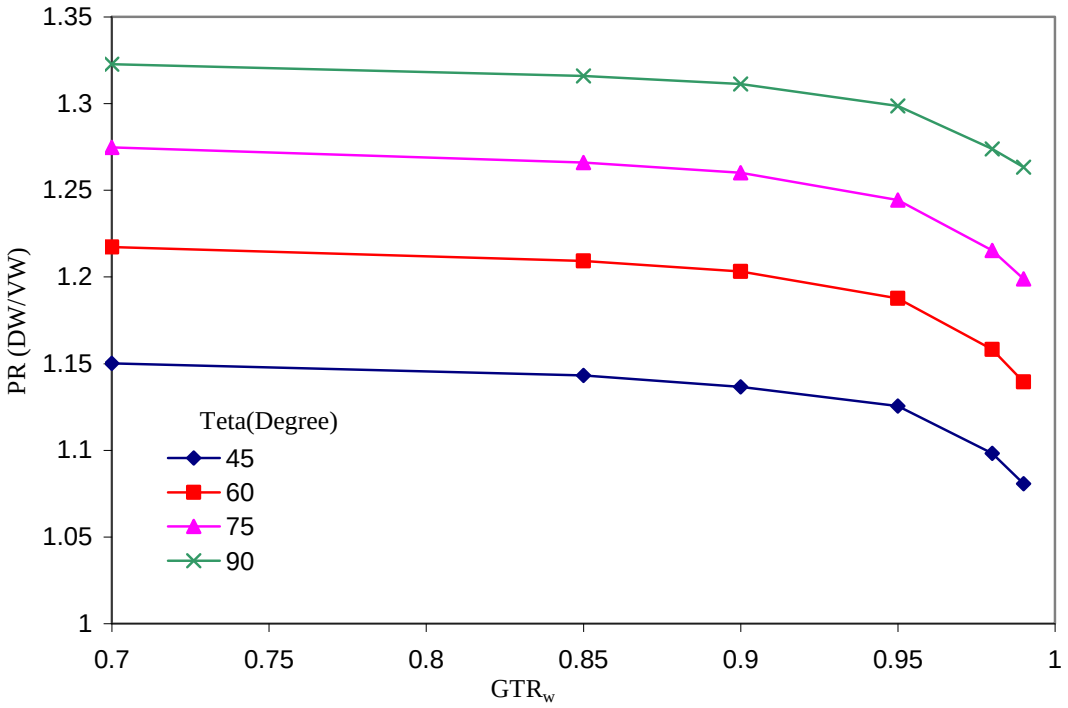

Figure 4.34: Productivity ratio (deviated to vertical well) versus GTR_w at different deviation angles, L_{DW}=15 m , h=15 m, P_w=1725 psi and P_{res}=1765 psi.

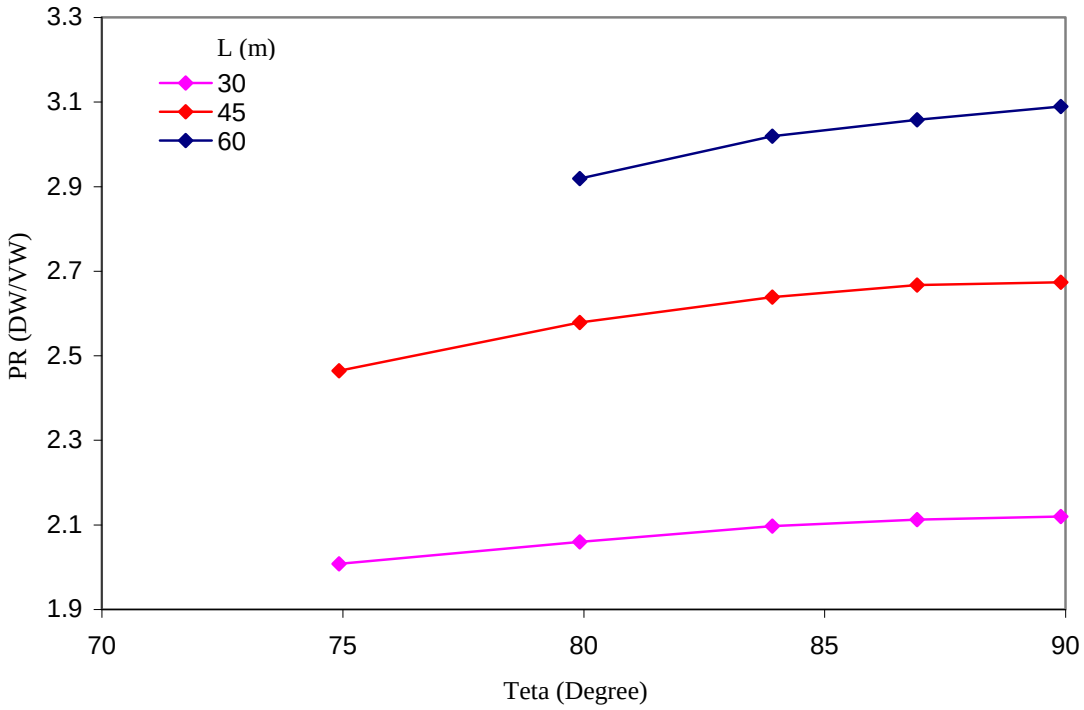

Figure 4.35: Productivity ratio versus deviation angle at different well lengths, GTR_w=0.7, $\Delta p = 50$ psi, $P_w = 1800$ psi, $r_w = 0.07$ m and $h = 15$ m.

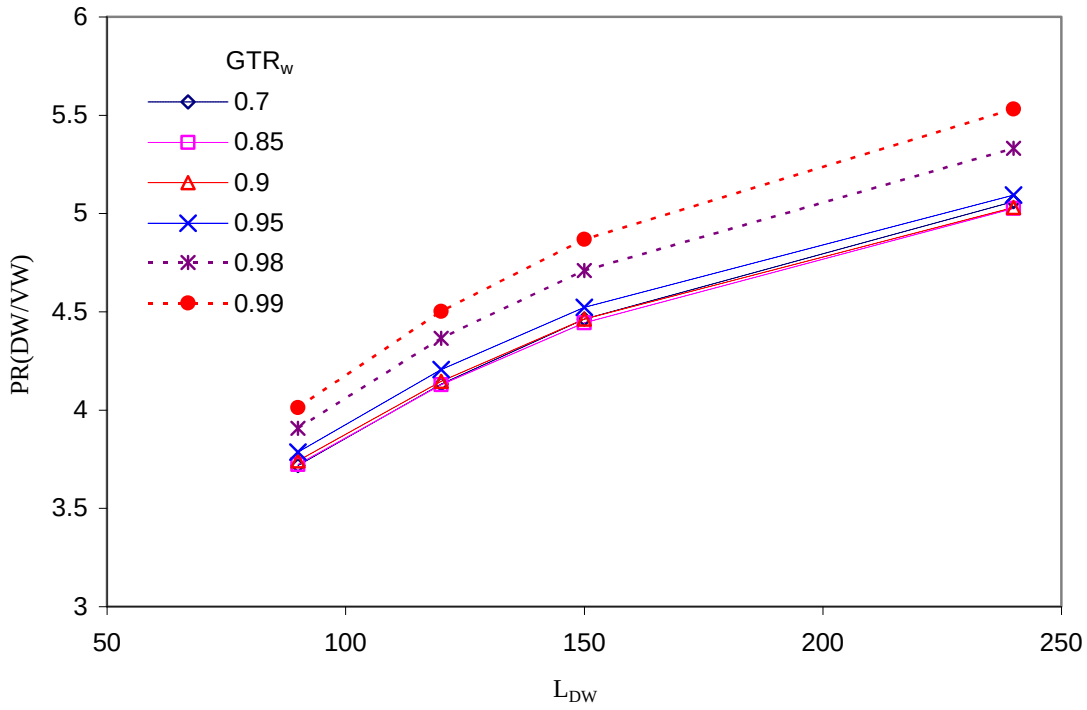

Figure 4.36: Productivity ratio of a DW with deviation angle of 87^0 to a VW versus the length at different GTR_w, h=15 m, P_w=1725 psi and P_{res}=1765 psi.

CLEANUP EFFICIENCY OF HYDRAULICALLY FRACTURED WELLS

5.1 INTRODUCTION

It is well documented that hydraulic fracturing, although generally a successful practice, sometimes does not respond as expected. Ineffective fracture cleanup is one of the main reasons put forward to explain this underperformance. Fracturing fluid (FF) is one of the most important components of hydraulic fracturing treatments. These fluids create fractures and transport the proppants, which in turn prevent the closure of the fracture after treatment. Fluid cleanup after treatment is meant to remove the fracture fluid from the fracture and the matrix.

Fracturing fluid (FF) impairs the gas production through various mechanisms, by invasion into the matrix and fracture. Over past four decades, numerous studies have been conducted to investigate the effect of fracturing fluid on the well performance of hydraulically fractured wells. The laboratory tests performed by Cooke (1973 and 1975) demonstrated the effect of fracturing fluid residue (FFR) and reservoir environment (closure pressure & reservoir temperature) on the fracture conductivity during the cleanup process. He developed a theoretical model to calculate fracture permeability (k_f) reduction, based on the volume of FFR after it degrades in the fracture and decreases the fracture porosity. He also measured the reduction of fracture porosity as a function of closure pressure and reservoir temperature and presented the results in the form of a chart. These latter results can also be used to calculate further fracture permeability reduction due to these effects, using the same equation developed for calculation of k_f reduction due to FFR.

Holditch (1979) studied the effects of fracture face (i.e., matrix blocks adjacent to the fracture) damage, including the elements of FF saturation and permeability reduction in this area, on the gas productivity from hydraulically fractured gas wells, using a finite difference based numerical simulator. The FF was defined as water in this work. The effect of capillary pressure in low permeability reservoirs was found noticeable in the case of pressure drawdown that did not exceed the formation capillary pressure. The non-Darcy flow has been considered but the effect of FFR on the fracture conductivity was not considered in this study. He reported that the complete water block occurs only when the permeability of the invaded zone beyond the fracture reduces by 99.9% or the pressure drawdown does not overcome the capillary (Laplace) pressure in

the invaded zone. The depth of FF invasion in their model was 5 in, with uniform distribution around the created fracture.

Gdanski et al. (2005) extended the previous work performed by Holditch (1979) to clarify the issues related to the two-phase flow of gas and FF and permeability reduction in the matrix invaded damaged zone. Their results, based on their numerical model, showed that the fracture face damage significantly decreased gas production if the permeability of the matrix in the damaged zone is reduced to 1% of the original matrix permeability. This is somewhat similar to the results of Holditch's work. They also showed that a higher original capillary pressure in the formation increased the effect of the damage on the gas production. The water was imbibed in the matrix rapidly, in the case of the higher capillary pressure, but it decreased the FF (defined as water) saturation in the fracture blocks. This, however, would increase the permeability of the propped fracture region, something that they did not consider.

The other parameters, which might affect the cleanup efficiency, such as filter cake (Wang 2009), yield stress (Barati 2008), non-Newtonian fluid (Friedel 2006), unbroken fracture fluid (Voneiff 1996), and capillary pressure (Holditch 1979) have also been studied to some extent.

The main purpose of this exercise is to study the cleanup efficiency in hydraulically fractured gas and gas-condensate wells. The author has extended the previous work to clarify some of the uncertainty about the impact of pertinent parameters affecting the cleanup efficiency in gas reservoirs. The author has also been able to reproduce the simulation results reported by Holditch (1979), which have been the basis of many numerical studies since then.

In particular the author considered two methods in the simulation process, to obtain a more realistic invasion of FF into both the fracture and matrix. This often overlooked in some of the numerical simulations of the process (e.g., Holditch, 1979, Adegbola, 2002 and Gdanski et al., 2005) and proved to be one of the main reasons for conflicting reports on the performance of cleanup efficiency found in the literature, (e.g., Bennion et al., 2000, Gdanski et al., 2005).

A comprehensive sensitivity exercise was conducted to evaluate the impact of following factors on the cleanup efficiency of a hydraulically (gas or gas-condensate) fractured well: fracture fluid residue and reservoir conditions (closure pressure and reservoir temperature) (k_{fd}), the fracturing fluid (FF) viscosity variation during cleanup, matrix capillary pressure (P_{cm}), FF invasion into matrix (i.e., the saturation of FF into the matrix, S_{ffm}), a reduction of permeability of the matrix invaded zone (k_{md}), an

increase in capillary pressure of the matrix invaded zone (P_{cmd}), initial water saturation, hysteresis, FF relative permeability and pressure drawdown.

The author first identified some of the key pertinent parameters and proposed a new method to simulate a more realistic FF invasion into the matrix and fracture. This proved to be one of the main reasons of the contradictory results found in the literature. None of these studies have embarked on the much needed extensive investigation of variation of all the pertinent parameters.

In the second part, based on the results of the first part, the author developed a methodology to further evaluate the effects of key important parameters varying over their practical ranges.

A two-level full factorial statistical experimental design method was used to sample a reasonably wide range of variation of pertinent parameters, covering many practical cases. The variation of a total of 16 parameters describing the matrix and fracture relative permeability of gas and FF and matrix capillary pressure curve were studied for two separate FF volume values.

Due to the large number of simulations required for this purpose, a computer code was developed using MATLAB mathematical package, which automatically linked different stages of the simulations conducted using ECLIPSE100. The details of the structure of the computer code will be explained in a separate section. Based on the experience gained from the first part and the procedure followed in the industry, the simulation of FF invasion was modified to reduce the required CPU time.

Since the efficiency of cleanup is significantly affected by the injected volume of FF, a sensitivity study was also conducted to compare the FF volume values used in this study with those estimated using the conventional methods followed in the industry to simulate this process. This exercise also aimed at evaluating the validity of the simplified method for injection of FF introduced in this part.

In these simulations, the gas production loss (GPL), compared to the 100% cleanup case, was also calculated automatically as an output data for each run, at different production periods after the FF injection. Different linear response surface methods, with and without interaction parameters, were used to map the GPL variations.

Presenting the results of over 130000 simulations, using Tornado Charts for the main linear terms, indicated that the cleanup efficiency is mainly affected by a limited number of parameters. The results particularly highlighted the scenarios where GPL can be significant or minimal at different time intervals, as described in the last section of the second part of this chapter.

5.2 FRACTURED WELL MODEL

Here, a pre fractured single-well model was considered to simulate the process, using ECLIPSE 300 numerical simulator.

Generally, vertical fractures are simulated using Cartesian models rather than radial ones. This is basically due to theirs flow regime, which is considered to be mainly linear from the reservoir into the fracture face, and through the fracture towards the wellbore. However, flow can be considered pseudo-radial in locations far away from the fracture. The significance of the latter flow regime depends upon how much the fracture improves the productivity index compared to an un-fractured case.

In this study it was assumed that the fracturing fluid (FF) is injected into a single-well model which has already been fractured, i.e., using an optimized Cartesian grid model. The dimension of the first row of grids in Y direction (dy) allocated to the fracture was equal to the same as fracture width, then it was gradually increased to reservoir boundary. The reservoir was modeled by one vertical cell, neglecting gravitational segregation.

FF was injected in the well at a maximum rate of 1000 bbl/day until the whole length of the stationary fracture was invaded with FF, to give a more realistic FF invasion. In this proposed method, injection time varied between 2 to 16 days depending on the mobility of the FF and capillary pressures in the matrix. Capillary pressure and highly viscous FF increased the time required to invade all the fracture cells, i.e. increased the injection time. Next the well is shut down for the next two days. In the second period, production time, the well is producing FF with gas, in the case of gas, or gas and condensate, in the case of gas-condensate fluid system, for 400 days unless otherwise stated. It will be later demonstrated that one of the main reasons for the conflicting reports on the impact of pertinent parameters on cleanup efficiency is the method used to simulate the FF invasion. In this exercise, the Holditch (1979) simulation results are reproduced as described in the section Results of Holditch Fracture Well Model. These results are also compared with the level of the FF damage when the new method is applied to the Holditch fracture well model.

The impact of FFR in the simulation models has been considered using the theoretical model given by Cook (1973 and 1975) to predict k_f reduction. According to his model, k_{fd} can be estimated using the Kozeny model, assuming the effect of surface area was negligible as follows:

$$\frac{k_{fd}}{k_f} = \left(\frac{\phi_{fd}}{\phi_f}\right)^3 \tag{5.1}$$

where k_{fd} and ϕ_{fd} are the permeability and porosity after damage; k_f and ϕ_f are the undamaged original permeability and porosity.

Here, initially, based on Cook's recommendation, the fracture porosity has been reduced from 35% to 20% due to stress and temperature effects. Then, according to his experimental results, the maximum FFR volume per volume of fracturing fluid was considered to be 30%. In this study, it was assumed that this amount of residue remained in the fracture during early production time, which was not simulated, i.e., it happened instantly in the simulations after the injection period. This FF liquid saturation was monitored for each simulation grid block and used to calculate the reduced porosity in the fracture. The reduced porosity values were then used in Equation 5.1 to calculate the reduced value of fracture permeability for each grid block. The new reduced liquid saturation was calculated for the fracture blocks for the production period. The restart file produced from the injection period, with the modified saturation, porosity and permeability, as described, was used as the initial conditions for the production period. For the cases without considering fracture fluid invasion into the matrix, the FF saturation within the matrix was changed to zero.

For the simulation runs in which the effect of an increase in matrix capillary pressure (P_{cm}) was investigated, it was assumed that matrix capillary pressure was affected by a reduction of permeability and porosity in the matrix invaded (damaged) zone. The J-function was used to correlate the permeability and porosity with P_c in this study, as follows:

$$J - function = \frac{Pc}{\delta}\sqrt{\frac{k}{\phi}} \tag{5.2}$$

Combining the above equation with Equation 5.1 gives the increased matrix capillary pressure (P_{cmd}) as a function of permeability reduction, as follows:

$$\frac{P_{cm}}{P_{cmd}} = \left(\frac{k_{md}}{k_m}\right)^{\frac{1}{3}} \tag{5.3}$$

During injection time, FF was imbibed into the matrix through the fracture faces and then was produced with the hydrocarbon fluid in a drainage process. Here, the capillary pressure and relative permeability hysteresis processes could play a role to control the cleanup of FF from the invaded zone. When investigating this process, the author

benefited from available formulations in the literature relating the imbibition and drainage processes.

Naar (1961) developed a model to establish a relationship between drainage and imbibition saturation expressed by:

$$S^*_{w,imb} = S^*_{w,dr} - \frac{1}{2} S^*_{w,dr} \tag{5.4}$$

The drainage capillary pressure curve used in this study comprised the experimental capillary pressure data measured in the Gas Condensate Group laboratory by the mercury porosimetry method. The author used, where stated, the above formulation to predict capillary pressure curve during the imbibition process (injection period). Figure 5.1 shows these two curves.

It is well documented that the hysteresis of the wetting phase relative permeability is negligible, whereas it decreases the relative permeability to the non wetting phase. In this study, the gas imbibition relative permeability to FF $(k_{rgff})_{imb}$ was that measured in the laboratory. This curve matched the exponent of the Corey type k_r curve with a value of 3. The author assumed a Corey exponent of 1.25 to obtain the higher drainage relative permeability value, $(k_{rgff})_{dra}$, as shown in Figure 5.2.

As mentioned earlier, for most simulation runs, the measured capillary pressure and relative permeability curves were used for the different scenarios studied here.

Reservoir Properties

The reservoir has an external radius of 5,300 ft producing with an initial reservoir pressure of 6,800 psia. The thickness of the reservoir model is 300 ft. A core of a sandstone reservoir rock with a low permeability value of 0.18 mD and porosity of 17% was used to measure matrix properties and yielded a reservoir pore volume of 260MMrb. This core has a measured single-phase inertial factor of 1.06E12 m^{-1}. In the case of simulating gas reservoirs the flowing bottom hole pressure was kept above the dew point, but for the gas-condensate runs it was allowed to fall below the dew point pressure.

Fracture Properties

A fracture with a permeability of 15 D and proppant porosity of 30% was used. A porous medium with a fracture packed with proppant was used to experimentally determine the required base relative permeability. The author has not studied the impact of the variation of relative permeability with interfacial tension and velocity due to

positive coupling and negative inertial effects (Jamiolahmady et al. 2006). The propped fracture had an experimentally measured single-phase inertial factor of 3.51E5 m^{-1}.

In this study, a propped fracture length of 400 ft and width 30 mm has been simulated. The optimized grid is 30x47 in the x and y directions.

Reservoir Fluid Properties

To simplify the internal calculation of the simulator, a model gas condensate fluid (C1-nC10 binary mixture) with 20 v/v maximum liquid dropout (MLDO) in the constant composition expansion test at the reservoir temperature of 250^{o}F was used in this study, unless otherwise stated. The corresponding dew point pressure value was 5280 psia. For the case of single-phase gas, the controlled wellbore flowing pressure of 5500 psia was used for the producing well, whilst for studying the two-phase flow of gas and condensate, the controlled wellbore flowing pressure was 4400 psia at the wellbore radius of 0.23 ft.

Fracturing Fluid Properties

The hydraulic fracturing fluid (FF) was defined as water but its relative permeability was varied to consider water or oil based FF. It was assumed that water-based FF behaved as the more wetting phase, compared to the condensate. The two-phase FF to gas relative permeability (k_{rffg}), in both fracture and matrix, was obtained using a Corey type relative permeability curve with n=6 but with end points similar to the corresponding values for condensate to gas relative permeability (k_{rcg}). That is, k_{rffg} is equal to k_{rcg} at the same residual gas saturation. Furthermore, it was assumed that there was no residual FF saturation. However the k_{rffg} is below 0.01 at FF saturation below 0.2 and 0.4 in the matrix and fracture, respectively. Figures 5.3 (a) and (b) show k_{rffg} and k_{rcg} curves used for matrix and fractures, respectively. The corresponding gas to condensate relative permeability (k_{rgc}) curves are also displayed in these two figures. The relative permeability of the oil based FF was similar to that of the condensate. The corresponding Corey exponents for k_{rcg} for matrix and fracture were around 2.2 and 1.4, respectively.

The FF viscosity during the injection period was always 10 cp. However, during the production period, two scenarios were considered: 1) when FF was produced with the same viscosity as it was injected or 2) it was degraded, resulting in a reduced viscosity (1 cp). This latter option also facilitated the modelling practice when there was an initial water saturation present in the model, as FF has been defined as water in the

simulations. However, when considering the hysteresis effects the FF during injection period is also 1 cp to increase the FF depth of invasion which would exaggerate the hysteresis effect.

5.3 RESULTS OF FRACTURED WELL MODEL

Numerous sensitivity studies were conducted to evaluate the impact of pertinent parameters on the cleanup efficiency of gas and gas-condensate hydraulically fractured wells. The author uses the following abbreviations to represent the prevailing conditions for a selected number of scenarios:

P_{cm} refers to the cases that the measured capillary pressure curve (mercury porosimetry) of the reservoir rock has been considered.

FFvP refers to the cases that FF viscosity was either 10 or 1 cp during the production period.

k_{fd} refers to the cases that the effect of a reduction in fracture permeability, as described previously, was included in the simulation.

k_{md} refers to the case that the fracture face damage, i.e., permeability reduction for matrix blocks invaded by FF, was studied.

P_{cmd} refers to the cases that the impact of k_{md} on P_{cm} was considered for the matrix invaded zone as described previously.

The author also varied the Corey exponent to vary relative permeability of the fracturing fluid (FF), i.e., n-k_{rffg}=6 or 1.2 for water based FF, and n-k_{rffg} =2.2 for oil based FF and n-k_{rgff}=1.25 for the scenario investigating the hysteresis effect. For hysteresis cases, as mentioned before, the corresponding imbibition capillary pressure was also employed.

The percentage of loss of gas production GPL% is defined as the reduction in gas production compared to the case with 100% cleanup, unless otherwise stated. For 100% cleanup, the saturation of fracturing fluid in the matrix and fracture is zero for the production period of the simulation, with no fracture or matrix damage.

In our simulations, the effect of the injected FF leakoff into the matrix, S_{ffm}, i.e., the saturation of FF into the matrix, was investigated by either artificially assigning a zero value to it or using the value obtained during the injection period of FF. GPL% due to S_{ffm} is obtained by subtracting the corresponding value when considering both k_{fd} and S_{ffm} effects from that of the case considering only the k_{fd} effect.

The simulations index runs R1 and R2 refer respectively to the cases with both S_{ffm} and k_{fd} effects ignored and both considered. R3 and R4 refer to the cases whereby the individual impact of S_{ffm} and k_{fd} has been considered, respectively. The same index reference is applied for the simulations with 1 or 10 FFvP, with or without P_{cmd} and with and without S_{wi}.

Single-Phase Gas

P_{cm}=0

In this section, the matrix capillary pressure is assumed to be zero. Figure 5.4 compares GPL compared to 100% cleanup case for simulation runs indexed R1-R4 with two FF viscosity values of 1 and 10 cp during the production period. For the simulation runs with FF viscosity 10 cp, when the reduction in fracture permeability and FF invasion into the matrix was neglected, R2, only 6% loss in gas production (GPL) was observed. However the combined effect of both k_{fd} and S_{ffm} in R3 caused a significant GPL, i.e., 66%. In runs R3 and R4 the individual impacts of k_{fd} and S_{ffm} were investigated. The results demonstrate 45% GPL for the latter (R5) compared to 15% GPL for the former (R4) confirming the more pronounced effect of k_{fd}. It should be noticed that for the cases considered, fracture permeability is significantly reduced, i.e. by 94% from 15 Darcy to around 1 Darcy, due to the impact of FF. It should be noted that fracture permeability reduction is different for different fracture blocks, depending on the FF saturation.

The resultant higher mobility of FF, when its viscosity is reduced to 1 cp, improved the FF cleanup from the matrix and fracture, which in turn resulted in a lower reduction in gas production for all the scenarios under study, i.e. simulation runs indexed R1-R4 in Figure 5.4. For example, considering the combined effect of both k_{fd} and S_{ffm}, R2 with FFvP=1cp, gives 52% GPL, a reduction of 14% compared to the case with non degraded fracturing fluid, for the same prevailing conditions, i.e., 66% GPL for R2 with FFvP=10cp. It should be noted that using a FF with lower viscosity will increase the FF invasion depth during the injection period, i.e. increasing the S_{ffm} effect.

A 90% reduction in the permeability of the matrix invaded zone in R5 (90%-k_{md}) only increased GPL% by a further 6%, from 52%, corresponding to R2, to 58%, Figure 5.5. A further 20% reduction (72% GPL) was noted when a 99% reduction in matrix permeability in R5 (99%-k_{md}) was included in the simulation. These values are much higher than the values reported by Holditch (1979) and Gdanski et al. (2005), due to a more realistic FF invasion, as described in the next section.

If S_{ffm} was assigned as zero and only k_{fd} was considered, it was noted that GPL was decreased by 12% and 13% for 90 and 99% reduction in k_m, respectively, compared to R3 with 7% GPL. This demonstrates the more pronounced effect of FF invasion into the matrix over a reduction of the matrix permeability.

Single-Phase Gas

P_{cm} #0

P_{cm} increases the FF leak off into the matrix with a larger depth of invasion. In the case of R1, where both k_{fd} and S_{ffm} are ignored, this results in a lower FF saturation in the fracture, and hence, higher gas production, i.e., 0.61 % GPL in R1, compared to 5% in R1 for the case with P_{cm}=0, Figure 5.6. Comparing the results of R4 cases without P_{cm}, 45% GPL, and with P_{cm}, 30% GPL, [both with S_{ffm}=0], highlights the impact of the reduction in FF saturation in the fracture, resulting in a reduction in GPL, Figure 5.6. However, when both kdf and S_{ffm} are considered, GPL increases from 66% in R2 without P_{cm} to 74% with P_{cm}: a further reduction of 8% due to P_{cm}. A comparison of gas production loss in R3 with $P_{cm,}$ (32% GPL) with the corresponding value without $P_{cm,}$ (15% GPL), demonstrates that the negative impact of P_{cm} is more pronounced when only S_{ffm} is included in the simulation.

These results highlight the importance of FF blockage in the matrix blocks adjacent to the fracture.

Since S_{ffm} is set to zero in R4, with FFvP=10 cp (30% GPL) and degraded FF, FFvP=1 cp (29% GPL), there is minimal difference between the gas production in these two scenarios, Figure 5.7. The impact of a reduction of FF viscosity during the production period is, however, evident when comparing R2 results for these two cases. In both these two runs both k_{fd} and S_{ffm} have been considered but the higher mobility of FF during the production period in the former reduces GPL from 74% to 54%, as can be seen in Figure 5.7. This difference of 20% is more than that between the corresponding R2 runs with P_{cm}=0, which showed 66% GPL for FFvP 10 cp case, compared to 52% GPL for the FFvP 1 cp case.

It was mentioned earlier that the inclusion of k_{md} in R5 with 90%-k_{md} and 99%-k_{md}, resulted in 58% and 73% GPL, respectively, which were not significantly different compared to the R2 case without $k_{md,}$ with 52% GPL. on the other hand , considering 90% and 99% permeability reduction in the matrix invaded zone in R5 (90%-k_{md}) and (99%-k_{md}), both with P_{cm}, increased GPL to 70% and 85%, respectively, as shown in Figure 5.8. Here, the combined effect of k_{md} and P_{cm} in R5 has increased the negative

impact of FF blockage in the blocks adjacent to the fracture, compared to the corresponding R2 case without k_{md} and with 54% GPL.

Two further simulations were performed considering an increased capillary function (P_{cmd}) for the matrix invaded zone, with 90% and 99% reduction in permeability. Figures 5.9 and 5.10 present the total gas and FF production versus time for Run 5 with and without considering P_{cmd}. The results show no significant increase in GPL, Figure 5.9. This is mainly due to the high pressure drawdown, 1300 psi, compared to the corresponding capillary pressure curve used for the invaded zone. However, the total FF production decreased, due to higher capillary pressure in the damage zone of the matrix in R5 with $P_{cmd,}$ compared to that without P_{cmd}, Figure 5.10. This is in agreement with the results of Holditch (1979) and Gdanski (2005).

The pressure drawdown was decreased to 600 psi. It was noted that the difference between P_{cm} and P_{cmd} was still not significant. However, when the pressure drawdown was reduced to an unrealistically low value of 200 psi the impact of P_{cmd} was noticeable.

S_{wi} =17.5%

Next the impact of the presence of initial water saturation on the performance of cleanup efficiency was investigated. Comparing the results of R4 (17% GPL) and R3 (27% GPL) with S_{wi}=17.5% with the corresponding ones without S_{wi}, (29% GPL) and (54% GPL), indicates that the presence of water has significantly improved the cleanup efficiency, Figure 5.11. This is mainly due to a lower loss of fracturing fluid into the matrix blocks adjacent to the fracture. The presence of S_{wi} has reduced the Laplace pressure differential and hence, the amount of FF invasion into the matrix. This reduces the impact of FF blockage in the matrix blocks adjacent to the fracture. It should be noted that S_{wi}=17.5% has already reduced the gas production by a factor of 2.8 for 100% cleanup, compared to the corresponding value without initial water saturation.

It was noticed that 90% and 99% permeability reduction in the matrix invaded zone in R5 caused 20% and 44% extra damage, respectively, compared to R2 with 27% GPL, Figure 5.12. This indicates that the effect of permeability reduction is more pronounced in this case, compared to the corresponding values (16% and 32%, respectively) for the cases without S_{wi}, Figure 5.8.

FF Relative Permeability

The effect of the FF relative permeability on the cleanup efficiency was studied by decreasing the Corey exponent from 6 to 1.2. The corresponding krff curves are shown

in Figure 5.3. Comparison of GPL in R2 for the case with higher k_{rffg} (n_{ff}=1.2) with the corresponding value for lower k_{rffg} (n_{ff}=6.0) demonstrates that the improved relative permeability of FF has reduced GPL from 58% to 49%. This is mainly due to a better matrix cleanup , noting that GPL due to S_{mff} is reduced by half (from 18% to 9%) in the latter compared to the former, Figure 5.13.

Hysteresis Effect

Invasion of FF into the matrix is an imbibition process during the injection period, whilst its production is a drainage process. In the previous simulations, gas relative permeability (k_{rgff}) has been that of the imbibition, Figure 5.3, and the matrix capillary pressure curve (P_{cm}) was that of drainage processes, Figure 5.1. Hence, in a series of simulation runs, the impact of hysteresis was investigated by changing the matrix k_{rgff} curve to a drainage curve (Figure 5.2) for the production period and P_{cm} to that of imbibition during the injection period. Furthermore, to exaggerate the effect of hysteresis in these simulations the viscosity of FF injected was 1 cp rather than 10 cp used for other simulations reported in this section, which increases the depth of FF invasion. Table 5.1 lists the prevailing conditions for a selected number of scenarios. Column 1 is an index. Column 3 shows the production time for each simulation run. In this exercise two production periods of 300 and 400 days were considered to investigate the impact of hysteresis on the production duration. Pc and relative permeability curves used for the selected case are listed in column 2. Column 4, k_{fd} and S_{ffm}, refers to the cases where the effect of a reduction in fracture permeability and the FF invasion into the matrix, as described previously, has been included in the simulations, respectively. As mentioned previously, for 100% cleanup, the saturation of fracturing fluid in the matrix and fracture is zero for the production period of the simulation with no fracture or matrix damage, i.e., runs indexed Rh1a-Rh1f. These cases are highlighted with bold index font in Table 5.1. The GPL values reported for Rh2a-Rh3a, Rh2b-Rh3b, Rh2c-Rh3c, Rh2d-Rh3d and Rh1e and Rh1f are those based on a 100% cleanup case of Rh1a, Rh1b, Rh1c, Rh1d, Rh1e and Rh1f, respectively.

In Rh1a-Rh3a both Pc and kr hysteresis were considered during 300 days of production, whilst in Rh1c-Rh3c and Rh1d-Rh3d only kr hysteresis was included, with production reported after 300 and 400 days, respectively. Rh1b-Rh3b corresponds to cases without hysteresis with both drainage kr and Pc curves used for the 300 days of production. In Rh1e-Rh3e and Rh1f-Rh3f, last two sets in Table 5.1, similarly to the

other simulations reported in this section, imbibition kr and drainage Pc curves was considered for both 300 and 400 days of production, respectively.

It is noticed that inclusion of the hysteresis effect for both kr and Pc in Rh2a slightly increased the GPL values compared to Rh3b (by 2%). When the effect of hysteresis on Pc was assumed to be negligible, for runs Rh1c to Rh3c, this difference was reduced to 1%. The higher GPL in these simulations is mainly due to the lower matrix imbibition k_{rgff} curve used for the hysteresis effects in Rh2a and Rh2c, compared to the higher matrix drainage k_{rgff} curve used for both injection and production periods in Rh2b. However, when Rh2a and Rh2c are compared with Rh2e where the lower matrix imbibition k_{rgff} curve has been used for injection and production periods, the GPL values are lower for the latter compared to the former. Increasing the production run to 400 days, in Rh1d-Rh3d and Rd1b-Rd3b, lowers GPL, because of higher production of FF. This is more pronounced for Rh1d-Rh3d with higher krg curve. It is noted that GPL due to k_{fd} remained the same for all these runs because the FF saturation in the matrix is set to zero for obtaining these GPL values. In summary, the impact of hysteresis is not significant in our results.

$P_{cmd}=0$

The capillary pressure within the matrix can usually be reduced by using surfactants in fracturing treatments. In another attempt, the effect of surfactants in reducing the matrix capillary pressure and its impact on FF damage was investigated. In this study, for an ideal case, it was assumed that the active agent decreased the capillary pressure in the matrix invaded zone to zero during the shut down time period. The effect can be observed during production time. It is noticed that this decrease in capillary pressure improved the total FF production; however, it increased GPL in R2 from 54% to 65% because the facilitated flow of FF impairs the flow of gas in the fracture. However, when the author increased the production time to fifty five years for these two simulations, it was noted that no further FF production was observed and FF was completely removed in the case with $P_{cmd}=0$, restoring the gas permeability, Figure 5.14.

Gas/Condensate/Water (three phase) Flow

The total gas production values obtained for the R2 to R4 cases with gas and condensate flow are shown in Figures 5.15. Comparing the results of cases when bottom hole pressure (P_{bh}) in the production period is below the dew point pressure (Pdew), (R2

50%), with the corresponding ones with $P_{bh}>P_{dew}$, (R2 54%, Figure 5.7) indicates that the presence of condensate has somewhat facilitated the flow of FF, giving a slightly lower reduction in gas production. The same observation was noted for the results with S_{wi}=17.5% and those of R5 with k_{md}=90% and 99%. Furthermore, a comparison of R5 with P_{cmd} for the case with $P_{bh}<P_{dew}$, further confirmed the low impact of discontinuity between P_{cm} and P_{cmd} for these simulations with high pressure drawdown.

Results of Holditch Fracture Well Model

In this section, the source of conflicting reports found in the literature on the impact of some of the parameters affecting cleanup efficiency in hydraulically fractured wells is addressed. First, some of the Holditch simulation results that were reproduced to confirm the integrity of our approach are presented. Then, the results of a series of sensitivity studies that were conducted to clarify the impact of pertinent parameters are discussed.

Holditch Reproduced Results

The Eclipse 100 numerical reservoir simulator was used in this exercise. Details of the fracture and reservoir properties were those from the Holditch paper, Table 5.2. The gas density and viscosity values were 0.032 lb/ft3 and 0.014 cp, respectively.

The total gas production figures were not reported in the original published paper. Hence, the GPL% values after 1-year of production for the damaged case compared to those obtained for the undamaged case as reported by Holditch (Table 5.2 of his paper) were used for comparison.

The viscosity of injected water was 0.3 cp. The fracture conductivity values were 100, 500 and 4000 (md-ft). The bottom hole flowing pressure of the single-phase gas reservoir, was 2000 psi. 1200 bbl of FF was considered as injected FF volume into the fracture. The depth of the damaged zone in the FF invasion zone into the matrix was considered uniform and equal to 5 in across the fracture. They did not look at the actual FF distribution in the matrix invaded zone. The capillary pressure and relative permeability curves reported by Holditch (1979) were used unless otherwise stated.

Table 5.3 (a) and (b) show the original results of Table 5.2 from Holditch and the author's simulations reproducing his results. It is noted that there is a good agreement between the two.

Based on his results, Holditch concluded that the presence of FF inside the fracture face and its damage to the permeability of this zone does not result in the loss of gas

production unless there is 99.9 % matrix permeability reduction in the matrix invaded zone. However Bennion (2002) showed that for low permeability gas reservoir, fracture face damage due to the effect of fracture fluid inside the matrix could cause significant damage to the gas production. As will be shown in the next section, when the results of our sensitivity studies are discussed, the main reason for these conflicting reports is the method of simulating the FF invasion.

Further Sensitivities

As mentioned above, Holditch (1979), in his simulations, assumed a fixed volume of injected FF with a uniform depth of invasion. However Figure 5.16, which shows the FF distribution, demonstrates that this is not a realistic assumption. It should be noted that in Figure 5.16 the size of grid blocks in the y-direction has been enlarged, i.e. they are not in real scale, to show the FF distribution more clearly. In this simulation 1227 bbl of FF was injected into the pre-fractured single well model that was used in Holditch's study. Although this amount of FF is very similar to the 1200 bbl of injected FF in his model, the FF distribution within the matrix blocks close to the fracture in this simulation is more than 5 Inches and more importantly, it is not uniform, i.e., the resultant damage of the matrix invaded zone could be greater and is always nonuniform. Furthermore, it is expected that the amount of injected FF and its distribution vary with rock, fracture and FF characteristics.

Below, the impact of some of the pertinent parameters on the amount of injected FF and the resultant distribution of FF is studied. The amount of injected FF for each case was estimated based on having all the fracture blocks invaded by FF.

Here, a different method was used to calculate GPL due to the impacts of FF on fracture permeability (k_{fd}), compared to that used in the previous section. That is, fracture permeability was uniformly reduced for these grid blocks. This procedure somewhat has facilitated the simulation exercise.

FF Viscosity

Here, fracture permeability was 96 Darcy and k_{fd} and k_{md} were not considered and GPL was due only to the presence of FF in the matrix invaded zone, S_{ffm}. Fracture fluid viscosity (FFv) was either 1 or 10 cp. Increasing FF viscosity increased FF injected volume from 1227 to 2206 (bbl). The FF invasion depth also increased as the injected FF volume increased. This resulted in 2.9% further reduction in GPL from 0.22% for the former, compared to 3.1% for the latter, after 400 days of production.

It was noticed that during the short term production period, GPL due to S_{ffm} was noticeable for the case with FFv of 10 cp, i.e. GPL values after 20 and 50 days were 25.8% and 14%, respectively. The corresponding values for FFv of 1 cp were minimal, 2.9% and 1.5% respectively. Figure 5.17 shows the saturation profile for the first fracture grid block, nearest to the wellbore. The same trend is also observed for the whole blocks across the fracture. Looking at the FF saturation inside the fracture, Figure 5.17, it is noted that increasing FF viscosity, reducing its mobility, initially results in higher average FF saturation inside the fracture, which in turn decreases the effective gas permeability. However, because average FF saturation inside the fracture decreases sharply with increasing the production time the effective permeability to gas inside the fracture is restored later on. That is, gas production rate (GPR) values for the case with less FF viscosity (higher mobility) were initially higher than the corresponding values for the case with higher FF viscosity but later on they were similar, Figure 5.18.

Fracture Permeability Reduction (k_{fd})

It was noted that when fracture permeability was decreased from 96 to 5 Darcy during production period, the combined effect of FF invasion into the matrix (S_{ffm}) and fracture (k_{fd}) increased GPL significantly from 3% to 51% for FFv=10 cp,. GPL due to S_{ffm} also increased from 3% without k_{fd} to 18% with k_{fd}. These observations were mainly due to the impact of average FF saturation inside the fracture. That is, decreasing fracture permeability during the production period from 96 to 5 Darcy (moderate k_{fd}) results in an increase of FF saturation inside the fracture, compared to the corresponding values for the former one without k_{fd}, Figure 5.19. This decreases the effective gas relative permeability and hence, gas production. The same observation was noted if k_f was reduced to 1 Darcy (high k_{fd}).

In the next simulation the initial fracture permeability during injection was reduced to 15 D whilst the fracture permeability during production was kept at 5 Darcy. This increased the injected time, injected FF volume, and hence, the FF depth of invasion. Therefore, GPL increased from 0.2% with k_f=96 D to 34% with k_f=15 D for FFv=1 cp.

When k_f was reduced to 1-D for the latter case, GPL was significantly increased by 40%, from 34% for k_f=5 D to 74% for k_f=1 D, Figure 5.20. This figure also shows that the damage due to S_{ffm} for the case with k_{fd}=5 Darcy, 13% GPL, is half that with K_{fd}=1 D, 24% GPL.

Permeability Reduction in Matrix Invaded Zone (k_{md})

Considering k_{md} for the case with moderate fracture permeability damage, k_{fd}=5 Darcy, Figure 5.21, increased GPL from 34 % for the case without k_{md} (Figure 5.20), to 45%, 50 and 61% with k_{md} of 90%, 99%, and 99.9%, respectively. It should be also noticed that GPL due to S_{ffm} is pronounced for all considered scenarios, and increases gradually with the increase in the percentage of permeability reduction in the matrix invaded zone, i.e. the increase in GPL is more pronounced for higher fracture permeability reduction.

FF Relative Permeability inside Fracture

The above results indicated that the FF relative permeability inside the fracture was an important factor in reducing the fracture face damage. Therefore, a study was conducted to evaluate the impact of FF relative permeability inside the fracture on the total gas production and cleanup efficiency. Four different FF relative permeability curves were used in this part, as shown in Figure 5.22.

For all considered cases, the FF relative permeability curve C2 in Figure 5.22 was used during the injection period. The impact of FF relative permeability can be readily seen by comparing the gas production rate and FF production of theses four cases. Improving FF relative permeability inside the fracture (curves C1- C4) improved both FF and gas production rates (see Figures 5.23 and 5.24). It is noted that the effect of FF in the matrix invaded zone (S_{ffm}) in the case with highest FF relative permeability curve, C4, is negligible. It can be concluded that the existence of FF inside the matrix doesn't have any effect on the total gas production, in this case. Producing FF from the fracture readily results in restoring the fracture effective permeability to gas, i.e. the more FF is produced, the higher gas production rate.

5.4 The Statistical Approach for Studying FF Damage

In the previous section, a series of numerical simulations were conducted highlighting the importance of parameters pertinent to cleanup efficiency of hydraulic fractured wells (HFWs). A new method was introduced to model a more realistic invasion of FF into both fracture and matrix. In the proposed method, FF is injected into the fractured well at a constant rate until the whole length of the stationary fracture is invaded with FF. Then the well is shut for two days. In the second period, production time, the well is producing FF with gas. During this simulation process, it was required

to track the pressure and FF saturation during the injection period after each time step, to check whether FF has invaded all the fracture blocks or not. If this was not the case the injection simulation progressed to the next time step. This was continued until all the fracture blocks were invaded by FF, at which time the injection period ended. From the first period of simulation, the program created the included files, which were used, as initial conditions, for the second period of simulation. These pressure and saturation data were also used to make changes to some of the parameters of grid blocks invaded by FF during the production period. This was conducted manually, which proved very time consuming and cumbersome. Following this painstaking exercise for this part of the study, where a large number of simulations were required, was impossible. A computer code was therefore, developed using MATLAB mathematical package, which linked automatically the different stages of the simulations conducted using ECLIPSE100.

A two-level full factorial statistical experimental design method was used to sample a reasonably wide range of variation of pertinent parameters, covering many practical cases, for a total of 16 parameters. The impact of the following parameters was studied for two separate FF volumes: fracture permeability (k_f), pressure drawdown, matrix permeability, pore size distribution index, threshold pressure, interfacial tension, porosity, residual gas saturation and the exponents and end points of Corey type relative permeability curve for gas and FF in the matrix and fracture.

As demonstrated in the previous section, a sensitivity study was also conducted to compare the FF volume values used in this study with those estimated using the conventional methods to simulate this process followed in the industry. This exercise also aimed at evaluating the validity of the simplified method for injection of FF introduced in this part.

Since over 130000 simulation runs were required, to cover the range of variation of all parameters during the simulation process, a computer code, which automatically links different stages of these simulations, was developed.

5.4.1 Determination of Volume and Method of Injecting FF

The literature survey indicated that the following procedure is usually followed to design a hydraulic fracturing job:

1. For a given fracture length and height, the width of fracture can be estimated by either Perkins-Kern-Nordgren (PKN) [(Perkins and Kern 1961 & Nordren 1972) or Kristianovich-Zheltov Geertsma-De-Klerk (KGD) (Khristianovic SA, Zheltov YP

1955 & J. Geertsma and F. de Klerk 1969) Equations]. These equations are based on the elastic theory and porous rock stress.

2. According to Howard et al. (1957), Figure 5.25, the volume of fracturing fluid leaked off from the fracture wall (h_f) along its length (x_f) into the matrix is estimated by

$$\text{Volume of leakoff fluid} = \left(2\, C_L h_f x_f\right)\sqrt{t}\,, \tag{5.5}$$

where C_L is the leakoff coefficient (ft/min$^{0.5}$) and t is the time. The determination of C_L is described below.

3. The injected fluid volume is calculated by applying a material balance as follows:

Total volume of FF injected= leaked off FF + Fracture volume

$$2(q_i)\,t = \left(2\, C_L h_f x_f\right)\sqrt{t} + (\overline{w}_e h_f x_f) \tag{5.6}$$

The fluid leakoff coefficient is determined by either conducting a fluid loss test or analysing the results of a minifrac test also known as a fracture calibration treatment. To obtain an estimate of fluid leakoff coefficients in these two experiments, a number of simplifying assumptions have been made.

In the fluid loss test, the rate of fracture fluid leakoff into the matrix under reservoir pressure and temperature conditions is estimated by applying a pressure difference of around 1000-1500 psia to the FF, positioned above the matrix in a container. For the analysis of the results, it is assumed that the governing equations to describe the fluid leakoff from the fracture into the matrix are Darcy (Equation 5.7) and mass conservation (Equation 5.8) equations.

$$v = \frac{k}{\mu}\cdot\frac{\Delta p}{x} \tag{5.7}$$

$$v = \phi\frac{dx}{dt} \tag{5.8}$$

where x is the depth of the fracture fluid invasion in the matrix.

Combining Equations 5.7 and 5.8, after some mathematical manipulations, gives:

$$v = \sqrt{\frac{k\phi\Delta p}{2\mu t}} = \frac{C_L}{\sqrt{t}} \tag{5.9}$$

$$C_L = \sqrt{\frac{k\phi\Delta p}{2\mu}} \tag{5.10}$$

It should be noted that Equation 5.6 suggests that the leakoff coefficient depends on the pressure differential, porosity, fluid viscosity and permeability. Hence, the injected

fracture fluid volume is not constant for different rock types but rather varies proportionally to the rock permeability and porosity. FF in the above procedure has been considered to display a Newtonian behaviour.

The minifrac test, on the other hand, is a practical small hydraulic fracturing treatment, albeit without proppant, introduced by Nolte (1981) and performed at the beginning of the hydraulic fracturing operation in a field. Its objective is to determine the hydraulic fracture design parameters. Here the aim is to identify leakoff characteristics from interpreting pressure versus dimensionless time curves during the treatment. In this analysis, the FF is assumed to be a non-Newtonian fluid.

In the first part of this work, the volume of FF was calculated following an iterative procedure, during the injection time. That is, as described in Section 5.2, FF was injected until it invaded the whole fracture length. As will be discussed later, due to the large number of simulation models required at this stage, following the proposed procedure proved to require unrealistically high CPU time, even using the computer code that automatically links different stages of the process. Thus it was decided to simplify this and inject a constant volume of FF. The amount of the injected FF volume was evaluated through a sensitivity study. The injection simulation procedure was also modified to ensure the distribution of the FF more realistically through the FF walls.

In this exercise, the simulation model used in the previous part of the study was employed. Table 5.4 shows fracture properties and reservoir dimension for the pre-fractured single-well model, constructed using ECLIPSE100 and used here. The FF relative permeability curve was assumed to be the 45 degree line for the two phase flow of gas and FF. The porosity of the fracture was also considered to be 1. Here, according to the proposed procedure for FF injection, FF was injected until it invaded the whole fracture length. Since the volume of injected FF strongly depends on the fracture permeability during the injection period, in this exercise the fracture permeability during the injection period was varied to be 15, 30, 150, 300, 1500, or 10000 Darcy. Table 5.5 shows the ratio of injected FF volume to fracture volume (FVR=FF injection volume/fracture volume) corresponding to each of these simulation runs. It is noted that increasing the fracture permeability decreases the total injected FF. The lowest value, 2.5 for FVR, was obtained for the run with very high fracture permeability of 10000 Darcy.

The value for the FF leak off volume predicted by the model was also compared with those estimated using the approach followed in the literature that was described above. The rock and fluid properties listed in Table 5.4 were used in Equation 5.10 to

calculate the fluid leakoff coefficient as 0.012 ft/min$^{0.5}$. It should be noted that the differential pressure across the core was assumed to be 1000 psi (Howard and Fast, 1970). Then, using Equations 5.5, 5.6 and 5.2; FVR was estimated to be 22. This value is close to the value obtained from the simulation with the fracture permeability of around 150 D, Table 5.5 and Figure 5.26. It should be noted that the FF viscosity used in such calculations is generally greater than 0.5 cp. In a sensitivity study, the FF viscosity was increased from 0.5 to 5, 50 or 500, giving FVR of 3.1, 1.3 or 1.0, respectively. These results indicate that the FF injection volume is very sensitive to the filtrated FF viscosity.

Based on the above investigation, it was decided to inject a constant volume of FF that invades all the fracture cells instantly, i.e. they are fully saturated with FF at the start of the injection simulation period and the additional injected FF volume is distributed across all the cells adjacent to the fracture cells. In this procedure, the FF saturation distribution within the matrix, which contributes to the performance of cleanup to much greater extent than that within fracture, is obtained by the simulator but that within the fracture is assumed to happen instantly, which is somewhat consistent with what happens in reality and is reported in the literature. Thus to be able to observe the impact of pertinent parameters, the author suggested using FVR values of 2 and 5 that correspond to fracture permeabilities of 10000 and 1500 Darcy.

5.4.2 Range and Number Of Investigated Variables

Tables 5.6 and 5.7 show the ranges of variation of pertinent parameters that need to be investigated in the numerical simulations. There are 16 parameters for both the injection and the production periods in these two Tables, a total of 32 . Equations 5.11-5.14 describe the capillary pressure and relative permeability curves for data of these Tables.

$$\frac{Pd}{IFT} = 0.0075 \times K^{-0.5} \tag{5.11}$$

- Threshold pressure Pd (bar)
- Interfacial tension IFT (dyne/cm)
- Matrix permeability (K (mD))

$$\left(\frac{Pd}{Pc}\right)^{\lambda} = \frac{Sw - Swr}{1 - Swr} \tag{5.12}$$

$$k_{rw} = K \max w \times \left(\frac{Sw - Swr}{1 - Swr - Sgr}\right)^{nw} \tag{5.13}$$

$$k_{rg} = K \max g \times \left(\frac{Sg - Sgr}{1 - Swr - Sgr} \right)^{ng} \quad (5.14)$$

To conduct these simulations, the author looked at a number of designs and used 2-level full factorial design. To obtain a response surface for a system with "p" parameters using the full factorial design of the second order, the number of required experiments is 2^p.

To cover the range of variation of all 32 parameters, based on full factorial design, 4.3E9 simulations are required, for which, assuming it takes only one second to complete each simulation, it would take 136 years to complete these simulations, for one of the two FVR values. As will be described below, each simulation will take around 15 second, which gives an unrealistic simulation time of 2040 years. Therefore, it was suggested to approach this in a stepwise manner. That is, initially, simulations using post treatment input parameters (Table 5.7) for both injection and production periods are conducted. This will reduce the number of simulations to 65536 for each of the two FVR values.

Computer Code

It was mentioned before that a computer code was developed which automatically linked different stages of the simulation process.

In this computer code, initially, the experimental design matrix is read, and then for each case, kr and Pc curves are generated as include-files. The program also creates another three include-files for porosity, permeability (matrix and fracture) and bottom hole pressure. It should be noted that these include-files are used for simulation of both injection and production periods. The initial conditions for the production period (pressure and saturation distribution) are those read using the restart files at the last time step of the injection period. To evaluate the FF cleanup efficiency for these cases a 100% cleanup efficiency case is also required to be simulated. This is performed by running a case with the injected FF volume set to zero. After running these cases using Eclipse, total gas and total FF production from summary files are read for three production times, 10, 30 and 365 days.

After performing one simulation with the above procedure it was noted that each simulation run takes about 15 seconds to complete. The estimated CPU time for the 65536 simulation runs, required to investigate the variation of 16 parameters of the production period (considering full factorial design of second order), is 23 days for each fracture volume. As mentioned above, if the previous procedure (FF injected until the

whole fracture is filled with FF) is followed, the required CPU time will be significantly more.

Response Surface Method (RSM)

The RSM is a useful tool to analyse sensitivity study. As discussed in chapter 3, the response surface method (RSM) is a combination of statistical and mathematical methods to find an appropriate relationship between the response y and independent variables x_1, x_2, x_3... x_n. It fits a polynomial function to the response of the y. The polynomial function f is called the response surface model. This model can be a linear (with or without interaction term) or quadratic model defined by Equations 5.11 and 5.12, respectively.

$$y = a_0 + \sum_{k=1}^{n} a_k x_n + \sum_{i=1}^{n} \sum_{j=i}^{n} a_i a_j x_i x_j \quad \text{(Linear response model)} \tag{5.11}$$

$$y = a_0 + \sum_{k=1}^{n} a_k x_n + \sum_{k=1}^{n} a_k x_k^2 + \sum_{i=1}^{n} \sum_{j=i}^{n} a_i a_j x_i x_j \quad \text{(Quadratic response model)} \tag{5.12}$$

The coefficient of the above function is determined by least square method.

In this research work, the author used only the linear response model to describe the dependency of gas production loss (GPL) on parameters affecting the cleanup efficiency of a HFW. This is mainly due to the fact that using a full factorial design, which covers a more representative range of variation of parameters, with quadratic terms requires a significantly higher number of simulations. Here, based on the 3-level full factorial experiment design, the number of the required simulations is 43046721, which requires a significant CPU time of 491 years to be completed if each run takes 5 second as described above. There are other experiment designs, requiring lower number of simulations e.g. Box-Behken and Central Composite Design (CCD), which are beyond of the scope of this work.

5.4.3 Results

Over 130000 runs were performed for two FF injection volumes. As mentioned earlier, the simulation procedure was automatically run by the computer code and output data were written into output files. These files were used to calculate GPL for each run at three different time steps, after 10, 30 and 365 production days. The linear response surface models with (referred to hereafter as LRSM) and without (referred to hereafter as ILRSM) the interaction terms were used to relate the response (GPL) to the

variation of the sixteen parameters. The least square method was used to estimate the regression coefficients in the models. Here, the author used the statistical tools of MATLAB software for this multiple-regression exercise.

As expected, the ILRSM gives a better prediction of GPL because of having more tuning parameters. That is, for the case of using LRSM there are the intercept and 16 coefficients of the main parameters whilst ILRSM has 120 additional interaction coefficients. Accordingly, the corresponding multiple determination coefficient (R^2) for ILRSM, 0.94, was higher than that for LRSM, 0.9.

Figure 5.27 shows the percentage of the cumulative frequency of the cases with FVR=2 versus the GPL% at three different production times. The results indicate that as production of gas and FF continues the number of the cases with severe production loss decreases. For example, 85% of the cases have GPL of more than 20% after 10 production days, while this is reduced to 70% of the cases and 25% for 30 and 365 days of production.

The coefficients of the LRSM of GPLs with and without interaction parameters when FVR=2 are shown in Tables 5.8 and 5.9.

The magnitude and significance of impacts of the parameters can be evaluated by comparing the corresponding coefficients, i.e. the parameter with higher absolute value of the coefficient has a higher impact on GPL. As illustrated in Table 5.9, the intercept has the highest value for all the time steps studied here. The absolute value of the coefficient of the fracture permeability is higher than the corresponding values for other parameters, highlighting the fact that GPL is significantly affected by this parameter. The impact of S_{grf} on the GPL is negligible compared to other parameters.

The relative importance of each parameter for different scenarios can be more easily compared with those under different prevailing conditions (e.g. different production time intervals or FFV) if they are scaled by dividing them by the coefficient which has the highest absolute value in the fitted response model. It should be noted that as gas and FF is produced, the GPL decreases. Therefore, the importance of the parameters affecting GPL varies with time. For early time of production, GPL is high for the most cases, which imposes the high value for the intercept. However, as the production time increases, GPL and consequently the absolute value of the intercept of the response surface model decreases. This can also be confirmed by comparing the intercept values of LRM for 10, 30 and 365 days of production, Table 5.8.

Figures 5.28, 5.29 and 5.30 show the scaled coefficients of all parameters affecting GPL at three different production periods. It is noted that all the scaled values of the

primary coefficients, after 10 days of production, are less than 0.5, Figure 5.28. This indicates the impact of the primary coefficient are more or less the same because during this period, a large amount of FF is produced. It is very clear that k_f with the scaled value of -0.39 has the most contribution to the GPL sensitivity. Six other important parameters, which influence GPL are n_{gf}, K_{maxwf}, dp , k_m, n_{gm} and n_{wf} with the scaled primary coefficient values of 0.21, -0.19, -0.18, -0.17 , 0.17 and 0.17, respectively. It seems that GPL decreases as K_{maxwf}, dp and k_m, increase and decreases by an increase in n_{gf} , n_{wf} and n_{gm}. The scaled values of the primary coefficients of λ , K_{maxwm}, K_{maxwgf},n_{wm},S_{grm} , K_{maxgm} and S_{grf} are negligible, i.e. less than or close to 0.1.

As gas and FF produces, GPL decreases and the variation and sensitivity of GPL to the variables under the study increases. The absolute value of the primary coefficient of k_f increases from 0.37 to -0.49. The observed trend of the scaled values of the primary coefficients of the parameters after 30 production days is more or less similar to those after 10 production days as the amount of FF being produced is still significant, Figure 5.29. However the number of the parameters which significantly affect GPL has slightly increased by 1.

Figure 5.30 shows the number of the parameters, which significantly affect GPL, after 1 year of gas production, has significantly increased because there is no FF to be produced after 365 days of production, i.e. the fracture is clean. GPL of the majority of cases under study were below 30%. The absolute values of the scaled primary coefficients increases significantly, i.e. the corresponding values for k_f and n_{gf} increase from -0.49 and 0.28 shown in Figure 5.29 to -0.7 and 0.38 in Figure 5.30, respectively.

Figure 5.31, which compares the three different scaled coefficients after 10, 30 and 365 days of production shows that the impact of the parameters is increasing with continued production of gas and FF. As noted earlier, this is mainly due to the fact that, as production continues the amount of FF produced with gas decreases, i.e. its adverse impact on gas production decreases, which in turn exaggerates the impact of parameters affecting the cleanup.

Figure 5.32 shows a comparison of the corresponding scaled coefficients of the variables for LRSM and ILRSM fits after 30 and 365 days of production, when FVR=2.0. The scaled coefficients are almost identical for 30 days of production. However, after 365 days of production, the scaled coefficients of RSM are significantly less than those of the ILRSM. The values of the scaled coefficients of the interaction terms, on the other hand, are small for 10 and 30 days of production but increases significantly after 365 days of production, Table 5.10. These results suggest that the

coefficients of the main parameters are controlling the extent of GPL, which was rather high at low production periods. Furthermore, it can be concluded that no direct comparison can be made between the coefficients of the main terms of LRSM and ILRSM after 365 production days.

From Table 5.10, it is noted that amongst the 120 interaction coefficients (120=p*(p-1)/2 where p, number of parameters is 16), only a few are considerable and those correspond to 1 year of production. These terms are interaction parameters between those parameters which affect the GPL significantly such as k_f, n_{wf}, K_{maxwf} , n_{gf}, n_{gm}, dp, IFT, λ , k_m.

The procedure explained above for analysing the results of simulations with FVR=2 was followed for the output data of the fracture models, with FVR=5. Figure 5.33 compares scaled coefficients for these two FVF values at two different time intervals. It is noted that the observed trends are more or less similar. The fracture permeability has the most significant impact on GPL and the sequences of the importance of the other parameters are somewhat similar. However, the relative importance of the pertinent parameters when FVR=5 are less than those for FVR=2, especially at higher production periods. This is mainly due to the increased required time for cleaning the fracture as FF injection volume increases. As discussed earlier, GPL is a function of time. An increase in the FF injection volume increases GPL and delays the fracture clean up. This dampens the relative importance of the parameters. It is also noted that the relative magnitude of scaled coefficients with higher FVR of 5 at 30 days of production was similar to that with lower FVR of 2 at 10 days of production, Figure 5.34.

As discussed earlier, increasing the FF volume significantly increases the percentage of the cases with severe FF damage as shown in Figure 5.35. It is interesting to point out that the curve of the cases with FVR=2 at 10 production days overlap that of the cases with FVR=5 at 30 production days, i.e. the GPL function for these two scenarios are similar.

5.5 SUMMARY AND CONCLUSIONS

This study aimed to evaluate the impact of pertinent parameters on the clean-up efficiency of a hydraulically (gas or gas-condensate) fractured well. In the first part, a series of numerical simulations were conducted using ECLIPSE 300 and ECLIPSE100. The general conclusion is that accurate modeling of FF invasion into the fracture and matrix is crucial. The main itemized conclusions of the first section are:

1. A model was created using ECLIPSE100, which reproduced the results of the published paper by Holditch (1979), thereby demonstrating the integrity of the proposed approach.

2. The presence of fracture fluid (FF) in the damage zone influences gas recovery by reducing the gas relative permeability. It can increase gas production loss (GPL) significantly, if FF invasion can be simulated more realistically, as was performed here by allowing the FF to invade all fracture blocks. This supports experimental work conducted by Bennion (2001). However, it does not agree with the numerical simulations conducted by several other investigators (Holditch 1979, Adegbola 2002, Gdanski et al. 2005).

3. The results also demonstrate that the combined effect of absolute permeability and effective gas relative permeability reduction in the matrix invaded zone is more pronounced for most of considered cases studied here, even for the cases with moderate to high fracture permeability reduction. This is in contrast with the previous numerical models, showing that fracture face damage is the important issue if it caused severe permeability reduction in the matrix invaded zone.

4. FF recovery is higher if it is degraded with a reduced viscosity, i.e., higher mobility for the production period.

5. The fracture conductivity reduction is the main factor in GPL, when matrix capillary pressure is zero. Matrix capillary pressure increases the extent of FF invasion into the matrix. This reduces the saturation of FF in the fracture, thus reducing the impact of fracture on cleanup efficiency.

6. Damage permeability reduction in the range of 90% and 99% can significantly increase GPL when matrix capillary pressure is considered.

7. The initial water saturation (S_{wi}) decreased GPL. This is due to a decrease in the capillary pressure driving force between matrix and fracture, which in turn reduces the FF invasion into the matrix. It should be noted that this conclusion is based on the 100% cleanup case with $S_{wi,}$ where the gas production has already dropped significantly due to the presence of S_{wi}.

8. The effect of a change in the matrix capillary pressure of the damaged zone is negligible unless unrealistically low pressure drawdown is assumed. This is in line with the findings in the literature (e.g., Holditch (1979) & Gdanski (2005)).

9. FF recovery was improved in the presence of condensate, which resulted in a decrease in the adverse effect of FF, giving lower GPL. It should be noted that this

conclusion is based on a 100% cleanup case with fixed bottom hole pressure below dew point, where the gas production has already dropped due to condensate dropout.

10. Improving the relative permeability of an oil based FF compared to a water based FF decreased GPL.

11. The hysteresis had a negligible effect on GPL.

In the second part of this study, a new methodology was developed to further investigate the impact of the pertinent parameters on the clean up efficiency. A 2-level full factorial statistical experimental design was used to sample a reasonably wide range of variation of pertinent parameters, covering many practical cases. The variation of a total of 16 parameters describing the matrix and fracture relative permeability of gas and FF, matrix capillary pressure were studied for two separate FF volume values (FVR=2 and 5). Due to the large number of simulations required for this purpose, a computer code was developed using MATLAB mathematical package, which linked automatically different stages of the simulations conducted using ECLIPSE100. Over 130000 simulation runs were performed for many different prevailing conditions. The gas production loss (GPL) compared to the 100% cleanup case was also calculated automatically as an output data for each run at different production periods after the FF injection. The linear repose surface without (LRSM) and with interaction parameters (ILRSM) models were used to relate the response (GPL) to the variation of the sixteen parameters. The least square method was used to estimate the regression coefficients in the models.

The analysis of the data for the fracture models with FVR=2 demonstrated that:

12. As FF and gas production continues, the number of the cases with severe gas production loss decreases but the relative importance of the pertinent parameters increases.

13. GPL is significantly affected by fracture conductivity.

14. The impact of residual gas saturation in the fracture and gas end point of a Corey type relative permeability curve on the GPL is negligible.

15. The other important parameters, which influence GPL are the FF exponent and end point of the Corey type relative permeability curve in the fracture, the gas exponent of the Corey type relative permeability curve in the fracture and matrix, differential pressure across the reservoir, interfacial tension, the pore size distribution index, matrix permeability, the end points of the Corey type relative permeability curve in the matrix, residual gas saturation in the matrix and porosity.

16. The presence of interaction parameters in the linear response surface fit resulted in better prediction because of having more tuning terms, i.e. interaction coefficients.

17. Amongst 120 interaction terms, only a few terms are considerable and they correspond to 1 year of production.

18. The scaled coefficients of the main terms of LRSM and those of ILRSM for GPL after 10 and 30 days of production, where GPL was large, were similar. It seems that the coefficients of the main terms were mainly affected the extent of GPL.

The analysis of the data for the fracture models with FVR=5 supports the main conclusion of those with FVR=2. However, there are some differences as follows:

19. Increasing the FF volume from 2 to 5 significantly increases the percentage of the cases with severe FF damage.

20. An increase in the FF injection volume increases GPL and delays the fracture clean up.

21. The relative importance of pertinent parameters when FVR=5 are less than those when FVR=2, especially at higher production periods.

References

Adegbola K. and Boney C., 20-21 Feb 2002: Effect of Fracture Face Damage on Well Productivity, SPE 73759.

Barati R., Hutchins R.D., Friedel T., Ayoub J.A., Dessinges M. and England K.W. , 13–15 February 2008: Impact of Yield Stress and Fracture-Face Damage on Production Using a Three-Phase, 2D Model, SPE 111457.

Bennion D. B., Thomas F. B. and Ma T., 12-15 March 2001: Recent Advances in Laboratory Test Protocols to Evaluate Optimum Drilling, Completion and Stimulation Practices for Low Permeability Gas Reservoirs, SPE 60324.

Cooke, C.E., October 1975: Effect of fracturing fluids on fracture conductivity, JPT, pp. 1273-83, Trans., AIME, 259.

Cooke, C.E., Sep 1973: Conductivity of Fracture Proppants in Multiple Layers, SPE 4117, JPT.

Gdanski, R., Weaver, J., Slabaugh, B., Walters H. and Parker M., May 2005: Fracture Face Damage-It Matters, SPE 94649.

Geertsma J. and de Klerk F., 1969: A rapid method of predicting width and extent of hydraulically induced fractures. J Pet Tech 1969; 21:1571–81 [SPE 2458].

Ghahri P., Jamiolahmady M. and Sohrabi M. , 27–29 May 2009: Investigation of Cleanup Efficiency of Hydraulically Fractured Wells in Gas Condensate Reservoirs, SPE 121916, SPE European Formation Damage Conference held in Scheveningen The Netherlands.

Holditch S. A., Dec 1979: Factors Affecting Water Blocking and Gas Flow from Hydraulically Fractured Gas Wells, JPT 1515-1524.

Howard G.C. and Fast, C.R., 1957: Optimum Fluid Characteristics for Fracture Extension, Drilling and Production Prac., API 24, 261–270.

Khristianovic S.A. and Zheltov Y.P., 1955: Formation of vertical fractures by means of highly viscous liquid. In: Proceedings of the fourth world petroleum congress, Rome, pp. 579–86.

Jamiolahmady M., Danesh A, Tehrani D.H. and Mehran Sohrabi, 2006: Variations of Gas-Condensate Relative Permeability with Production Rate at Near Wellbore Conditions, A general Correlation, SPE Reservoir Engineering and Evaluation Journal, 9 (6), pp.688-697.

Naar J. and Henderson J.H., June 1961: An Imbibition Model-Its Application to Flow Behaviour and Prediction of Oil Recovery, SPE1550-G.

Friedel T., Mtchedlishvili G., Behr A., Voigt H-D. and Hafner F. , 30 May-1 June 2007: Comparative Analysis of Damage Mechanism in Fractured Gas Wells, SPE 107662.

Nolte K.G. and Smith M.B., 1981: Interpretation of fracturing pressures, J Pet Tech 1981; (September):1767–75.

Nordren R.P., 1972: Propagation of a vertical hydraulic fracture, SPE J 1972; 12(8):306–14 [SPE 7834].

Perkins, T.K. and Kern L.R., 1961: Width of Hydraulic Fractures, paper SPE 89, Journal of Petroleum Technology (Sep 1961) 13, No. 9, 937-949.

Voneiff G.W., Robinson B.M. and Holditch S.A., Nov 1996: The Effects of Unbroken Fracture Fluid on Gaswell Performance, SPE-26664.

Wang J.Y., Holditch S.A. and MacVay D., Jan 2009: Modelling Fracture Fluid Cleanup in Tight Gas Wells, SPE-119624.

Table 5.1: The prevailing conditions and loss of gas production due to the effect of S_{ffm} and k_{fd} for a selected number of scenarios simulating the effect of hysteresis on the cleanup efficiency of the hydraulically fractured single well model.

Index	**hysteresis**	**Time(days)**	**R2(S_{ffm}&k_{fd})%**	**R3(S_{ffm})%**	**R4(k_{fd})%**
Rh1a	(Pc, krg)dra&imb	300	-	-	
Rh2a	(Pc, krg)dra&imb	300	70	30	40
Rh3a	(Pc, krg)dra&imb	300	30		30
Rh1b	(Pc, krg)dr	300	-	-	-
Rh2b	(Pc, krg)dr	300	68	30	38
Rh3b	(Pc, krg)dr	300	30		30
Rh1c	(Pc)dra, (krg)dra&imb	300	-	-	-
Rh2c	(Pc)dra, (krg)dra&imb	300	69	30	39
Rh3c	(Pc)dra, (krg)dra&imb	300	-	30	30
Rh1d	(Pc)dra, (krg)dra&imb	400	-	-	-
Rh2d	(Pc)dra, (krg)dra&imb	400	65	30	35
Rh3d	(Pc)dra, (krg)dra&imb	400	-	30	30
Rh1e	(Pc)dra, (krg)imb	300	-	-	-
Rh2e	(Pc)dra, (krg)imb	300	72	30	42
Rh3e	(Pc)dra, (krg)imb	300	-	30	30
Rh1f	(Pc)dra, (krg)imb	400			
Rh2f	(Pc)dra, (krg)imb	400	68	29	39
Rh3f	(Pc)dra, (krg)imb	400		29	29

Table 5.2: Reservoir and fracture Properties, Holditch well model study (1979).

Matrix Porosity	0.08
Matrix Permeability	0.1
Fracture Length	660 ft
Fracture width	0.006 m
Fracture Porosity	0.20

Table 5.3: Reproduction of Holditch Damage Effect- a) the original work–Holditch (1979) b) Reproduced data.

(a)

$(J_{Damage}/J_{Undamage})\times 100$				
C_f (md-ft)	100	10	1	0.1
100	100	99.2	93	61.6
500	100	99	91.3	54.2
4000	100	98.2	90.2	50.8

(b)

$(J_{Damage}/J_{Undamage})\times 100$				
C_f (md-ft)	100	10	1	0.1
100	100	99.1	93.1	61.0
500	100	99.0	91.5	55.8
4000	100	98.7	90.5	53.8

Table 5.4: The basic input data for the cases A and B.

X_f(m)	w_f(m)	Xres(m)	Yres(m)	Zres(m)	$V_f(m^3)$	K_f(D)*	k_m(mD)*	ϕ(%)*	μ(cp)*
400	0.004	2000	2000	40	64	15	0.18	17	0.5

* For both injection and production period

S_{wi}=0, P_{cm}=0

Table 5.5: The ratio of injected FF per fracture volume for different fracture permeability used in this study.

kinj(D)	Vinj(m3)	Vinj/Vf
15	3096	96.7
30	1887	59.0
150	615	19.2
300	361	11.3
1500	149	4.7
3000	112	3.5
10000	80	2.5

Table 5.6: Uncertain parameters before treatment.

	Parameter	Min	Max
Fracture Conductivity	**K_f (D)**	**1**	30
Pressure Drawdown	Δp (bar)	30	250
Matrix Permeability	K_m	1 μD	0.1 mD
Matrix capillary pressure curve (P_c)	**Pore size index λ**	**1**	**3**
Matrix capillary pressure curve (P_c)	Threshold pressure	Eq. (5.11)	Eq.(5.11)
Matrix capillary pressure curve (P_c)	**Interfacial Tension (mNm/m)**	**10**	50
Porosity	ϕ	0.05	0.15
Matrix krg curve	S_{gr}	0.25	0.6
Matrix krw curve	**S_{wr}**	**0.1**	**0.3**
Matrix krg curve	**n_g**	2	**6**
Matrix krw curve	**n_w**	1.5	**6**
Matrix krg curve	K_{maxg}(end point)	0.7	1.0
Matrix krw curve	**K_{maxw}(end point)**	**0.1**	**0.5**
Fracture krg curve	S_{gr}	**0.1**	0.3
Fracture krw curve	**S_{wr}**	**0.1**	**0.3**
Fracture krg curve	**n_g**	**2**	**6**
Fracture krw curve	**n_w**	**2**	**6**
Fracture krg curve	K_{maxg}(end point)	0.9	1
Fracture krw curve	**K_{maxw}(end point)**	0.15	**0.55**

Table 5.7: Uncertain parameters after treatment.

	Parameter	Min	Max
Fracture Conductivity	**K_f (D)**	**1**	30
Pressure Drawdown	Δp (bar)	30	250
Matrix Permeability	K_m	1 μD	0.1 mD
Matrix capillary pressure curve (P_c)	**Pore size index λ**	**1**	**4**
Matrix capillary pressure curve (P_c)	Threshold pressure	Eq. (5.11)	Eq. (5.11)
Matrix capillary pressure curve (P_c)	**Interfacial Tension (mNm/m)**	**2**	**50**
Porosity	ϕ	0.05	0.15
Matrix krg curve	S_{gr}	0.1	0.6
Matrix krw curve	**S_{wr}**	**0.1**	**0.1**
Matrix krg curve	**n_g**	1.5	**5**
Matrix krw curve	**n_w**	1.2	**4**
Matrix krg curve	K_{maxg}(end point)	0.5	1.0
Matrix krw curve	**K_{maxw}(end point)**	**0.05**	**0.6**
Fracture krg curve	S_{gr}	0.1	**0.3**
Fracture krw curve	**S_{wr}**	**0.1**	**0.1**
Fracture krg curve	**n_g**	1.5	**5**
Fracture krw curve	**n_w**	1.2	**4**
Fracture krg curve	K_{maxg}(end point)	0.5	1.0
Fracture krw curve	**K_{maxw}(end point)**	**0.1**	**0.75**

Table 5.8: The coefficients estimated for the linear response model of GPL by least square method

Parameters \ Production days	After 365	After 30	After 10
Intercept	22.1	60.1	76.6
K_f (x_1)	-15.3	-29.4	-28.7
dp (x_2)	-7.4	-13.9	-14.0
k_m (x_3)	-5.3	-12.9	-13.3
Lam (λ)(x_4)	5.3	9.6	8.3
IFT(x_5)	-5.5	-10.0	-8.9
Porosity (ϕ)(x_6)	-3.0	-5.9	-5.9
S_{grm} (x_7)	3.2	6.7	7.3
n_{gm} (x_8)	7.4	13.8	13.3
n_{wm} (x_9)	3.6	4.6	3.9
K_{maxgm} (x_{10})	-1.0	-2.2	-2.5
K_{maxwm} (x_{11})	-4.6	-7.4	-6.6
S_{grf} (x_{12})	-0.4	-0.3	-0.2
n_{gf} (x_{13})	8.5	15.9	16.5
n_{wf} (x_{14})	12.2	16.0	13.6
K_{maxgf} (x_{15})	-4.0	-5.6	-5.2
K_{maxwf} (x_{16})	-9.0	-15.5	-15.1

Table 5.9: The coefficients of the main effects estimated for the linear interaction response model of GPL by least square method.

Parameters \ Production days	After 365	After 30	After 10
Intercept	22.6	68.5	83.1
K_f (x_1)	-20.6	-39.3	-32.7
dp (x_2)	-7.2	-9.6	-6.5
k_m (x_3)	-6.1	-11.6	-7.6
Lam (λ)(x_4)	10.8	10.1	5.0
IFT(x_5)	-15.1	-23.4	-16.9
Porosity (ϕ)(x_6)	-4.2	-7.0	-5.1
S_{grm} (x_7)	5.3	8.5	7.6
n_{gm} (x_8)	13.3	17.8	12.7
n_{wm} (x_9)	0.1	-2.1	-3.0
K_{maxgm} (x_{10})	-2.2	-3.4	-3.4
K_{maxwm} (x_{11})	-4.5	-5.2	-2.6
S_{grf} (x_{12})	-0.8	-0.6	-0.3
n_{gf} (x_{13})	14.1	16.9	12.7
n_{wf} (x_{14})	17.5	2.8	-6.1
K_{maxgf} (x_{15})	-4.8	-5.0	-3.9
K_{maxwf} (x_{16})	-12.6	-18.6	-13.6

Table 5.10: The scaled coefficients for interaction terms (IRSM)

Production days / Scaled Coefficients	After 365	After 30	After 10
x1x2	0.24	0.02	-0.06
x1x3	0.41	0.13	0.02
x1x4	-0.29	0.01	0.07
x1x5	0.46	0.04	-0.07
x1x6	0.10	0.02	-0.01
x1x7	0.00	0.01	0.03
x1x8	-0.22	0.00	0.07
x1x9	-0.10	-0.01	0.01
x1x10	0.05	0.01	0.00
x1x11	0.13	0.02	-0.02
x1x12	0.02	0.00	0.00
x1x13	-0.37	-0.04	0.03
x1x14	-0.46	0.04	0.11
x1x15	0.13	0.00	-0.03
x1x16	0.36	0.04	-0.06
x2x3	-0.08	-0.11	-0.14
x2x4	-0.23	-0.14	-0.10
x2x5	0.24	0.14	0.10
x2x6	0.11	0.03	0.01
x2x7	-0.20	-0.07	-0.03
x2x8	-0.27	-0.07	-0.01
x2x9	-0.04	0.01	0.01
x2x10	0.03	0.00	0.00
x2x11	0.14	0.03	0.00
x2x12	0.00	0.00	0.00
x2x13	-0.13	-0.02	0.01
x2x14	-0.05	0.07	0.08
x2x15	0.03	-0.01	-0.02
x2x16	0.18	0.00	-0.05
x3x4	-0.24	-0.08	-0.03
x3x5	0.23	0.05	-0.01
x3x6	0.08	0.01	-0.01
x3x7	-0.19	-0.05	-0.01
x3x8	-0.22	-0.03	0.01
x3x9	0.01	0.01	0.01
x3x10	0.03	0.00	-0.01
x3x11	0.08	0.01	0.00
x3x12	0.00	0.00	0.00
x3x13	-0.14	-0.04	-0.01
x3x14	0.01	0.09	0.10
x3x15	0.00	-0.02	-0.02
x3x16	0.09	0.00	-0.04
x4x5	0.06	0.17	0.14
x4x6	-0.02	0.02	0.02
x4x7	0.05	0.02	0.01
x4x8	0.07	-0.02	-0.04
x4x9	0.02	-0.03	-0.03
x4x10	-0.01	0.00	0.01
x4x11	-0.01	0.04	0.04
x4x12	0.00	0.00	0.00
x4x13	0.12	0.02	0.00
x4x14	0.09	-0.01	-0.02
x4x15	-0.03	0.00	0.00
x4x16	-0.06	-0.02	0.00
x5x6	-0.02	-0.03	-0.04
x5x7	0.08	0.03	0.02
x5x8	0.03	0.07	0.08
x5x9	0.02	0.03	0.03
x5x10	0.00	-0.01	-0.01
x5x11	-0.04	-0.06	-0.05
x5x12	0.00	0.00	0.00

x5x13	-0.21	-0.07	-0.03
x5x14	-0.15	0.00	0.03
x5x15	0.04	0.01	0.00
x5x16	0.11	0.04	0.01
x6x7	-0.05	0.00	0.00
x6x8	-0.10	-0.01	0.01
x6x9	-0.05	-0.01	0.00
x6x10	0.01	0.00	0.00
x6x11	0.06	0.01	0.00
x6x12	0.00	0.00	0.00
x6x13	-0.03	-0.01	0.00
x6x14	0.02	0.03	0.03
x6x15	0.00	-0.01	-0.01
x6x16	0.01	-0.01	-0.02
x7x8	0.13	-0.01	-0.05
x7x9	0.09	0.03	0.03
x7x10	0.03	0.03	0.03
x7x11	-0.10	-0.04	-0.03
x7x12	0.01	0.00	0.00
x7x13	0.04	0.00	-0.01
x7x14	-0.04	-0.04	-0.04
x7x15	0.01	0.01	0.01
x7x16	-0.02	0.01	0.03
x8x9	0.21	0.09	0.06
x8x10	-0.02	0.00	0.01
x8x11	-0.20	-0.11	-0.09
x8x12	0.00	0.00	0.00
x8x13	0.07	0.00	-0.03
x8x14	0.05	-0.04	-0.05
x8x15	-0.01	0.01	0.02
x8x16	-0.05	0.01	0.03
x9x10	-0.01	0.00	0.00
x9x11	0.04	0.05	0.04
x9x12	0.00	0.00	0.00
x9x13	0.04	0.00	-0.01
x9x14	0.15	0.05	0.03
x9x15	-0.04	-0.01	-0.01
x9x16	-0.01	0.00	0.00
x10x11	0.01	0.00	0.00
x10x12	0.00	0.00	0.00
x10x13	-0.02	-0.01	0.00
x10x14	0.00	0.01	0.01
x10x15	0.00	0.00	0.00
x10x16	0.02	0.00	0.00
x11x12	0.01	0.00	0.00
x11x13	-0.05	0.00	0.02
x11x14	-0.12	-0.03	-0.01
x11x15	0.03	0.01	0.00
x11x16	0.04	0.00	-0.01
x12x13	0.00	0.00	0.00
x12x14	-0.04	-0.01	-0.01
x12x15	0.01	0.00	0.00
x12x16	0.04	0.01	0.00
x13x14	0.46	0.18	0.12
x13x15	0.02	0.04	0.04
x13x16	-0.29	-0.09	-0.05
x14x15	-0.21	-0.04	-0.01
x14x16	-0.18	0.08	0.11
x15x16	0.10	0.00	-0.01

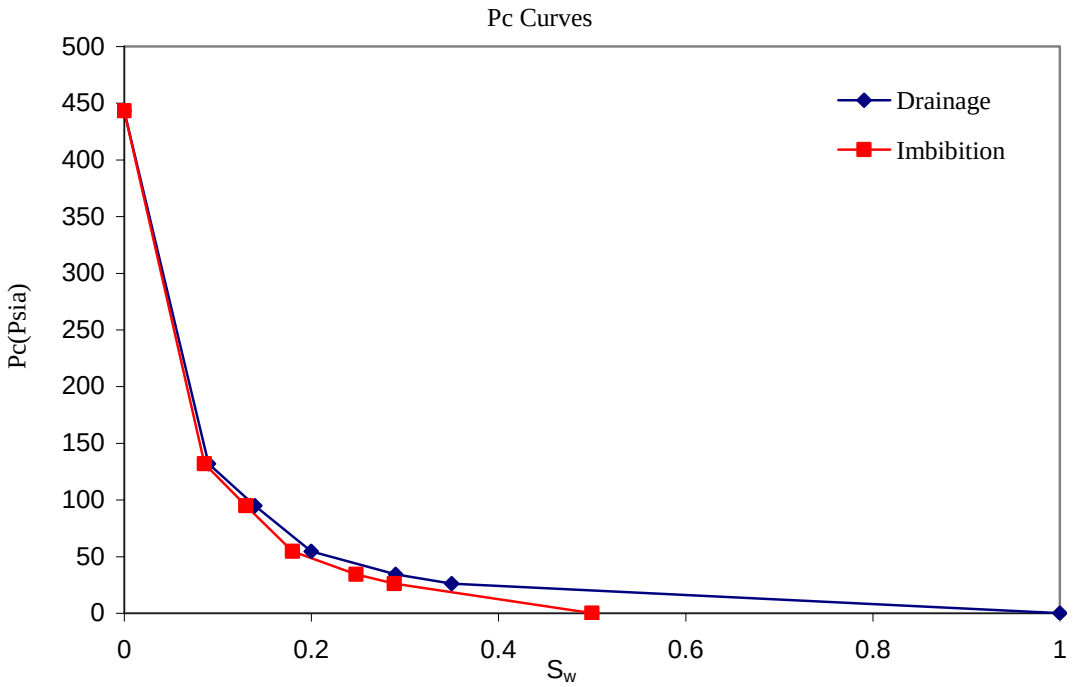

Figure 5.1: Capillary pressure curves used here.

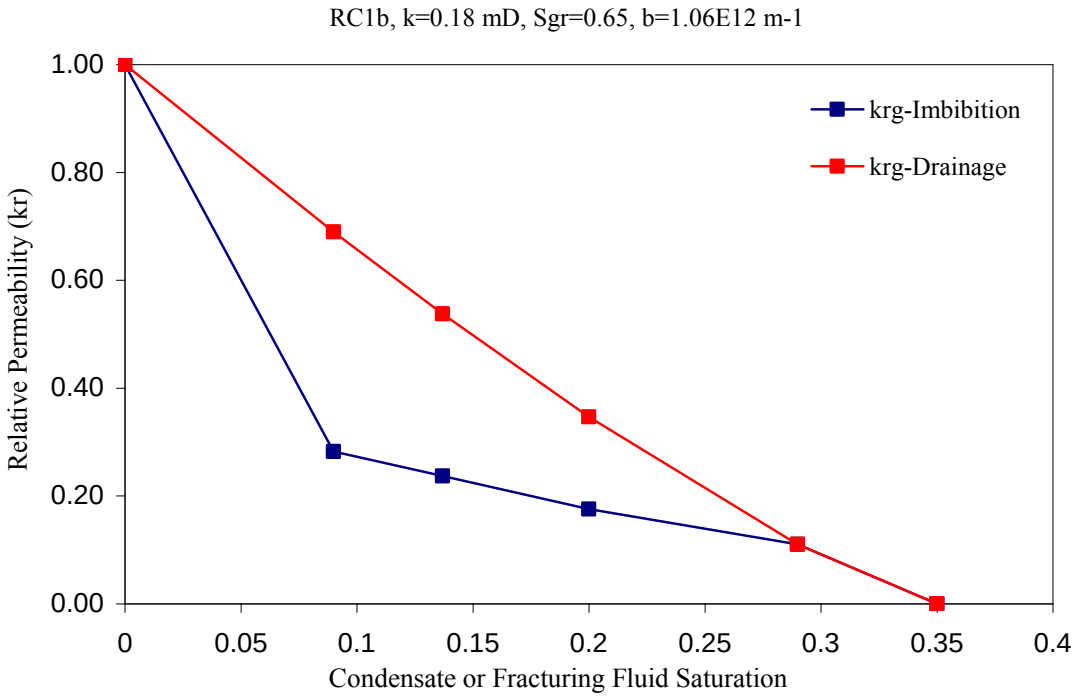

Figure 5.2: Relative permeability curves used for the effect of hytestersis on cleanup efficiency.

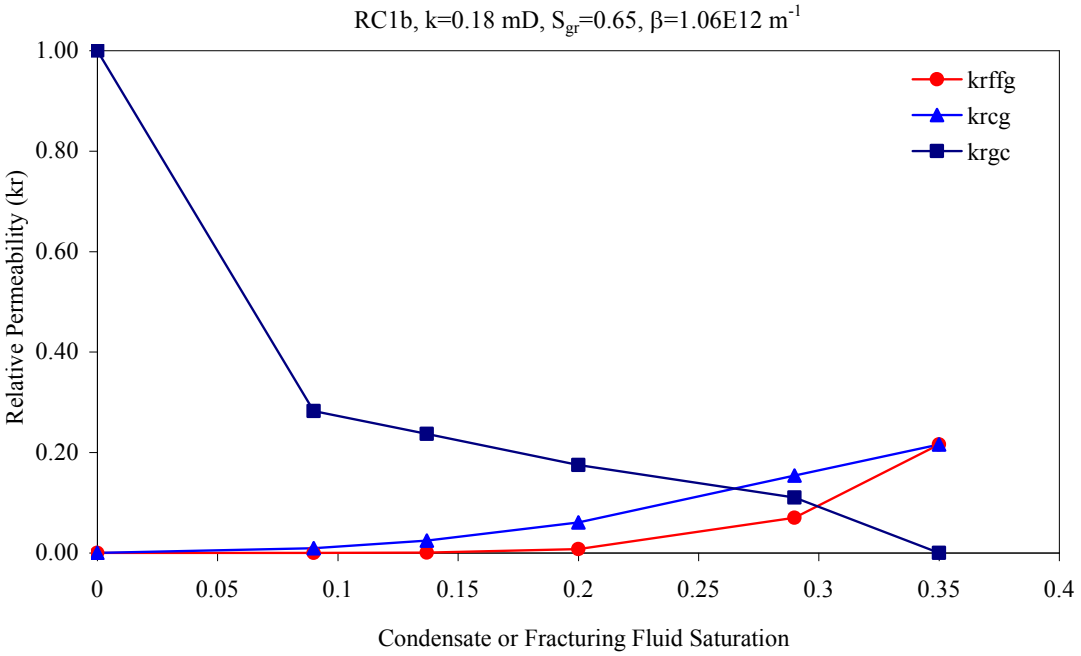

(a)

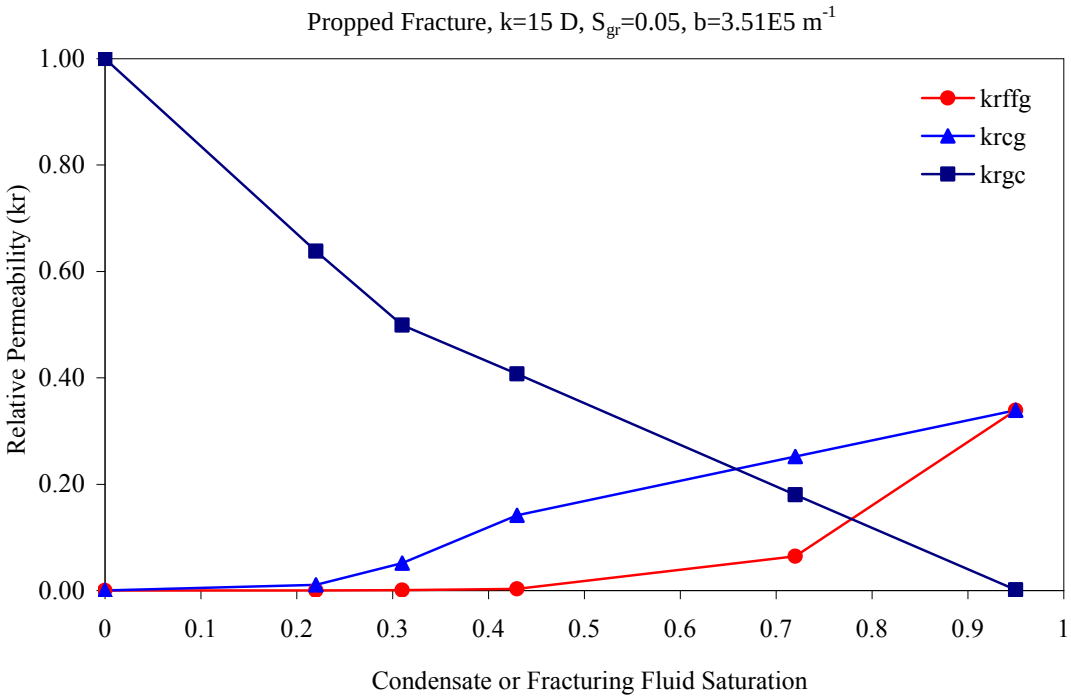

(b)

Figure 5.3: Condensate and (water based) fracturing fluid to gas and gas to condensate relative permeability curves for (a) matrix and (b) fracture.

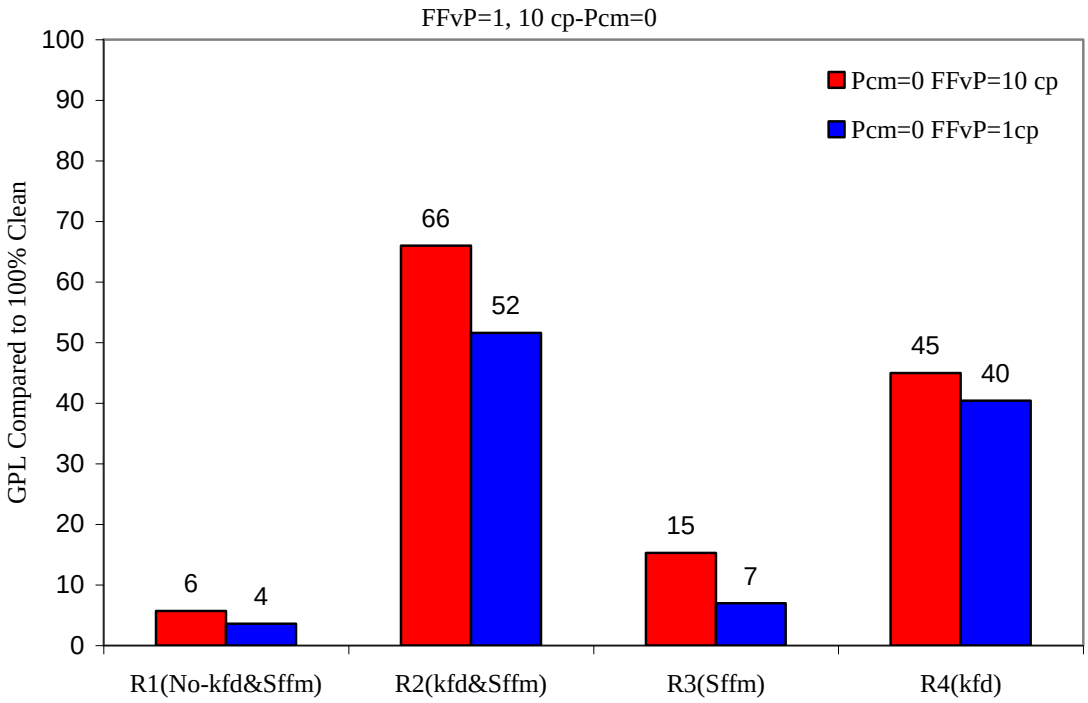

Figure 5.4: GPL compared to 100% cleanup case for simulation runs indexed R1-R4 without P_{cm} at two different FFvPs.

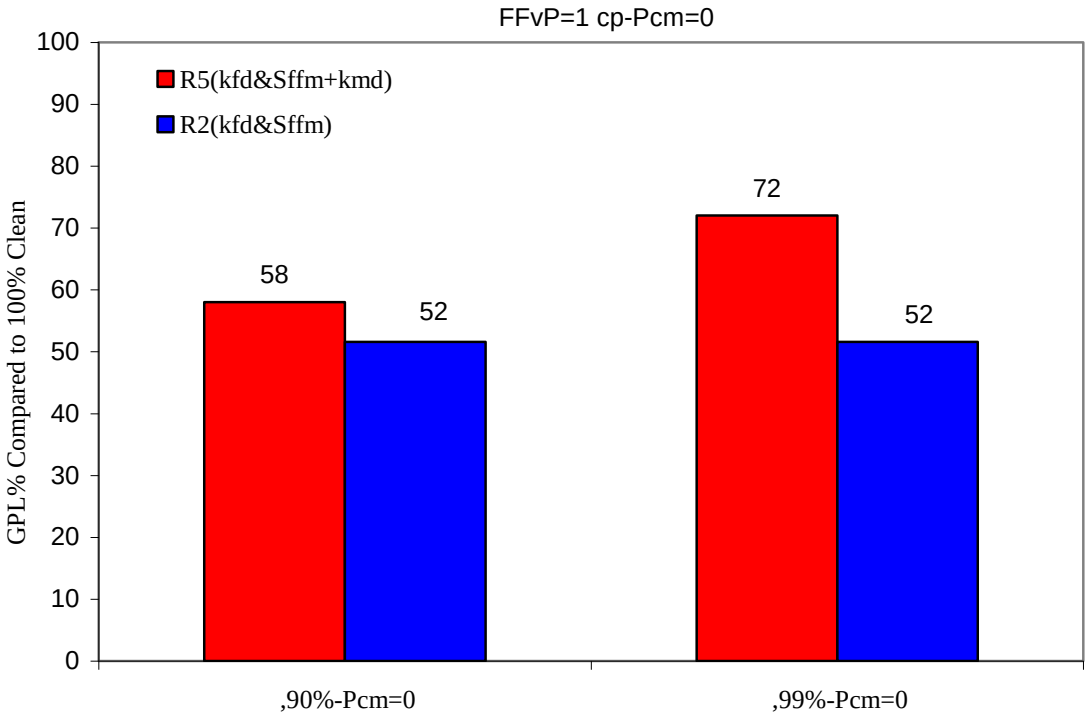

Figure 5.5: GPL compared to 100% cleanup for simulation runs indexed R5 (with 90% and 99% k_{md}) and R2 (without k_{md}) both without P_{cm}.

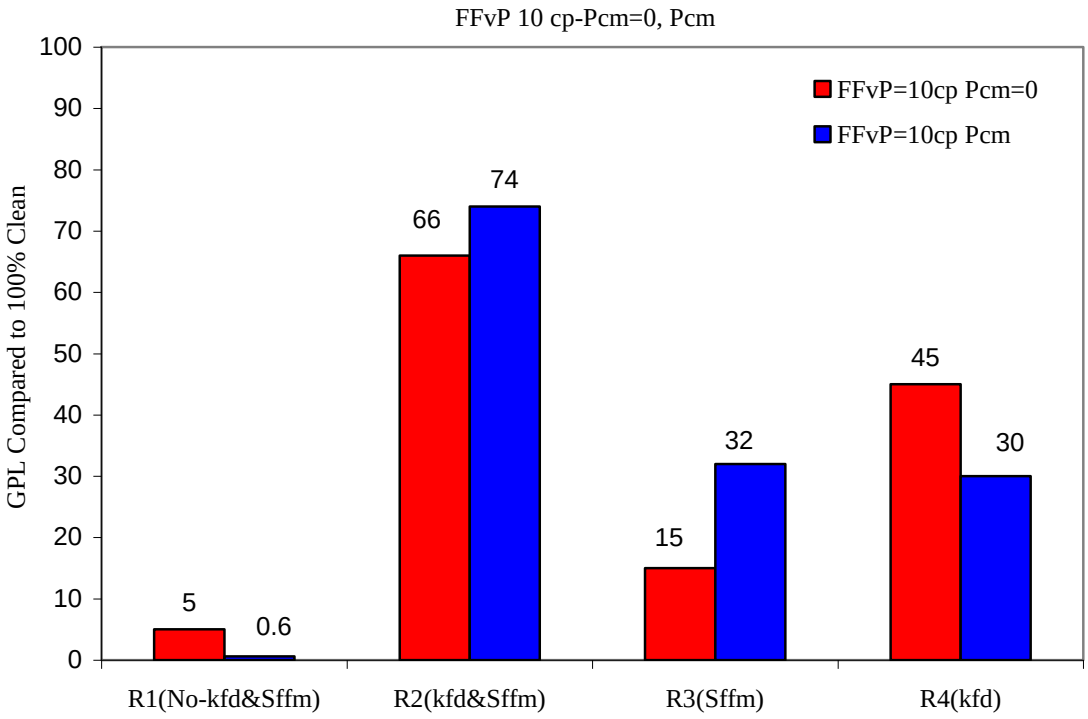

Figure 5.6: GPL compared to 100% cleanup for simulation runs indexed R1-R4, the measured matrix capillary pressure effect.

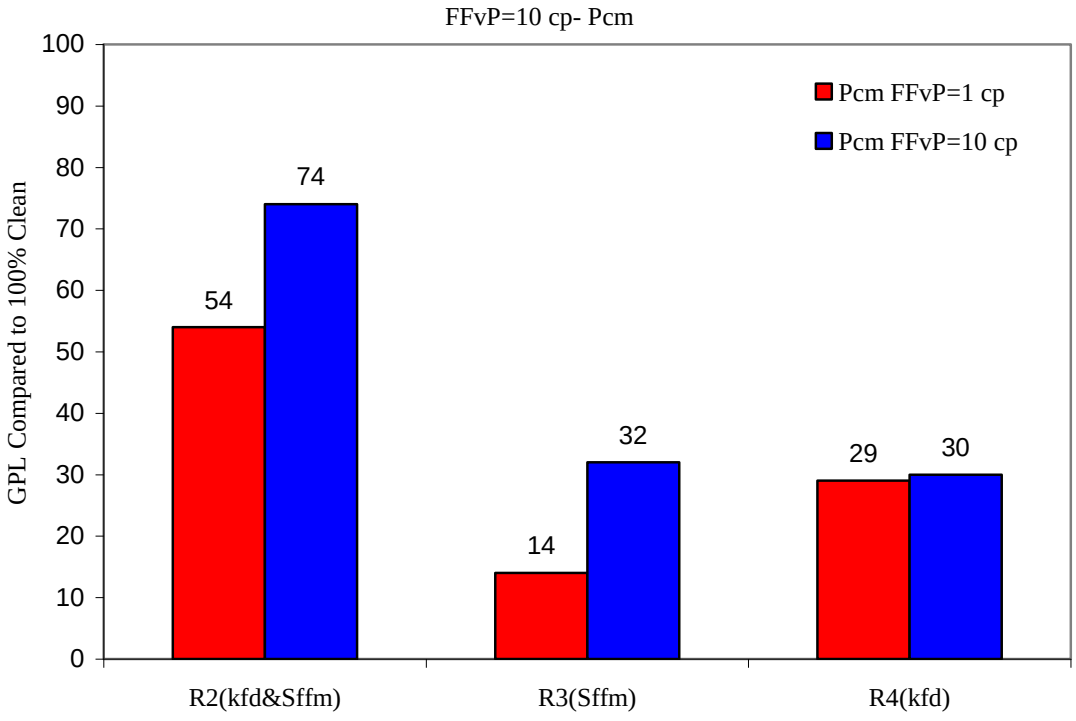

Figure 5.7: GPL compared to 100% cleanup for simulation runs indexed R2-R4 with P_{cm} at two different FFvPs.

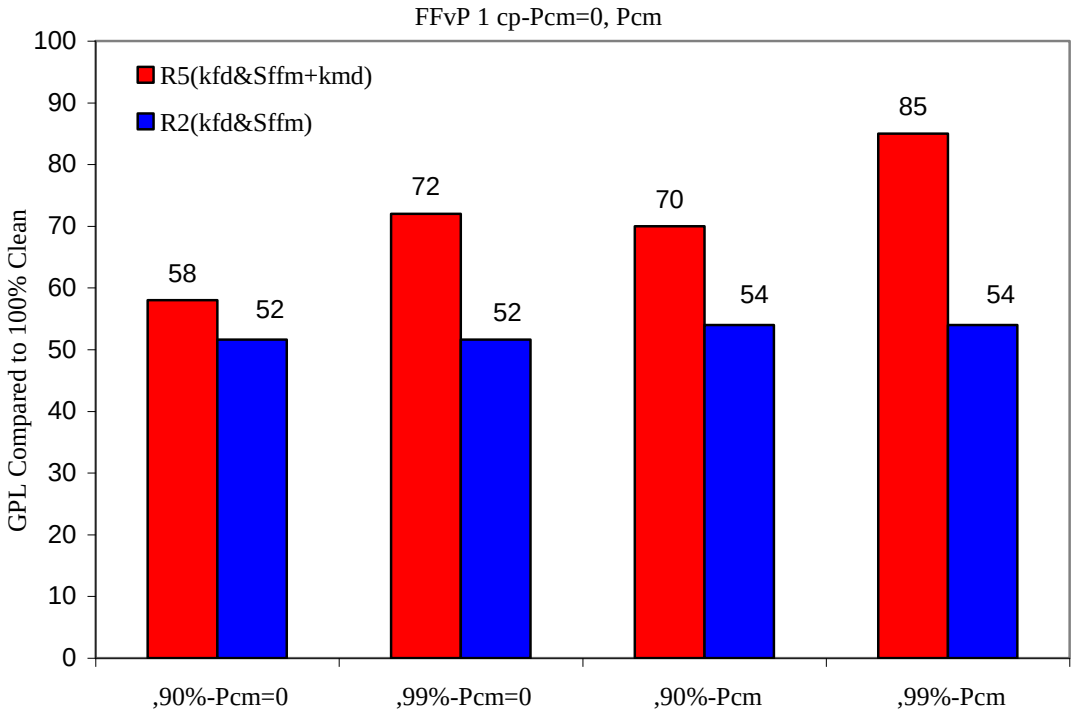

Figure 5.8: GPL compared to 100% cleanup for simulation runs indexed R5 (with 90% and 99% k_{md}) & R2 (without k_{md}) both with and without P_{cm}.

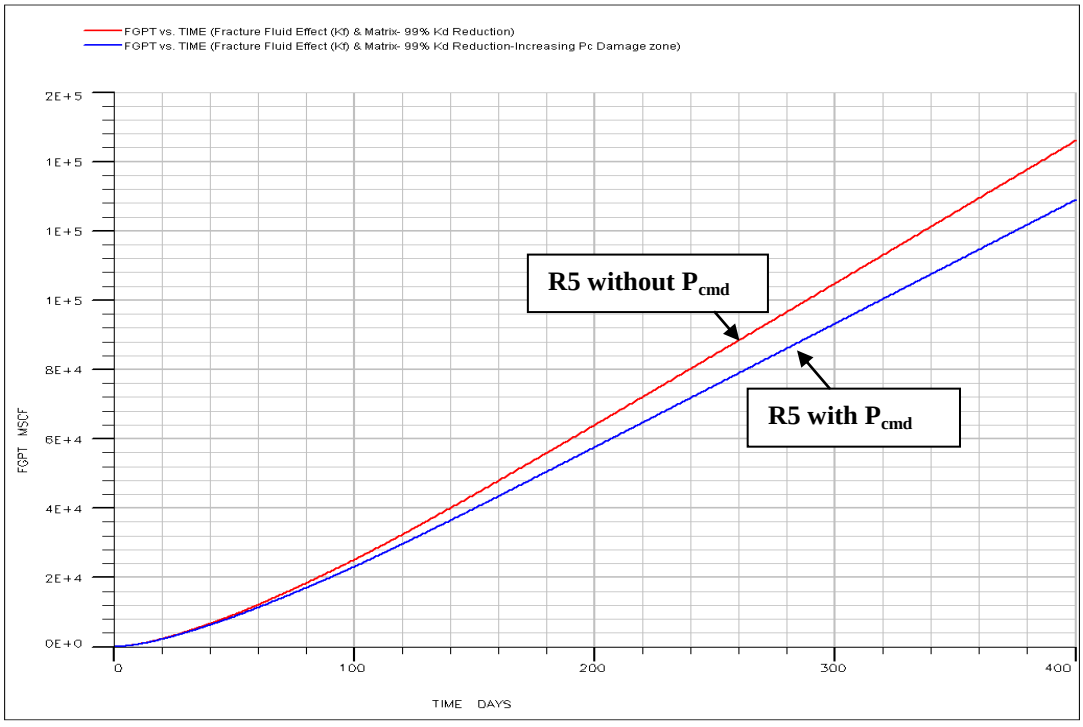

Figure 5.9: Gas production versus time for simulation runs indexed R5 with and without considering P_{cmd}.

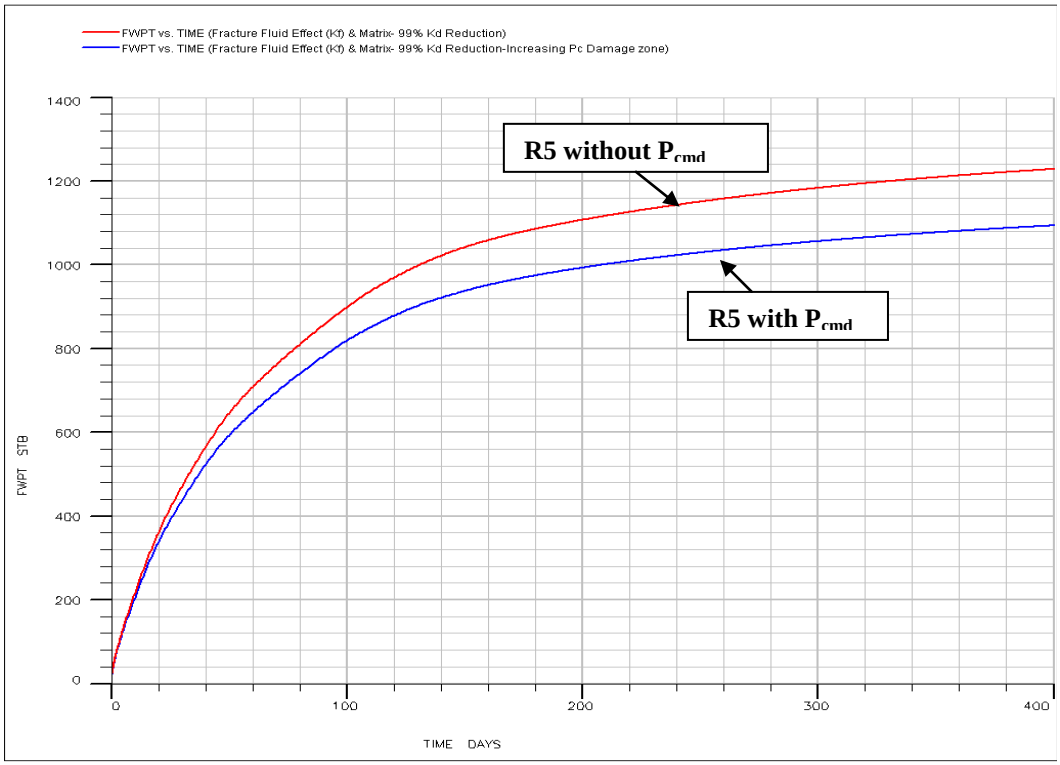

Figure 5.10: FF production versus time for simulation runs indexed R5 with and without considering P_{cmd}.

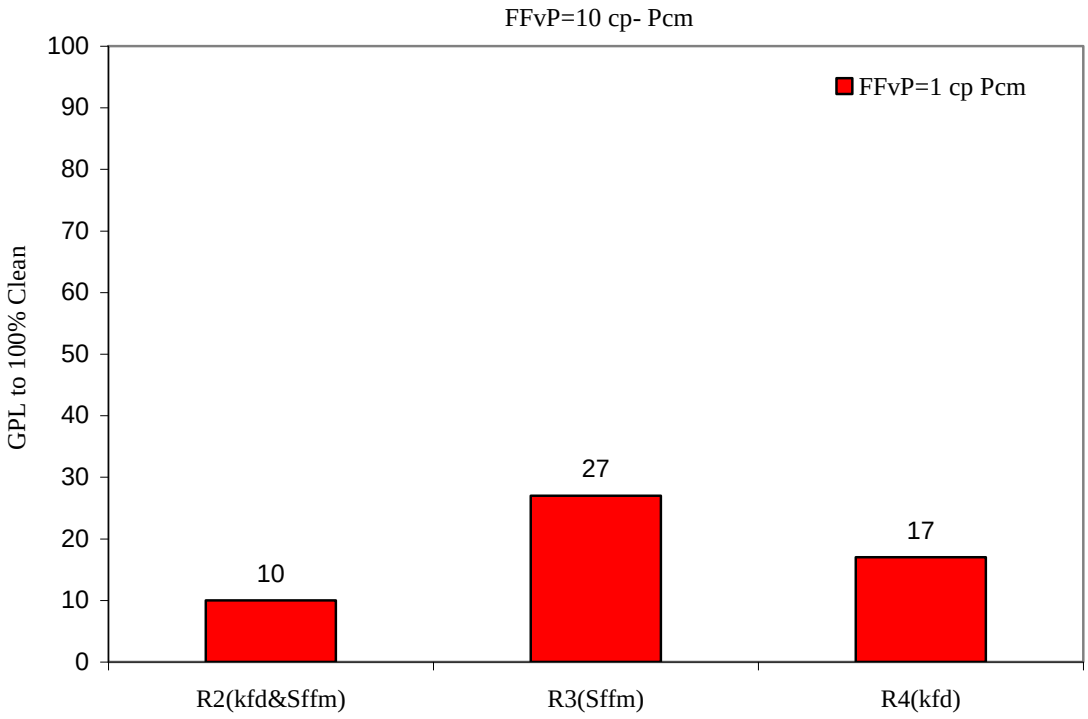

Figure 5.11: GPL compared to 100% cleanup for simulation runs indexed R2-R4 with P_{cm} corrected for S_{wi}= 17.5%.

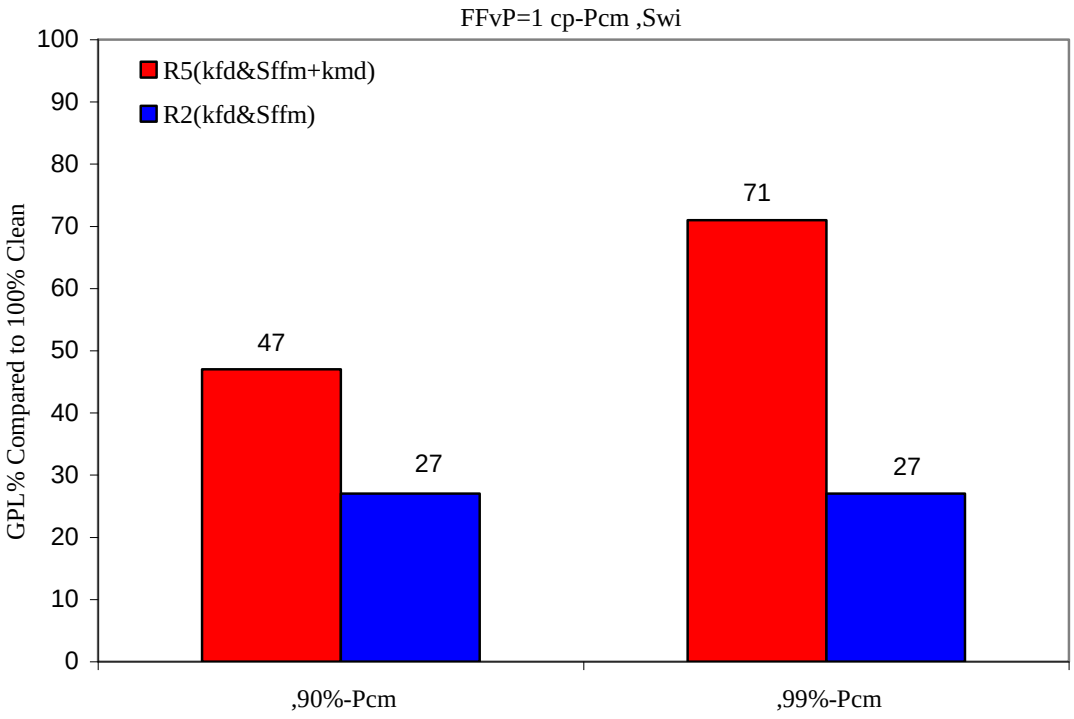

Figure 5.12: GPL compared to 100% cleanup for simulation runs indexed R5 (with 90% and 99% k_{md}) & R2 (without k_{md}), both with P_{cm} and S_{wi}=17.5%.

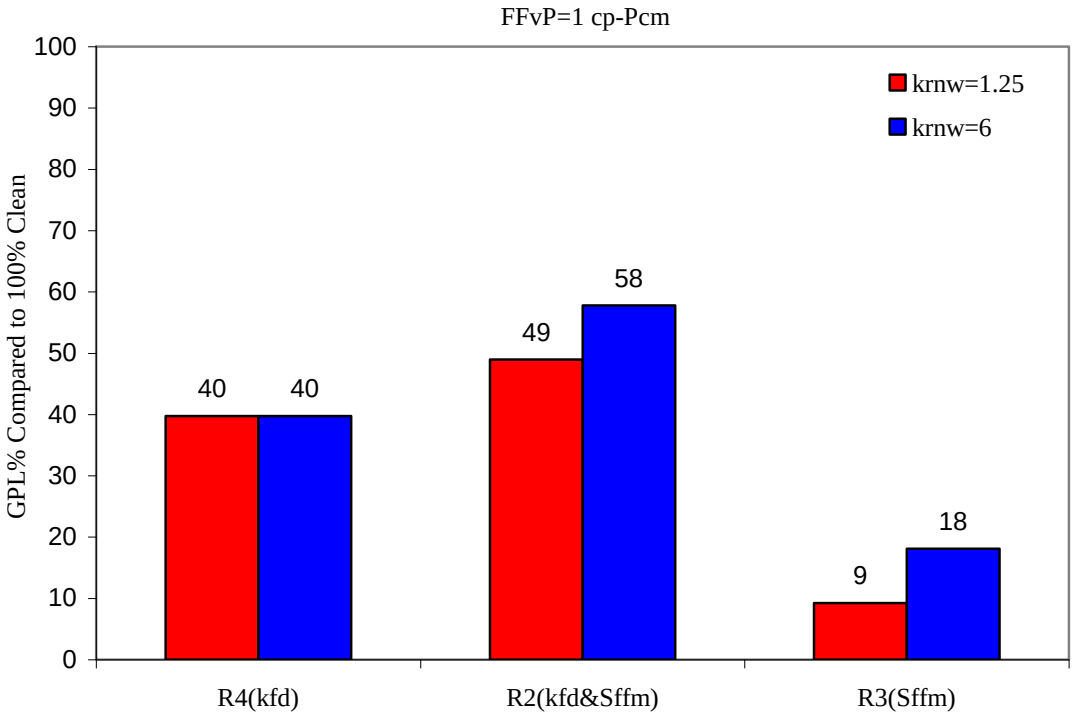

Figure 5.13: GPL compared to 100% cleanup for simulation runs indexed R2-R4 with P_{cm}, considering two different FF k_r curve.

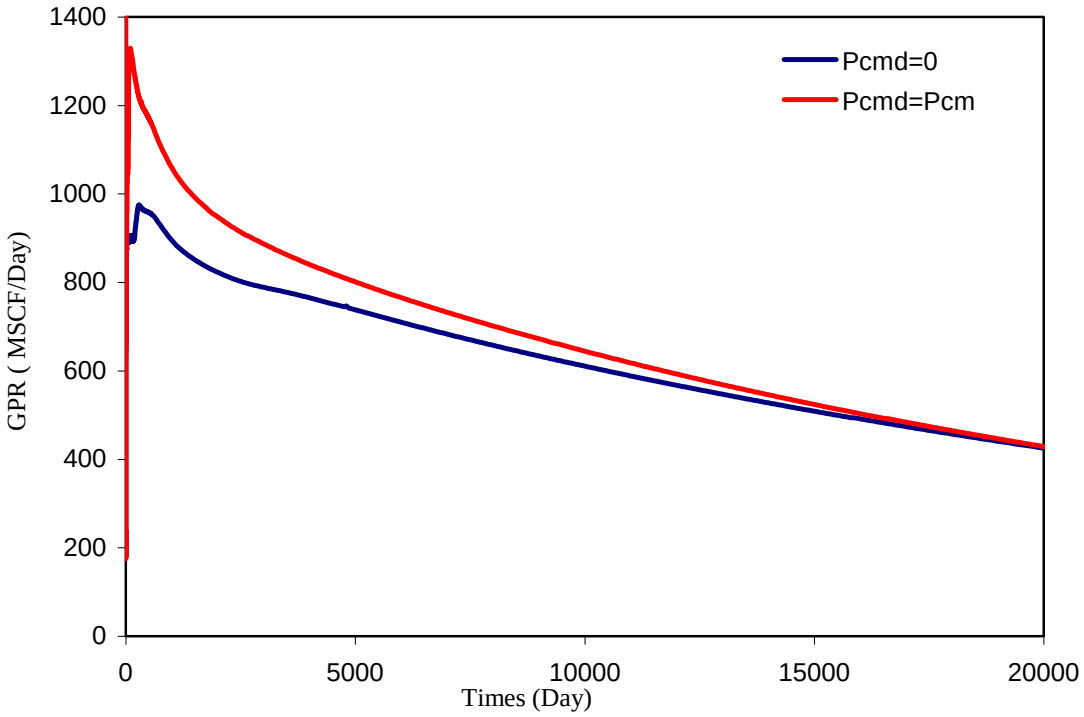

Figure 5.14: Gas production rate vs. times for two cases with $P_{cmd}=P_{cm}$ and $P_{cmd}=0$.

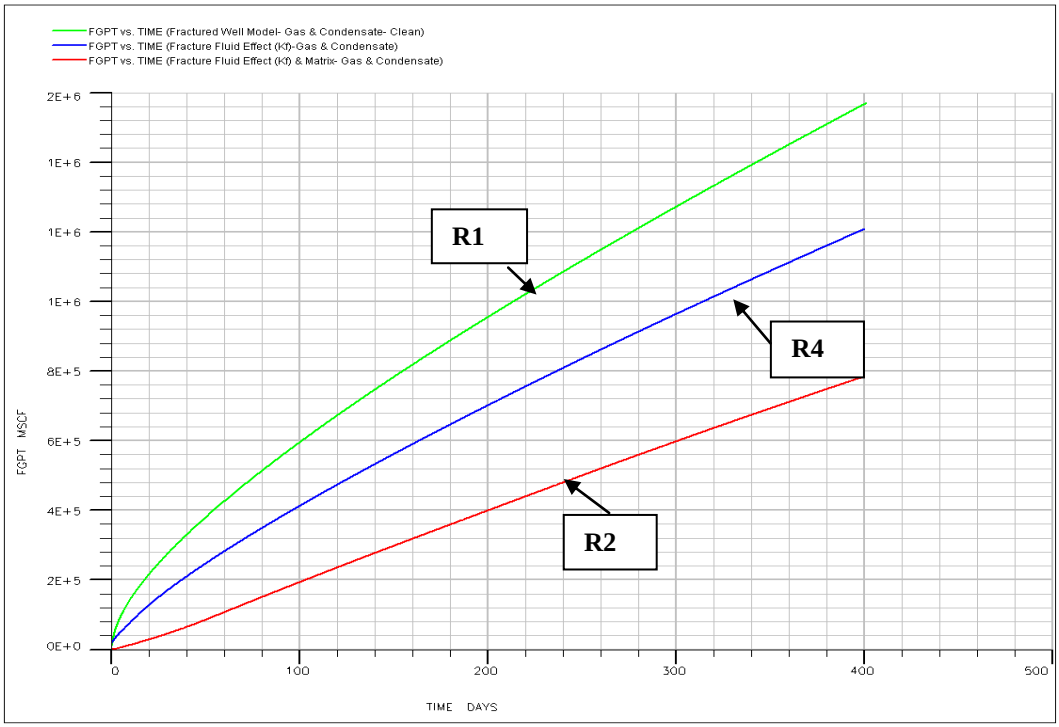

Figure 5.15: Gas production versus time for simulations R1-R4 with gas and condensate flow.

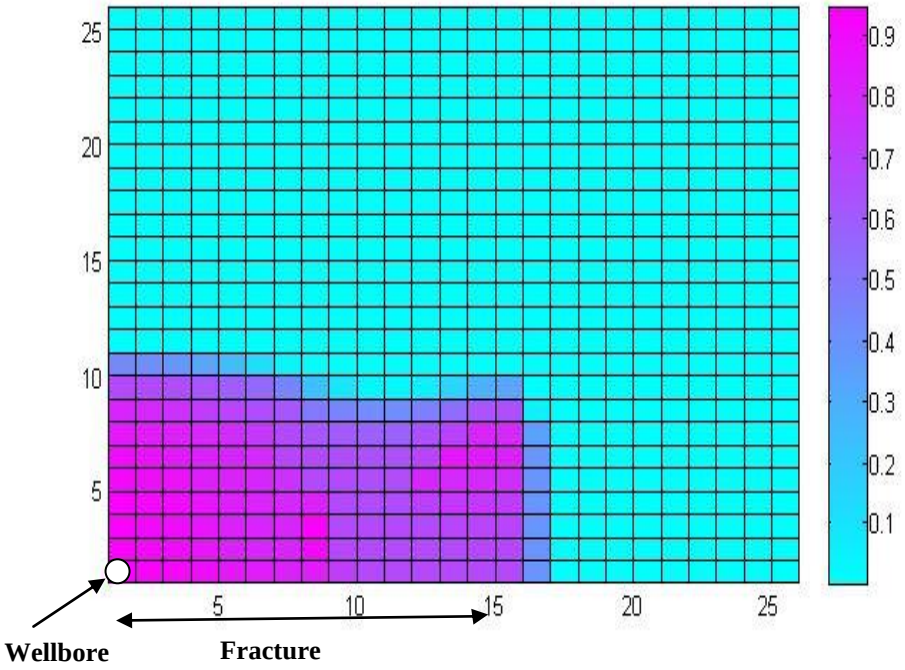

Figure 5.16: FF saturation map after injection of 1227 bbl of FF.

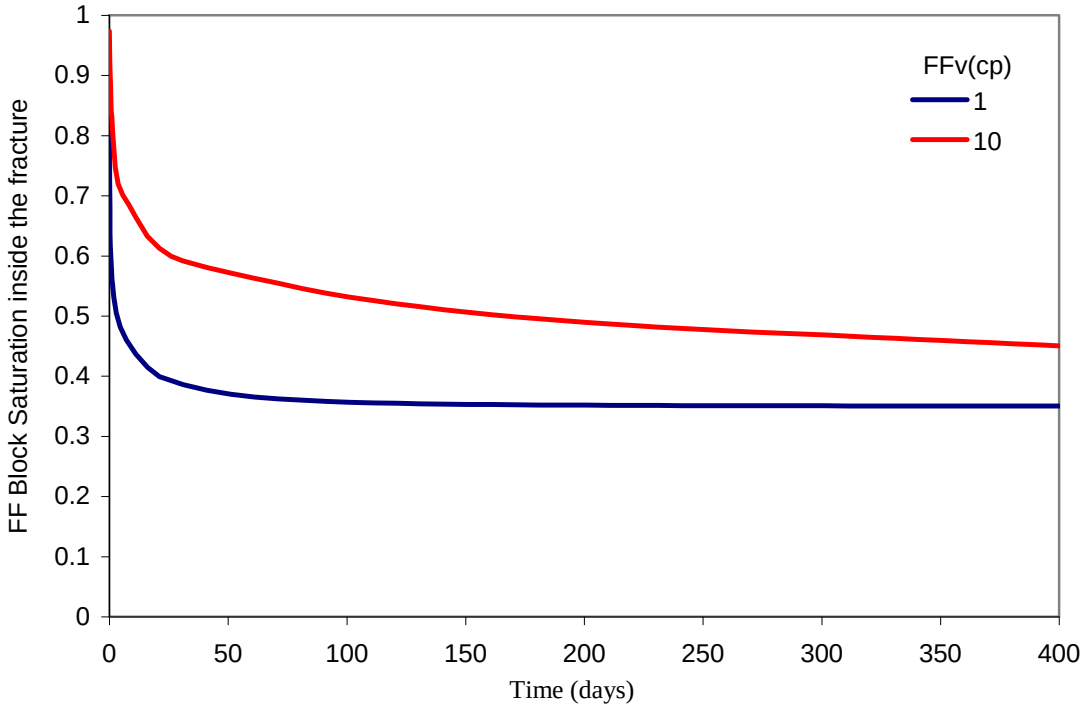

Figure 5.17: FF saturation in the first fracture grid block versus time.

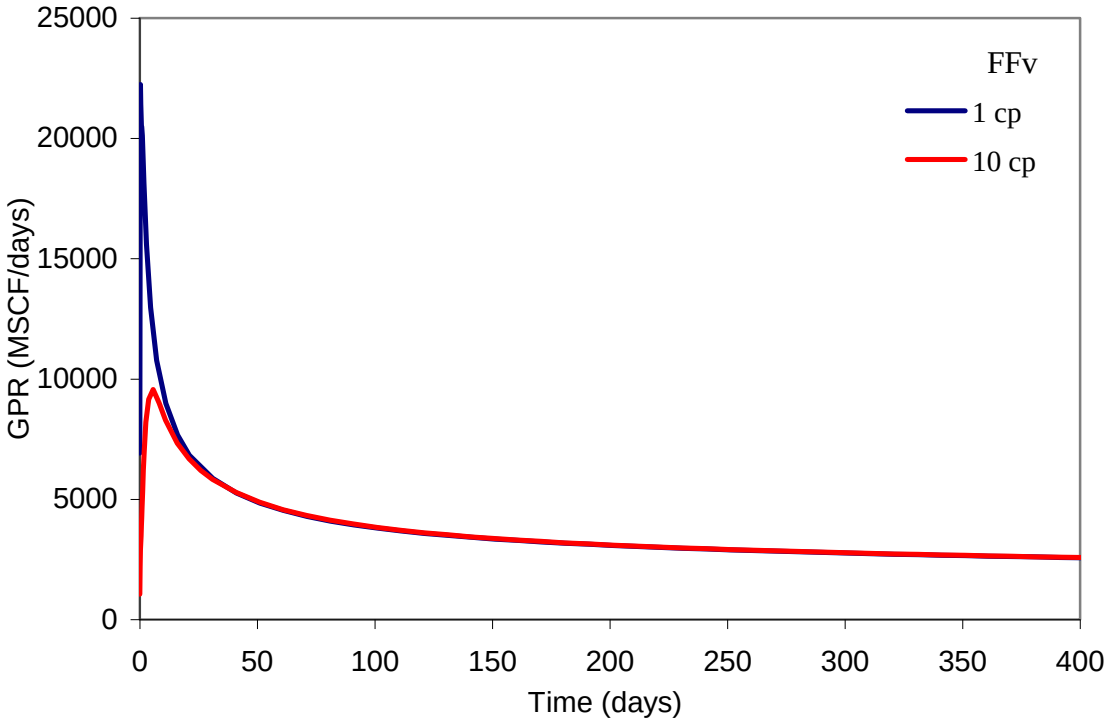

Figure 5.18: GPR versus time at two different FF viscosities of 1 and 10 cp.

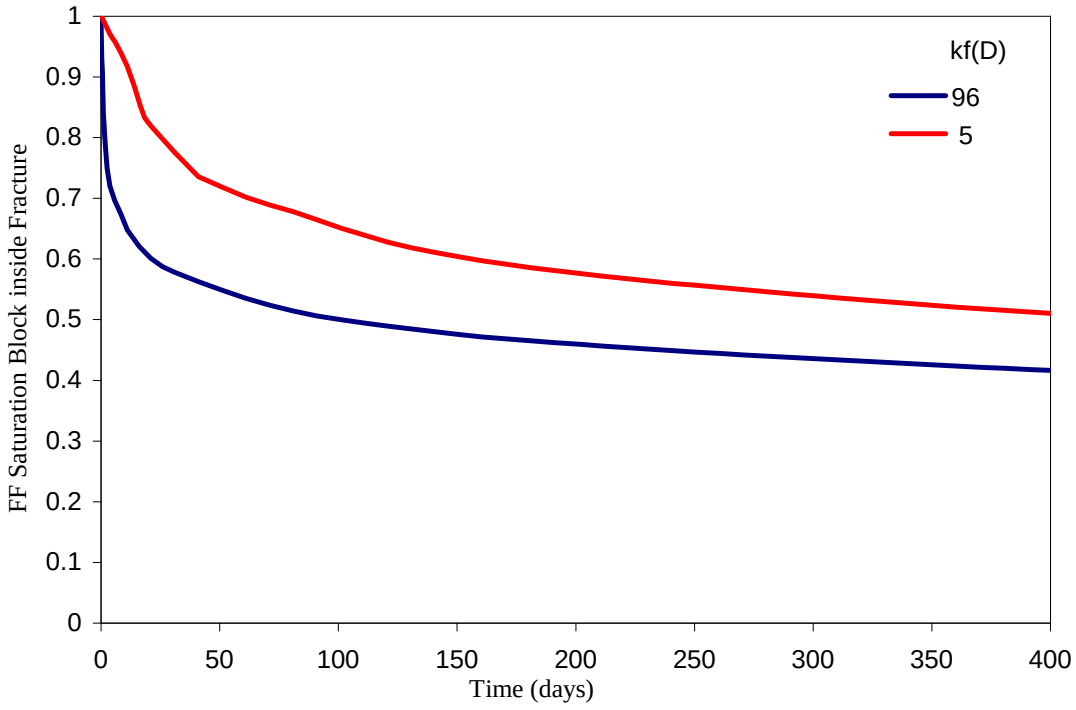

Figure 5.19: FF saturation in the first fracture grid block versus time with and without considering k_{fd} ,FFv=10 cp, both cases with S_{ffm}.

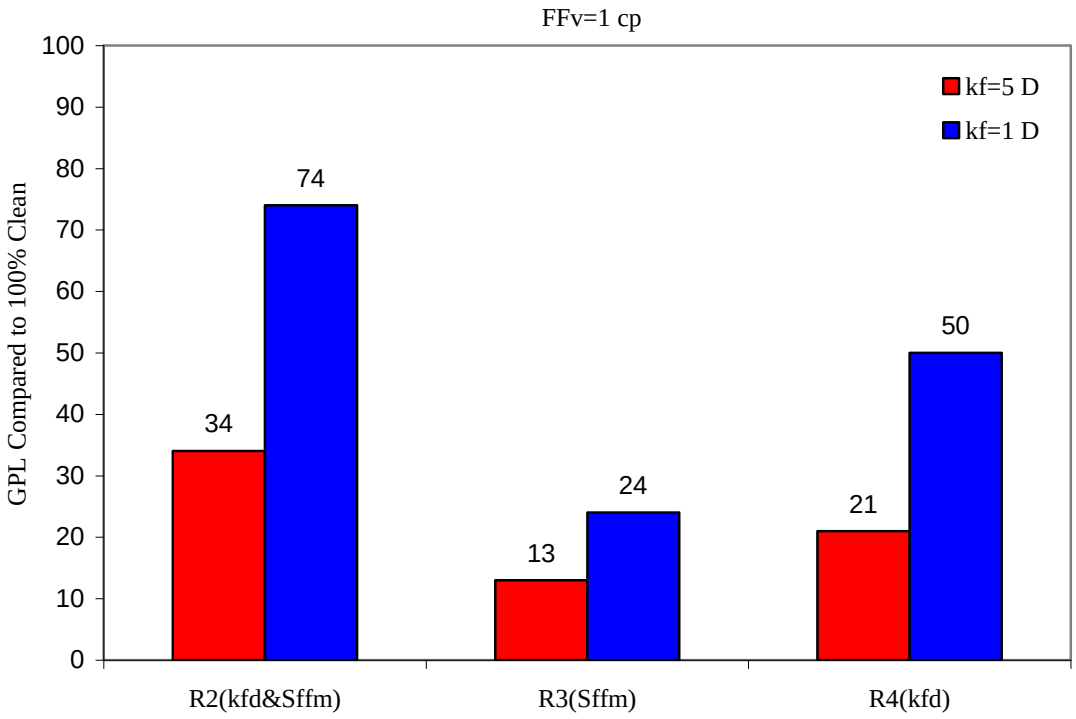

Figure 5.20: GPL compared to 100% cleanup for simulation runs indexed R2-R4, FFv=1 cp.

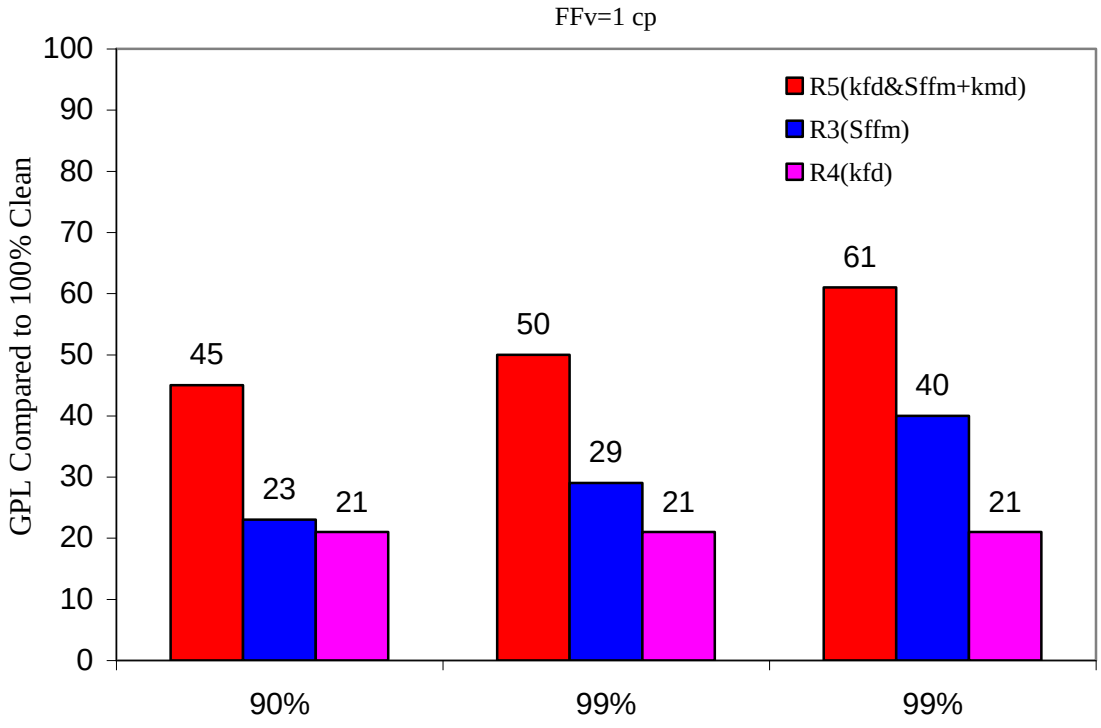

Figure 5.21: GPL compared to 100% cleanup for simulation runs indexed R3-R5.

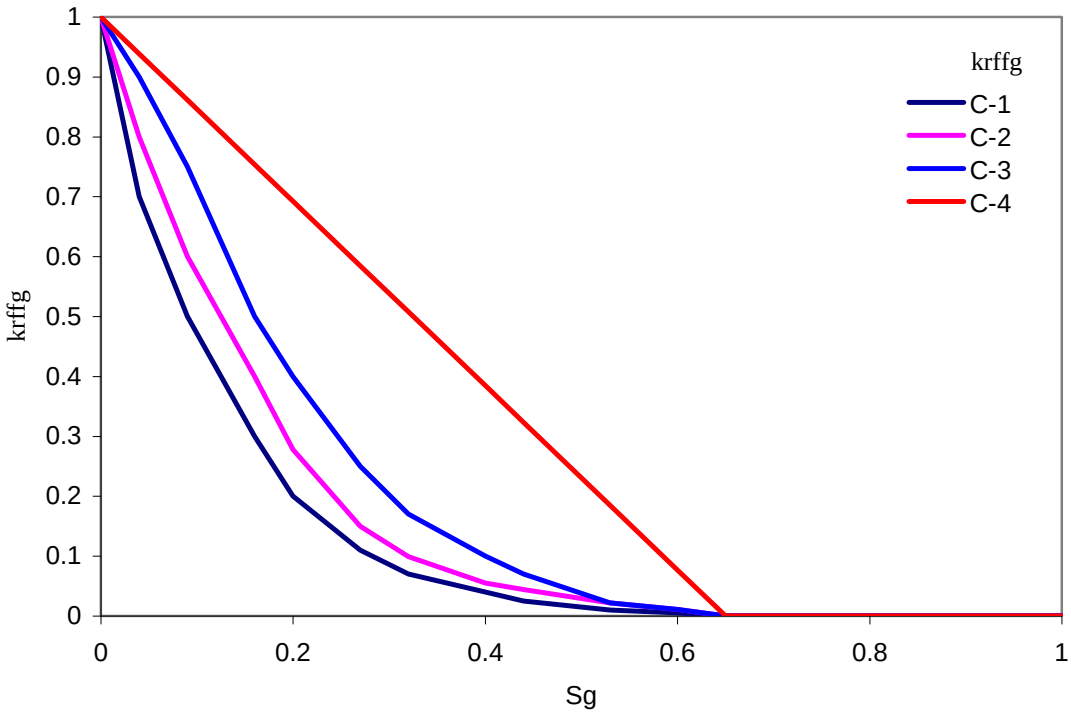

Figure 5.22: FF relative permeability curves versus gas saturation.

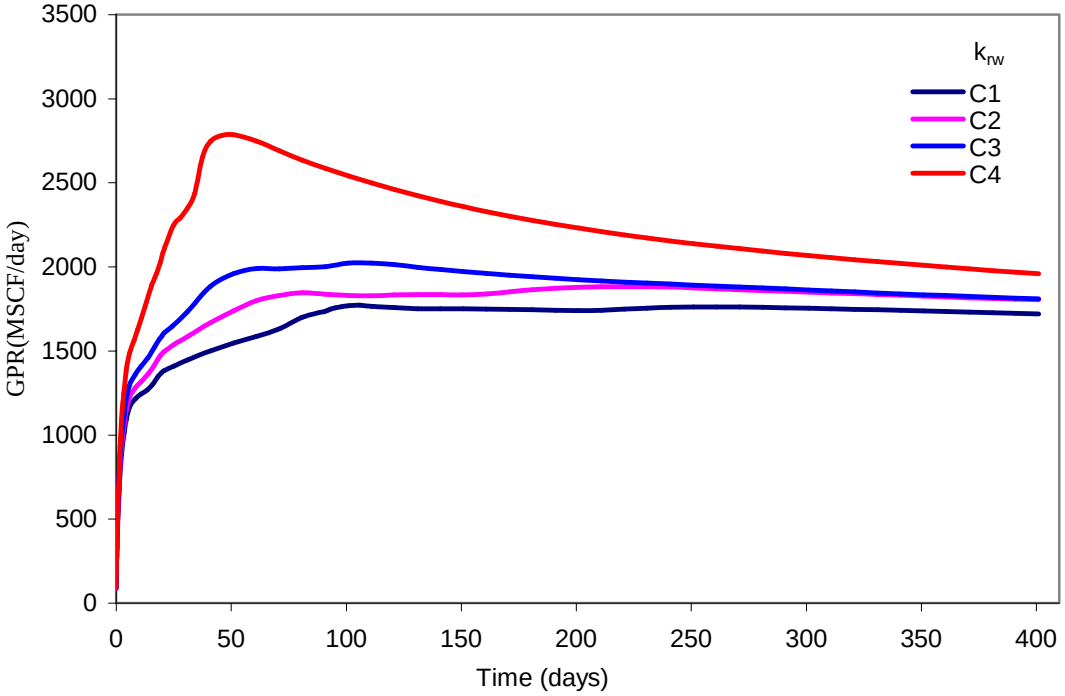

Figure 5.23: The gas production rate versus time with different FF relative permeability curves inside the fracture.

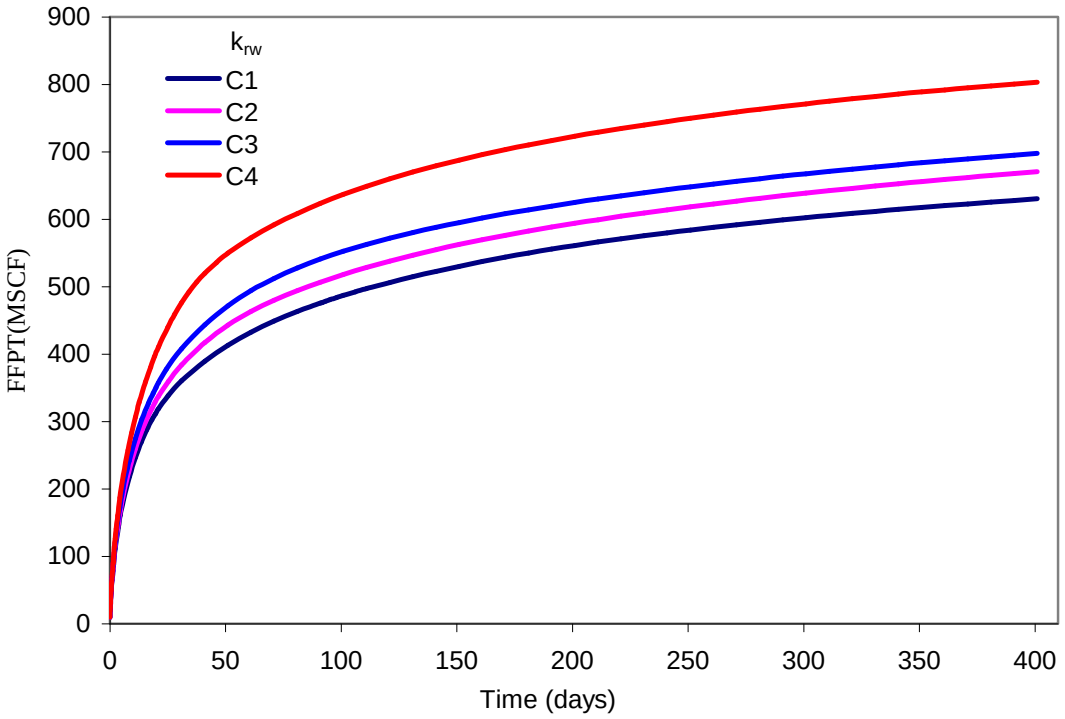

Figure 5.24: The total FF production versus time for the fractured well model with four different FF relative permeability curves inside the fracture during production time.

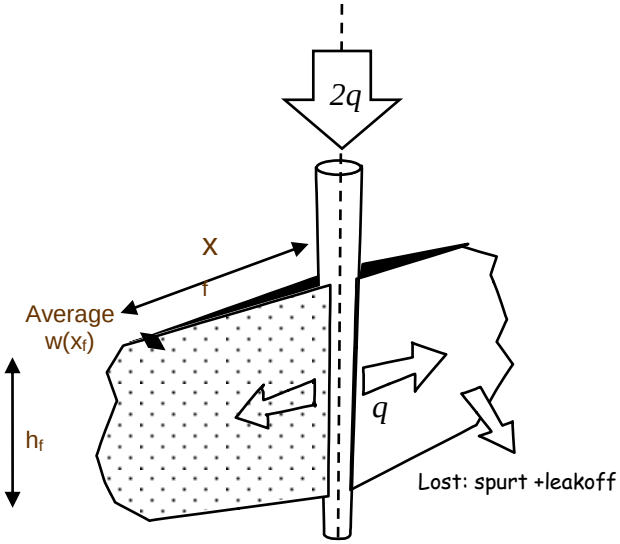

Figure 5.25: Schematic of hydraulic fractured well model

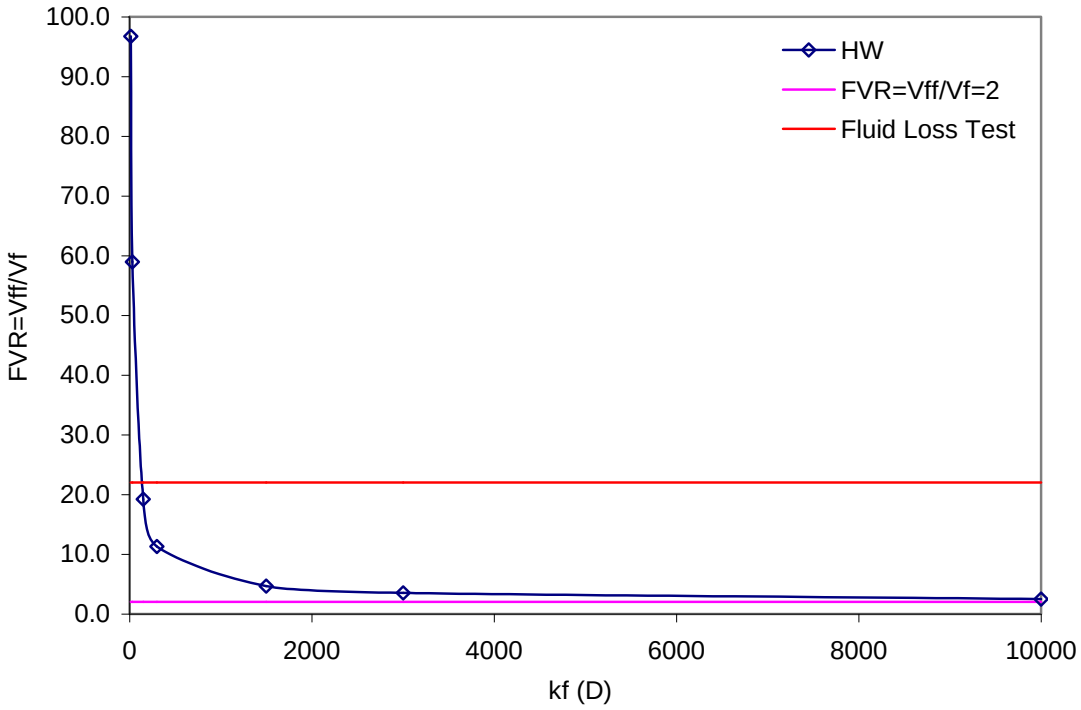

Figure 5.26: FF injected volume per fracture volume, FVR, versus fracture permeability.

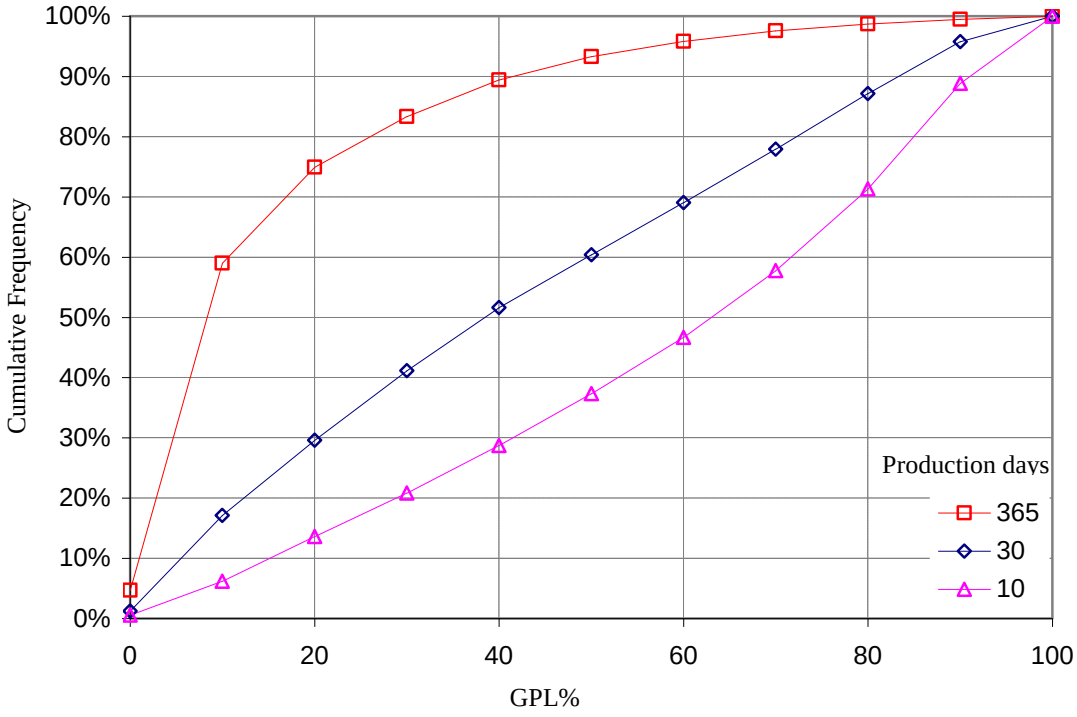

Figure 5.27: Cumulative frequency of the percentage of the cases studied here for FVR=2 at different production time versus GPL.

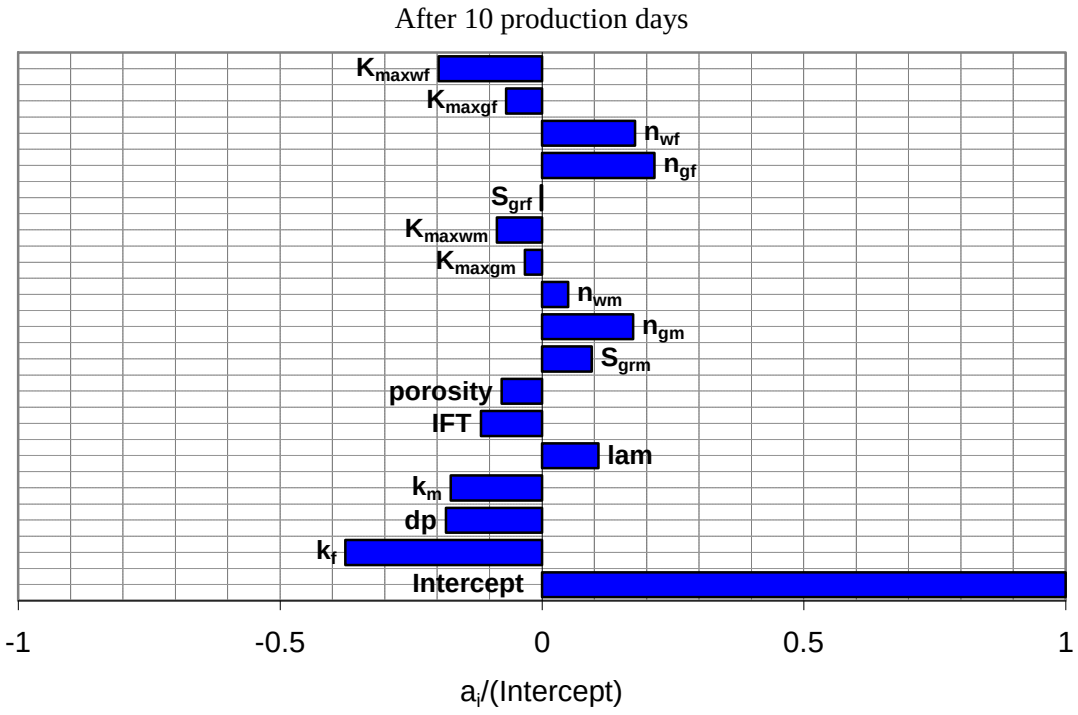

Figure 5.28: The impact of scaled coefficients (a_i/ (Intercept)), LRSM after 10 production days, FVR=2.

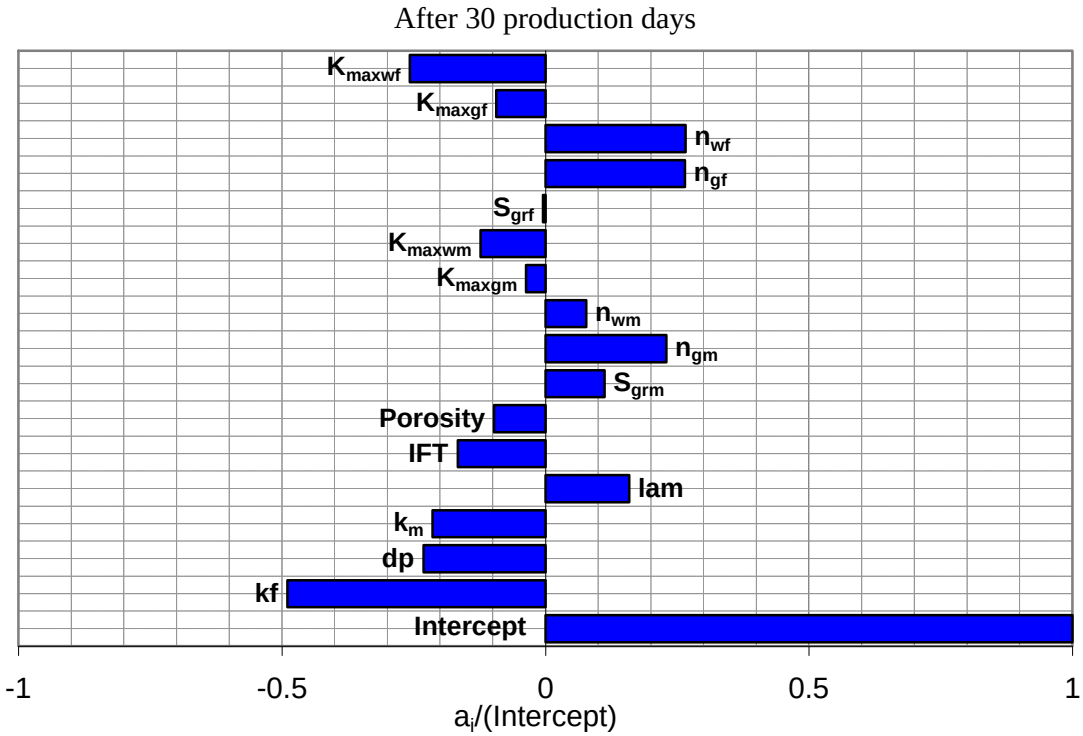

Figure 5.29: The impact of scaled coefficients (a_i/ (Intercept)), LRSM after 30 production days, FVR=2.

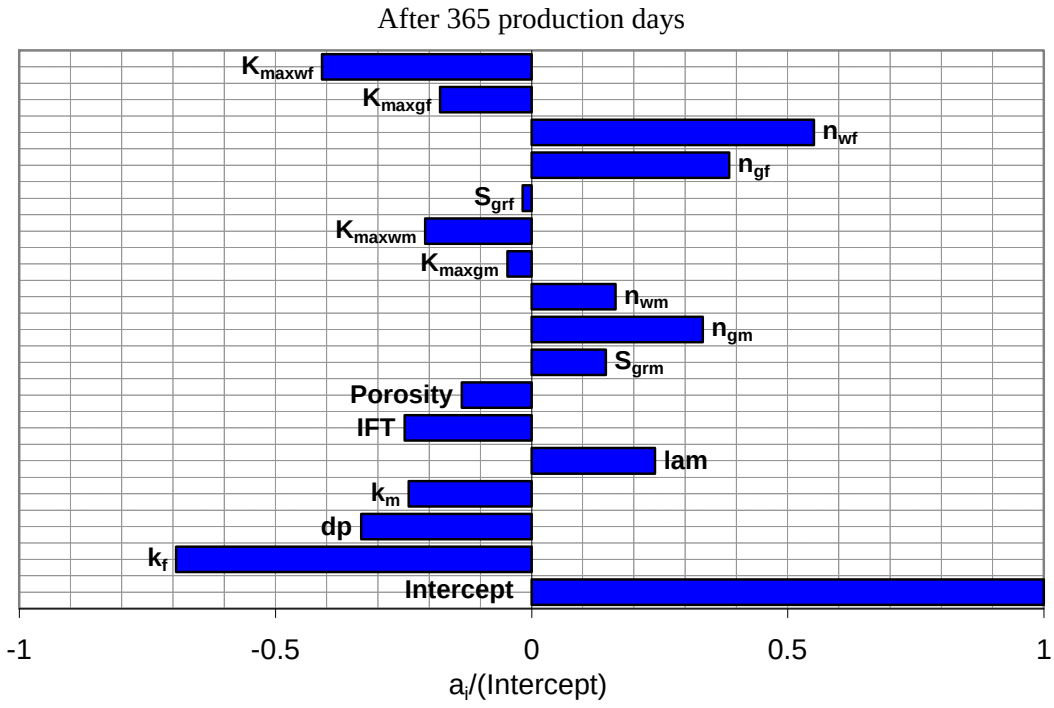

Figure 5.30: The impact of scaled coefficients (a_i/ (Intercept)), LRSM after 365 production days, FVR=2.

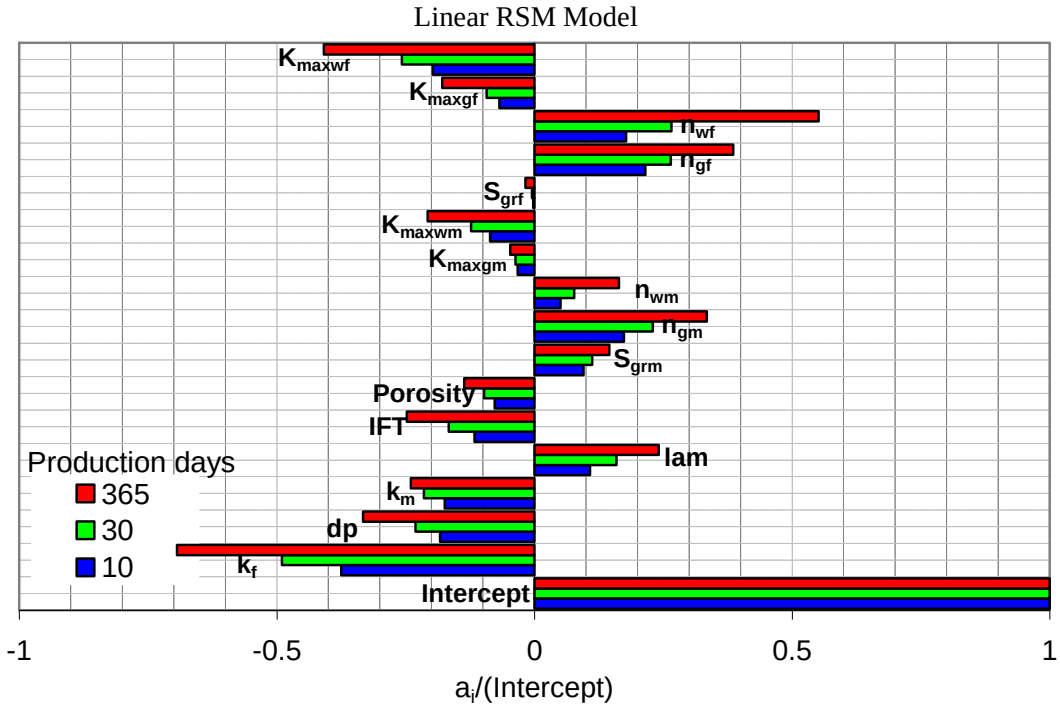

Figure 5.31: Comparison of the impact of scaled coefficients (a_i/ (Intercept)), LRSM after 10 with 30 and 365 production days, FVR=2.

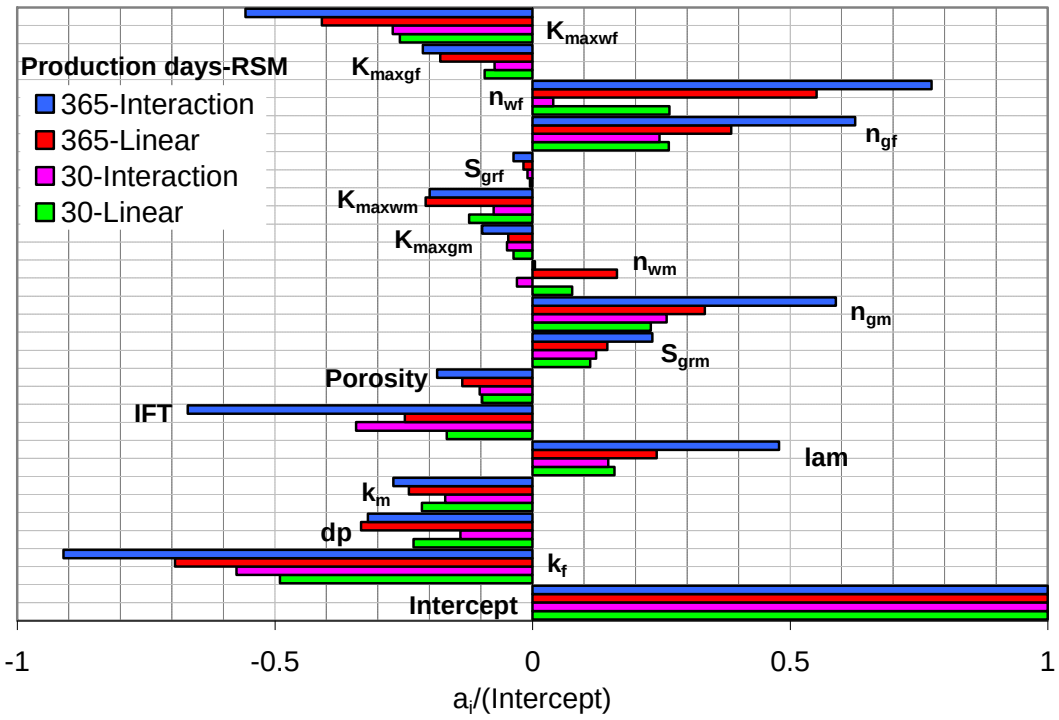

Figure 5.32: Comparison of the impact of scaled coefficients (a_i/ (Intercept)) of LRSM with IRSM after 30 and 365 production days, FVR=2.

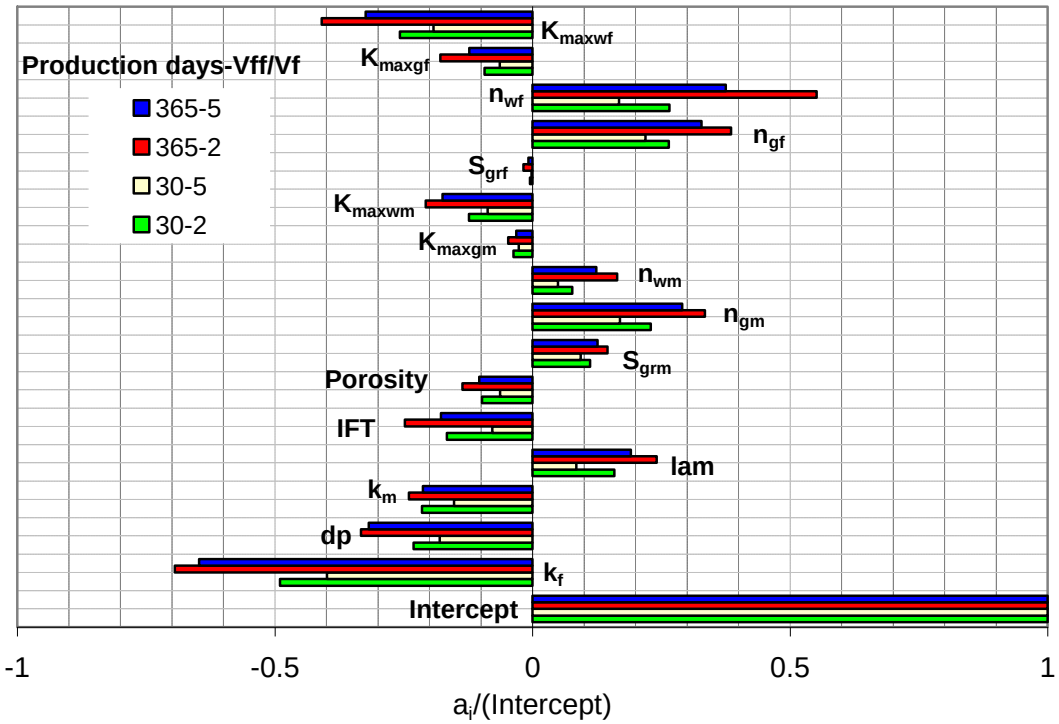

Figure 5.33: Comparison of the impact of scaled coefficients (a_i/ (Intercept)), LRSM after 30 and 365 production days for FVR=2 with that for FVR=5.

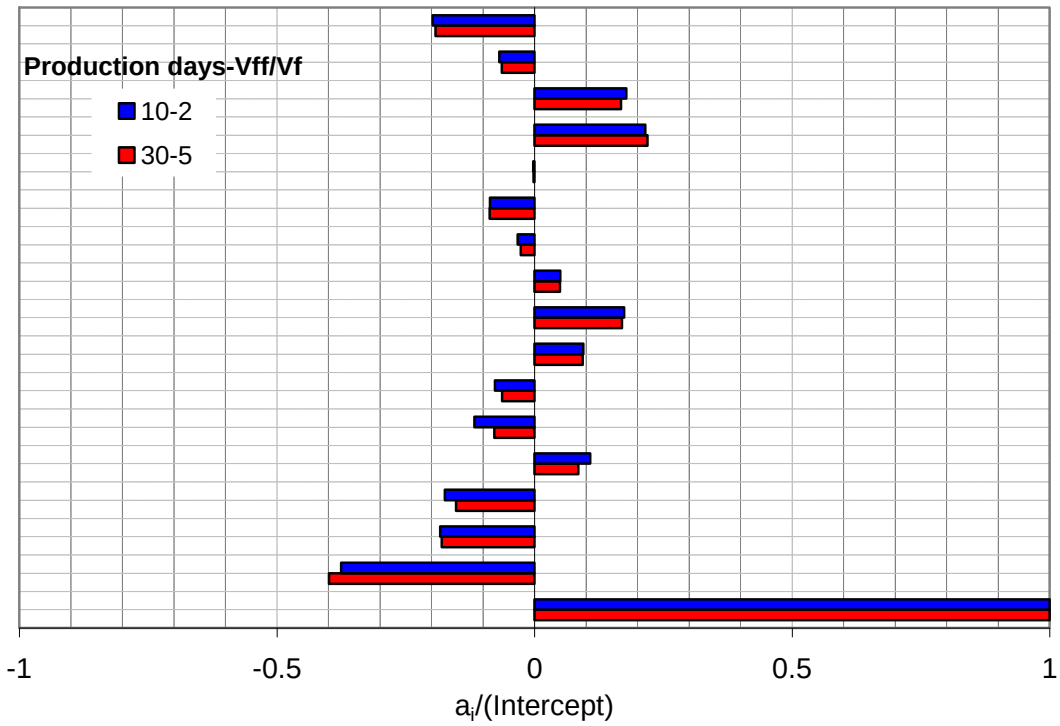

Figure 5.34: Comparison of the impact of scaled coefficients (a_i/ (Intercept)), LRSM after 10 production days for FVR=2 with that for after 30 production days with FVR=5.

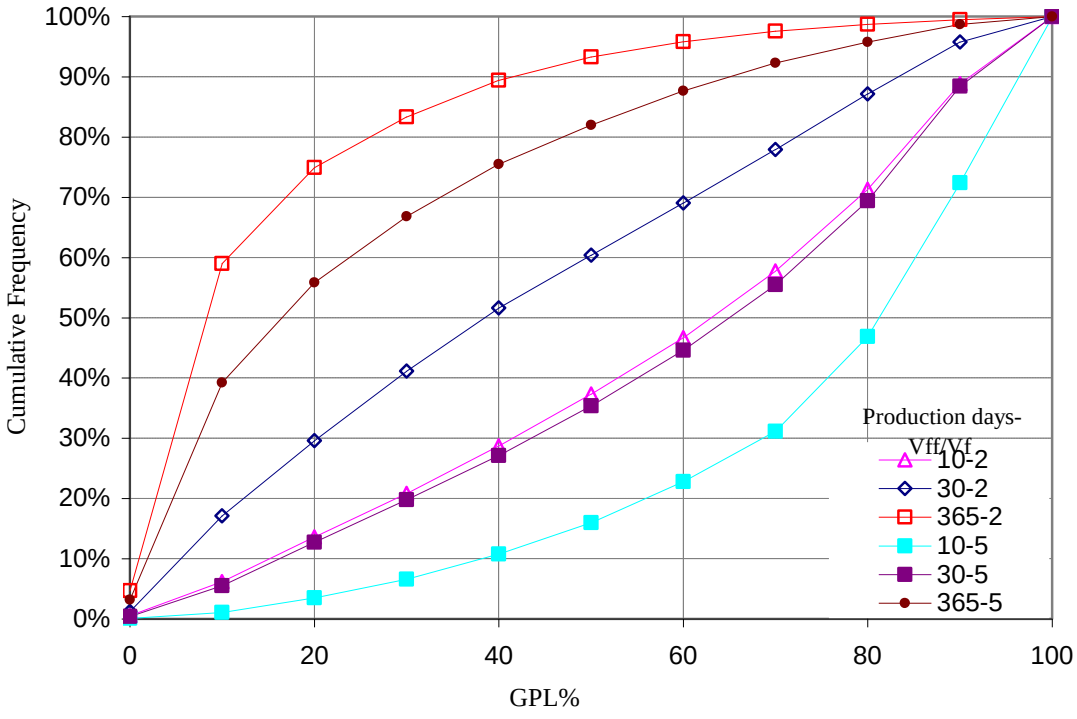

Figure 5.35: Cumulative frequency of the percentage of the cases studied here for FVR=2 and FVR=5 at different production time versus GPL.

CONCLUSIONS AND RECOMMENDATIONS

In the last two decades, drilling horizontal (HWs) and deviated (DWs) wells has become a common practice around the world. An accurate estimation of productivity of such flow geometries using a numerical simulator is a challenging task. This is mainly because the 3-D simulation of flow requires a fine grid exercise to capture the abrupt variation of fluid and flow parameters around the wellbore. This is cumbersome and impractical for field applications. There are formulations available in the literature for calculation of productivity of such wells but they are for single-phase flow conditions. The flow behavior of gas condensate systems, when pressure drops below dew point, is different from conventional gas oil systems. The phase change and dependency of the relative permeability to IFT and velocity in the form of coupling and inertia requires a different approach for these low IFT systems. This study was aimed to propose a practical methodology, which accounts for the impact of geometrical and flow parameters, for improved prediction of the performance of HWs and DWs in gas condensate reservoirs under steady state and pseudo steady state conditions. This was achieved following a systematic approach as described in Chapters 3 and 4.

Hydraulic fracturing is one of the most important stimulation techniques especially for tight gas reservoirs. Over the last 60 years, there have been many reports on the poor performance of some of the hydraulically fractured wells. Poor cleanup efficiency of the injected fracture fluid (FF) has been considered as one of the factors contributing to the low productivity of such wells. A number of parametric studies have been conducted evaluating the impact of a number of pertinent parameters affecting the FF cleanup efficiency. There are conflicting reports in some of these studies mainly due to the assumptions made when simulating this process. Therefore to address these issues, the cleanup efficiency of hydraulically fractured gas and gas-condensate wells was considered as the other objective of this study. Initially a series of sensitivities were conducting to clarify some of the uncertainty on the impact of pertinent parameters affecting the process. Then using statistical methods the effects of key important parameters, varying over their practical ranges, were extensively investigated by conducting over 130000 simulations as described in Chapter 5.

The chapter is devoted to present the main conclusions and recommendation for the future works in these two areas of research.

6.1 CONCLUSIONS

The present research work has three main elements, i) gas condensate flow around horizontal well, ii) gas condensate flow around deviated wells and iii) cleanup efficiency of hydraulically fractured wells.

6.1.1 Horizontal Wells (HWs):

This part mainly focuses on proposing practical methods for improved simulation and well productivity calculation of horizontal wells in gas condensate reservoirs. Here several single phase and two phase compositional in-house simulators were developed to model accurately the 3-D complex flow behaviour around a horizontal well in gas and gas condensate reservoirs under steady state (SS) or pseudo steady state (PSS) conditions. The integrity of the in-house simulators were confirmed by comparing their results with those performed using ECLIPSE100 or ECLIPSE300 commercial reservoir simulators with fine grid under the same privilege conditions. Using the 3-D in-house simulators a large data bank was generated covering a wide range of variations of pertinent geometrical and flow parameters. A new formulation and approach was proposed for calculation of effective wellbore radius of a 1-D open hole radial system replicating flow around a 3-D system. Series of sensitivity studies were also performed aimed at investigating the impact of pertinent parameters on the performance of such wells including identifying the limitations of formulations currently available in the literature. The major conclusions of this study can be summarized as follows:

1. Horizontal well performance is affected strongly by anisotropy values for horizontal well length (L) to the reservoir thickness (Z), (L/h) less than 25.
2. Extremely fine grid is required using the commercial simulator (ECLIPSE) to capture the effect of anisotropy with good accuracy.
3. A combination of increased number of mesh elements and using second order Lagrange function were required in the finite element based in-house simulator to obtain accurate results for anisotropic formations.
4. A deviation between the results of the in-house simulator with those obtained using two well-known equations (Joshi 1991 and Economides et al. 1996) indicated that these equations may not predict horizontal well performance properly in anisotropic formations for L/h less than 25.
5. Based on the results of the single phase HW in-house simulator, a geometric skin was developed using the efficient statistical Response

Surface method. The geometric skin varies with length of horizontal well, radius of the well, reservoir thickness and anisotropy, the integrity of the geometric skin formulation was validated by comparing its results for data points not used in its development. This exercise also included comparing some of its predictions with those of Joshi (1985) and Borosiv (1984)'s semi-analytical equations, with reasonable accuracy. These later data points were carefully selected to be within the range of applicability of these equations.

6. The effect of partial penetration (PP) on the well performance of HW and geometric skin was studied comprehensively. The results indicated that the partial penetration ratio (horizontal well length (L) to reservoir dimension in x direction (X_{res})) does not have a significant impact on the geometric skin unless one works at L/X_{res} >0.6 and low L values or at L/(reservoir thickness (h)) <12 and low h values.
7. The impact of asymmetry of the HW location in the z direction was studied. It was found that its impact on the HW flow performance is negligible for long HWs. Based on the results of the in-house simulator, a separate geometric skin formulation was developed, to account for asymmetrical position of HW in the formation.
8. A SS single-phase inertial flow skin formulation, based on the effective wellbore radius of an equivalent open hole system replicating 3-D flow around a HW, was developed. The integrity of the proposed formulation was validated by comparing its prediction with the corresponding estimated values using the in-house simulator. Because of the dependency of the effective wellbore radius on velocity, its implementation in the pseudo-pressure calculation requires an iterative procedure.
9. The study of flow around HWs in gas and condensate systems indicated that for long HWs, the assumption of the effective radius of the EOH based on the geometric skin is a good approximation. However for short to medium length HWs, this assumption is not valid and the results could be highly erroneous. Therefore a generalized formulation for estimation of the effective radius of an equivalent open hole system was developed, which captures the impact of important flow parameters and can be correctly extended to single-phase flow conditions. Similarly to the

single-phase inertial flow case, the implementation of this wellbore radius also requires an iterative procedure. The accuracy of this formulation was confirmed by comparing its results with the corresponding values obtained using the HW in-house simulator.

10. The results of another exercise showed that the proposed SS effective wellbore radius formulation is applicable to PSS conditions.

A sensitivity study was also conducted to evaluate the impact of pertinent parameters on the HWs performance for single phase (non-Darcy flow) and two-phase gas condensate flow. The results demonstrated that:

Single-phase Non-Darcy flow:

11. The flow skin increases as the velocity increases. However, as HW length increases, flow skin decreases sharply.
12. Flow skin increases as the thickness of the reservoir increases, due to increased inertial effect at higher flow rates.
13. The flow skin approaches zero for the horizontal well length to reservoir thickness greater than 20, i.e. (L/h)>=20.
14. Productivity ratio (PR) (ratio of HW to vertical well (VW) flow rates for the same pressure drop) is almost constant for short HW lengths at different velocity values. However, it increases as L increases, due to a decrease in the inertial effect for HW.

Two-phase flow of gas and condensate:

15. At higher the total gas fractional flow rate (GTR), the impact of positive coupling is less pronounced in the HW, whilst inertia is still dominant in the VW system.
16. As the total gas fractional flow decreases the PR(HW/VW) increases that is, the positive coupling effect is more dominant in HW compared to that in VW, resulting in an increase in PR as GTR is reduced.
17. The effect of the wellbore radius on PR is negligible.

b) Deviated Wells (DWs):

This study was aimed to investigate the well performance of DWs (both partially and fully penetrating) in gas and gas condensate reservoirs. Therefore, similarly to the study of flow around HWs a number of in-house simulators were developed. The integrity of

the results of the in-house simulators was confirmed by comparing some of their results with those obtained using ECLIPSE with fine grid for the same prevailing flow conditions. Based on the effective wellbore radius approach, a new formulation was proposed, which links the skin of deviated wells to that of horizontal wells. A comprehensive sensitivity study was also conducted to evaluate the impact of pertinent parameters including inertia and coupling on the performance of such wells. The main conclusions of this study can be summarised as follows:

1. It was confirmed that at low velocities, Darcy flow regime, any well deviation from vertical results in an improved performance, i.e. there is a negative geometric skin.
2. A study was conducted to determine the range of application of some of equations (Cinco-Ley (1975), Besson (1990) and Rogers (1996) Equations) widely used in the literature for DWs. The results indicated that these equations cannot accurately predict DWs productivity in an anisotropic formation with anisotropy values less than 0.6.
3. It was shown that the DWs geometric skin depends on the same pertinent parameters as those for HWs, i.e., length of horizontal well, radius of the well, reservoir thickness, and anisotropy. Therefore, an easy to use formulation for geometric skin of DWs was developed, which correlated the geometric skin of HWs to that of DWs, using the deviation angle. The integrity of the geometric skin formulation was validated by comparing its results for data points not used in its development.
4. Similarly to geometric skin, a single-phase inertial flow skin formulation was developed for DWs, which is related to that for HWs. Based on this formulation; initially the effective wellbore radius of an equivalent open-hole system should be estimated for HW with the same well length. Then, this effective wellbore radius is converted to the HW flow skin to be included in the proposed formulation to calculate the DW flow skin. This flow skin is then converted to an effective wellbore radius to be used in an open-hole well model replicating flow around the corresponding 3-D DW. The integrity of the flow skin formulation was validated by comparing its predictions with the corresponding values estimated using the in-house simulator, thereby confirming the integrity of the proposed approach.

5. In the case of a two-phase flow of gas and condensate, a similar approach to that for the single-phase non-Darcy flow skin was followed to develop the two-phase flow skin for the DWs. The integrity of the proposed procedure was confirmed by comparing its predictions with the corresponding estimated values using the in-house simulator. This equation is general and converts to single-phase flow conditions when gas fractional flow is one.

A comprehensive sensitivity study was also conducted evaluating the impact of important parameters on PR of DW to VW at single phase flow and two-phase flow conditions. From these results the following conclusions can be made.

Single-phase Non-Darcy flow:

For the same DW length as that of a VW

6. An increase in velocity decreases PR, due to the more pronounced effect of inertia for the DW compared to that for the VW, especially for smaller well deviation angles.
7. PR is always higher for low reservoir thickness values.
8. The negative impact of inertia on DW productivity compared to that on VW productivity is more pronounced for thicker reservoirs, due to the higher production rate.

Similarly to the HW cases, PR strongly depends on the DW lengths:

9. At higher DW length, the negative impact of inertia is less for DWs compared to that for VW, thus improving the PR, especially at higher velocities.

Two-phase flow of gas and condensate:

For the same DW length as that of the VW:

10. As the deviation angle increases, PR increases for all GTR_w (gas fractional flow at the wellbore), due to higher negative geometric skin.
11. Decreasing GTR_w below 0.95 improves PR because of the more pronounced effect of positive coupling in DW compared to that in VW, but the extent of this improvement is almost constant when GTR_w varies between 0.7 and 0.85.

12. PR decreases at GTR_w values greater than 0.95, where the negative impact of inertia is more pronounced for DW compared to that for VW.
13. The DW performance is better for thinner reservoirs.

Similarly to the HW cases, PR strongly depends on the DW lengths

14. Higher Length (L) means higher PR.
15. At higher DW lengths, the negative impact of inertia is less for DWs compared to that for VWs, improving the PR, especially at higher velocities
16. Wellbore radius has minimal impact on DW performance.
17. At higher GTR_w, the trends of variation of PR for long and short DWs are in opposite directions. That is, in the former, an increase in GTR_w increases the negative impact of inertia on the DW performance more than in the case of VW (PR decreases at higher GTR_w). However in the latter, the velocity of long DWs decreases significantly compared to that of a VW, resulting in a decrease in the negative impact of inertia on the DW performance compared to that of VW and PR increases as GTR_w increases.

c) Cleanup Efficiency of Hydraulically Fractured Wells:

This part of the study is divided into two sections.

The first section was devoted to evaluate the impact of pertinent parameters on the clean-up efficiency of a hydraulically (gas or gas-condensate) fractured well. A series of numerical simulations were conducted using ECLIPSE 300 and ECLIPSE100. The general conclusion is that accurate modelling of FF invasion into the fracture and matrix is crucial. The main itemized conclusions of the first section are:

1. A model was created using ECLIPSE100, which reproduced the results of the published paper by Holditch 1979, thereby demonstrating the integrity of the proposed approach.
2. The presence of fracture fluid (FF) in the damage zone influences the gas recovery by reducing the gas relative permeability. It can increase gas production loss (GPL) significantly, if FF invasion was simulated more realistically, as was performed here by allowing the FF to invade all fracture blocks. This supports experimental work conducted by Bennion 2001. However it does not agree with the numerical simulations

conducted by several investigators (Holditch 1979, Adegbola 2002, Gdanski et al. 2005).

3. The results also demonstrates that the combined effect of absolute permeability and effective gas relative permeability reduction in the matrix invaded zone is more pronounced for most of cases studied here, even for the cases with moderately to high fracture permeability reduction. This is in contrast with the pervious numerical models showing that fracture face damage is the important issue if it caused sever permeability reduction in the matrix invaded zone.
4. FF recovery is higher if it is degraded with a reduced viscosity, i.e., higher mobility for the production period.
5. The fracture conductivity reduction is the main factor in GPL when matrix capillary pressure is zero. Matrix capillary pressure increases the extent of FF invasion into the matrix. This reduces the saturation of FF in the fracture thus reducing the impact of fracture on cleanup efficiency.
6. Damage permeability reduction in the range of 90% and 99% can significantly increase GPL when matrix capillary pressure is considered.
7. The initial water saturation (S_{wi}) decreased GPL. This is due to a decrease in the capillary pressure driving force between matrix and fracture, which in turn reduces the FF invasion into the matrix. It should be noted that this conclusion is based on 100% cleanup case with S_{wi} where the gas production has already dropped significantly due to the presence of S_{wi}.
8. The effect of a change in the matrix capillary pressure of the damaged zone is negligible unless unrealistically low pressure drawdown is assumed. This is in line with the findings in the literature (e.g., Holditch 1979 and Gdanski et al. 2005).
9. FF recovery was improved in the presence of condensate, which resulted in a decrease in the adverse effect of FF giving lower GPL. It should be noted that this conclusion is based on 100% cleanup case with fixed bottom hole pressure below dew point where the gas production has already dropped due to condensate dropout.
10. Improving the relative permeability of an oil based FF compared to a water based FF decreased GPL.
11. The hysteresis had a negligible effect on GPL.

In the second part of this study, the impact of the pertinent parameters on the clean up efficiency was further evaluated using a statistical approach. A 2-level full factorial statistical experimental design was used to sample a reasonably wide range of variation of pertinent parameters covering many practical cases. The variation of total of 16 parameters describing the matrix and fracture relative permeability of gas and FF, matrix capillary pressure were studied for two separate FF volume values (FVR=2 and 5). Due to the large number of simulations required for this purpose, a computer code was developed using matlab mathematical package, which linked automatically different stages of the simulations conducted using ECLIPSE100. Over 130000 simulation runs were performed for many different prevailing conditions. The gas production loss (GPL), compared to 100% cleanup case, was also calculated automatically as an output data for each run at different production periods after the FF injection. The linear repose surface without (LRSM) and with interaction parameters (ILRSM) models were used to relate the response (GPL) to the variation of the sixteen parameters. The least square method was used to estimate the regression coefficients in the models.

The analysis of the data for the fracture models with FVR=2 demonstrated that:

12. As FF and gas production continues, the number of the cases with severs gas production loss decreases but the relative importance of the pertinent parameters increases.
13. GPL is significantly affected by fracture conductivity.
14. The other important parameters, which influence GPL are FF exponent and end point of Corey type relative permeability curve in the fracture, gas exponent of Corey type relative permeability curve in fracture and matrix, differential pressure across the reservoir, interfacial tension, pore size distribution index, matrix permeability, the end points of Corey type relative permeability curve in the matrix, residual gas saturation in the matrix and porosity.
15. The impact of residual gas saturation in the fracture and gas end point of Corey type relative permeability curve on the GPL is negligible.

16. The presence of interaction parameters in the linear response surface fit resulted in better prediction of because of having more tuning terms, i.e. interaction coefficients.
17. Amongst 120 interaction terms, only few terms are considerable and they correspond to 1 year of production.
18. The scaled coefficients of the main terms of LRSM and those of ILRSM for GPL after 10 and 30 days of production, where GPL was large, were similar. It seems that the coefficients of the main terms were mainly affected the extent of GPL.
19. The analysis of the data for the fracture models with FVR=5 supported the main conclusions corresponding to those with FVR=2. However there were some differences as follows:
20. Increasing FF volume from 2 to 5 significantly increases the percentage of the cases with severs FF damage.
21. An increase in the FF injection volume increases GPL and delays the fracture clean up.
22. The relative importance of pertinent parameters when FVR=5 are less than those when FVR=2, especially at higher production periods.

2.8 RECOMMENDATIONS

In this study, some simplifying assumptions were made, which can be relaxed as described below:

a) Horizontal and Deviated wells:

1. The pressure drop along the horizontal and deviated well length was assumed negligible. A study can be conducted to investigate its impact on the effective wellbore radius approach. If the impact is significant it can be incorporated in the effective wellbore radius calculation of 1-D open hole system (EOH).

2. The impact of the formation damage due to the effect of drilling fluid was not considered here. The distribution of damage around the horizontal and deviated wells influences the well performance of HWs. It is recommended to extend the study to evaluate the impact of this damage on the HWs and DWs performance. It is suggested to define this effect as

another skin, which can be simply employed in the effective wellbore radius calculation.

3. The effect of gravity was not considered here, it is suggested to include gravity term in the governing equations solved here.

b) Cleanup Efficiency:

1. Here a pre-fractured well was considered to model fracture fluid invasion during a hydraulically fractured job. In order to model the process more realistically it is recommended that a mathematical model be developed which include the dynamics of creating a fracture with corresponding equations describing, simultaneously, the impact of stress and flow parameters.

It is also recommended to expand this study in other directions as follows:

a) Horizontal and Deviated Wells:

1. The application of the proposed effective wellbore radius approach can be investigated for fractured horizontal wells.
2. Study of flow around perforated horizontal and deviated wells can also be another area of the research.

b) Cleanup Efficiency:

1. As noted here, the statistical tool linear LRSM (with and without interaction terms) has been used for analysis data. Performing the same exercise using quadratic RSM is recommended.
2. The statistical approach followed here to evaluate the impact of parameters on the GPL for a fractured well can be extended to cover a wide range of the variation of fracture dimensions.
3. Recently an optimum fracture design was proposed for hydraulically fractured gas condensate wells by the Heriot Watt gas condensate research group (Mahdiyar et al. 2009). It estimates fracture dimensions giving the maximum productivity for a given fracture volume. This method is based on an ideal fracture with no contribution of cleanup efficiency. The results presented here can be used to improve this optimum fracture design.

Reference

H. Mahdiyar, Shiraz University, and M. Jamiolahmady and M. Sohrabi, 2009, Optimization of Hydraulic Fracture Geometry, SPE 123466-MS.